Department of Civil, Environmental and Architectural Engineering

Ph.D. in Geotechnical Engineering – XXVIII curriculum

Development and assessment of a numerical model for non-linear coupled analysis on seismic response of liquefiable soils

Anna Chiaradonna

A dissertation submitted in partial fulfillment of the

requirements for the degree of

Doctor of Philosophy

in

Geotechnical Engineering

2016

Supervisors

Prof. Ing. Francesco Silvestri

Prof. Ing. Anna d'Onofrio

Coordinator

Prof. Ing. Claudio Mancuso

TABLE OF CONTENT

LIST OF TABLES

LIST OF FIGURES

NOTATION

α is the steep of the cycli resistance curve

SR is the shear stress ratio

N is the number of cycles

N_{eq} is the number of equivalent cycles

SR_t is the trheshold value of the shear stress ratio

SR_r is the reference value of the cyclic resistance curve

N_r is the reference number of cycles, equals to 15

a is a parameter of the pore water pressure relationship

b is a parameter of the pore water pressure relationship

c is a parameter of the pore water pressure relationship

n is the number of elements

m_j is the mass of the generic sub-layer *j*

c_j is the viscous damping coefficient of the generic sub-layer *j*

k_j is the spring stiffness of the generic sub-layer *j*

r_j is the reaction of plastic slider (i.e. the limit shear strength) for a generic sub-layer *j*

ρ_j is the density of the *j*-th sub-layer

h_j is the thickness of the *j*-th sub-layer

G_j is the shear stiffness of the *j*-th sub-layer

$\ddot{u}_a$ is the absolute acceleration

$\dot{u}_a$ is the absolute velocity

u_a is the absolute displacement

$\ddot{u}_g$ is the base ground motion acceleration

$\dot{u}_g$ is the base ground motion velocity

u_g is the base ground motion displacement

a_{max} is the peak ground acceleration of the input motion

$\mathbf{M}$ is the mass matrix

$\mathbf{C}$ is the viscous damping matrix

$\mathbf{K}$ is the stiffness matrix

$\mathbf{f}$ is the vector of applied forces

$\mathbf{i}$ is the vector with each element equal to zero except for the last that is equal to unity

ρ_r is the density of the bedrock

$V_{S,r}$ is the shear wave velocity of the bedrock

V_S is the shear wave velocity

$f_{\max}$ is the maximum frequency of the input motion

$\mathbf{M}_s$ is the mass matrix for the sliding part of the dynamic system

$\mathbf{C}_s$ is the viscous damping matrix for the sliding part of the dynamic system

$\mathbf{K}_s$ is the stiffness matrix for the sliding part of the dynamic system

$\ddot{u}$ is the relative acceleration

$\ddot{u}_0$ is the sliding acceleration

$\ddot{u}_{eq}$ is the equivalent acceleration

$\dot{u}_0$ is the sliding velocity

u_0 is the relative sliding displacement

$h_{\max}$ is the maximum sub-layer thickness

α_R is the constant of the viscous damping matrix which multiplies the mass matrix

β_R is the constant of the viscous damping matrix which multiplies the stiffness matrix

ξ is the soil damping ratio

γ is the shear strain

γ^* is the actual shear strain of the spring above the sliding base

$\xi_{\exp}$ is the hysteretic damping measured in laboratory tests

G_0 is the initial shear modulus

γ_r is the reference shear strain of the MKZ model

β is the dimensionless factor of the MKZ model

s' is the dimensionless factor of the MKZ model

γ_c is the reversal shear strain

τ is the shear stress

τ_c is the reversal shear stress

γ_m is the maximum shear strain

$F(\gamma)$ is the generic stress-strain relationship

$F_{bb}(\gamma)$ is the back-bone curve

$F_{ur}(\gamma)$ is the unloading-reloading curve

$F^*(\gamma_m)$ is the damping reduction factor

ξ_{Mas} is the hysteretic damping calculated using the Masing rules

p_1 is the first non-dimensional parameter of the damping reduction factor $F^*(\gamma_m)$

p_2 is the second non-dimensional parameter of the damping reduction factor $F^*(\gamma_m)$

p_3 is the third non-dimensional parameter of the damping reduction factor $F^*(\gamma_m)$

$G(\gamma_m)$ is the secant modulus corresponding to the maximum shear strain level, γ_m

$\mathbf{x}$ is the vector of unknown variables

$\mathbf{x_t}$ is the vector of unknown variables at time t

γ_N is the default coefficient used in the Newmark β method

β_N is the default coefficient used in the Newmark β method

$\mathbf{q}$ is the vector of external applied forces

$\mathbf{q_{t+1}}$ is the vector of external applied forces at time *t*+1

$\mathbf{A}$ is the matrix of the Newmark β method

$\mathbf{B}$ is the matrix of the Newmark β method

$\mathbf{I}$ is the unit matrix

$\mathbf{0}$ is the null matrix

$\Delta\tau_j$ is the shear stress increment of the *j*-th soil layer

Δt is the time interval

$\Delta\gamma_j$ is the incremental value of shear strain

$u_j{}^t$ is the displacement at time *t*

$u_j{}^{t+1}$ is the displacement at time *t*

Δu_j is the displacement variation in time interval Δ*t* of the *j*-th soil layer

ε_{rel} is the maximum value of relative error

ε_{toll} is the fixed tolerance value

$\left[x_j\right]_k^{t+1}$ is the generic matrix calculated at the *t*+1 time as *k*-th attempt of the *j*-th soil layer

p' is the mean effective stress

p_{ref} is the reference pressure (100 kPa)

K_G is the stiffness coefficient

IP is the plasticity index

M_w is the moment magnitude

M_L is the local magnitude

I_A is the Arias intensity

PWP is the acronym of pore water pressure

PARI is the acronym of Port and Airport Research Institute

USGS is the acronym of United States Geological Survey

ACKNOWLEDGEMENTS

I would like to express my deepest and sincere gratitude to my supervisors, Professors Francesco Silvestri and Anna d'Onofrio, for their valuable support throughout the course of this study, and for everything I have learned from them. Special thanks to the researcher and friend Giuseppe Tropeano, for all his tireless work and help with the computer code.

Further appreciation goes to Professor Steve Kramer and Professor Pedro Arduino, for their guidance and never ending encouragement and enthusiasm during my internship at University of Washington. Thanks also to the PhD students that I met in Seattle for their friendship, support and help.

Special thanks to all my undergraduate students for their significant contribution to this study.

I would like also to extend my sincere thanks to three generations of PhD students at University of Naples. From Luigi Landolfi to Domenico De Sarno, I am definitely grateful to them for every suggestion, advice and shared experience.

Finally, I extend my deepest gratitude to my family for their patience, understanding and encouragement, and I dedicate this thesis to them.

ABSTRACT

Widespread liquefaction evidences characterized the most recent earthquakes in Italy (Emilia, 2011) and in the world (Canterbury, New Zealand, 2010-2011), resulting in a renewed interest on the characterisation and modelling of pore pressure build-up during seismic events. In particular, it has been highlighted the roughness of some traditional tools for assessing the liquefaction susceptibility as well as the overall complexity of the available numerical models. Therefore, it seems necessary to develop reliable analysis method that comprehensively take into account for the complexity of the mechanical behaviour of soils, even though remaining accessible for professional practice.

In this work, a simplified constitutive model, incorporated in a one-dimensional code, is proposed. It allows to pursuing a simplified dynamic analysis: it is easy to be applied as the semi-empirical methods and reliable as an advanced numerical approach. The proposed model is based on the results of laboratory undrained cyclic tests. It is easy to calibrate and reasonably approximates the main features of soil behaviour. The numerical formulation of the model has been incorporated in a one-dimensional computer program for seismic soil response, in order to develop a useful tool for engineering practice. In the same code it has been also implemented a numerical routine modelling the pore pressure dissipation thus allowing to simulate both the pore pressure build-up during the seismic event as well as its dissipation.

The upgraded code has been validated using test sites data in order to provide an extensive documentation of the capabilities and limitations of the implemented model in prediction the seismic site response under strong ground motions.

Finally, the developed code has been used to perform specific analyses on a dyke, severely damaged by the 2012 Emilia earthquake sequence. Taking into account the aftershocks that followed the main seismic event, effective stress analyses have been allowed a better understanding of the damage source detected along the embankment.

I. INTRODUCTION

Since the catastrophic failures due to soil liquefaction occurred during Niigata and Good Friday (Alaska) 1964 earthquakes, increasing efforts have been devoted to the understanding and modeling of the phenomenon as well as to the development of effective methods for the prediction the liquefaction potential of soil deposits. In the last 40 years since these earthquakes, liquefaction has been extensively studied extensively by hundreds of researchers around the world. Much has been learned, but the road has not been smooth.

Pioneering studies on liquefaction phenomena were based on measurements of pore pressure build up during undrained cyclic laboratory tests carried out on loose and dense sand. These studies highlighted the dependence of cyclic resistance on factors such as soil density and shear stress amplitude. Subsequent work showed that cyclic resistance measurements are strongly influenced by soil fabric, stress history, overconsolidation ratio and lateral earth pressure coefficient. All these factors can be easily destroyed by sampling disturbance and hardly replicable in reconstituted specimens. For these reasons and thanks to the increasing availability of field data related to liquefaction case histories, these data started to be used to characterize liquefaction resistance in terms of measured in situ test parameters.

The Cone Penetration Test (CPT) and Standard Penetration Test (SPT) are the two most widely used indices for evaluating the liquefaction characteristics of soils. Shear wave velocity (V_S) tests, tend to be used in special situations and thus are used less often than the SPT and CPT in liquefaction evaluations.

Both the approaches, eventually used in conjunction with a simplified dynamic analysis, permit to evaluate the conditions (seismic demand and soil capacity) than can trigger liquefaction but does not allow analyzing the stress-strain evolution of a soil volume. Furthermore, they have some limitations and need some assumptions, such as to convert the irregular earthquake history into an equivalent uniform load. For this reason, in the last fifteen years, a number of constitutive models have been developed to simulate the cyclic loading of non-cohesive soils, with emphasis on cyclic mobility and/or flow liquefaction, basically built on the theory of incremental plasticity. Adequate complexity of constitutive modeling allows efficient prediction for widely different boundary value problems and different loading paths. On the other hand, complex models need specific expertise and often require a great number of geotechnical parameters that are not easily available. Nevertheless, simpler approaches based on empirical charts or simplified dynamic analyses have been also developed over the years. These approaches still remain the most used tools in geotechnical engineering practice since the difficulty to use demanding constitutive models.

In this thesis, a simplified constitutive model aimed at simulating the pore pressure buildup in a soil element is proposed. It has been implemented in a one-dimensional code thus allowing to carry out simplified 1D dynamic analyses in effective stress conditions. The performances of the code are evaluated by analyzing different liquefaction case histories. The comparison between recorded and simulated data highlighted that notwithstanding the simplicity of the proposed approach the code provides reliable results.

I.1. Definition of the problem

Dependence of soil response on the level of seismic loading involves rather complex mechanical processes, which may be grouped roughly in two main classes. The first is the degradation of mechanical properties of the material, which is characterized by a decrease in the shear modulus coupled with an increase in energy dissipation; while the second is related to the volumetric-distortional coupling, that takes place at higher stress state and could induce either volumetric strains of the soil skeleton under shear stress in drained conditions, or pore pressure changes in water-saturated soils in undrained conditions, that, in turn may evolve into liquefaction (in the case of loose sandy soils).

While the importance of first class of non linear effects has been widely recognized and modelled in the most common and commercial codes performing seismic site response (Hashash et al., 2015; Geostudio, 2007; ITASCA, 2011), the modelling of pore pressure

change still remains a challenging issue, due to the limitations of simplified approaches and the specialized knowledge required by advanced constitutive models.
The first goal of the present study is to search and develop a constitutive model that is easy to calibrate utilizing the limited data usually available and that can reasonably approximate the main characteristics of soil behaviour. The second goal is to incorporate the model in a simple computer program in order to develop a useful tool functional for engineering practice. An extensive documentation of the capabilities and limitations of the implemented model in predicting the seismic soil response under strong ground motions is finally provided.

I.2. Organization of the text

The present research consists of seven different and related chapters.
Chapter one reports the description of the problem and the definition of the aim of the study.
Chapter two contains a general overview of the gained experience on liquefaction as results of the recent seismic events and the existing analysis methods.
Chapter three describes the original and updated formulation of a simplified pore water pressure build up model. The model is based on the results of cyclic laboratory tests; the calibration of the model parameters has been analyzed in details considering both simulated and experimental data. A pore pressure dissipation model based on one-dimensional consolidation theory has been also integrated in the formulation in order to simulate both generation and dissipation of excess pore water pressure.
Chapter four details the implementation of the integrated pore water pressure and dissipation model inside a numerical computer program.
In Chapter five, the performances of the upgraded code are assessed on well documented case histories in which vertical array records and, sometimes, pore pressure buildup measurements, are available. Both the accuracy and practical usefulness of the code are assessed by comparing calculated predictions and field records.
Chapter six presents the case history of a dyke damaged during the seismic sequence occurred in Emilia plain (Italy) in May, 2012. Effective stress analyses have been adopted for studying deeply the source of damage induced by the earthquake, taking into account also the sequence of three seismic events occurred in less than ten minutes.
Finally, Chapter VII presents the conclusions and the future perspectives of the research.

I.3. References

GEOSTUDIO International Ltd. (2007). QUAKE/W User's manual. Calgary, Alberta, Canada.

Hashash Y.M.A., Musgrove, M., Groholski D.R., Phillips C.A., and Park D. (2015) DEEPSOIL 6.0, User Manual 104 p.

ITASCA (2011). FLAC –Fast Lagrangian Analysis of Continua– Version 7.0. User's Guide, Itasca Consulting Group, Minneapolis, USA.

II. BACKGROUND

In this chapter, a brief review of the lessons learned from the occurrence of liquefaction due to strong seismic events in Italy and around the world is described. A classification of the available methods to evaluate the site liquefaction susceptibility is therefore presented in the second paragraph highlighting advantages and limitations of the different approaches. Finally, the last paraghaph focuses on evaluating the capabilities of one-dimensional, fully nonlinear effective stress procedures in modeling the seismic response of sites where significant pore water pressure buildup is expected.

II.1. Deformation phenomena and liquefaction occurred in recent earthquake

Most of the liquefaction phenomena observed during the last strong earthquakes interested reclaimed lands, landfills and natural or artificial enbankments.

One of the most popular case is the massive liquefaction phenomena occurred during the strong earthquake which struck Kobe city (Japan) in 1995. All the damaged sites correspond to the land reclaimed since 1868 (Figure II.1.1), which confirms that the occurrence of liquefaction is due to both in-situ conditions and applied horizontal acceleration. Loose riverbank sand deposits liquefied causing damages to leeves; liquefaction was also observed in inland areas characterised by high ground water levels (Shibata et al., 1996).

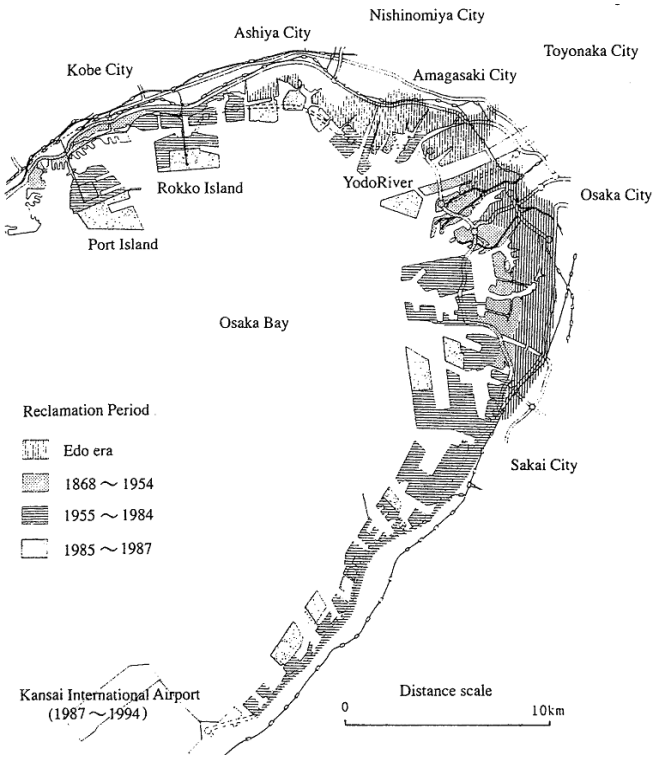

Figure II.1.1 – History of reclamation along the coastal areas of Osaka Bay (Shibata et al., 1996)

Reclamation islands, constructed to expand the Kobe port, were severely damaged even if they were made of gravelly soils, apparently no liquefiable. Indeed, Figure II.1.2 shows the situation of ejected sand and gravel in the southern side of Rokko Island, where it is possible to notice that also cobbles with a grain size larger than 10 cm were ejected.

A wide description of a reclaimed island, Port Island, will be reported in chapter V, with a focus on the vertical seismic array installed at that site.

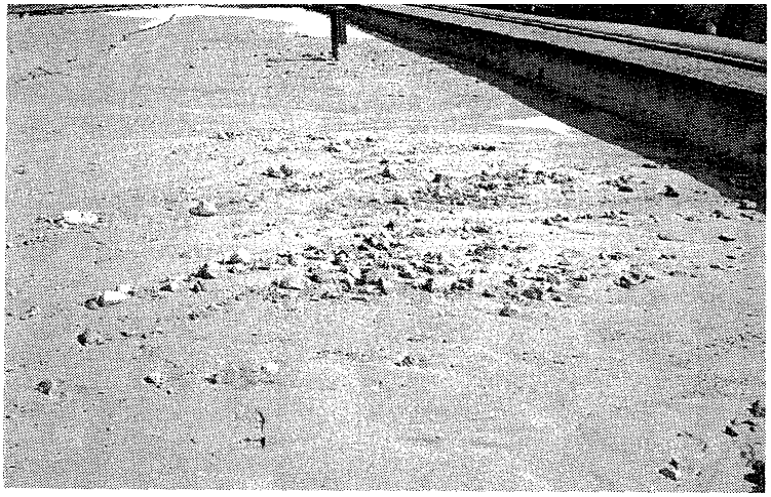

Figure II.1.2 – Liquefaction of gravel at Rokko Island (Shibata et al., 1996)

River dikes built to control flood also suffered extensive damage consisting of cracking, settlement, lateral spreading and slumping. As shown in Table II.1.1, the damage was observed on six rivers for a total of about 9 km of levees damaged. At most of the sites, sand boils were observed on the ground surface near the dikes (Matsuo, 1996).

Table II.1.1 – Summary of damage to river dykes (Matsuo, 1996)

River	Location (Prefecture)	Number of damage sites	Total length of damaged sites (in m)
Yodo-gawa	Osaka	18	6590
Kanzaki-gawa	Osaka	1	30
Ina-gawa	Hyogo	3	610
Mo-kawa	Hyogo	5	680
Kako-gawa	Hyogo	3	1180
Yura-kawa	Kyoto	2	200
Total		32	9290

The most severely damaged were Torishima and Nishijima dikes, located along the left and right side, respectively, of the Yodo river, which flows through Osaka city (Figure II.1.1).

Figure II.1.3 reports the cross section of Torishima dyke, before and after the earthquake. The dyke was designed to protect land against the high sea tide of 5.2 m above the mean sea level. The core of the structure was a soil embankment and the river side surface was protected by a concrete parapet wall, 8.1 m height from the sea level.

After the seismic event, the parapet at the top of the levees tilted and settled, sliding about 8 m into the river. The embankment also cracked severely and settledup to 3 m. Sand boils along the fissures were observed on the ground surface along the dike, suggesting that the damage was caused by liquefaction of the loose sand layer under the embankment.

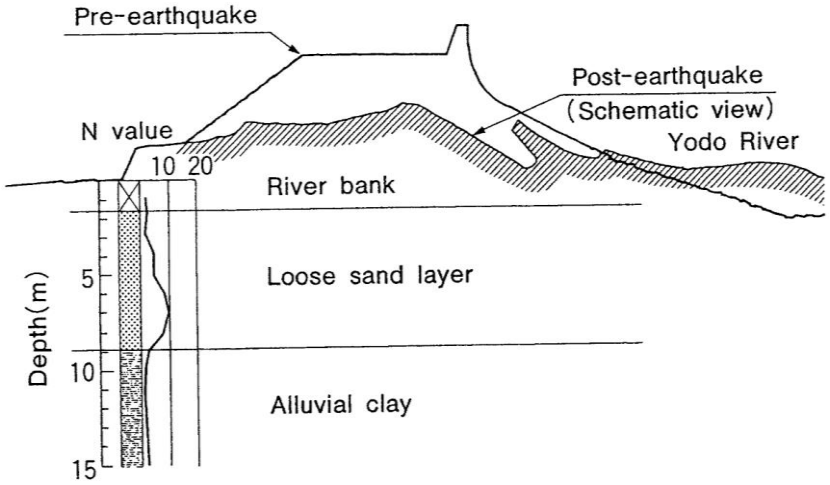

Figure II.1.3 – Cross section of the Torishima dyke (Shibata et al., 1996)

Figure II.1.4 shows the cross section of the failed Nishijima dyke together with the boring data and the soil profile. The embankment has a structure similar to that of Torishima dyke, but in this case no damage to the parapet was observed. Embankment slope failure occurred in the rear slope and cracks were about 20 to 150 cm wide at the crest. Sand boils were observed near the toe, which displaced about 1 m. Also in this case, the liquefaction of the Holocene sand deposit (As2) under the dyke seems to have induced the embankment slope failure (Figure II.1.4).

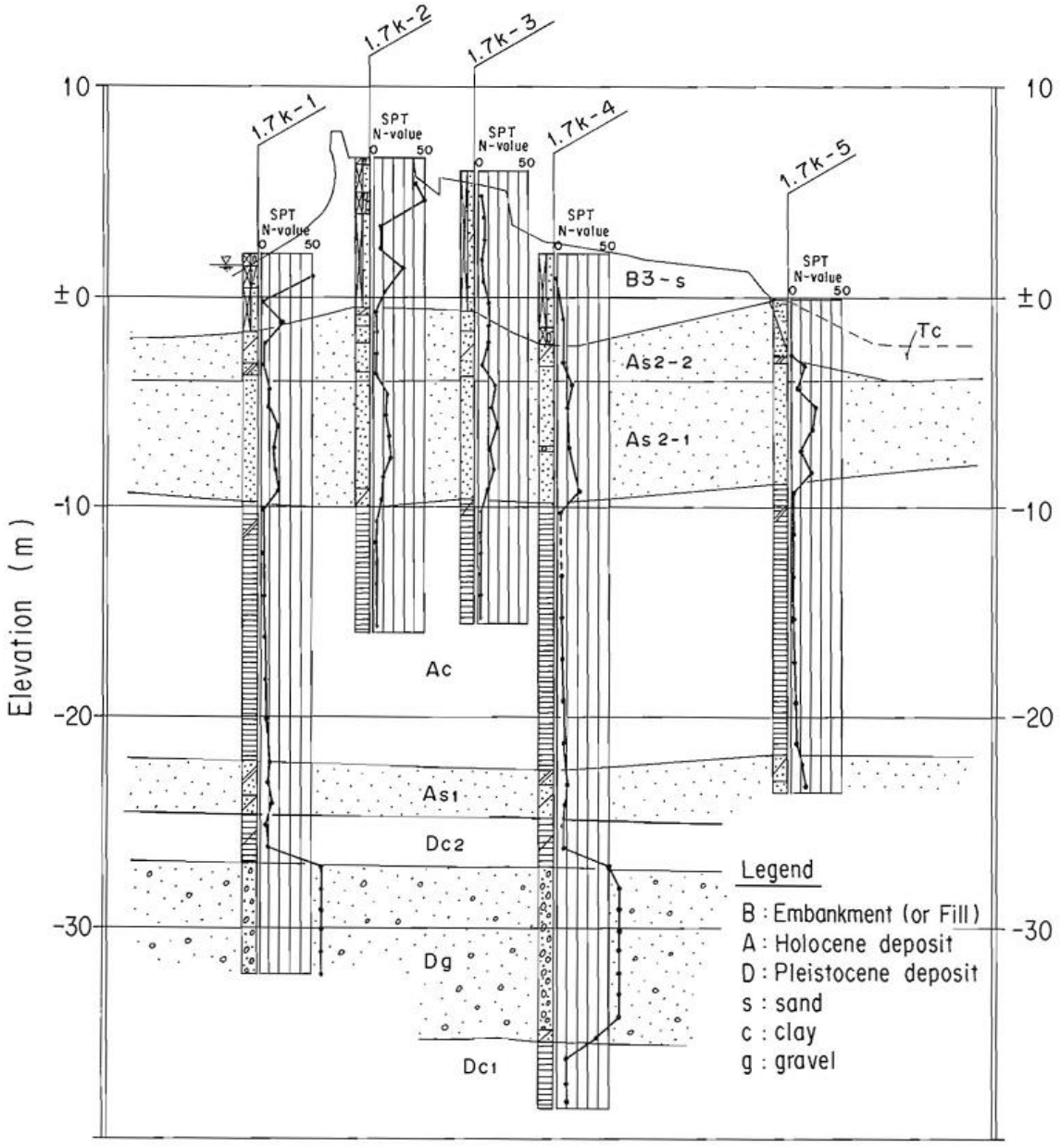

Figure II.1.4 – Cross section of Nishijima dyke

Liquefaction induced dyke failures also during the 1993 Kushiro-oki earthquake (M= 7.8) which struck the Hokkaido region in the northern of Japan (Figure II.1.5). Along the Kushiro river, very close to the epicenter, dikes were damaged over a length of 10124 km (Sasaki, 2009).

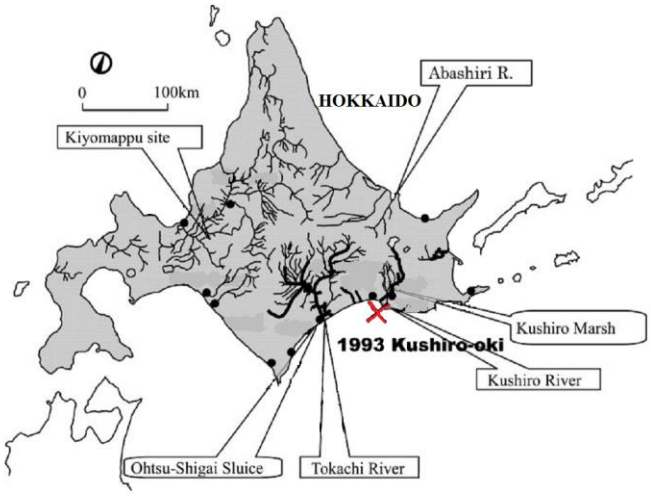

Figure II.1.5 – Kushiro-oki earthquake and most damaged river dykes (mod. after Sasaki, 2009)

Figure II.1.6 reportes a typical section of the right side bank of the Kushiro river and related damages. At this section, the crest of the dyke subsided and deep cracks were generated near the top of the slope.

It was found that the failure was induced by liquefaction occurred in the body of the dyke. Indeed, construction of the dyke, using sand fill directly resting on highly compressible peat deposit, resulted in consolidation settlement (2 – 3 m) under the weight of the embankment. This settlement brought the lower part of the sand fill below the water table that existed at the time of the earthquake. The saturated bottom part of the dyke liquefied during the earthquake triggering the failure.

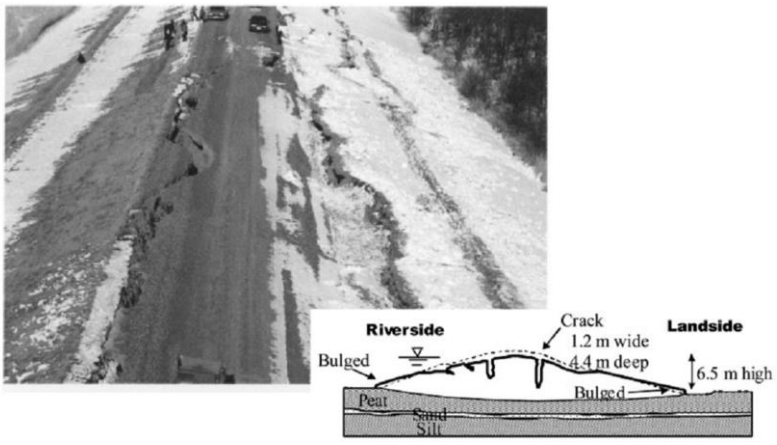

Figure II.1.6 – Damage and cross section of Kushiro dyke (Sasaki, 2009)

More recently, a long seismic sequence devastated much of the city of Christchurch (New Zealand) and surrounding areas from September 2010 to February 2011 (Figure II.1.7).

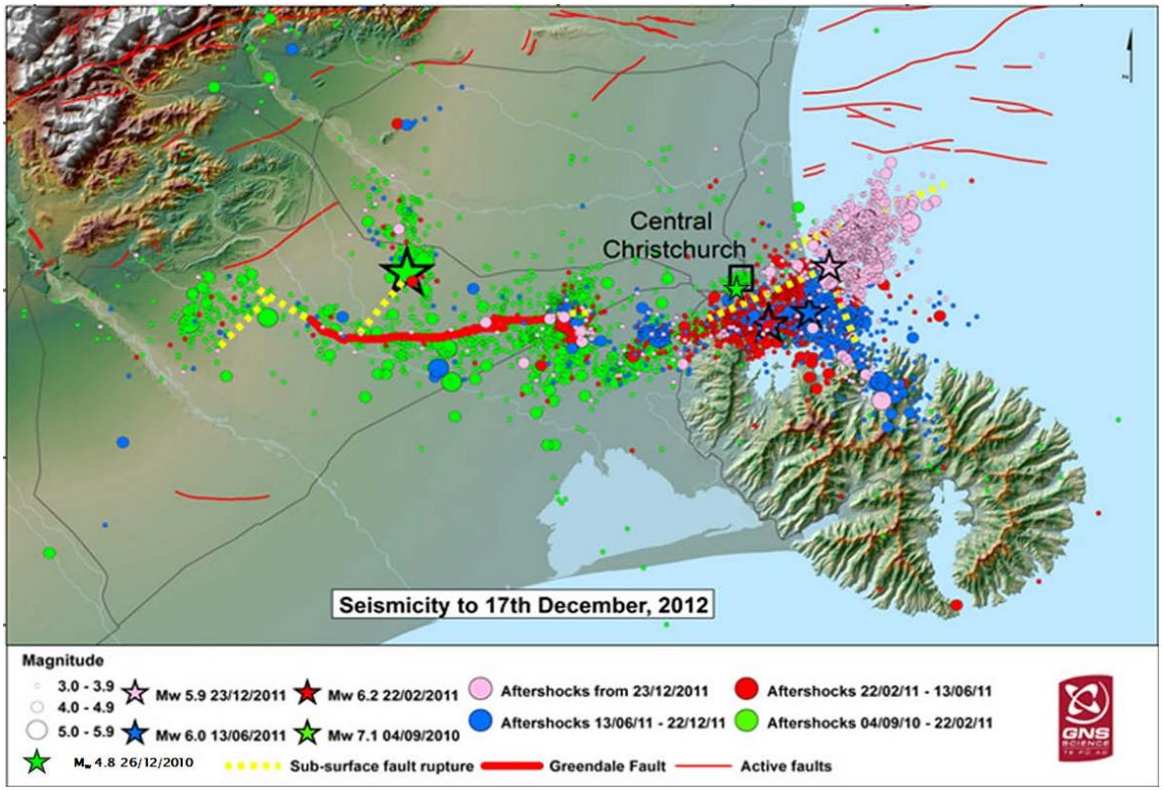

Figure II.1.7 – Location mainshocks and aftershocks up to 17 December 2012 (Markham et al., 2014)

Liquefaction during the 4th September 2010 Darfield event (M_w 7.1) affected approximately 10% of the area of Christchurch, while the 22nd February 2011 Christchurch event (M_w 6.2) affected over 50% of the developed land (Figure II.1.8). Including these two events, there were a total of seven events with moment magnitude greater than or equal to 5.5 between the 4th September 2010 and 23rd December 2011 that caused varying degrees of liquefaction in and around Christchurch. Moreover, the M_w 4.7 event that occurred on the 26th December 2010 and M_w 5.0 event of the 16th April 2011 triggered isolated cases of liquefaction (Markham et al., 2014).

The damaged area is located inside the Canterbury plain, formed by overlapping alluvial fans produced by glacier-fed rivers from the mountain range in the south of island (Figure II.1.9a). Most of Christchurch was built on floodplains and swamps behind a series of barrier dunes composed of fine-grained beach/dune sand, and lagoons. The Waimakariri river regularly flooded Christchurch before levees construction and river realignment, shortly after the city was established in 1850 (Green at al., 2014). Of particular relevance to liquefaction susceptibility in Christchurch and its environs are the locations of abandoned paleo-channels

of the rivers. These areas were filled with young loose sandy sediments, which result highly susceptible to liquefaction in combination with shallow groundwater levels (from 1 m to 5 m below ground surface),

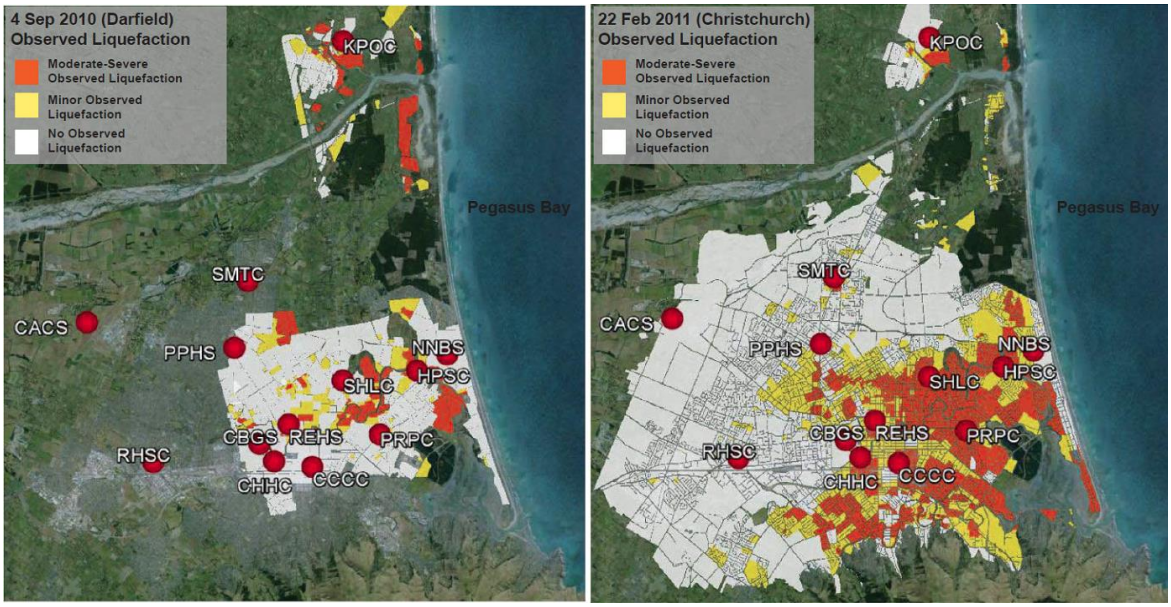

Figure II.1.8 – Liquefaction maps for the Darfield and the Christchurch events (Markham et al., 2015)

One of the worst hit locations was the small town of Kaiapoi north of Christchurch, established on the banks of the Kaiapoi river, a branch of the Waimakariri river (Figure II.1.9a,b). This latter was extensively modified both by natural and human processes, consequently many areas in and around the town were once former river channels (Wotherspoon et al., 2012).

Using historical accounts and maps of the region, Wotherspoon et al. (2012) identified areas of land reclamation and old channels that were cut off from the river since the beginning of European settlement in the 1850s. Significant liquefaction damage were observed in these areas after the Darfield event. Significant lateral spreads and sand boils developed in areas of reclamation along the current river path, with fissures up to 2 m deep and 1 m wide (Figure II.1.9c,d). The damaged river banks caused settlement and tilting of structures in the surroundings area, with several residential structures severely damaged. Moreover, in all former channel areas, underground services, roads and railways were severely impacted as a result of cracking and ground movements (Wotherspoon et al., 2012).

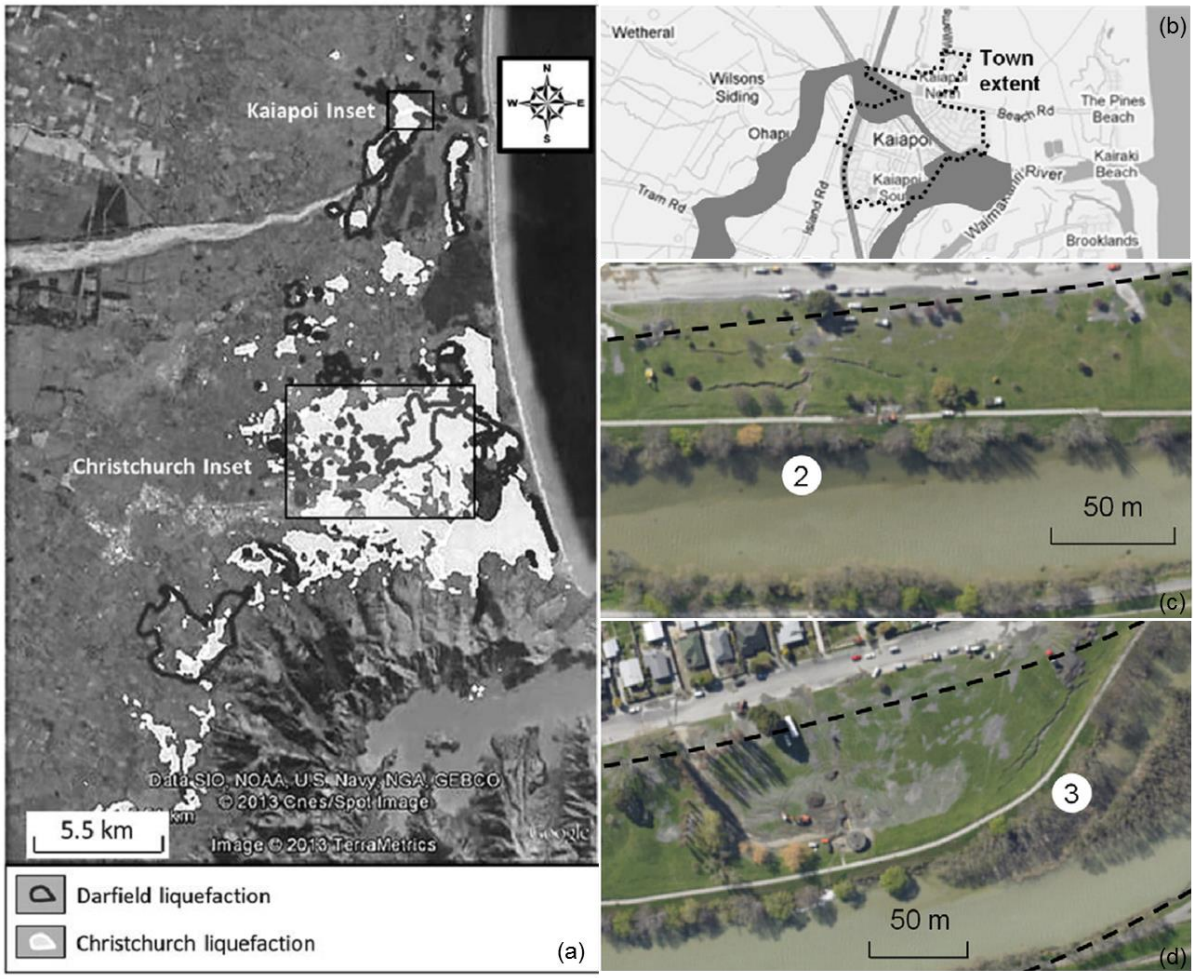

Figure II.1.9 – Liquefied areas during the Darfield and Christchurch earthquakes (a); Focus on Kaiapoi town (b) large lateral spread fissures (c) and sand ejecta (d) in reclaimed land along Kaiapoi river

Similar evidences have been characterized the seismic sequence that occurred in the Emilia Romagna region in May – June 2012. This sequence of events consisted of two main shocks occurred on May 20 (M_W=6.1) and May 29 (M_W=5.9), five more shocks with M_L>5 and about 2500 smaller earthquakes (Figure II.1.10).

The hit area is located in the south of the Po plain, in the foreland basin of two mountain range constituted by the Alps and the northern Appennine. A complex system of tectonic structures is buried under a thick sedimentary fills, so that the thrusts are generally buried (Fioravante et al., 2013). The main tectonic structure is a buried ridge known as Ferrara folds, which reaches its maximum height, about 120 m below the ground surface, near the city of Ferrara.

The subsoil is characterized by alluvional deposits of different depositional environment, which consists of alternated layers of silty-clayey deposits and sandy soils of channel and levees. Along ancient rivers banks many small villages were establishes in order to safeguard buildings from floods (Figure II.1.11).

Figure II.1.10 – Epicenters of the shocks with M_L > 3.5 from May to June 2012

Widespread liquefaction phenomena mainly involved the old river bed deposits and levees of rivers and channels (Figure II.1.11). Significant liquefaction effects particularly interested two villages constructed above the abandoned channel of the Reno river, San Carlo e Mirabello. After the 20 May earthquake, typical soil liquefaction evidences were observed: sand boils, surface ruptures and extensional fissures (Figure II.1.12b-e). wide areas were covered of erupted material, whose thickness was more than 30 cm in many cases. In some locations, such as Sant'Agostino, bulges and fractures were observed at the bottom of artificial channels due to the sand eruption (Figure II.1.12d).

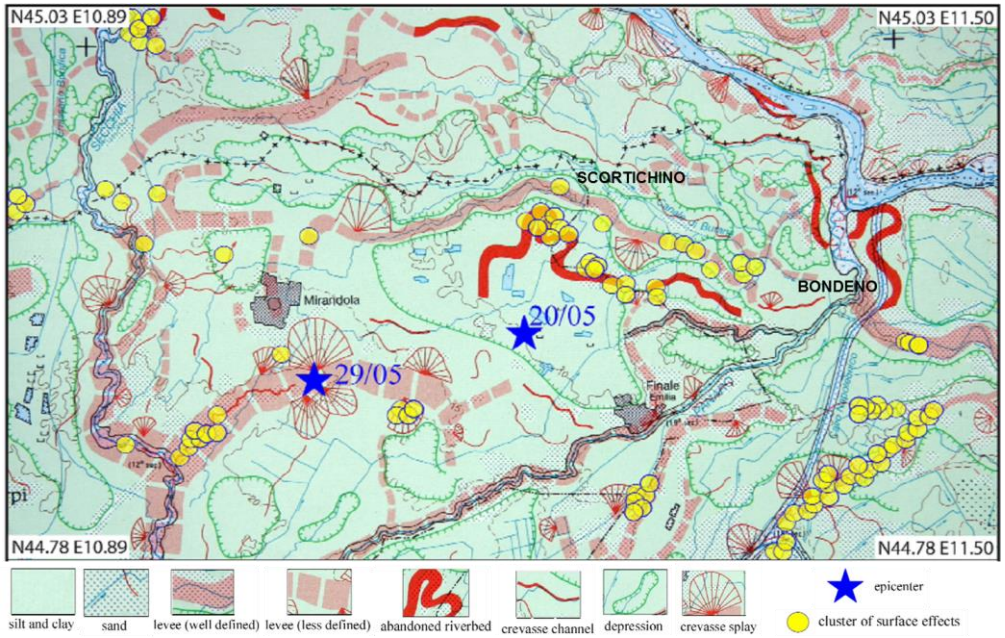

Figure II.1.11 – Map of superficial effects and geomorphological features (Bertolini and Fioroni, 2012)

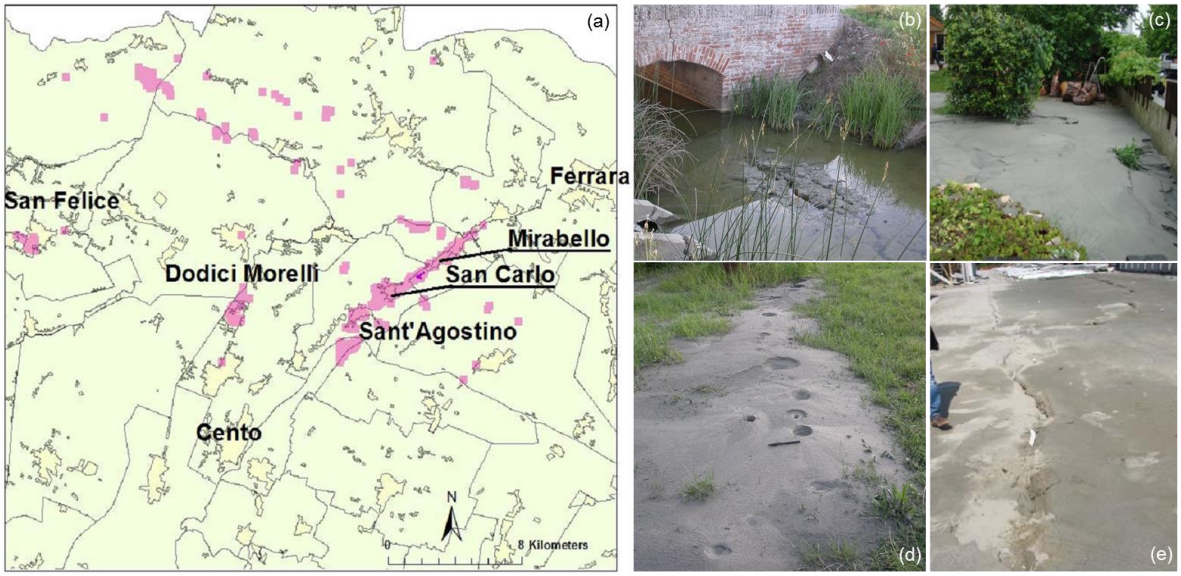

Figure II.1.12 – Map of soil liquefaction phenomena (a) and damage observed at the bottom of artificial channel (b) sand eruption (c), sand boils (d) and longitudinal fractures (e) (from Fioravante et al., 2013 and ISPRA, 2012)

Bertolini and Fioroni (2012) inventoried more than 700 superficial effects thanks to aerial photographs. Seventy percent of the observed effects occurred within town and village boundaries, while the remaining 30% was observed in open agricultural fields and was characterized almost exclusively by sand vulcanoes and eruption of wet sands from ground fissures. Figure II.1.13 shows long tension cracks (up to 1 m width and 2 m depth) and eruptions (yellow spots) from wells, cracks and foundations inside the town of San Carlo, which help to understand the extension of the mapped surficial effects.

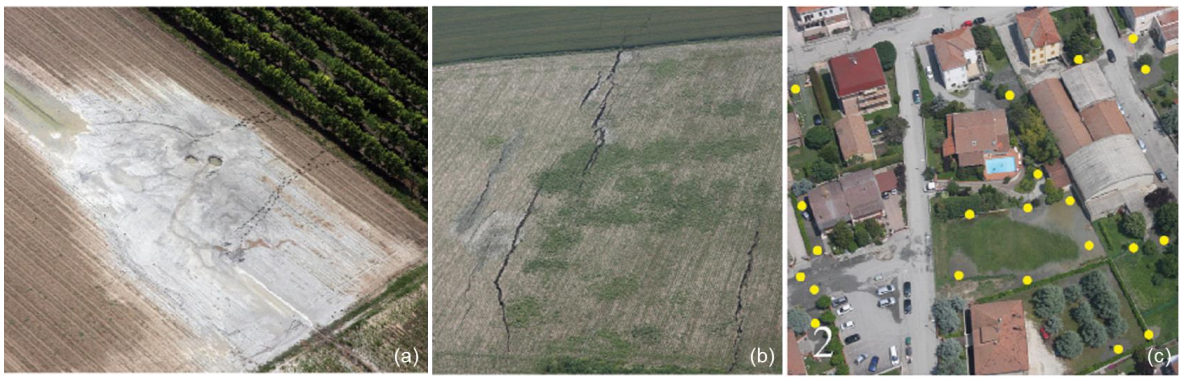

Figure II.1.13 – Sand eruption (a) and cracks (b) in field and sand eruptions (yellow spots) in the town of San Carlo (c) (mod. after Bertolini and Fioroni, 2012)

Moreover, the Agenzia Regionale Prevenzione e Ambiente (ARPA) of the Emilia Romagna region manages an automatic monitoring network composed of 40 stations for monitoring the water levels and the temperatures inside wells, at a rate of one measure per hour (Marcaccio

and Martinelli, 2012). In concomitance with the May-June 2012 seismic sequence, sudden water uprising phenomena were recorded by some automatic station located in the provinces of Modena and Ferrara (Figure II.1.14).

Water levels increased up to 1.5 m after the mainshock of the 20th May, and then decreased in the days following the earthquake. After the second mainshock of the 29th May, a second increase of the water levels was observed, even if less prominent respect to the first one.

These data have been considered useful to understand the relationships between seismic events and the local groundwaters.

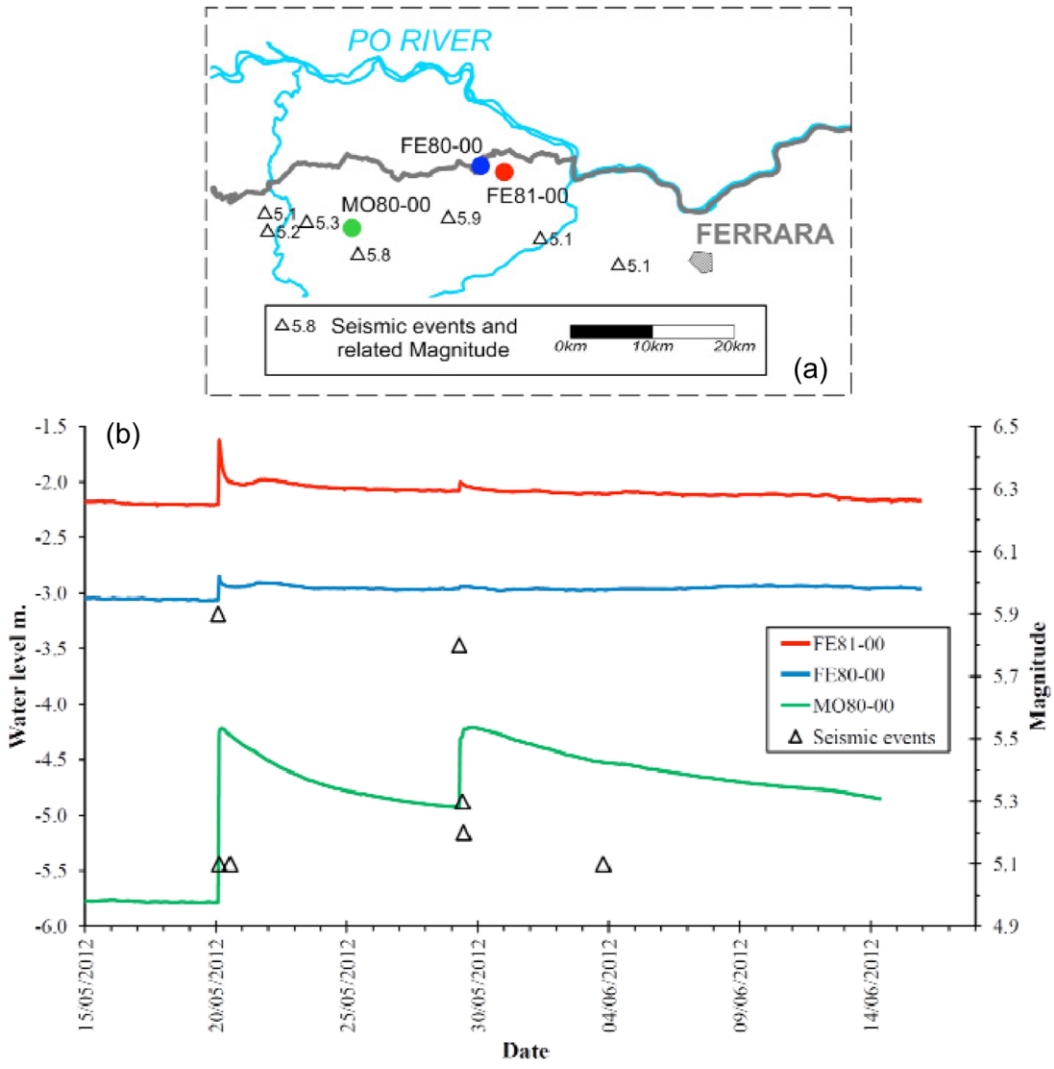

Figure II.1.14 - Monitoring stations location (a) and water-level changes in concomitance with some significant seismic events (b) (Marcaccio and Martinelli, 2012)

II.2. Limits of simplified approaches and total stress analysis

The engineering understanding of the seismic behaviour of soil structures subjected to extensive and damaging liquefaction can be widely improved by taking advantage of the experiences provided by the above mentioned case histories.

A reliable computation of damages due to liquefaction, starts with a correct evaluation of the seismic response of sites potentially prone to develop significant pore water pressures during earthquake shaking. This evaluation in turn can be achieved by adopting approaches characterized by an incrasing level of complexity, as shown in table Table II.2.1 where a hierarchical classification of the possible approaches is reported (Silvestri and d'Onofrio, 2014).

The methods of analysis for the liquefaction assesment are listed in table II.2.1 as an increasing function of the refinement and degree of detail of the results, which in turn are proportional to the effort spent in terms of experimental and numerical resources as well as in term of complexity of the constitutive model adopted.

Table II.2.1 – Hierarchy of analysis methods for liquefaction assessment (mod. after Silvestri and d'Onofrio, 2014)

<table>
<tr><th>Analysis method</th><th>Reference input motion</th><th>Constitutive model</th><th>Investigation and tests</th><th>Typical output</th></tr>
<tr><td>Screening criteria</td><td>Magnitude and distance</td><td>-</td><td>-</td><td>Liquefaction yes/no</td></tr>
<tr><td>Semi-empirical methods</td><td>Maximum acceleration a_{max}
Magnitude</td><td>Rigid - plastic</td><td>Ordinary investigation in-situ and laboratory
Shear wave belocity measures, VS</td><td>Safety factor</td></tr>
<tr><td>Simplified dynamic</td><td rowspan="3">Accelerograms $a(t)$</td><td>Equivalent linear/ non-linear</td><td rowspan="3">As above plus cyclic and dynamic laboratory tests</td><td>Accelerogram
Displacement
Total stress
Strain
Safety factor profile</td></tr>
<tr><td rowspan="2">Advanced dynamic</td><td>Polyphase medium approximate coupled</td><td rowspan="2">As above plus
Excess pore water pressure
Effective stress</td></tr>
<tr><td>Polyphase medium Stricly coupled</td></tr>
</table>

As regard to the semi-empirical methods, there are basically two different approaches for evaluating the liquefaction potential of saturated soils: (1) evaluation based on the performance of soil deposits in previous earthquakes and extrapolation of such data to new conditions; and (2) evaluation based on comparison of the stresses induced in the ground by

the earthquake with the stress conditions causing liquefaction of the soils as measured by laboratory tests.

In both cases, the safety against liquefaction to a generic depth is reviewed in terms of safety factor defined as the ratio between the available resistance to liquefaction (state of critical effort associated with liquefaction condition or occurrence of large plastic deformation) and stress induced by the seismic action. Both stress parameters are normalized with respect to the vertical effective stress acting at the considered depth, so as to define a cyclic resistance ratio, CRR, and a cyclic stress ratio, CSR. If the first semi-empirical method is adopted the cyclic resistance ratio, CRR, is estimated using the results of in-situ tests (CPT penetration resistance, SPT blow count, or shear wave velocity, Vs); otherwise a cyclic resistence curveobtained from laboratory tests (simple shear test, torsional shear test, cyclic triaxial test), provides the proper CRR

The definition of seismic demand has inherent the concept of converting the irregular seismic action into an equivalent number of cycles of uniform shear stress, as introduced by Seed and Idriss (1971). Indeed, the cyclic stress ratio, CSR is computed as

$$CSR = \frac{\tau_{eq}}{\sigma'_{v0}} = 0.65 \frac{a_{\max}}{g} \frac{\sigma_v}{\sigma'_v} r_d \qquad \text{(II.2.1)}$$

Where a_{max} is the peak acceleration at the ground level for the design earthquake; g is the gravity acceleration; σ_v and σ'_v are respectively the total vertical stress and the vertical effective stress to the considered depth; r_d is a reductive coefficient of the seismic action, taking into account the deformability of the soil. In the described approaches, the cyclic stress ratio, CSR, is the normalized amplitude, τ_{eq}, of an equivalent uniform history of shear stress, in which the earthquake is converted. The uniform load is defined equivalent because, in principle, should produce the same pore pressure build-up expected at the site by the irregular seismic action.

In order to apply the semi empirical approach based on the cyclic resistance measured from laboratory tests it is necessary to define also the number of cycles, N_{eq}, of the uniform equivalent load. A wide range of conversion procedures is available in literature (Seed et al., 1975; Annaki and Lee, 1977; Biondi, 2002; Green and Terri, 2005). These procedures, however, are rather complex and their results strictly depend on the adopted conversion curve and on the techniques for choosing and counting the stress cycles that significantly affect the pore pressure build-up (Biondi et al., 2012).

As a consequence, a number of empirical relationships for the assessment of N_{eq}, bypassing the conversion procedure, were developed over the years. These models relate N_{eq} to the magnitude of selected design earthquake, to site-source distance and, finally, to parameters

describing the energy and frequency content and the significant duration of the imposed ground motion (Figure II.2.1).

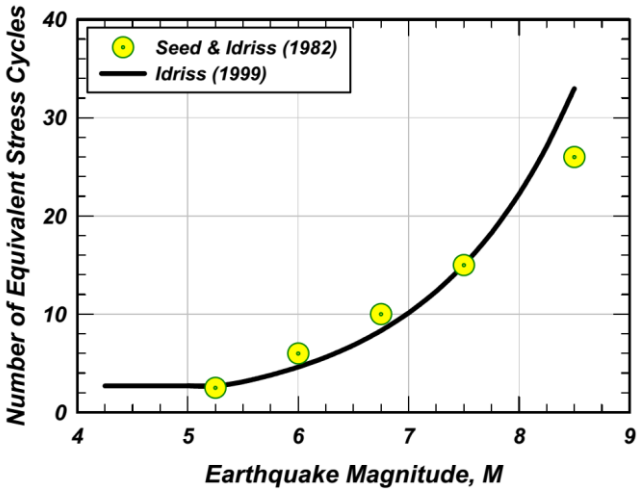

Figure II.2.1 - Number of equivalent uniform cycles versus earthquake magnitude, M_w (Idriss and Boulanger, 2004)

In the case of the simplified dynamic approach, a safety factor can still be computed along a vertical soil profile but, in this last case, the seismic response of the soil column is taken into account. The stress- strain behavior is usually modeled as linear equivalent visco-elastic, independent from the failure condition typically modeled with a rigid -plastic approach.
The seismic demand is expressed as

$$CSR = 0.65 \frac{\tau_{\max}}{\sigma'_{v0}} \qquad \text{(II.2.2)}$$

where τ_{max} is the peak value of the shear stress history computed by a seismic response analysis in total stresses (Figure II.2.2).

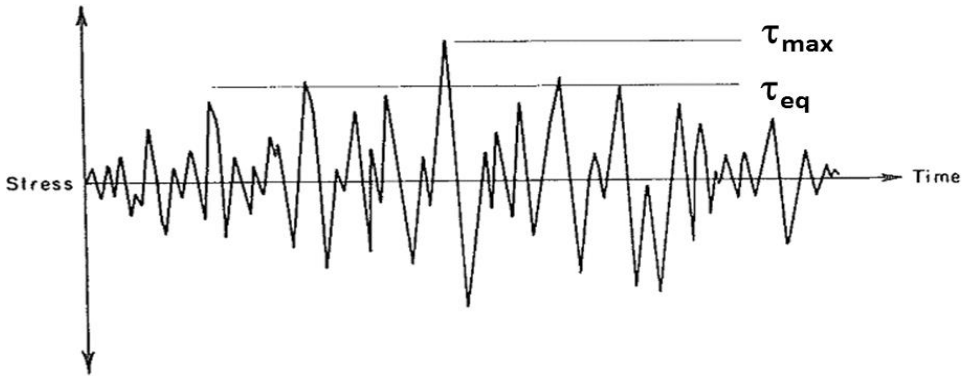

Figure II.2.2 – Definition of equivalent shear stress (mod. after Seed and Idriss, 1971)

Finally, the advanced dynamic methods allow the predictions of the dynamic behavior of the soil volume in terms of stress-strain magnitudes. Within this level of approach the analysis methods are classifiable based on:

- The different method adopted to compute the stresses induced by the earthquake in the soil, typically related to the way of treating the non-linearity of the stress-strain relationship (linear analysis, equivalent linear, non-linear);
- The different constitutive model adopted: e.g. Hypoelastic models (such as the hyperbolic), elasto-plastic with isotropic hardening (e.g. Cam Clay type) or kinematic, elasto-visco-plastic, and so on;
- The different geometric discretization adoptable, which leads to the finite element method (FEM), the finite difference (FDM), or distinct elements (DEM).

It is worth noting that only coupled non linear analyses allow the prediction of effects related to pore pressure buildup; on the other hand, such rigorous approach require a high number of constitutive parameters to be experimentally measured by non conventional apparatuses; furthermore their results are strongly influenced by the adopted earthquake scenario. On the other hand, it is possible to evaluate the excess pore pressure induced by the earthquake at every depth and time istant whithin the analised domain.

The advanced effective stress analyses can be further divided into two categories based on the way the intaraction between the two phases is modelled: (1) approximate methods, in which the interaction is expressed through simple empirical correlations; and (2) strictly coupled methods, also called rigorous methods in effective stresses, in which the interaction between phases is modelled through a system of differential equations describing the theory of consolidation generalized to the dynamic field (Sica, 2000).

The rigorous analyses are generally carried out to solve two-dimensional problems (rarely three-dimensional) using numerical codes based on finite elements or finite differences and constitutive models based on the incremental plasticity theory. For this reason, at the moment, their application is generally limited to structures with strategic relevance (e.g. earth dams) which can justify the use of such methods of analysis and sophisticated investigations.

Also 1D effective stress analyses are included in the category of the advanced dynamic analyses. Even if they allow modeling simple geometry several one-dimensional codes adopt advanced constitutive models, e.g. Cyclic 1D (Elgamal et al., 2006). In the following a focus on the existing 1D codes working in effective stresses will be presented, highlighting limits and peculiliarities.

II.2.1. Existing models for 1D effective stress analysis

Table II.2.2 reportes some of the most popular 1D codes performing effective stress analyses. Moreover, Table II.2.3 reports several commercial two-dimensional codes that can be adopted also for one-dimensional analyses.

As described in the previous paragraph, the pore water pressure variation during seismic loading can be modeled in two different ways: by adopting (1) semi-empirical pore water pressure, pwp generation relationships used in combination with models working in total stress; and (2) by effective-stress models whereby the pwp variation is computed as the difference between total stresses (or loads) and effective stresses, computed through an advanced constitutive model.

Given the enhanced capability of actual hardwere resources, the number of codes adopting a fully coupled formulation to model pore pressure buildup is rapidly increasing, as shown in Table II.2.2. Neverthless the evaluation of material parameters for these models requires significant expertise and detailed site-specific soil properties (Matasovic and Hashash, 2012), often not available.

Table II.2.2 - 1D codes for effective stress analyses

Dynamic analysis	Code	Reference	Constitutive model	Pwp generation model	Pwp dissipation /redistribution model
Approximate coupled	DESRA - 2	Lee and Finn (1978)	Konder and Zalasko (1963)	Martin et al. (1975)	Finn et al. (1977)
	DESRAMOD	Vucetic (1986)	Konder and Zalasko (1963)	Dobry et al. (1985)	Finn et al. (1977)
	DMOD2000	Matasovic and Ordonez (2011)	MKZ (Matasovic and Vucetic, 1993)	Vucetic and Dobry (1988) – for sand Matasovic and Vucetic (1995) – for clay	Finn et al. (1977)
	DEEPSOIL	Hashash (2009)	Extended MKZ (Phillips and Hashash, 2009)	Vucetic and Dobry (1988) – for sand Matasovic and Vucetic (1995) – for clay	Terzaghi 1D consolidation Theory
Stricly coupled	DYNA1D	Prevost (1989)	Multiyield surface plasticity (Prevost, 1989)		Biot theory
	SUMDES	Li et al. (1992)	Bounding surface hypoplasticity model		Biot theory
	CYCLIC 1D	Elgamal et al. (2004)	Multiyield surface plasticity (Parra, 1996)		u – p formulation
	CyberQuake	Modaressi and Foester (2000)	Multiyield surface plasticity (modified Aubry et al., 1982)		u – p formulation

Examples of plasticity-based constitutive laws include Prevost (1989), Beaty and Byrne (1998), and Elgamal et al. (2004). These advanced constitutive models are capable of simulating complex soil behavior under a variety of loading conditions. Key elements of these models include yield surfaces, flow rules, and hardening (or softening) laws.

As stated in the Introduction chapter, the aim of the thesis is to develop a simplified pore water pressure model to be implemented into a computer code, aimed at performing 1D effective stress analysis. The attention will then be concentrated on codes that simulate the pore pressure buildup by adopting empirical relationship, based on the results of cyclic undrained laboratory tests, and allow to carry out an approximate coupled effective stress analyses.

Table II.2.3 – Most popular 2D codes for effective stress analyses

Dynamic analysis	Code	Reference	Constitutive model	Pwp model
Approximate coupled	QUAKE/W	Geostudio (2006)	Ishibashi and Zang (1993)	Martin et al. (1975)
	FLAC 2D	ITASCA (2005)	Sigmoidal/Hardin and Drenevich (1972)	Martin et al. (1975) Beaty and Byrne (1998)
Stricly coupled	GEFDYN	Aubry and Modaressi (1996)	Multiyield surface plasticity ECP model (Aubry et al., 1982)	
	FLIP	Iai et al. (1992)	Strain space multiple mechanism model Iai et al. (1992)	
	CYCLIC ED	Elgamal et al. (2004)	Multiyield surface plasticity (Parra, 1996)	
	PLAXIS 2D	Brinkgreve et al. (2013)	UBC 2D (Beaty and Byrne, 1998)	

In this class of models, pore water pressure buildup is computed based on semi-empirical models. At the beginning of shaking (i.e., at time t= 0), the stress-strain behavior is modeled as in total stress conditions because pwp is zero. As shaking progresses, pwp is generated and cyclic degradation (of clay microstructure) starts. Subsequently, the effects of pwp generation and, in some models, of cyclic degradation are included by modeling the degradation of soil strength and stiffness.

Pore pressure generation models can generally be categorized into stress-based, strain-based, and energy-based models which can be applied in one-, two-, and three-dimensional analyses. Whereas initial models were primarily based on the results of cyclic stress-controlled tests, further studies showed a better correlation between pwp buildup and and the shear strain level (Dobry et al., 1985) or the energy dissipated within the soil deposit (Green et al. 2000).

An extensive description of the pore water pressure models is reported in Biondi et al. (2010).
A number of pwp generation models have been developed, starting with Martin and Seed (1978) and Martin et al. (1975). The Martin et al. (1975) pwp generation model was used in DESRA-2 (Lee and Finn 1978). An other example of the semi-empirical pwp model for saturated sand is the Dobry et al. (1985) model. This model was based on the results of strain-controlled cyclic direct simple shear and cyclic triaxial tests. The model was later modified by Vucetic (1986) and further by Matasovic (1993), that accurately modeled pwp induced degradation of shear modulus and shear stress. The Vucetic (1986) modification of this pwp model has been successfully incorporated in DESRAMOD (Vucetic 1986), and the Matasovic (1993) modification has been incorporated in D-MOD (Matasovic and Vucetic 1995), D-MOD2000 (Matasovic and Ordonez 2007), and DEEPSOIL (Hashash 2009).
The major drawback of all the described pwp generation models is the requirement of an equivalent number of cycles to represent earthquake shaking. Even if a great number of empirical relationships have been developed to define the $N_{eq,}$ they all cannot take into account for the complexity of the seismic action. Also for this reason Polito et al. (2008) introduced an energy-based model (GMP model) for the generation of pwp based on a large number of laboratory tests, which does not require the development of an equivalent number of cycles. This model has been implemented in DEEPSOIL (Hashash 2009) combined with the degradation index framework introduced by Matasovic and Vucetic (1993). With the exception of the modified Dobry et al. (1985) model, as implemented in D-MOD2000, there is limited information to guide the user in selecting the appropriate pwp model parameters (Matasovic and Hashash, 2012).

II.3. References

AGI (2005). Aspetti geotecnici della progettazione in zone sismiche. Guidelines of the Italian Geotechnical Society. Pàtron Editore, Bologna (in Italian).

Annaki M., Lee K.L. (1977). Equivalent uniform cycle concept for soil dynamics. *Journal of the Geotechnical Engineering Division*, ASCE, 103 (GT6): 549 - 564.

Aubry D., Hujeux J.C., Lassoudiere J.C., Meimon Y. (1982). A double memory model with multiple mechanisms for cyclic soil behaviour. Proceedings of the International Symposium Numerical Mododelling in Geomechanics, Balkema: 3–13.

Aubry D., Modaressi A. (1996). GEFDYN, Manuel Scientifique, Ecole Centrale Paris, France.

Beaty M., Byrne P.M. (1998). An Effective-stress Model for Predicting Liquefaction Behavior of Sand. Geotechnical Earthquake Engineering and Soil Dynamics III, P. Dakoulas, M. Yegian, and R. Holtz, Eds., ASCE, Geotechnical Special Publication 75(1): 766–777.

Bertolini G., Fioroni C. (2012). Aerial inventory of surficial geological effects induced by the recent Emilia earthquake (Italy): preliminary report. Annals of geophysics, 55 (4): 705 – 711.

Biondi G. (2002). Instabilità sismica dei pendii sabbiosi causata da incrementi di pressione interstiziale. PhD Thesis in Geotechnical Engineering, University of Catania, Italy. (in Italian).

Biondi G., Cascone E., Di Filippo G. (2012). Affidabilità di alcune correlazioni empiriche per la stime del numero di cicli di carico equivalente. *Italian Geotechnical Journal*, 2: 11-41.

Booker J.R., Rahman M.S., Seed H.B. (1976). GADFLEA - A computer program for the analysis of pore pressure generation and dissipation during cyclic or earthquake loading. Earthquake Engineering center, University of California, California, USA.

Brinkgreve R.B.J., Engin E., Swolfs W.M. (2013). Plaxis 2D Material Model Manual, Delft, Netherlands.

Dobry R., Pierce W.G., Dyvik R., Thomas G.E., Ladd R.S. (1985). Pore Pressure Model for Cyclic Straining of Sand. Research Report, Civil Engineering Department, Rensselaer Polytechnic Institute, Troy, N.Y., USA, 56 pp.

Elgamal A.-W., Yang Z., Lu J. (2004). A Web-based Platform for Computer Simulation of Seismic Ground Response," Advances in Engineering Software, 35 (5): 249–259.

Fioravante V., Boldini D., Crespellani D. et al. (2013). Earthquake geotechnical engineering aspects of the 2012 Emilia-Romagna earthquake (Italy). Seventh International conference on case Histories in Geothenical Engineering, 29 April - 4 May, Chicago, USA.

Finn W.D.L., Kwok W.L., Martin G.R. (1977). An effective stress model for liquefaction. Journal of the Geotechnical Engineering Division, (GT6): 517 – 533.

Geostudio International Ltd. (2006). QUAKE/W for Finite Element Dynamic Earthquake Analysis," User's Guide, GSI, Calgary, AB, Canada, 624 pp.

Green R. A., Mitchell J. K., Polito C. P. (2000). An energy-based pore pressure generation model for cohesionless soils. John Booker Memorial Symp. Developments in Theoretical Geomechanics, Rotterdam, The Netherlands, 383–390.

Green R., Cubrinovski M., Cox B., Wood C., Wotherspoon L., Bradley B., Maurer B. (2014). Select liquefaction case histories from the 2010 – 2011 Canterbury earthquake sequence. Earthquake Spectra, 30(1): 131 - 153.

Green R.A., Terri G.A. (2005). Number of equivalent cycles concept for liquefaction evaluations-Revisited. *Journal of Geotechnical and Geoenvironmental Engineering*, ASCE, 131 (4): 477- 488.

Hardin B.O., Drnevich, V.P. (1972). Shear modulus and damping in soils: Measurement and parameter effects. Journal of Soil Mechanics and Foundation Engineering Division, 98(SM6): 603-624.

Hashash Y. M. A. (2009). DEEPSOIL, Tutorial and User Manual. 2002-2009. University of Illinois at Urbana-Champaign, Illinois, USA.

Hashash Y.M.A., Phillips C., Groholski D.R. (2010). Recent advances in non-linear site response analysis. The 5th International Conference in Recent Advances in Geotechnical Eartqhuake Engineering and Soil Dynamics, San Diego, CA. CD-Volume: OSP 4.

Iai S., Matsunaga Y., Kameoka T. (1992): Strain space plasticity model for cyclic mobility. Soils and Foundations, Japanese Society of Soil Mechanics and Foundation Engineering, 32 (2) :1- 15.

Idriss I.M., Boulanger R.W. (2004). Evaluating the potential for liquefaction or cyclic failure of silts and clays. Report No UCD/GCM-04/01, University of California at Davis, California, USA.

Ishibashi I., Zhang X. (1993). Unified dynamic shear moduli and damping ratios of sand and clay. Soils and Foundations, 33(1): 182-191.

ISPRA (2012). Annuario dei dati ambientali. Eds 2012. Istituto superiore per la protezione e la ricerca ambientale. http://annuario.isprambiente.it/ada/scheda/4277/10

ITASCA (2005). FLAC (Fast Lagrangian Analysis of Continua) Version 5.0. Itasca Consulting Group, Inc., Minneapolis, Minneapolis, USA.

Kondner R.L., Zelasko J.S. (1963). A Hyperbolic Stress-strain Formulation of Sands. Proceedings of the 2nd Panamerican Conference on Soil Mechanics and Foundation Engineering, Sao Paulo, Brazil, 289–324.

Lee M.K.W., Finn W.D.L. (1978). DESRA-2, Dynamic Effective Stress Response Analysis of Soil Deposits with Energy Transmitting Boundary Including Assessment of Liquefaction Potential. Soil Mechanics Series No. 36, University of British Columbia, Vancouver, Canada, 60 pp.

Li X.S., Wang Z.L., Shen C.K. (1992). SUMDES: A Nonlinear Procedure for Response Analysis of Horizontally Layered Sites Subjected to Multi-Directional Earthquake Loading," Department of Civil Engineering, University of California, Davis.

Marcaccio M., Martinelli G. (2012). Effects on the groundwater levels of the May-June 2012 Emilia seismic sequence. Annals of geophysics, 55 (4): 811 – 814.

Markham C.S., Macedo J., Bray J.D. (2014). Evaluating fully nonlinear effective stress site response analyses using records from the Canterbury Earthquake sequence. Final technical report. USGS Award number G13AP00029.

Markham C.S., Bray J.D., Macedo J. (2015). Deconvolution of surface motions from the Canterbury earthquake sequence for use in nonlinear effective stress site response analyses. Proceedings of the 6th International Conference on Earthquake Geotechnical Engineering, paper 176.

Martin G.R., Finn W.D.L., Seed H.B. (1975). Fundamentals of Liquefaction under Cyclic Loading. Journal of the Geotechnical Engineering Division, 101 (GT5): 423–438.

Matasovic N. (1993). Seismic Response of Composite Horizontally Layered Soil Deposits. Ph.D. dissertation, Civil and Environmental Engineering Department, University of California, USA.

Matasovic N., Hashash Y.M.A. (2012). Practices and procedures for site – specific evaluations of earthquake ground motions. National Cooperative Highway Research Program (NCHRP) Synthesis 428, Washington DC, USA.

Matasovic N., Ordonez G. (2012). D-MOD2000 - A computer program for seismic site response analysis of horizontally layered soil deposits, earthfill dams and solid waste landfills. Geomotions, LLC, Lacey, Washington, USA.

Matasovic N., Vucetic M. (1993). Cyclic characterization of liquefiable sands. Journal of Geotechnical Engineering, ASCE, 119(11): 1805-1822.

Matasovic N., Vucetic M. (1995). Generalized Cyclic Degradation-Pore Pressure Generation Model for Clays. Journal of Geotechnical Engineering, 121 (1) :33–42.

Matsuo O. (1996). Damage to river dikes. Special issue of Soil and Foundations, 235 - 240.

Modaressi H., Foerster E. (2000) CyberQuake. User's Manual, BRGM, France.

Parra E. (1996) Numerical Modeling of Liquefaction and Lateral Ground Deformation Including Cyclic Mobility and Dilation Response in Soil Systems. Ph.D. dissertation, Department of Civil Engineering, Rensselaer Polytechnic Institute, Troy, N.Y., USA.

Phillips C., Hashash Y. M. A. (2009). Damping formulation for nonlinear 1D site response analyses. Soil Dynamics and Earthquake Engineering, 29(7): 1143–1158.

Prevost J. H. (1989). DYNA1D: A computer program for nonlinear site response analysis, technical documentation. National Center of Earthquake Engineering Research, Sunny at Buffalo, NY, USA.

Sasaki Y. (2009). River dike failures during the 1993 Kushiro-oki earthquake and the 2003 Tokachi-oki earthquake. Earthquake geotechnical case histories for performance-based design. Kukusho edition. Taylor & Francis Group, London, 131-157.

Seed, H.B., Idriss, I.M. (1971). Simplified procedure for evaluating soil liquefaction potential. Journal of Soil Mechanics and Foundations Division, ASCE, 97(9): 1249-1273.

Seed H.B., Idriss I.M., Makdisi F., Banerjee N. (1975). Representation of irregular stress time histories by equivalent unifrom stress series in liquefaction analyses. Earthquake Engineering Research Center, University of California, Berkeley, California, USA.

Shibata T., Oka F., Ozawa Y. (1996). Characteristics of ground deformation due to liquefaction. Special issue of Soil and Foundations, 65-79.

Sica S. (2000). Analisi del comportamento dinamico di dighe in terra. PhD Dissertation in Geotechnical Engineering. University of Rome 'La Sapienza' and University of Naples 'Federico II' (in Italian).

Silvestri F., d' Onofrio A. (2014). Risposta sismica e stabilità di centri abitati e infrastrutture. General report. XXV National Conference on Geotechnics, Baveno, Italy (in Italian).

Vucetic M. (1986). Pore pressure buildup and liquefaction at level sandy sites during earthquakes. PhD Dissertation. Rensselaer Polytechnic Institute, Troy, NY, USA.

Vucetic M., Dobry R. (1988). Cyclic triaxial straincontrolled testing of liquefiable sands. Advanced Triaxial Testing of Soil and Rock, ASTM STP 977, American Society for Testing and Materials, Philadelphia, USA, 475-485.

Wotherspoon L.M., Pender M.J., Orense R.P. (2012). Relationship between observed liquefaction at Kaiapoi following the 2010 Darfield earthquake and former channels of the Waimakariri river. Engineering Geology, 125: 45 – 55.

III. DEVELOPMENT OF A SIMPLIFIED MODEL

In this chapter, the original and updated formulation of a simplified pore water pressure build up model is described. The model is based on the results of cyclic laboratory tests; the calibration of the model parameters has been analysed in details considering both simulated and experimental data. A pore pressure dissipation model based on monodimensional consolidation theory has been also integrated in the formulation in order to simulate both generation and dissipation of excess pore water pressure.

III.1. Formulation of cyclic strength and pwp buildup

The proposed model is formulated within the framework of the endochronic theory. This Theory is based on the concept of intrinsic time, firstly introduced in the early 1950's. Valanis (1971) applied this concept to describe the inelastic, viscoplastic behaviour of metals. The theory is called endochronic (endo: within, chronic: related with time) because stress is defined with respect to an intrinsic time scale, which is a material property and depends on the deformation history.

Bažant and Krizek (1976) developed an endochronic constitutive law for soils under quasi-static and cyclic loads. This model is based on the postulate that exists a series of internal state variables and intrinsic material functions that express, on a macroscopic level, the microstructural changes that take place in the soils during load application and their build up along a stress or strain path.

Finn and Bathia (1982) applied endochrocnic theory to develop a direct relationship between the pore pressure buildup in a cyclic laboratory test and the dynamic response parameters of the sand-water system. In this case, the endochronic model can be considered as 'black-box' approach that allow to to express important parameters of dynamic soil response such as pore pressure build up as monotonically increasing functions of suitable variables. It does not attempt to model the actual physical process involved and therefore can be considered as useful prospect for eliminating the need to measure complex mechanical parameters of soil behaviour in undrained cyclic conditions.

Bathia (1982) verified the endochronic formulation on both strain-controlled and stress-controlled simple shear tests carried out on Ottawa sand, Crystal Silica sand and Toyoura sand. Since in cyclic tests stress-controlled conditions are still the most widely used laboratory procedure for evaluating the liquefaction potential, only for this type of test the analytical formulation of the model will be described in the following.

III.1.1. Analytical formulation

Pore water pressure ratio, $r_u=u/\sigma'_0$, is a function of the shear stress ratio, SR, and the number of cycles, N, as clearly shown in Figure III.1.1a where data measured by Silver and Park (1976) on Crystal Silica sand (Dr=60%) are reported.

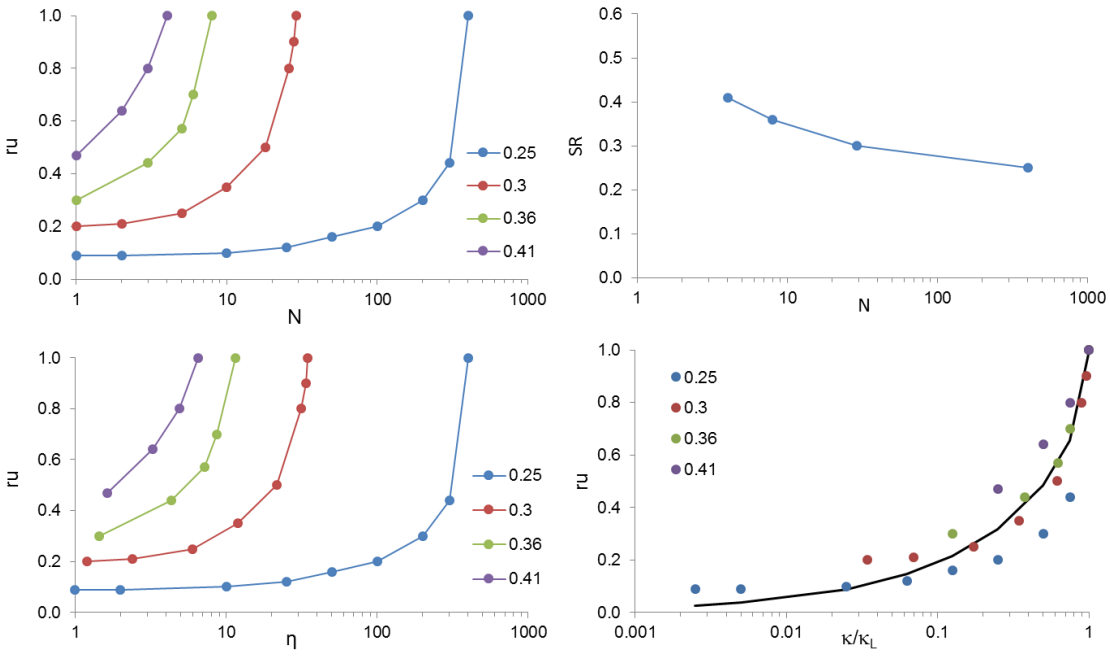

Figure III.1.1 – Porewater pressure ratio vs number of cycles related to stress-controlled cyclic triaxial tests on Crystal Silica sand (mod. after Silver and Park, 1976)

$$ru = f(SR, N) \tag{III.1.1}$$

Starting from this evidence Finn and Bathia (1982), proposed an alternative to N in describing the stress history applied to the sample: the length, η, of the stress path corresponding to N cycles of SR. The variable, η, is a monotonically increasing and continuous variable since, for definition, an increment in the length of the stress path equates an increment of shear stress, as suggested by Ivšić (2006)

$$d\eta = \frac{|d\tau|}{\sigma'_0} \qquad \text{(III.1.2)}$$

Following this definition the stress path length corresponding to one cycle at a given shear stress level, SR, is four times SR thus the length of the stress path at the end of the N^{th} cycle of a stress controlled test will be

$$\eta = 4 \cdot N \cdot SR \qquad \text{(III.1.3)}$$

Based on equation (III.1:3) the total length of the stress path was calculated for all the data of Figure III.1.1a and the pore water pressure ratio was then plotted as a function of η in Figure III.1.1b.

The pore pressure ratio in a constant stress test may now be expressed as

$$ru = g(SR, \eta) \qquad \text{(III.1.4)}$$

SR and η are related each other through a further variable introduced by Finn and Bathia (1982), known as damage parameter, κ, which synthesizes all the parameters defining the stress history, including variable stress amplitudes and number of cycles. For definition, the damage parameter is a transformation of η, if a transformation T exists so that

$$\kappa = T \cdot \eta \qquad \text{(III.1.5)}$$

The parameter κ is called damage parameter because the increase of stress path length induce pore pressure build up and weaken the resistance of sand.

The transformation T should be a function of shear stress ratio, SR, expressing that at equal stress path length the damage increases as SR increases (Figure III.1.1c).

Porewater pressure ratio can be then expressed as function of the damage parameter, κ, as

$$ru = h(\kappa) \qquad \text{(III.1.6)}$$

The equation III.1.6 represents the time history of excess pore pressure, ru, and expresses a strict one-to-one relationship between damage parameter and porewater pressure ratio.

Several authors proposed different relationships for the transformation *T* and the function *h* summarized in Table III.1.1.

Table III.1.1 – Damage parameter and pore pressure ratio relationships

Authors	Damage parameter $\kappa = T \cdot \eta$	Excess pore pressure ratio $ru = h(\kappa)$
Finn and Bathia (1982)	$\kappa = e^{\lambda SR} \cdot \eta$	$ru = \frac{F\kappa + G}{H\kappa + I} \cdot \kappa$
Ivšić (2006)	$\kappa = \frac{\eta}{SR} \cdot \left(\frac{SR}{SR_t} - 1 \right)^{\alpha}$	$ru = 0.5 \cdot \kappa^{0.4}$ for $\kappa \le 2.5$ $ru = (1.01 \cdot \kappa - 0.72)/\kappa$ for $\kappa \ge 2.5$ *or* $ru = \kappa/(1+\kappa)$
Park et al. (2014)	$\kappa = (\eta / SR) \cdot \left(SR - SR_t \right)^{\alpha}$	$ru = \frac{2}{\pi} arcsen\left[\left(\frac{\kappa}{\kappa_L} \right)^{1/2\beta} \right]$
This study	$\kappa = (\eta / SR) \cdot \left(SR - SR_t \right)^{\alpha}$	$ru = a\left(\frac{\kappa}{\kappa_L} \right)^{b} + c\left(\frac{\kappa}{\kappa_L} \right)^{4}$

III.1.1.1. Damage parameter and cyclic strength

As regard to the transformation *T*, Finn and Bathia (1982) adopted an exponential relationship of the stress ratio, SR, where λ is an experimentally determined constant.

Ivšić (2006) proposed a different function for the transformation T, to better take into account for some peculiar features of the cyclic response of sand. As a matter of fact, laboratory tests show that the number of cycles required to produce liquefaction decreases with increasing amplitude of the cyclic stress ratio, SR, and with decreasing relative density. The relationship among relative density, cyclic stress ratio and number of cycles can be expressed graphically by the cyclic resistance curve (Figure III.1.1c).

The curve in Figure III.1.1c tends to an asymptotic value of SR as the number of cycles increases; it means that exists a limit value of cyclic stress ratio below which the failure will never be reached. This threshold stress ratio, SR_t, is the value below which excess pore pressure are not induced and it is analogous to the volumetric threshold strain, γ_v (Vucetic, 1994) observed in strain controlled cyclic tests.

The damage parameter should take into account that for stress levels below SR_t pore pressure build up does not occur. Ivšić (2006) computed the net stress path length, being the difference between the total length, η and that characterized by a stress ratio SR ≤ SR_t, η_v $\eta' = \eta - \eta_v$ (III.1.7)

In case of cyclic stress-controlled test, η' can be expressed as follows:

$$\eta' = 4 \cdot N \cdot SR - 4 \cdot N \cdot SR_t = 4 \cdot N(SR - SR_t) \quad \text{(III.1.8)}$$

Based on the net length of stress path introduced by Ivšić (2006) it is possible to define the damage parameter as:

$$\kappa = \eta' \cdot \left(SR - SR_t \right)^m , \quad m \geq 0 \tag{III.1.9}$$

Where *m* is a positive exponent which affects both smaller and larger testing shear stress.

Rewriting equation (III.1.9) including equation (III.1.8) and (III.1.3), the damage parameter can be written as follows $\kappa = (\eta / SR) \cdot \left(SR - SR_t \right)^{\alpha}$ (III.1.10)

Where α is (1+*m*).

This formulation of the damage parameter is that adopted by Park et al. (2014) and also in this study (Table III.1.1).

The above expression of the damage parameter differs from that proposed by Ivšić (2006) since he suggested to divide *k* in the equation (III.1.10) by SR_t^{α} with $SR_t \neq 0$ (Table III.1.1). The damage function proposed by Ivsic (2006) was disregarded in th present study since it give rise to some numerical problems as SR_t values approach zero.

The parameters SR_t and α define the cyclic strength of the soil and can be evaluated from the cyclic resistance curve obtained from a stress-controlled cyclic test. In detail, the parameter α describes the steepness of the cyclic resistance curve, that is defined adopting the equation proposed by Park and Ahn, 2013, rewriting as

$$\frac{\left(SR - SR_t \right)}{\left(SR_r - SR_t \right)} = \left(\frac{N_r}{N} \right)^{\frac{1}{\alpha}} \tag{III.1.11}$$

where (N_r, SR_r) is a reference point on the cyclic resistance curve. A reference number of cycles equal to 15 is considered in this study (that is the number of equivalent cycles corresponding to a magnitude of 7.5 if the relationship proposed by Idriss (1999) is considered).

The physical meaning of the damage parameter can be easily deduced from the expression (III.1.10), whereas it is the product of two quantities: the first, η/SR, is proportional to the number of cycles (see equation III.1.3), while the second, $(SR - SR_t)^{\alpha}$, takes into account the amplitude of the applied stress exceeding the threshold value. The damage parameter is therefore an integral parameter that corresponds to the colored areas reported in Figure III.1.2a for two different values of stress ratio. If the points (SR,N) below to a cyclic resistance curve the two areas are equivalent since they all corresponds to a unique value of damage parameter, that can be computed substituting equation (III.1.11) in the equation (III.1.10)

$$\kappa_L = 4 \cdot N_r (SR_r - SR_t)^{\alpha} \tag{III.1.12}$$

Moreover, due to the functional relationship between the damage parameter and the pore pressure ratio (equation III.1.6), it is possible to design isodamage lines in the SR–N plane,

which corresponds to different value of pore pressure ratio (Figure III.1.2b). Substantially, during a stress-controlled cyclic test, the damage parameter increases with the number of cycles until reaching the liquefaction condition expressed by the cyclic resistance curve corresponding to $k=k_L$

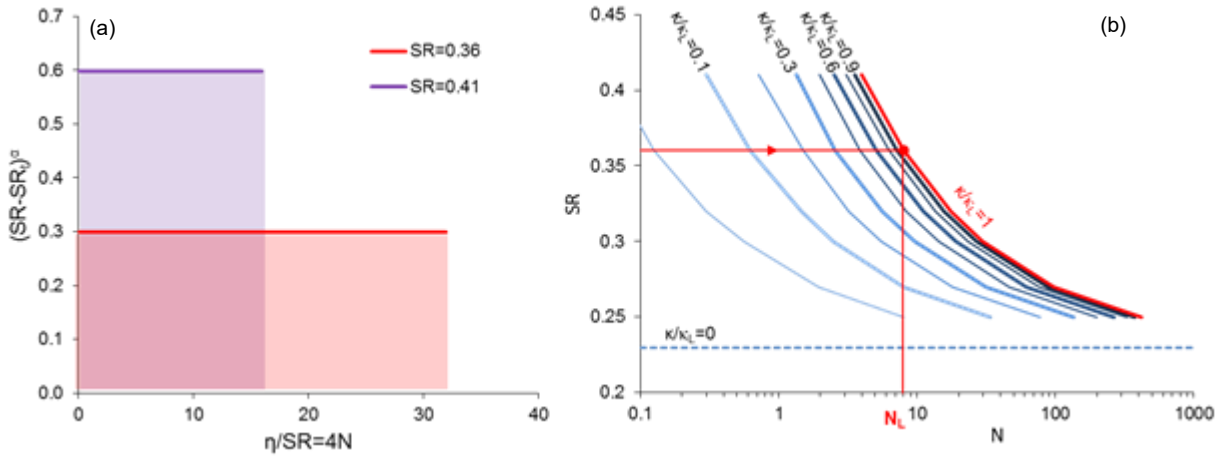

Figure III.1.2 - Graphical representation of the damage parameter (a) and isodamage curves in the N-SR plane (b)

It is then possible to define the damage ratio, being the ratio between the damage, k, corresponding to a generic point along the stress path and that evaluated at liquefaction, k_L as follows

$$\frac{\kappa}{\kappa_L}=\frac{4\cdot N(SR-SR_t)^\alpha}{4\cdot N_r(SR_r-SR_t)^\alpha} \tag{III.1.13}$$

A unique relationship exists between the number of cycles at liquefaction, N_L and the stress ratio, SR, the cyclic resistance curve thus, expressing SR as a function of N_L, through equation (III.1.11), it can be found that the damage ratio is equal to the ratio between the generic number of cycles and the number of cycles to liquefaction, as

$$\frac{\kappa}{\kappa_L}=\frac{4\cdot N\cdot\frac{N_r}{N_L}(SR_r-SR_t)^\alpha}{4\cdot N_r(SR_r-SR_t)^\alpha}=\frac{N}{N_L} \tag{III.1.14}$$

III.1.1.2. Excess pore pressure ratio

The analytical functions modeling the pore pressure ratio dependency on the number of uniform cycles are all based on the best fitting of the experimental data (Table III.1.1). Finn and Bathia (1982) defined a relationship applying a non linear least squares fitting method of the experimental data, where *F*, *G*, *H*, *I* are constant of the soil. A similar expression was adopted by Ivšić (2006) in combination with an exponential function. Booker et al. (1976) developed an

empirical expression for r_u as a function of cycle ratio. This expression was subsequently proposed by Park et al. (2014) and is given as Equation (III.1.15) below:

$$ru = \frac{2}{\pi} arcsen\left[\left(\frac{N}{N_L}\right)^{1/2\beta}\right] \quad \text{(III.1.15)}$$

Equation (III.1.15) has two calibration parameters, N_L and β, both of which can be determined from stress controlled cyclic triaxial tests. For a given soil, N_L is proportional to relative density and inversely proportional to the magnitude of loading; β is an empirical constant that depends on the soil type and test conditions. It has been the object of an extensive studies in the past decades. Booker et al. (1976) recommended β=0.7 for clean sands, while Polito et al. (2008) correlate β to the fine content, relative density and shear stress ratio.

A wide review of the excess pore pressure relationships is reported in Biondi (2002) that distinguished empirical relations based on laboratory test measurements of excess pore pressure from that based on an energetic approach.

More recently, Khashila et al. (2015) modeled the relationship between excess pore pressure for uniform strain controlled tests and normalized number of cycles adopting a power function:

$$ru = 0.9\left(\frac{N}{N_L}\right)^{r} \quad \text{(III.1.16)}$$

where *r* is a material parameter function of the strain levels, determined from laboratory tests.

In this study, a non linear least square curve fitting method has been used to determine the relationship between ru and N/N_L. The following relationship has been proposed

$$ru = a\left(\frac{N}{N_L}\right)^{b} + c\left(\frac{N}{N_L}\right)^{4} \quad \text{(III.1.17)}$$

where a, b and c are curve-fitting parameters. A validation of the proposed curve will be described in the next paragraph.

III.2. Calibration of PWP model parameters

The calibration of the PWP model parameters is aimed at:

- identifying soil properties that mainly affect the model parameters,
- evaluating the sensitivity of the model parameters to soil mechanical properties and
- definitining some simple relationships between soil mechanical properties and model parameters.

More in details the parameters describing the damage ratio function as well as those characterizing the pore water ratio relationship should be calibrated. As regard to the parameters of the damage ratio function, their calibration requires the availability of data in terms of cyclic resistance curves from laboratory tests. Since it is very difficult to find a meaningful amount of data in literature, it was preliminary set up a general procedure to generate cyclic resistance curves (N,SR) from empirical relationship based on the corrected number of blow count from SPT test, $(N1)_{60}$.

The empirical relationship proposed by Idriss and Boulanger (2014) has been used since it includes data obtained from the most recent events (2010-2011 Canterbury earthquake sequence in New Zealand and the 2011 Tohoku earthquake in Japan). The calibration of the parameters of the damage ratio function has been then carried out on the set of generated cyclic resistance curves.

As regard to the proposed pore pressure ratio relationship the calibration of the parameters has been carried out based on a careful analysis of more than 200 experimental curves collected in literature.

III.2.1. Generation of cyclic resistance curves from empirical relationships

Starting from Idriss and Boulanger (2014) triggering relationship a set of cyclic resistance curves has been generated, each corresponding to a given number of corrected blow counts, $N1_{60}$. To this aim it has been necessary to define the dependency of CRS on magnitude, through the magnitude scaling factor (MSF), as well as the relationship between magnitude and number of equivalent stress cycles. The Idriss and Boulanger (2014) relationship here reported

$$CRR_{M=7.5,\sigma'=1} = \exp\left(\frac{(N1)_{60cs}}{14.1} + \left(\frac{(N1)_{60cs}}{126}\right)^2 - \left(\frac{(N1)_{60cs}}{23.6}\right)^3 + \left(\frac{(N1)_{60cs}}{25.4}\right)^4 - 2.8\right) \quad \text{(III.2.1)}$$

allows to define the cyclic resistance ratio of the soil characterized by a given value of corrected blow counts at a reference earthquake of 7.5 magnitude. It is well known that the soil's CRR is dependent on the duration of shaking (which is expressed through an earthquake magnitude scaling factor, MSF) and the effective overburden stress (expressed through a K_σ factor). The effect of the initial effective confining pressure is accounted by introducing a correction factor k_σ, as in the following equation

$$k_\sigma = 1 - C_\sigma \cdot \ln\left(\frac{\sigma'_{v0}}{p_a}\right) \leq 1.1 \quad \text{(III.2.2)}$$

where

$$C_\sigma = \frac{1}{18.9 - 2.55\sqrt{(N1)_{60cs}}} \leq 0.3 \quad \text{(III.2.3)}$$

On the other end, to take into account for the dependency on shaking duration Boulanger and Idriss (2014) suggest an upgraded relationship for the magnitude scaling factor that take into account for the soil properties.

Fundamentally, the MSF is known to be physically affected by numerous factors, including the earthquake source characteristics, distance from the site to the source, soil profile characteristics, and depth in the soil profile (e.g., Liu et al. 2001, Green and Terri 2005), but the inclusion of all dependencies may not be warranted in practice. The MSF relationship proposed by B&I (2014) includes functional dependence on an index of the soil properties in addition to the earthquake magnitude M.

The magnitude scaling factor is based on the original weighting scheme introduced by Seed et al. (1975) for converting an irregular cyclic loading history to some equivalent number of uniform loading cycles. A key parameter in this procedure is the slope of the relationship between the CRR and number of uniform loading cycles to failure (N) obtained from laboratory tests. The CRR versus N relationship, over the range of N values important to earthquake loading, can often be reasonably approximated using a power law as,

$$CRR = aN^{-b} \quad \text{(III.2.4)}$$

where the fitting parameter b describe the slope of the relationship. For two individual stress cycles having magnitudes CSR_A and CSR_B, the relative number of cycles to cause failure at these two stress ratios can be obtained from the above relationship as,

$$\frac{CRS_A}{CSR_B} = \left(\frac{N_B}{N_A}\right)^b \quad \text{(III.2.5)}$$

The damage from one cycle of stress at CSR_B would then be equivalent to the damage from X_A cycles at CSR_A if their numbers of cycles are an equal fraction of the number of cycles to failure at their respective CSRs. This leads to the expression,

$$X_A = \left(\frac{CSR_B}{CSR_A}\right)^{\frac{1}{b}} (1 \text{ cycle at } CRS_B) \quad \text{(III.2.6)}$$

This expression can be used to convert individual stress cycles into an equivalent number of uniform cycles at some reference stress level. The total number of equivalent uniform cycles at a reference stress level can then be determined for a wide range of earthquake ground motions, from which a representative number of equivalent uniform cycles can be obtained for a given earthquake magnitude (N_M). The MSF can then be determined as,

$$MSF = \frac{CSR_M}{CSR_{M=7.5}} = \left(\frac{N_{M=7.5}}{N_M} \right)^b \quad \text{(III.2.7)}$$

where N_M=7.5 is the number of uniform cycles for M = 7.5.

The effect of b on the MSF relationships is illustrated in Figure III.2.1

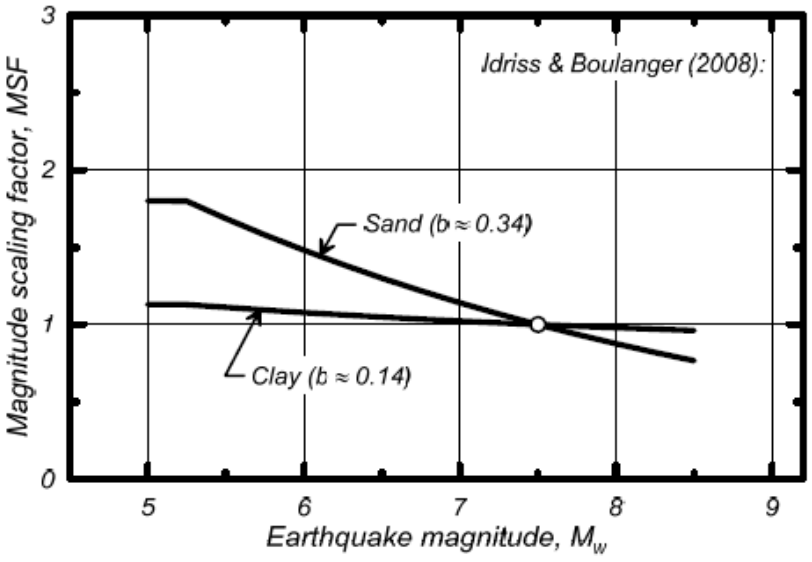

Figure III.2.1 - MSF relationships for clay and sand (Boulanger and Idriss 2007)

The MSF relationship derived by Idriss (1999) for sands used b = 0.34 based on cyclic test data by Yoshimi et al. (1984) for samples of Niigata sand obtained using frozen sampling techniques. The MSF relationship by Boulanger and Idriss (2007) for clays and plastic silts used b = 0.135 for clays and plastic silts based on a compilation of cyclic testing data. The smaller b value for clays and plastic silts results in a much flatter MSF relationship than that obtained for sands, as shown in Figure III.2.1.

It is clear that the coefficient *b* influences the number of equivalent loading cycles and then MSF.

The effect of b on the number of equivalent uniform loading cycles is illustrated in Figure III.2.2 for earthquakes with M ≈ 7.5. This figure shows $N_{M=7.5}$ computed for b values of 0.06 to 0.40 for a set of 42 motions at category D sites with peak ground accelerations (PGA) of 0.11 to 0.51 g during M = 7.3-7.6 earthquakes. At any given value of b, the N_M=7.5 values varied by factors of 2 to 3. The geometric mean values for $N_{M=7.5}$ were relatively constant at about 15 for b values of 0.2 to 0.5, and then increased rapidly for b values progressively smaller than about 0.2. Also shown on this figure is the trend in mean values obtained by Kishida and Tsai (2014) based on their analyses of more than 3500 ground motion recordings at category D sites from the PEER strong ground motion database.

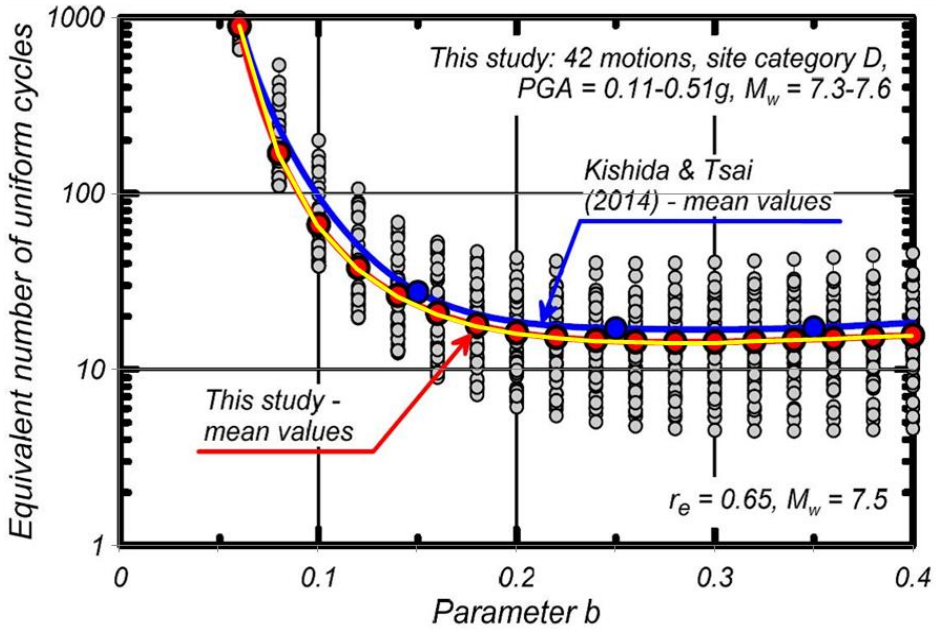

Figure III.2.2 – Variation of $N_{M=7.5}$ with the parameter b and analytical relationship used in this study (mod. after Idriss and Boulanger, 2014)

The relationship between $N_{M=7.5}$ and the *b* parameter has been described analytically in this study as

$$N_{M=7.5} = \frac{18.61 \cdot b^2 - 3.71 \cdot b + 0.38}{b^2 - 0.091 \cdot b + 0.0021} \quad \text{(III.2.8)}$$

Which is the yellow curve represented in Figure III.2.2.

The maximum value of the magnitude scaling factor, MSF_{max}, is related to small magnitude earthquake and corresponds to the case where the motion is dominated by a single strong acceleration pulse. If this single pulse scenario is represented by ¾ of a cycle at its peak stress, then the equivalent number of uniform cycles at 65% of the peak stress would be (Idriss and Boulanger 2008),

$$N_{min} = \left(\frac{1}{0.65}\right)^{1/b} \cdot \left(\frac{3}{4}\text{cycles}\right) \quad \text{(III.2.9)}$$

This minimum number of equivalent cycles can be used to compute the upper limit on MSF as

$$MSF_{max} = \left(\frac{N_{M=7.5}}{N_{min}}\right)^{b} \quad \text{(III.2.10)}$$

The resulting relationship between MSF_{max} and b is shown in Figure III.2.3.

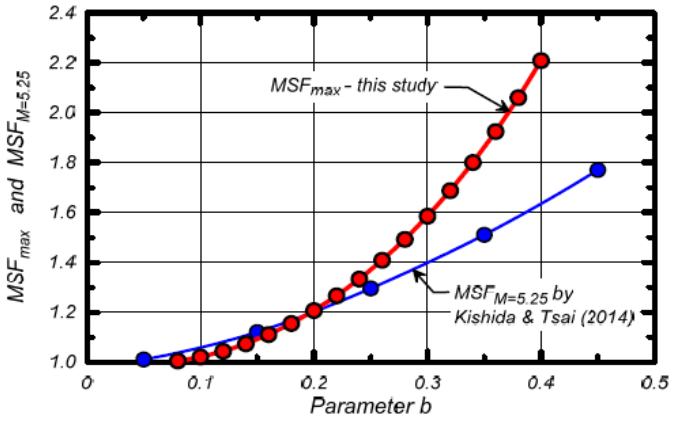

Figure III.2.3 – Variation MSF_{max} with the parameter b (Boulanger and Idriss, 2014)

The MSF relationships used by Idriss and Boulanger (2008), as shown in Figure III.2.4, can be rewritten in a more general form as:

$$MSF = 1 + (MSF_{max} - 1)\left(\frac{\exp\left(-\frac{M}{4}\right) - \exp\left(\frac{-7.5}{4}\right)}{\exp\left(\frac{-5.25}{4}\right) - \exp\left(\frac{-7.5}{4}\right)} \right) \quad \text{(III.2.11)}$$

where MSF_{max} is related to a minimum magnitude equal to 5.25. This form of the MSF relationship, coupled with a relationship between MSF_{max} and b, allows generation of MSF curves for different values of b, as shown in Figure III.2.4.

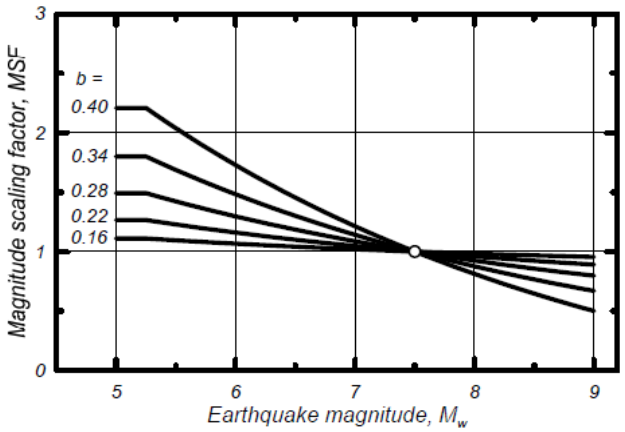

Figure III.2.4 – Variation of MSF relationship with the parameter b (Boulanger and Idriss, 2014)

The last step in deriving a revised MSF for SPT-based liquefaction triggering procedures requires relating the parameter MSF_{max} (via the parameter b) to some combination of soil characteristics (e.g., FC, PI), SPT parameters (e.g., $(N1)_{60}$, $(N1)_{60cs}$).

Boulanger and Idriss (2014) reviewed a meaningful amount of laboratory test data to compute MSF_{max} for different b values and plot them versus equivalent values $(N1)_{60cs}$. The equivalent

$(N1)_{60cs}$ values in the figure were determined as the values for which the applicable triggering correlation produces the same $CRR_{M=7.5,\sigma'=1}$ value as obtained from the laboratory test data.

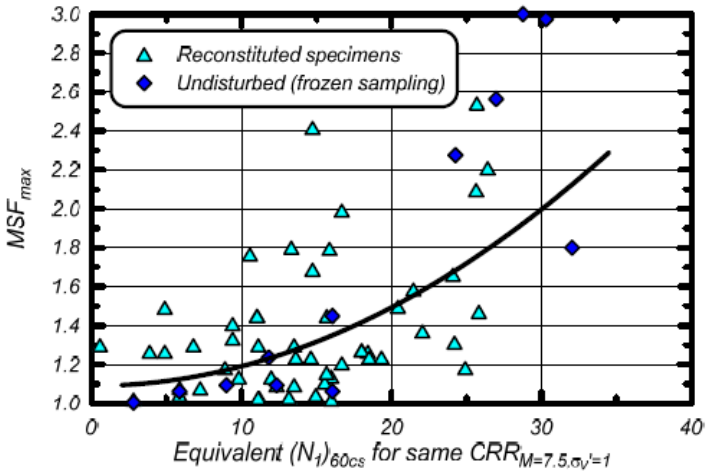

Figure III.2.5 – Variation in MSF_{max} with equivalent $(N1)_{60cs}$ for cohesionless soils (Boulanger and Idriss, 2014)

Since the resulting relationship between MSF_{max} and $(N1)_{60cs}$ values is not well constrained by the data in Figure III.2.5 alone, Boulanger and Idriss (2014) considered a number of other factors in guiding the form of this relationship.

The final adopted relationship between MSF_{max} and $(N1)_{60cs}$ is:

$$MSF_{max} = 1.09 + \left(\frac{(N1)_{60cs}}{31.5}\right)^2 \leq 2.2 \qquad \text{(III.2.15)}$$

Substituting equations (III.2.8) and (III.2.9) in the (III.2.10), the MSF_{max} can be directly expressed as function of the soil parameter b

$$MSF_{max} = 0.65\left[\frac{4}{3}\left(\frac{18.61\cdot b^2 - 3.71\cdot b + 0.38}{b^2 - 0.091\cdot b + 0.0021}\right)\right]^b \qquad \text{(III.2.13)}$$

Since the univocal relation between MSF_{max} and *b*, a defined *b* value can be associated to any MSF_{max} known from equation (III.2.12).

Known *b*, $N_{M=7.5}$ can be computed through equation (III.2.8), and the magnitude scaling factor can be computed for any number of cycles as, for definition

$$MSF = \left(\frac{N_{M=7.5}}{N}\right)^b \leq MSF_{max} \qquad \text{(III.2.14)}$$

Definitely, to each number of cycles, N, corresponds a MSF value, and then CSR_M value as

$$CSR = MSF \cdot k_\sigma \cdot CRR_{M=7.5,\sigma'=1} \qquad \text{(III.2.15)}$$

As a result, different CSR-N curves have been obtained for different values of the effective confining pressure and corrected SPT blow count.

A range of $(N1)_{60}$ from 6 to 25 has been considered, because it is the range of SPT values that characterize the liquefiable soils. A wide range, from 50 to 800 kPa, has been assumed for the effective confining pressure, while, for the number of cycles, a range from 7 to 300 has been used for defining the cyclic resistance curve in order to have a good prediction of SR_t.

III.2.1.1. Calibration

The calibration procedure has been divided in two steps: the first step is related to the calibration of SR_r and the second part is related to the calibration of SR_t and α.

SR_r data points, which are related to 15 cycles, have been plotted as function of $(N1)_{60}$ and σ'_{v0} (Figure III.2.6). It is worth highlighting that SR_r increases with $(N1)_{60}$ and decreases with σ'_{v0}, so it could be interpreted with a polynomial function of $(N1)_{60}$, where the coefficients x_1, x_2, x_3, x_4 and x_5 are ruled by σ'_{v0} with a logarithmic function. Finally, the following relationship has been obtained

$$SR_r = x_1 \cdot (N1)_{60}^4 + x_2 \cdot (N1)_{60}^3 + x_3 \cdot (N1)_{60}^2 + x_4 \cdot (N1)_{60} + x_5 \qquad \text{(III.2.16)}$$

where

$$x_i = x_{i,1} \cdot \ln\left(\frac{\sigma'_{v0}}{p'_0}\right) + x_{i,2} \qquad \text{for i=1, 2, 3, 4, 5} \qquad \text{(III.2.17)}$$

with p'_0 equal to the atmospheric pressure. The parameters of the expression (III.2.17) have been clearly defined through a non linear regression procedure and are reported in Table III.2.1. The predicted curves are reported also in Figure III.2.6.

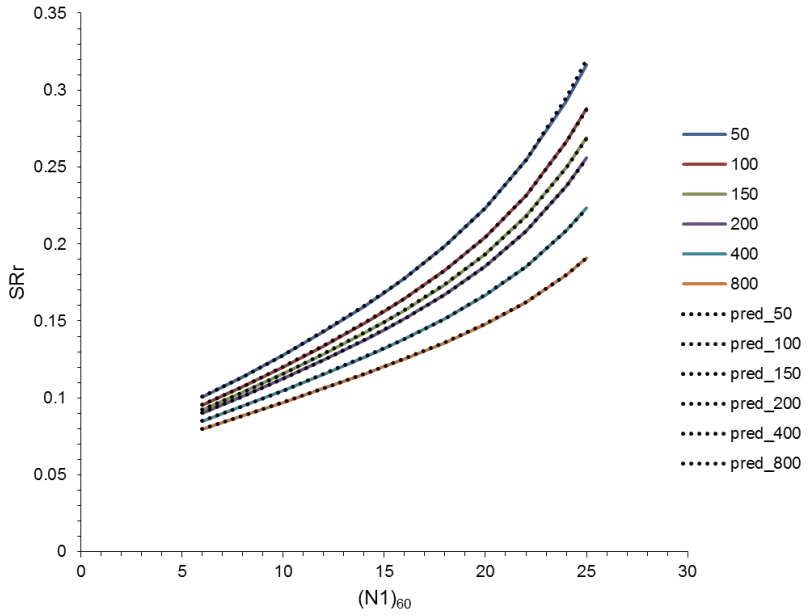

Figure III.2.6 – Reference shear stress ratio, SR_r and predicted values vs the corrected number of blow count, $(N1)_{60}$ and for different effective confining pressure

Table III.2.1 - Coefficients of the relationships (III.2.12)

$X_{1,1}$	$X_{1,2}$	$X_{2,1}$	$X_{2,2}$	$X_{3,1}$	$X_{3,2}$	$X_{4,1}$	$X_{4,2}$	$X_{5,1}$	$X_{5,2}$
-3.07E-07	1.23E-06	1.35E-05	-5.46E-05	-2.57E-04	1.01E-03	1.27E-03	-1.94E-03	-8.45E-03	8.12E-02

As regard to the calibration of the parameter α, governing the steepness of the cyclic resistance curve, Idriss and Boulanger (2014) relates the slope of the curve to the corrected number of blow count, so the parameter α is ruled by $(N1)_{60}$. Essentially a linear dependence can be observed in Figure III.2.7a, but a cubic function is associated with a R-squared equal to unity

$$\alpha = x_6 \cdot (N1)_{60}^3 + x_7 \cdot (N1)_{60}^2 + x_8 \cdot (N1)_{60} + x_9 \qquad \text{(III.2.18)}$$

Finally the threshold shear stress ratio, SR_t, was defined as the shear stress ratio corresponding to one million of cycles and plotted in Figure III.2.7b as a function of $(N1)_{60}$ for different values of effective stress, σ'_{v0}. Due to the small values of shear stress ratio, the effect of σ'_{v0} has been neglected and the following expression has been adopted for modelling SR_t

$$SR_t = x_{10} \cdot (N1)_{60}^4 + x_{11} \cdot (N1)_{60}^3 + x_{12} \cdot (N1)_{60}^2 + x_{13} \cdot (N1)_{60} + x_{14} \qquad \text{(III.2.19)}$$

The coefficients have been computed using an optimization procedure based on the non-linear regression method and are reported in Table III.2.2.

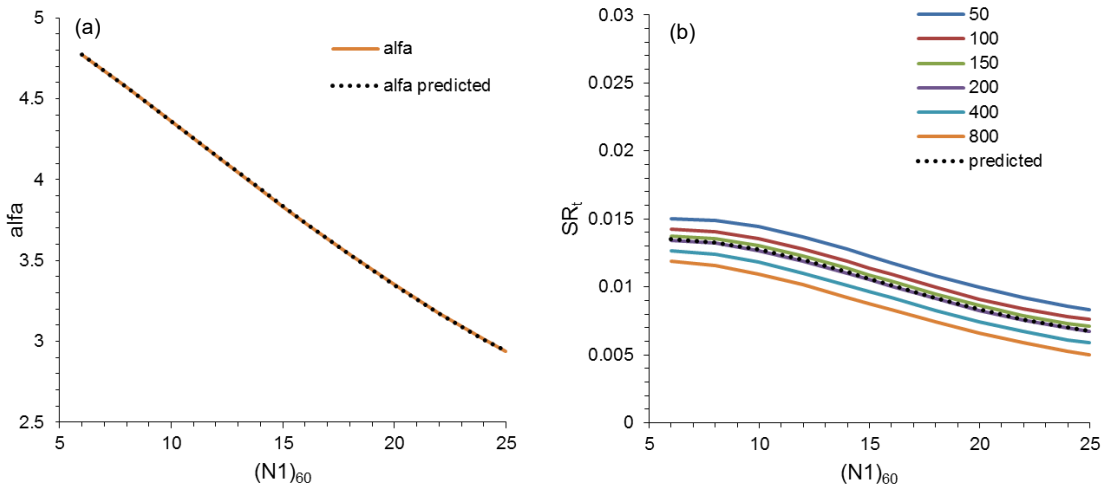

Figure III.2.7 - Plot α and SR_t vs $(N1)_{60}$ for different σ'_{v0} values

Table III.2.2 - Coefficients of the relationships (III.2.18) and (III.2.19)

X_6	X_7	X_8	X_9	X_{10}	X_{11}	X_{12}	X_{13}	X_{14}
6.50E-05	-2.25E-03	-7.92E-02	5.31E+00	-3.73E-08	3.67E-06	-1.16E-04	1.03E-03	1.08E-02

Finally, Figure III.2.8 reports the comparison between the generated cyclic resistance curves and the curves that come from the previous equations. It could be noticed a good match in the whole range of $(N1)_{60}$ and σ'_{v0}.

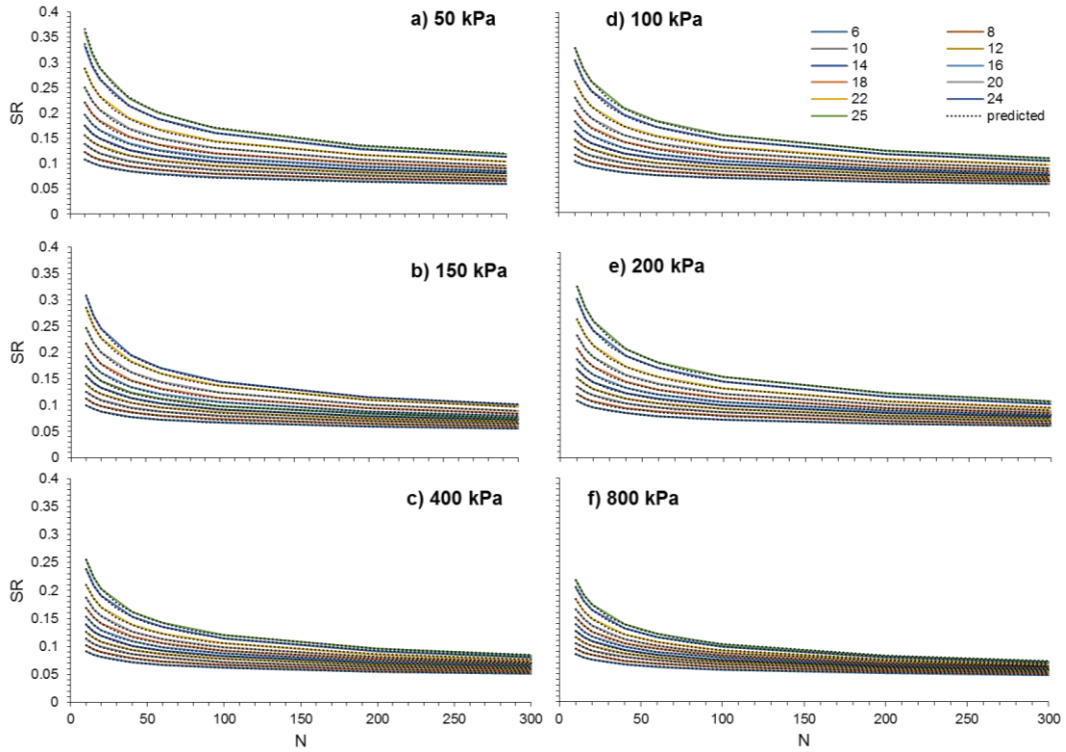

Figure III.2.8 - Comparison between generated and predicted CRC

III.2.2. Calibration of the pwp buildup parameters

Differently from the cyclic resistance curves, pore pressure ratio curves, ru – N/N_L, cannot be generated elaborating the in situ triggering relationships. Consequently, the only feasible way is that of considering experimental data reported in the literature. The collection of experimental data allows verifying the capability of the proposed model (Equation III.1.17) to reproduce the cyclic behaviour of soils. In addition, the database of experimental data can be used in the calibration of the model parameters in case of lack of experimental laboratory tests.

For this purpose, 213 experimental curves have been collected from scientific papers, related to soils coming from 19 different countries all over the world (Figure III.2.5).

The experimental data refer to undisturbed or reconstituted specimens, subjected to cyclic stress-controlled laboratory tests, i.e. cyclic simple shear or cyclic triaxial tests. All the soil properties and any other useful information on the tests have been collected inside a database (e.g. grain size distribution, relative density, effective confining pressure and cyclic stress ratio

(CSR) applied during the tests, etc). Table III.2.3 reports an esemplificative record of the database. Every curve is identified by an identification number (ID) in the database.

Figure III.2.9 – Origin of soil samples whose experimental data were collected (Spiedo, 2016)

The experimental excess pore pressure curves have been digitalized and normalized in order to obtain ru – N/N_L curves. Where necessary, a normalization procedure has been applied considering that the liquefaction condition is reached at ru = 0.95. This assumption implies that a residual 5% of the initial effective stress characterizes the liquefied soil. This assumption in turn implies a soil residual strength that results particularly advantageous when the liquefaction condition should be introduced inside a computer code, since it guarantees numerical stability. This stress approach has been preferred to the strain approach, since it is compatible with the PWP model developed.

All the collected curves have been then processed carrying out a non-linear regression analysis in order to evaluate the parameters of the proposed pore pressure ratio relationship, here recalled

$$ru = a\left(\frac{N}{N_L}\right)^b + c\left(\frac{N}{N_L}\right)^4 \qquad \text{(III.2.15)}$$

Figure III.2.6 reports an example of the results of regression analysis on the experimental curve of the Yatesville sand (Polito, 1999). All the data collected in the database and the parameters of the regression analysis are reported in Appendix B.

Table III.2.3 – Example of record of the database

ID	Soil	Specimen	Test	Grain size	σ'_0 [kPa]	CSR	Dr [%]	PI	Reference
187	Yatesville sand	Reconstituted	CTX	100% sand	200	0.22	40	-	Polito (1999)

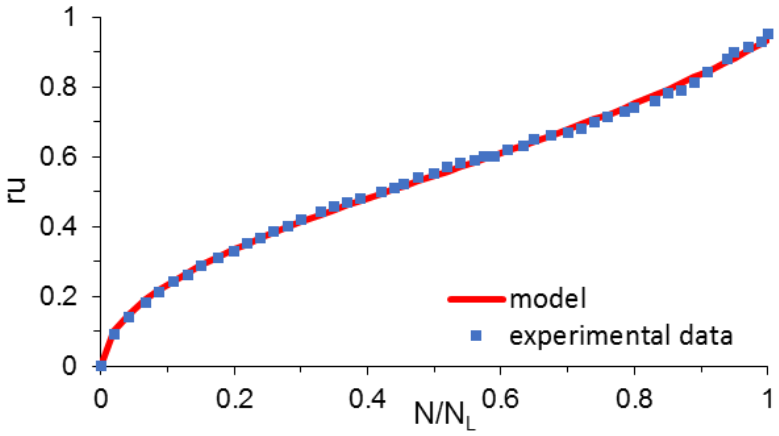

Figure III.2.10 – Experimental (Polito, 1999) and modelled pore pressure ratio curve

The quality of the fitting has been computed using a statistic index: the adjusted coefficient of determination. As known, the coefficient of determination, R^2, is a number that indicates the goodness of fitting; a value of 1 indicates that the regression model perfectly fits the data, while an R^2 of 0 indicates that the model does not fit the data at all. The adjusted R^2, R_{adj}^2, takes into account also the phenomenon that the R^2 automatically and spuriously increases when extra explanatory variables are added to the model. Analytically, R_{adj}^2 is defined as

$$R_{adj}^{\ 2} = R^2 - (1-R^2)\frac{p}{n-p-1} \qquad \text{(III.2.15)}$$

where p is the total number of explanatory variables in the model, and n is the number of experimental points. In this way, it is possible compare the fitting goodness obtained using different models, independently from the number of parameters characterizing the model.

As an example, the regression analysis carried out on the experimental data of Figure III.2.6 is characterized by R_{adj}^2 equal to 0.998. Figure III.2.7 summarizes the results of the regression analyses in terms of goodness of fitting. The result highlights that the proposed relationship is applicable on the 95% of the experimental curves, and 77% of the fitting curves are characterized by R_{adj}^2 is greater than 0.98.

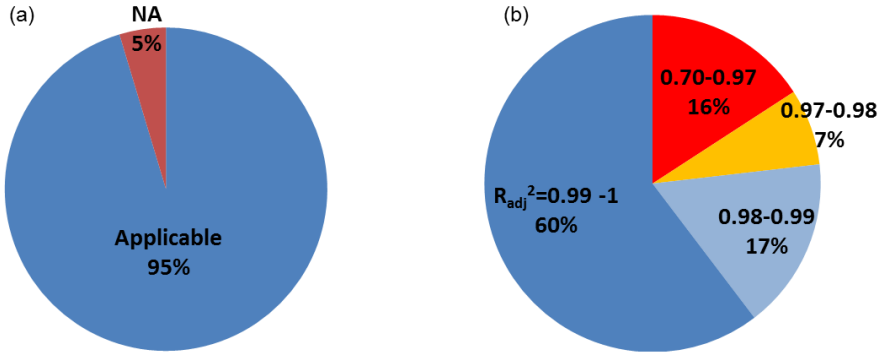

Figure III.2.11 – Applicability of the pore pressure relationship (a) and quality of fitting (b)

The experimental curves that could not be fitted by the proposed relationship are characterized by high values of CSR, relative density or effective confining pressure.

Moreover, the analysis of the experimental data allowed to identify the soil properties that mostly influence the evolution of the pore pressure buidup during an undrained cyclic test on liquefiable soil. An accurate analyses of the collected experimental curves is reported in Spiedo (2016), while a summary is here described.

The grain size distribution has an important role in defining the shape of the pore pressure ratio curve. In particular, it was observed that: (1) soils with high fine content exhibit a curve with a horizontal asymptote at the liquefaction; (2) sandy and gravelly soils show a sudden change in the pore pressure growth and an almost vertical asymptote at the liquefaction (run-away behavior); (3) it seems that a fine fraction (d<0.06mm) higher than 30% can be considered as a threshold value since a further increase of fine fraction does not change the shape of the curve.

III.3. Performance of the pwp buildup model on a soil element

The main advantage of damage parameter is that it can be easily implemented in a code working in time domain to perform coupled effective stress dynamic analyses. In fact, a recorded acceleration time history is a sequence of acceleration values sampled with a preset time interval and the general formulation of the damage parameter (equation III.1.10) can be specified for each time step.

III.3.1.1. Numerical formulation

The numerical formulation of the model can be easily described with reference to a monotonic load, such as in Figure III.3.1.

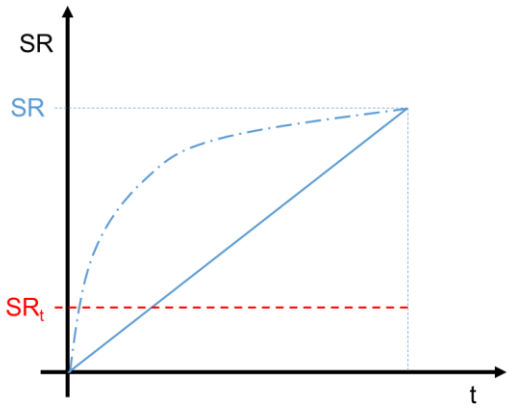

Figure III.3.1 – two examples of monotonic load

Applying the general formulation of equation (III.1.10), the damage parameter could be computed as

$$\kappa = \frac{SR}{SR} \cdot \left(SR - SR_t \right)^{\alpha} = \left(SR - SR_t \right)^{\alpha} \tag{III.3.1}$$

Which substantially means that the damage parameter is a power function of the portion of shear stress ratio that exceeds the threshold value. It is also clear that different stress histories with the same final value of stress ratio cause the same final damage (Figure III.3.1).

For a regular cyclic history of given amplitude, SR, remembering equation (III.1.3), the damage parameter is proportional to the number of cycles, as shown it the following equation:

$$\kappa = \frac{4 \cdot N \cdot SR}{SR} \cdot \left(SR - SR_t \right)^{\alpha} = 4 \cdot N \cdot \left(SR - SR_t \right)^{\alpha} \tag{III.3.2}$$

that can be rewritten as

$$\kappa = \sum_{i=1}^{4N} \left(SR - SR_t \right)^{\alpha} \tag{III.3.3}$$

Where *i* is the number of quarter of cycles in the stress history. For a periodic history with variable amplitude as that reported in Figure III.3.2a, the damage parameter can be expressed as

$$\kappa = \sum_{i=1}^{4N} \left(SR_{\max,i} - SR_t \right)^{\alpha} \tag{III.3.4}$$

Where $SR_{max,i}$ is the amplitude of the i-th half cycle of the time history. The latter can be applied to any loading pattern (Figure III.3.2b) and expressed as function of the time, *t*,

$$\kappa(t) = \kappa_0 + \Delta\kappa(t) = \sum_{i=1}^{n} \left(SR_{\max,i} - SR_t \right)^{\alpha} + \Delta\kappa(t) \tag{III.3.5}$$

Where *n* is the number of monotonic stretches at the time *t* with maximum stress ratio $SR_{max,i}$ and $\Delta\kappa$ is the increment of the damage parameter in the time step

$$\Delta\kappa(t) = \begin{cases} |SR_0 - SR|^{\alpha} & \text{per } SR \geq SR_t \\ 0 & \text{per } SR < SR_t \end{cases} \qquad \text{(III.3.6)}$$

Where SR_0 is the initial shear stress ratio of the current stretch at the time *t*. It is equal to $SR_{max,i}$ for decreasing stretches and SR_t for increasing stretches. The portion of the damage parameter κ_0 takes into account the past stress history and it is updated every time a maximum or minimum value is attained in the time history.

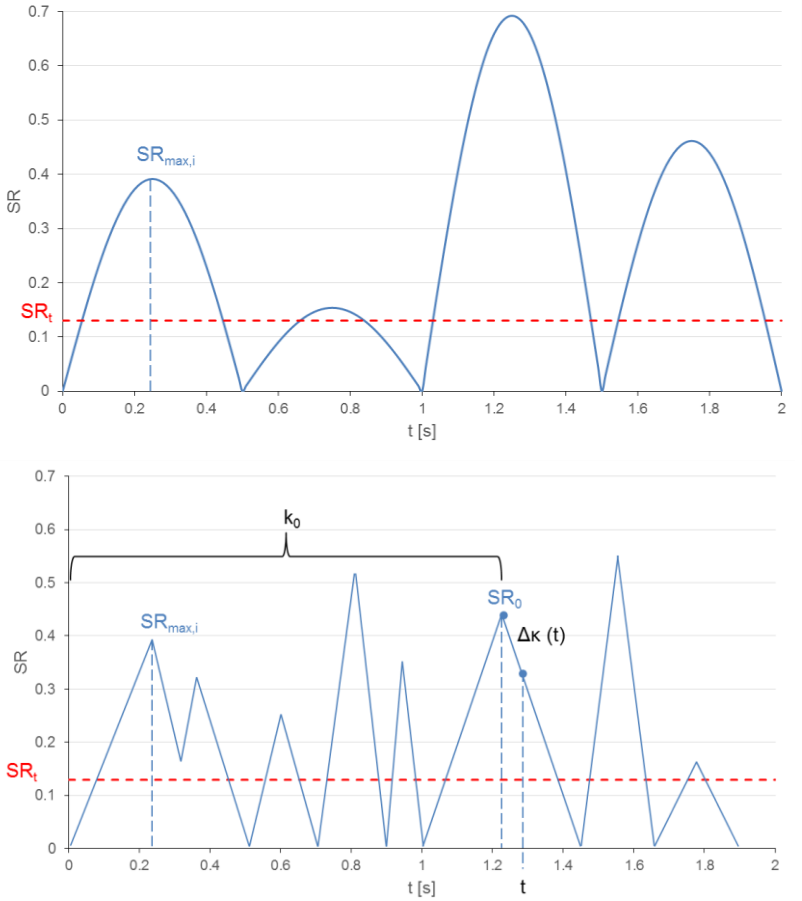

Figure III.3.2 - Periodic history with variable amplitude (a) and general loading pattern with damage parameter at time instant t (b)

The model has been applied with reference to the periodic history of shear stresses shown in Figure III.3.3a. The damage parameter has been computed based on the time history of the shear stress for given values of α and SR_t. as it is expected the parameter k cumulates when the cyclic stress ratio exceeds the threshold value otherwise it remains constant.

The time history of excess pore water pressure, can be then calculated once the pore pressure ratio is expressed as a function of the damage parameter.

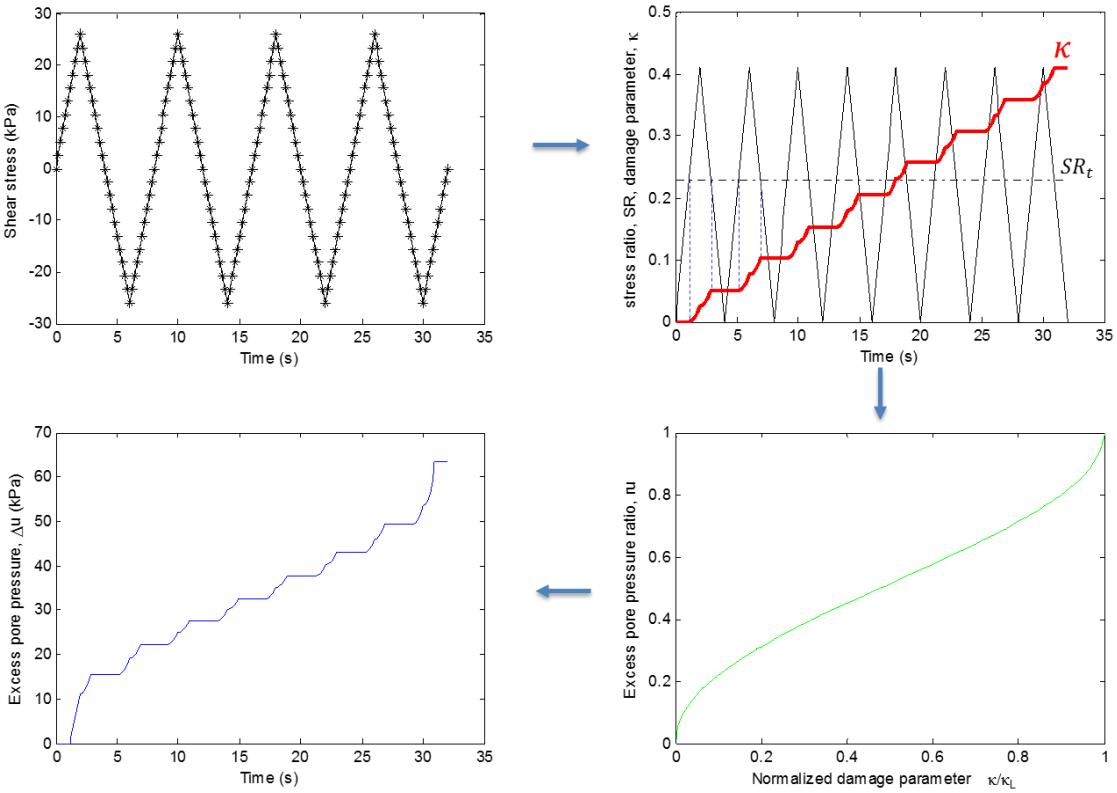

Figure III.3.3 – Generation of excess pore pressure induced by a regular cyclic shear stress history

III.3.1.2. Performance of the model on an ideal soil profile

An ideal profile of 25 m of saturated Crystal Silica sand has been considered for the application of the model. It is characterized by parabolic velocity profile as shown in figure III.3.4 while the non-linear and dissipative behavior of the sand has been characterized adopting the curves proposed by Seed and Idriss (1970).

A total stress dynamic analysis has been carried out using the one-dimensional code SCOSSA (Tropeano et al., 2016) The accelerometric time history recorded at Assisi station on 26th of September 1997 has been adopted as input signal (PGA=0.275 g) (Figure III.3.4e). The results of the analysis are reported in terms of profile of maximum shear stresses (Figure III.3.4c) and maximum shear stresses normalized with respect to the lithostatic effective vertical stresses, σ'_0 (Figure III.3.4d). By knowing the induced time histories of shear stress at different depths (Figure III.3.5a-c).

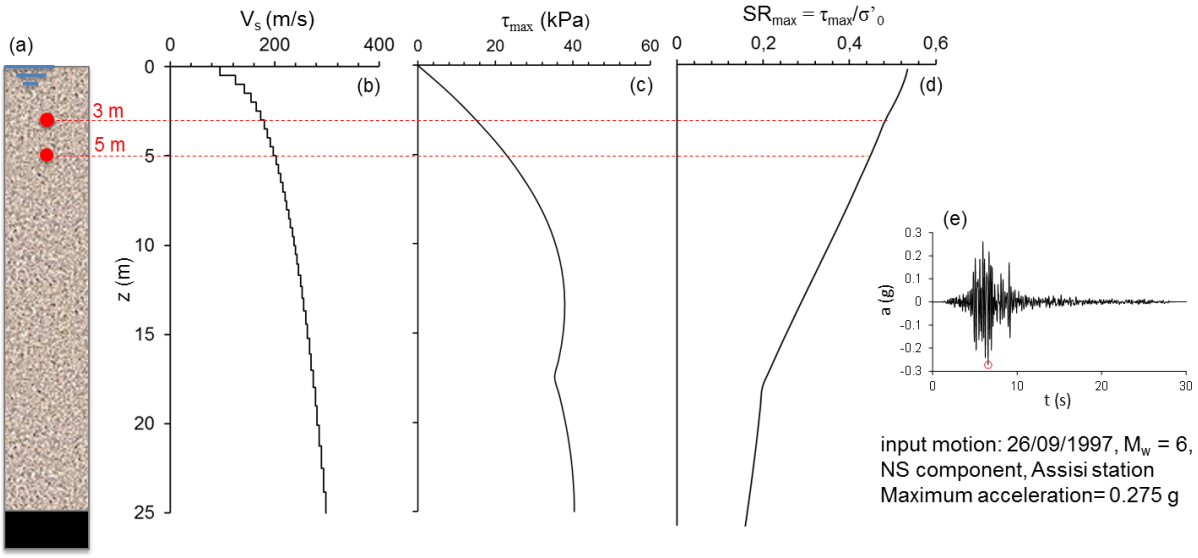

Figure III.3.4 – Ideal column of a sandy soil (a) with relative velocity profile (b) and results of seismic response analysis expressed as maximum shear stress (c) and shear stress ratio (d) for the recorded input motion (e)

It has been then possible to apply the pwp model. As an example the pore pressure model has been applied at a depth of 3 and 5 m from the ground level, where the cyclic stress ratio is high enough and a phenomenon of liquefaction can be expected. The results are reported in figure III.3.5. It can be noted that at 5 m depth (Figure III.3.5a-b-c-d) excess pore pressure cumulates in the first 10 s of the stress history reaching a final value of pore pressure ratio slightly less than 0.8. On the other hand, at 3 m depth (Figure III.3.5e-f-g-h) liquefaction triggers after 6.69 s. The low value of the initial effective stress at 3 m depth determines a cyclic stress ratio greater than that calculated at 5 m depth. It should be pointed out that, once the condition of liquefaction ($\kappa=\kappa_L$) is reached, successive peaks of shear stress ratio (circled in blue in Figure III.3.5f) are ineffective in inducing further increase of excess pore pressure. In both simulations the results show that pore pressure generation is concentrated in the critical phase of seismic motion.

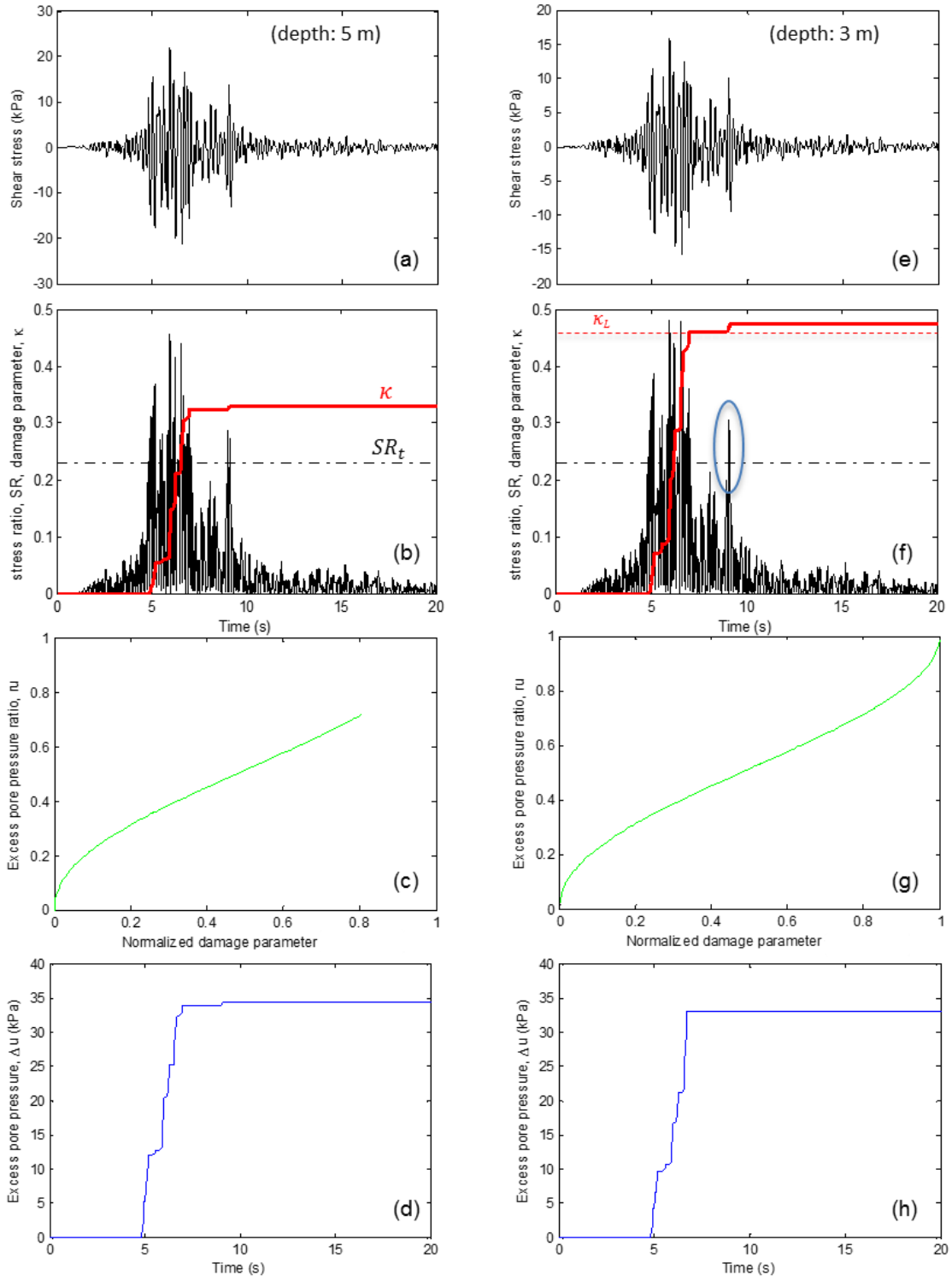

Figure III.3.5 – Time histories of the shear stresses (a-e), damage parameter (b-f) and excess pore water pressure (d-h); pore pressure ratio vs the normalized damage parameter (c-g) at 5 m (a-b-c-d) and at 3 m (e-f-g-h) from the ground surface

III.4. Formulation of pore pressure dissipation

A MATLAB subroutine has been written to simulate the 1D consolidation process of a soil column. The subroutine is designed to be implemented together with the PWP model in the non-linear code SCOSSA (carefully described in chapter IV) in order to simulate the dissipation of excess pore water pressure caused by earthquake shaking. The subroutine should have been written so as to be compatible with the code as well as with the physics of the phenomenon.
A first step consisted in reproducing the consolidation of a homogenous soil profile, then the consolidation of a two layered soil profile and as well as that of a multi-layered system with different initial condition of excess pore water pressure were simulated. Finally, the results of the MATLAB routine were compared with theoretical solutions of the one-dimensional problem and with other published solutions in order to test the rightness and reliability of the routine.

III.4.1. Numerical formulation of consolidation equation

The Terzaghi 1D consolidation equation, also known as diffusion equation, is written as follows

$$\frac{\partial u}{\partial t} = c_v \cdot \frac{\partial^2 u}{\partial z^2} \qquad \text{(III.4.1)}$$

where the consolidation coefficient is indicated with c_v, u is the pore water pressure, function of both the depth, z, and the time, t.
A homogeneous compressible soil layer can be divided into n sublayers, so that the depth at the bottom of the generic sublayer i is equals to $i \cdot \Delta z$ .The depth-time space can be divided as in Figure III.4.1, so that $u_{i,t}$ represents the excess pore pressure at depth, z_i, and time, t.

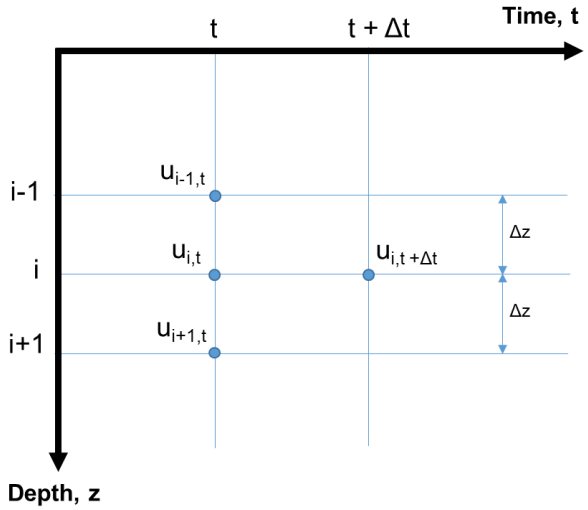

Figure III.4.1 – Identification of the variables in the depth – time space

By applying the definition of derivative to the partial derivative, it can be written

$$\left(\frac{\partial u}{\partial t}\right)_i = \lim_{\Delta t \to 0} \frac{u_{i,t+\Delta t} - u_{i,t}}{\Delta t} \tag{III.4.2}$$

For small, finite value of Δt, the expression (III.4.2) can be approximate to

$$\left(\frac{\partial u}{\partial t}\right)_i \approx \frac{u_{i,t+\Delta t} - u_{i,t}}{\Delta t} \tag{III.4.3}$$

Were the smaller the time interval, Δt, the more accurate will be the solution. The time interval is here defined as forward difference, since it goes forward in time.

Performing same operations on the *u* variable with respect to depth, Z, it can be written

$$\left(\frac{\partial u}{\partial z}\right)_t^F \approx \frac{u_{i+1,t} - u_{i,t}}{\Delta z} \tag{III.4.4}$$

$$\left(\frac{\partial u}{\partial z}\right)_t^B \approx \frac{u_{i,t} - u_{i-1,t}}{\Delta z} \tag{III.4.5}$$

Which are the forward and the backward difference in space, respectively.

Finally, the second derivative of the excess pore water pressure respect to the depth can be approximated as

$$\left(\frac{\partial^2 u}{\partial z^2}\right)_t \approx \frac{\left(\frac{\partial u}{\partial z}\right)_t^F - \left(\frac{\partial u}{\partial z}\right)_t^B}{\Delta z} = \frac{\frac{u_{i+1,t} - u_{i,t}}{\Delta z} - \frac{u_{i,t} - u_{i-1,t}}{\Delta z}}{\Delta z} = \frac{\left(u_{i-1} - 2u_i + u_{i+1}\right)_t}{\Delta z^2} \tag{III.4.6}$$

The consolidation equation (III.4.1) can now be written in differential form, taking into account equation (III.4.3) and (III.4.6), as

$$\frac{u_{i,t+\Delta t} - u_{i,t}}{\Delta t} \approx c_v \cdot \frac{\left(u_{i-1} - 2u_i + u_{i+1}\right)_t}{\Delta z^2} \tag{III.4.7}$$

Or, rearranging as

$$u_{i,t+\Delta t} \approx u_{i,t} + \beta \cdot \left(u_{i-1} - 2u_i + u_{i+1}\right)_t \tag{III.4.8}$$

Which is the explicit finite difference form of the consolidation equation, where

$$\beta = c_v \frac{\Delta t}{\Delta z^2} \tag{III.4.9}$$

According to equation (III.4.8) the pore pressure at any time and depth can be calculated knowing the initial conditions at time *t* (u_{i-1}, u_i and u_{i+1} in Figure III.4.1) and moving through the time by small time increments, *Δt*.

The more Δt and Δz are small, the more the solution is accurate, but also more calculations will be necessary. The expression (III.4.8) is numerically stable for $\beta<0.5$ and in machine calculation β is generally assumed equal or less than 0.1.

In case of a layered system, a boundary separates the above material , characterized by a definite value of permeability, k_i, and consolidation coefficient, c_{vi}, from that below, characterized by different values of permeability, k_{i+1} and consolidation coefficient, c_{vi+1} (Figure III.4.2). Since β and Δt must be the same for the whole profile, the discretization for each layer, Δz_i and Δz_{i+1}, must be different.

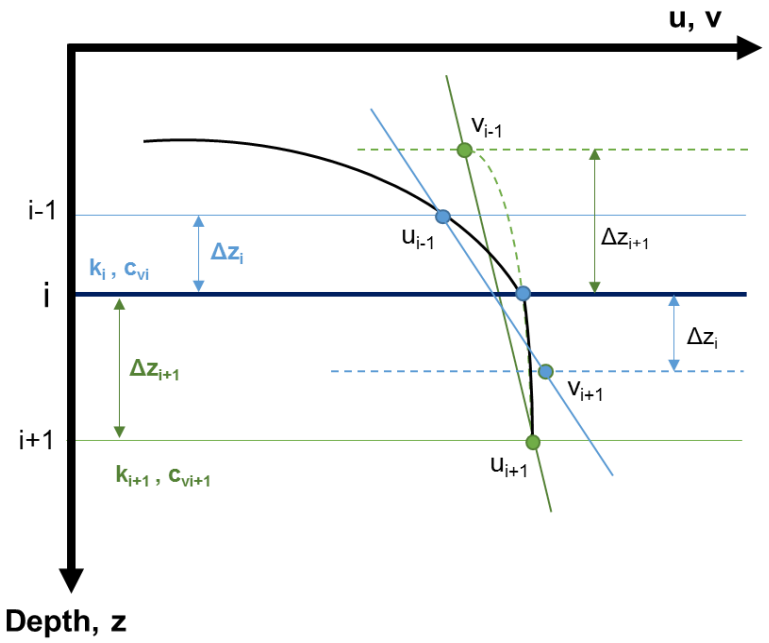

Figure III.4.2 – consolidation of a two layered system

For continuity, at the boundary between two soil layers the the volume of water coming from one soil layer should be equal to that passing in the second layer, and for Darcy's law it should be that

$$\frac{k_i}{\gamma_w}\left(\frac{\partial u}{\partial z}\right)_i = \frac{k_{i+1}}{\gamma_w}\left(\frac{\partial u}{\partial z}\right)_{i+1} \qquad \text{(III.4.10)}$$

This introduces the problem of evaluating $\partial u/\partial z$ at the boundary between the two layers, which is a non-differentiable point.

If u is named the excess pore pressure at the point (i-1) belonging to the first layer and at the point(i+1) belonging to the second layer and v is named the pore pressure that it would be obtained at the same points if the material would be homogenous and characterized by the properties of layer 1 or two, $\partial u/\partial z$ at point *i* can be approximated by the slope of one of the two lines in Figure III.4.2, as

$$\frac{v_{i+1}-u_{i-1}}{2\Delta z_i} \text{ or } \frac{u_{i+1}-v_{i-1}}{2\Delta z_{i+1}} \tag{III.4.11}$$

If the $\partial u/\partial z$ is assumed to be equal to the average of these values, the equation (III.4.10) can be written as

$$k_i \frac{v_{i+1}-u_{i-1}}{2\Delta z_i} = k_{i+1} \frac{u_{i+1}-v_{i-1}}{2\Delta z_{i+1}} \tag{III.4.12}$$

Remembering the expression of β (III.4.9) and defining

$$\alpha = \frac{k}{\Delta z} \tag{III.4.13}$$

the equation (III.4.12) can be written as

$$\alpha_{i+1} \cdot v_{i-1} + \alpha_i \cdot v_{i+1} = \alpha_i \cdot u_{i-1} + \alpha_{i+1} \cdot u_{i+1} \tag{III.4.14}$$

In the layer immediately above the boundary, for equation (III.4.7),

$$\frac{\partial u_i}{\partial t} \approx \frac{c_{vi}}{\Delta z_i^{\,2}} \left(u_{i-1} - 2u_i + v_{i+1} \right) \tag{III.4.15}$$

and in the layer immediately below the boundary

$$\frac{\partial u_{i+1}}{\partial t} \approx \frac{c_{vi+1}}{\Delta z_{i+1}^{\,2}} \left(v_{i-1} - 2u_i + u_{i+1} \right) \tag{III.4.16}$$

Solving equation (III.4.15) for v_{i+1} and equation (III.4.16) for v_{i-1}, substituting into equation (III.4.14) and rearranging, it results

$$(\beta_{i+1} \cdot \alpha_i + \beta_i \cdot \alpha_{i+1}) \cdot u_i \cdot \Delta t = 2\beta_i \cdot \beta_{i+1} (\alpha_i \cdot u_{i-1} - (\alpha_i + \alpha_{i+1}) \cdot u_i + \alpha_{i+1} \cdot u_{i+1}) \tag{III.4.17}$$

Finally, equation (III.4.17) can be rewritten as

$$\left(\frac{\partial u_i}{\partial t} \right) \Delta t = A \cdot u_{i-1} - 2 \cdot B \cdot u_i + C \cdot u_{i+1} \tag{III.4.18}$$

where

$$A = \frac{2\beta_i \cdot \beta_{i+1}}{\beta_{i+1} \cdot \alpha_i + \beta_i \cdot \alpha_{i+1}} \alpha_i \tag{III.4.19}$$

$$B = \frac{2\beta_i \cdot \beta_{i+1}}{\beta_{i+1} \cdot \alpha_i + \beta_i \cdot \alpha_{i+1}} \left(\frac{\alpha_i + \alpha_{i+1}}{2} \right) \tag{III.4.20}$$

$$C = \frac{2\beta_i \cdot \beta_{i+1}}{\beta_{i+1} \cdot \alpha_i + \beta_i \cdot \alpha_{i+1}} \alpha_{i+1} \tag{III.4.21}$$

It can be noticed that if $cv_i = cv_{i+1}$ and $k_i = k_{i+1}$ the coefficients become coincident and the original equation for a homogeneous soil layer is obtained.

In the explicit finite difference form, the time derivative of excess pore water pressure is represented by a forward difference, so the equation (III.4.18) can be rewritten as

$$u_{i,t+\Delta t} \approx u_{i,t} + \left(Au_{i-1} - 2Bu_i + Cu_{i+1} \right)_t \qquad \text{(III.4.22)}$$

Which is the analog of equation (III.4.8) for a layered system.

III.4.1.1. Description of two simple examples

Equation (III.4.8) and (III.4.22) have been used to solve the consolidation problem for two simple examples. The first is related to a homogeneous soil profile and has been useful to understand the explicit finite difference form of consolidation equation. The second is related to a system of two layers with different permeability and consolidation coefficients. In detail, the lower layer has a permeability four times higher than the upper layer.

In both cases, a constant initial distribution of excess pore water pressure has been assumed, while the boundary drainage conditions at the bottom are assumed locked in both cases.

The consolidation coefficient, c_v, of each layer is computed as

$$c_v = \frac{k \cdot E_{oed}}{\gamma_w} \qquad \text{(III.4.23)}$$

in function of the unit weight of the water, γ_w, the permeability, k, and the oedometric modulus, E_{oed}, of the soil. For the elasticity theory, the oedometric modulus can be directly correlated to the stiffness of the soil, G_0, and the coefficient of Poisson, ν, as

$$E_{oed} = \frac{2 \cdot G_0 \cdot (1-\nu)}{(1-2\nu)} \qquad \text{(III.4.24)}$$

The results of the two simulations, expressed as isochrones of excess pore water pressure, are reported in Figure III.4.3.

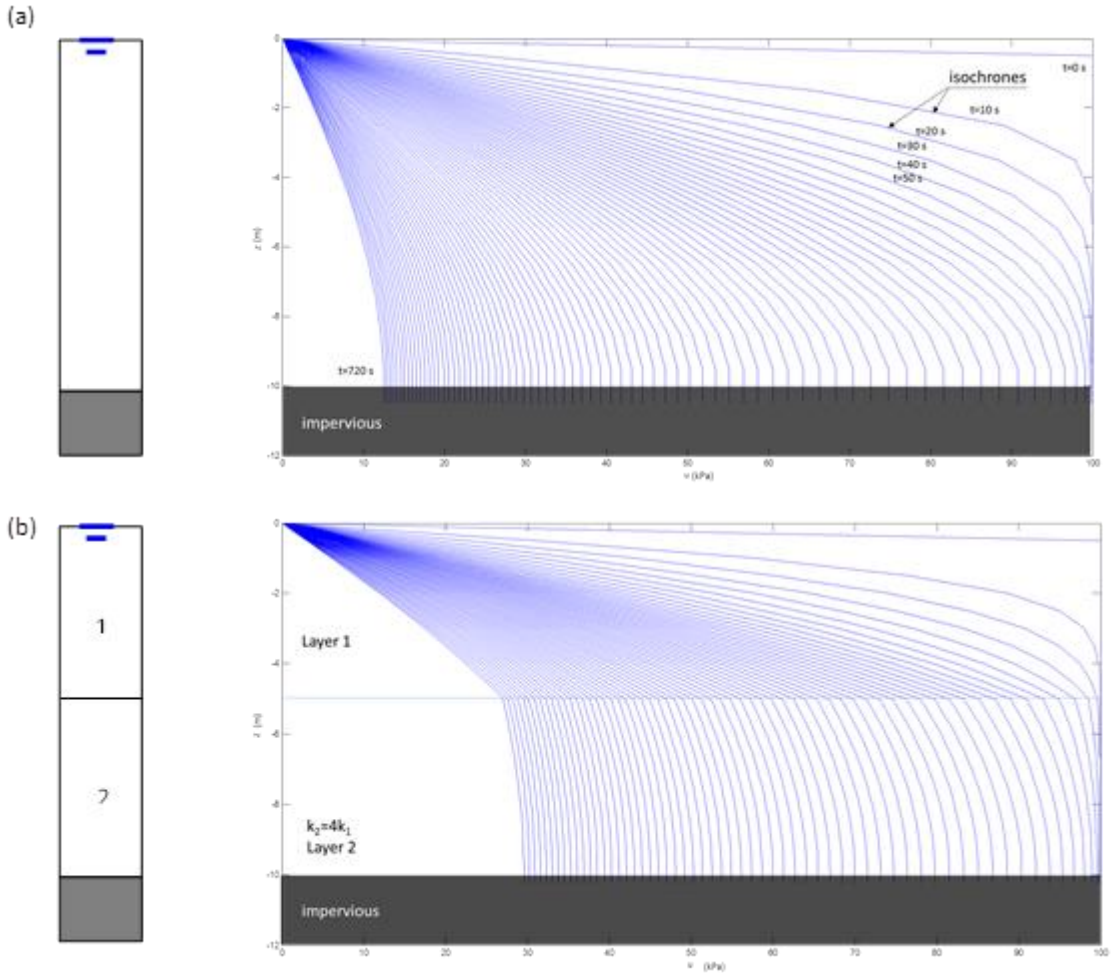

Figure III.4.3 - Two simple examples related to the consolidation of a homogeneous soil layer (a) and a system of two layers, with the lower layer having permeability higher than the upper layer (b)

III.4.2. Validation of the dissipation subroutine

For the verification of the MATLAB subroutine, the problem of one-dimensional consolidation has been simulated with different initial excess pore pressure distributions and boundary conditions. All the considered closed form solutions are reported in Figure III.4.4.where the comparisons with the numerical solutions is also shown.

The comparison is shown in terms of excess pore water pressure normalized respect to the initial value, U/U_0, and in terms of time factor, T_v, which is defined as

$$T_v = \frac{c_v \cdot t}{H^2} \qquad \text{(III.4.25)}$$

where H is the drainage path.

In the first scheme, the isochrones are perfectly coincident with the theoretical solution, while in the other two schemes the isochrones are generally well-reproduced and no delay is present

respect to the theoretical solution; sometimes differences are related only to the shape of the isochrones.

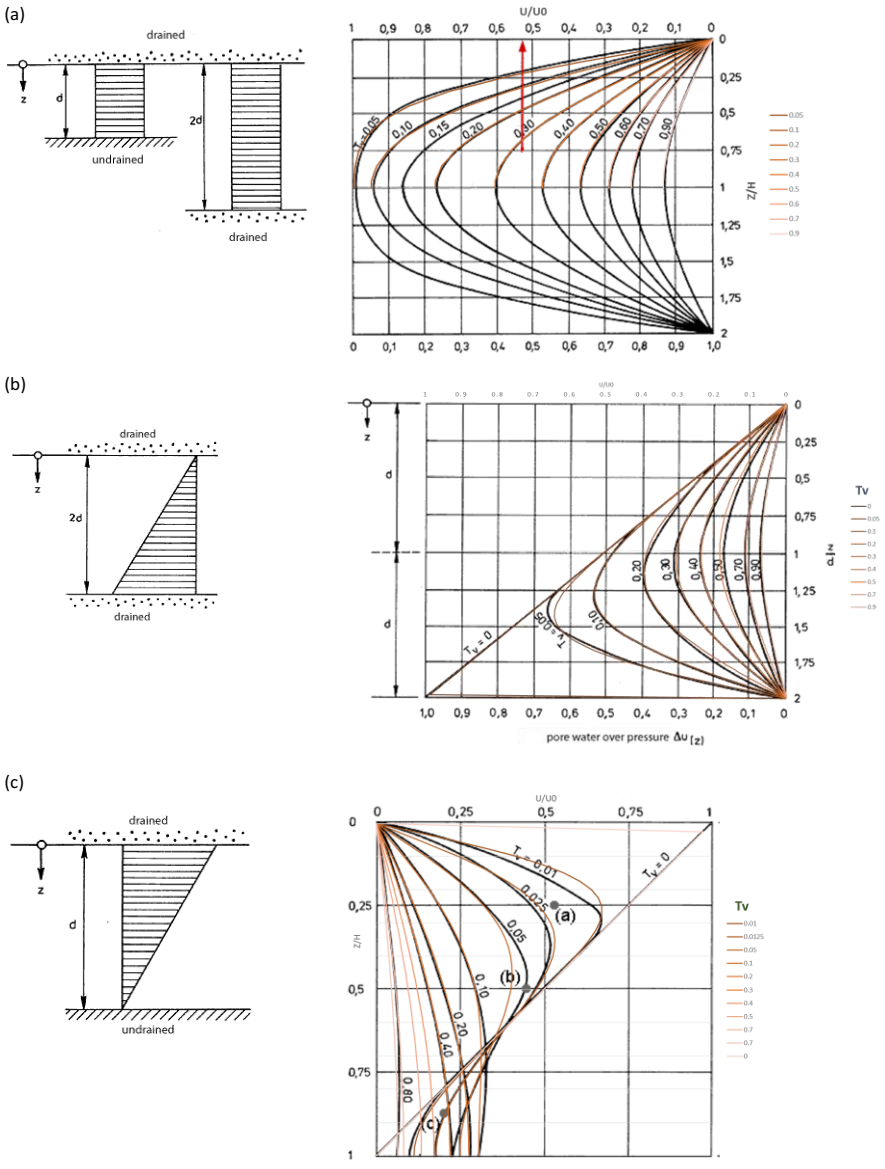

Figure III.4.4 - Comparison between the simulated isochrones (in brown) and the solutions of the 1D consolidation equation for several excess pore pressure initial distributions: rectangular (a), triangular (b) and inverse triangular (c) (mod. after Lang et al., 2011)

The most simple case, related to a rectangular initial distribution, has been performed also with the finite element code PLAXIS (version 8.2) for understanding the degree of approximation performed by one of the most popular commercial codes and, consequently, assessing if the error of subroutine solution is tolerable. Simulation has been performed according to ''validation and verification'' plaxis manual, version 8.2 (Brinkgreve, 2002). In the Plaxis model, the upper side is draining, while the closed consolidation boundary condition is applied on the other sides.

The finite element mesh is shown in the Figure III.4.5a. From the comparison between the simulation and the solution reported by Lang et al., 2011, it can be noticed that the overlapping decreases as the time factor increases (Figure III.4.5b) and Plaxis solution seems to be less reliable if compared to MATLAB results (Figure III.4.4a).

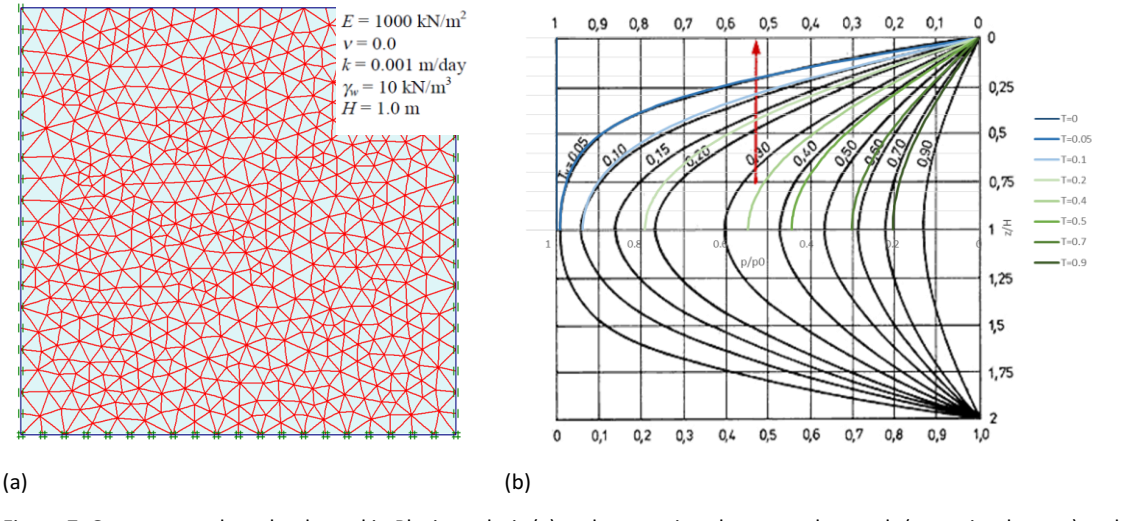

(a) (b)

Figure III.4.5 - Geometry and mesh adopted in Plaxis analysis (a) and comparison between the result (green isochrones) and the 1D solution (mod. after Lang et al., 2011)

The consolidation of two layered system has been simulated for different values of soil permeability and compared with solutions available in literature (Figure III.4.6). In particular, an approximated solution of a two layered system is proposed by Luscher (1965), based on an electric analog model. As stated by the author, Luscher's model drains slower than Terzaghi's theoretical model, so the comparison with the MATLAB simulation is consistent with the expected results.

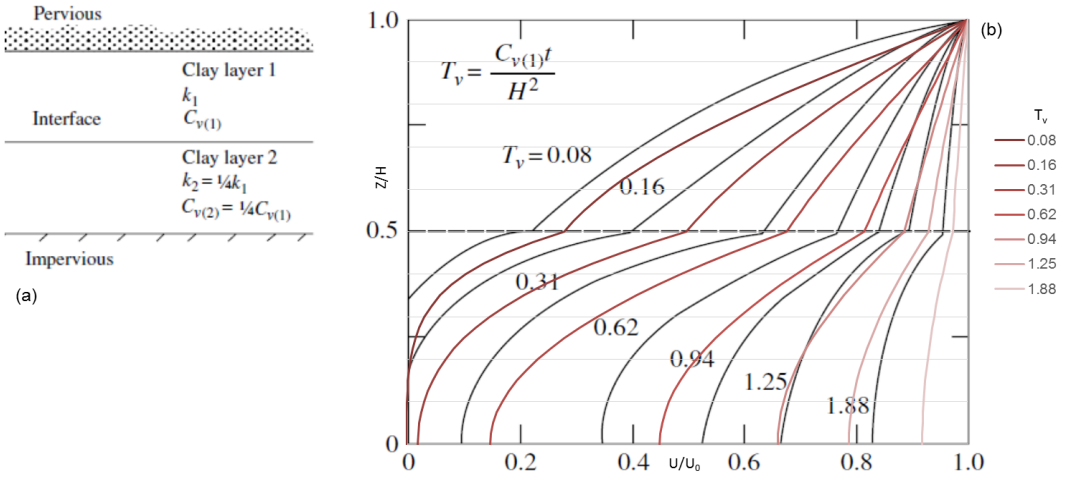

Figure III.4.6 - Scheme of a two layered system (a) and MATLAB simulation compared to the Luscher solution (Luscher, 1965 mod. Das, 2007) (b)

III.5. References

Bathia S.K. (1982). The verification of relationships for effective stress method to evaluate liquefaction potential of saturated sands. PhD dissertation, University of British Columbia, Canada.

Bažant Z.P., Krizek R.J. (1976). Endochronic constitutive law for liquefaction of sands. Journal of Soil Mechanics and Foundations Division, 102(EM2): 225-238.

Biondi G. (2002). Instabilità sismica dei pendii sabbiosi causata da incrementi di pressione interstiziale. PhD Dissertation in Geotechnical Engineering, University of Catania, Italy.

Booker J.R., Rahman M., Seed H.B. (1976). GADFLEA: a computer program for the analysis of pore pressure generation and dissipation during cyclic or earthquake loading. California University, Berkeley, USA.

Brinkgreve R.B.J. (2002). Plaxis 2D Version 8 - Validation and Verification Manual. Delft University of Technology and PLAXIS v.b., The Netherlands. A.A. Balkema Publishers.

Das B.M. (2008). Advanced soil mechanics. Third edition, Taylor and Francis Group.

Finn W.D.L., Bhatia S. (1982). Prediction of seismic porewater pressures. Proceedings of the 10th Int. Conference on Soil Mechanics and Foundation Engineering, Stockholm, Norway, 3: 201–206.

Green R.U., Terri G.A. (2005). Number of equivalent cycles concept for liquefaction evaluations revisited. Journal of Geotechnical and Geoenvironmental Engineering, ASCE, 71(4): 477–88.

Idriss I.M., Boulanger R.W. (2014). CPT and SPT liquefaction triggering procedures. Report No UCD/GCM-14/01, University of California at Davis, California, USA.

Idriss I.M., Boulanger R.W. (2014). CPT and SPT liquefaction triggering procedures. Report No UCD/GCM-14/01, University of California at Davis, California, USA.

Ivšić T. (2006). A model for presentation of seismic pore water pressures. Soil Dynamics and Earthquake Engineering, 26(2-4): 191-199.

Khashila M., Hussien M.N., Karray M., Chekired M. (2015). Evaluation of equivalent cycle liquefaction concept based on TxSS test results. GEOQuébec 2015, Québec, Canada.

Lang H.J., Huder J., Amann P., Puzrin A.M. (2011). Bodenmechanik und Grundbau. Springer.

Liu A.H., Stewart J.P., Abrahamson N.A., Moriwaki Y. (2001). Equivalent number of Uniform stress cycle for soil liquefaction analysis. Journal of Geotechnical and Geoenvironmental Engineering, 127 (12): 1017 – 1026.

Luscher U. (1965). Electric analogs in time-settlements problems. Discussion. Journal of Soil Mechanics and Foundations Division, ASCE, 91 (SM1): 190-195.

Park T., Ahn J.K. (2013). Accumulated stress based model for prediction of residual pore pressure. Proceedings of the 18th Int. Conf. on Soil Mechanics and Geotechnical Engineering, Paris, France.

Park T., Park D., Ahn J.K. (2014). Pore pressure model based on accumulated stress. Bulletin of Earthquake Engineering. 13(7): 1913-1926.

Polito C. P. (1999). The effects of non-plastic and plastic fines on the liquefaction of sandy soils. PhD Dissertation in Civil Engineering. Virginia Polytechnic Institute, Blacksburg, VA, USA.

Polito C.P., Green R.A., Lee J. (2008). Pore pressure generation models for sands and silty soils subjected to cyclic loading. Journal of Geotechnical and Geoenvironmental Engineering, ASCE, 134(10): 1490-1500.

Seed H.B., Idriss I.M., Makdisi F., Banerjee N. (1975). Representation of irregular stress time histories by equivalent uniform stress series in liquefaction analysis, Report No. EERC 75-29, Earthquake Engeneering Research Center, University of California, Berckeley, California, USA.

Silver M.L., Park T.K. (1976). Liquefaction potential evaluated from cyclic strain-controlled properties tests on sand. Soils and Foundations, 16(3): 51-65.

Spiedo F. (2016). Fattori di influenza sul comportamento ciclico non drenato dei terreni liquefacibili. Master thesis in Environmental Engineering. University of Naples Federico II (in Italian).

Tropeano G., Chiaradonna A., d'Onofrio A., Silvestri F. (2016). An innovative computer code for 1D seismic response analysis including shear strength of soils. Géotechnique, 66(2): 95-105.

Tropeano G., Chiaradonna A., d'Onofrio A., Silvestri F. (2016). An innovative computer code for 1D seismic response analysis including shear strength of soils. Géotechnique, 66(2): 95-105.

Valanis K.C. (1971). A theory of viscoplasticity without a yield surface. Archives of Mechanics (Archiwum Mechaniki Stosowanej), 23(4): 517-555.

Vucetic M. (1994). Cyclic threshold shear strains in soils. Journal of Geotechnical Engineering Division, ASCE, 120(12): 2208-2228.

IV. IMPLEMENTATION ON SCOSSA CODE

In this chapter, after a brief description of SCOSSA code, the implementation of the integrated pwp and dissipation model inside the numerical computer program is detailed. The performance of the code in total and effective stress conditions are finally compared with the procedure inplemented in others one-dimensional computer codes.

IV.1. The SCOSSA computer code

SCOSSA, acronym of *'Seismic Code for Stick-Slip Analysis',* is a computer code for one-dimensional seismic response analysis including shear strength of soils (Tropeano et al., 2016). In fact, the code is able to model both the 'transient' seismic response ('stick' mode) and the permanent deformation mechanisms accounting for the coupled effects of deformability and strength ('slip' mode).

For the purposes of this study, only the stick mode will be described because useful to the implementation of the integrated pwp model.

The code models the soil profile as a system of consistent lumped masses, connected by viscous dampers and springs with hysteretic non-linear behaviour (Figure IV.11).

The discretization of the subsoil profile into the lumped parameter system is performed on Lysmer and Kuhlemeyer (1969) criterion, where the maximum sub-layer thickness is a fraction (1/6 - 1/8) of the minimum wavelength to be transmitted.

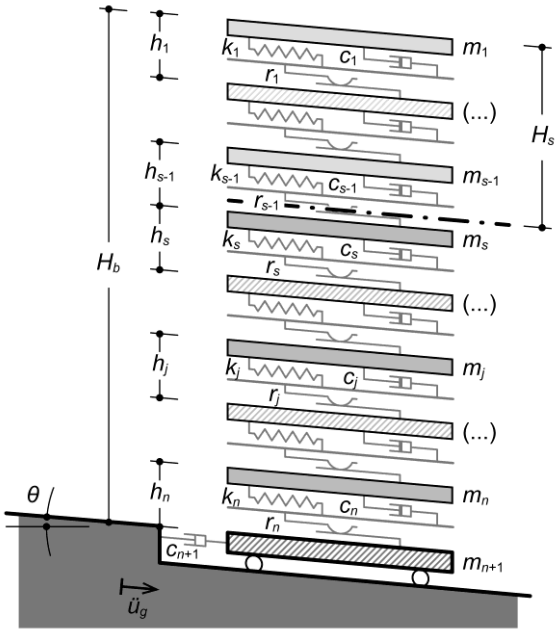

Figure IV.1.1 – Soil column modelled as multi-degrees of freedom system

In the stick phase, the seismic response in terms of absolute displacements, u_a, to a base ground motion, $\ddot{u}_g$, can be computed by integrating the following system

$$\mathbf{M}\ddot{\mathbf{u}}_\mathbf{a} + \mathbf{C}\dot{\mathbf{u}}_\mathbf{a} + \mathbf{K}\mathbf{u}_\mathbf{a} = \mathbf{f} \tag{IV.1.1}$$

where **M**, **C** and **K** are the mass, damping and stiffness matrices, **f** is the vector of applied forces. This latter depends on the input accelerogram, $\ddot{u}_g$, which can be applied as 'within' or 'outcrop' motion and on the bedrock impedance. The **f** vector can be set as equal to

$$\mathbf{f} = \mathbf{i} \cdot \begin{cases} c_n \dot{u}_g + k_n u_g & \text{(within motion - rigid bedrock)} \\ 2c_n \dot{u}_g & \text{(within motion - deformable bedrock)} \\ c_{n+1} \dot{u}_g & \text{(outcrop motion - deformable bedrock)} \end{cases} \tag{IV.1.2}$$

where

- **i** is a vector with each element equal to zero, except for the *n*-th (for inside motion), or (*n*+1)-th (for outcrop motion), equal to unity;
- c_n and k_n are the viscous damping coefficient and the spring elastic stiffness of the *n*-th element, respectively;
- $c_{n+1} = \rho_r V_{S,r}$ is the seismic impedance of the bedrock.

The elements of the **M** and **K** matrices are defined from the mass, m_j, and the spring stiffness, k_j, for a generic layer *j*, as follows

$$m_1 = \frac{\rho_1 h_1}{2}\ ;\ m_j = \frac{\rho_j h_j + \rho_{j-1} h_{j-1}}{2}\ ;\ m_{n+1} = \frac{\rho_n h_n}{2} \tag{IV.1.3}$$

$$k_j = \frac{G_j}{h_j} \tag{IV.1.4}$$

where ρ_j, h_j, and G_j are the density, thickness and shear stiffness of the j-th layer, respectively. The viscous damping matrix, **C**, is defined according to the full Rayleigh damping formulation (Hashash and Park, 2002)

$$\mathbf{C} = \alpha_R \mathbf{M} + \beta_R \mathbf{K} \tag{IV.1.5}$$

The constants α_R and β_R are set as functions of the minimum soil damping ratio, ξ_{min}, the fundamental frequency of the subsoil profile and the predominant frequency of the input motion. The non-linear hysteretic response of the springs is modelled with an extended version of the modified Kondner-Zelasko (1963) hyperbolic model, MKZ (e.g. Matasovic and Vucetic, 1993), defined by two different relationships for loading and for unloading-reloading conditions. The stress-strain relationship (i.e. the backbone curve) for loading is given by

$$F_{bb}(\gamma) = \frac{\gamma G_0}{1+\beta(\gamma/\gamma_r)^{s'}} \tag{IV.1.6}$$

where γ is the shear strain level, G_0 is the initial shear modulus, γ_r is the reference shear strain and β and s' are two dimensionless factors. The stress-strain relationship for unloading-reloading condition can be either defined by the conventional Masing (1926) criteria or by the more general formulation recently proposed by Phillips and Hashash (2009)

$$F_{ur}(\gamma) = F^*(\gamma_m) \cdot \left[\frac{G_0(\gamma-\gamma_c)}{1+\beta\left(\frac{\gamma-\gamma_c}{2\gamma_r}\right)^{s'}} - \frac{G_0(\gamma-\gamma_c)}{1+\beta\left(\frac{\gamma_m}{\gamma_r}\right)^{s'}} \right] + \frac{G_0(\gamma-\gamma_c)}{1+\beta\left(\frac{\gamma_m}{\gamma_r}\right)^{s'}} + \tau_c \tag{IV.1.7}$$

In equation (IV.1.7), γ_c and τ_c are, respectively, the reversal shear strain and shear stress, γ_m is the maximum shear strain attained during the time history, and $F^*(\gamma_m)$ is a damping reduction factor, defined as follows

$$F^*(\gamma_m) \doteq \frac{\xi_{\exp}(\gamma)}{\xi_{Mas}(\gamma)} = p_1 - p_2\left(1 - \frac{G(\gamma_m)}{G_0}\right)^{p_3} \tag{IV.1.8}$$

In equation (IV.1.8), p_1, p_2 and p_3 are non-dimensional parameters obtained from the best fit of the ratio between the strain-dependent hysteretic damping measured in laboratory tests, $\xi_{exp}(\gamma)$, and that calculated using the conventional Masing rules, $\xi_{Mas}(\gamma)$; $G(\gamma_m)$ is the secant modulus corresponding to the maximum shear strain γ_m (see Phillips and Hashash, 2009, for details). The updated formulation modifies the Masing unloading-reloading rules, providing a better agreement with the experimental damping-strain curves for large shear strains.

IV.2. Verification of SCOSSA code in total stress analysis

The SCOSSA code (Tropeano et al., 2016) in the first version in total stress analysis has been verificated and validated with other codes during an international benchmark: the PRENOLIN Project. The details about the project and the description of the main results about SCOSSA code will be described in the next paragraphs.

IV.2.1. The PRENOLIN Project

PRENOLIN is an international benchmark part of two French larger projects: SINAPS@, funded by the ANR (French National Research Agency) and SIGMA, funded by a consortium of nuclear operators (EDF, CEA, AREVA, ENL).

One of the objectives of the PRENOLIN (*PREdiction of soil NOn LINear effects*) project is the assessment of uncertainties associated with non-linear simulation of 1D site effects. An international benchmark is underway to test several numerical codes, including various non-linear soil constitutive models, to compute the non-linear seismic site response. Table IV.2.1 reportes the list of the partecipating teams and the numerical codes used.

Twentyone participating teams have tested twentythree different numerical codes, which are characterized by more than ten different constitutive models (Regnier et al., 2016). Essentially three different, non-exclusive, code groups were identified by the organization team, according to three main characteristics: 1) numerical implementation scheme; 2) damping formulation, both in the low strain range and in the large strain range; and 3) cyclic hysteretic behaviour formulation (Regnier et al., 2016).

A preliminary verification phase (i.e. comparison between numerical codes) on simple and ideal cases has been performed with 23 different codes. It is followed by a validation phase, with the aim to compare the predictions of the numerical computation with actual strong motion data recorded in a selection of well-characterized sites. The verification was initially conducted by using elastic and visco-elastic soil-behaviour model to ensure a common understanding of the parameters by comparing the results with the available analytical solution. Then, the non-linear results provide a quantification of the epistemic uncertainties linked to wave propagation modeling using different non-linear rheological models (Regnier et al., 2015a).

Table IV.2.1 – Numerical codes and related partecipating teams to the Prenolin Project

Code	Identification team code	Team	Team istitution
SeismoSoil	A - 0	Assimaki D. & Shi J.	Caltech, USA
FLIP	B - 0	Iai S.	DPRI, Japan
PSNL	C - 0	Kramer S.	Univesity of Washington, USA
CYBERQUAKE	D - 0	Foerster E.	CEA, France
NOAH – 2D	E - 0	Gelis C. & Delavaux E.	IRSN, France
NTUA	G - 0	Gazetas G., Garini E. & Gerolymos N.	NTUA, Greece
UCSD - OpenSees	H - 0	Gingery J.	UCSD, USA
DEEPSOIL NL	J – 0 F – 0 L – 2 M - 2	Hashash Y. & Harmon J. Giannakou A. Foti S. Lanzo G. & Pagliaroli A.	University of Illinois, USA Fugro, France PoliTo, Italy Università Roma La Sapienza, Italy
DEEPSOIL EL	J - 1	Hashash Y. & Harmon J.	University of Illinois, USA
1DFD – NL - IM	K - 0	Moczo P., Kristek J. & Richterova A.	CUB, Slovakia
ICFEP	L -1	Foti S. & Kontoe S.	PoliTo, Italy & Imperial College, UK
FLAC	M - 0	Lanzo G. & Pagliaroli A.	University Roma La Sapienza, Italy
Dmod2000	M - 1	Lanzo G. & Pagliaroli A.	University Roma La Sapienza, Italy
GEFDyn	N - 0	Lopez - Caballero F. & Montoya-Noguera	ECP, France
EFISPEC1D	Q - 0	De-Martin F.	BRGM, France
real ESSI	R - 0	Jeremic B., Pisano F.	UCD, USA & TU Delft, Netherlands
ASTER	S - 0	Nieto-Ferro A.	EDF, France
SCOSSA 1.2	T - 0	Tropeano G., Silvestri F. & Chiaradonna A.	UniCa & UniNa, Italy
STRATA	T - 1	Tropeano G., Silvestri F. & Chiaradonna A.	UniCa & UniNa, Italy
SWAP – 3C – 1C	U - 0	d'Avila Santisi M.P.	UNS Nice, France
SWAP – 3C – 3C	U - 1	d'Avila Santisi M.P.	UNS Nice, France
GDNL	Y - 0	Mercerat D.	CEREMA, France
SANISAND – Opensees	W - 0	Taiebat M. & Arduino P.	UBC, Canada & University of Washington, USA
EERA	Z - 0	Boldini D. & Amorosi A.	UniBo & PoliBa, Italy
Plaxis	Z - 1	Boldini D. & Amorosi A.	UniBo & PoliBa, Italy

IV.2.1.1. The verification phase

The verification phase was devised around three 1D canonical cases, chosen to represent simple and ideal soil conditions overlying rigid bedrock substrata; however, varying in complexity (Regnier et al., 2015a)

- Profile 1 (P1): A homogeneous soil layer of 20 m thickness with significant velocity contrast with V_S equal to 300 and 2000 m/s for the soft and sediment layers respectively in order to have significant amplification effects at the intermediate frequency (2-10 Hz);
- Profile 2 (P2): A soil layer of 100 m thickness with a positive vertical velocity gradient (from 150 m/s at the surface to 500 m/s at the soil-bedrock interface) leading to significant amplification at frequencies below 1 Hz;
- Profile 3 (P3): Two homogeneous layers of 20 and 30 m thickness with significant velocity contrasts with V_S equal to 300, 600 and 2000 m/s for the first two soft layers and sediment layers respectively. It was constructed to investigate non-linearity effects within both layers (amplification effects begin around 2.5 Hz), since significant strains can develop at soil interfaces.

P-wave velocity was computed from V_S profiles by setting the Poisson ratio equal to 0.4 for the soil and 0.3 for bedrock. Attenuation parameters were constrained to vary according to *V*s, using the relationship $\xi = 5/V_S$. No soil shear strength was provided.

The non-linear soil properties provided are typical degradation curves of the normalised shear modulus, $G/G_0(\gamma)$, and those than describes the damping ratio increase with the shear strain, $D(\gamma)$, characterizing the rheological behavior of each layer per profile. It does not represent a complete description of the non-linear soil behaviour because it is restricted to shear deformation and volumetric ones and coupling between both are ignored. These curves were constructed using a simple hyperbolic law that was calibrated adopting the soil properties at the middle of each soil layers (Regnier at al., 2015a).

The soil profile and related shear modulus reduction and damping curves are reported in Figure IV.2.1.

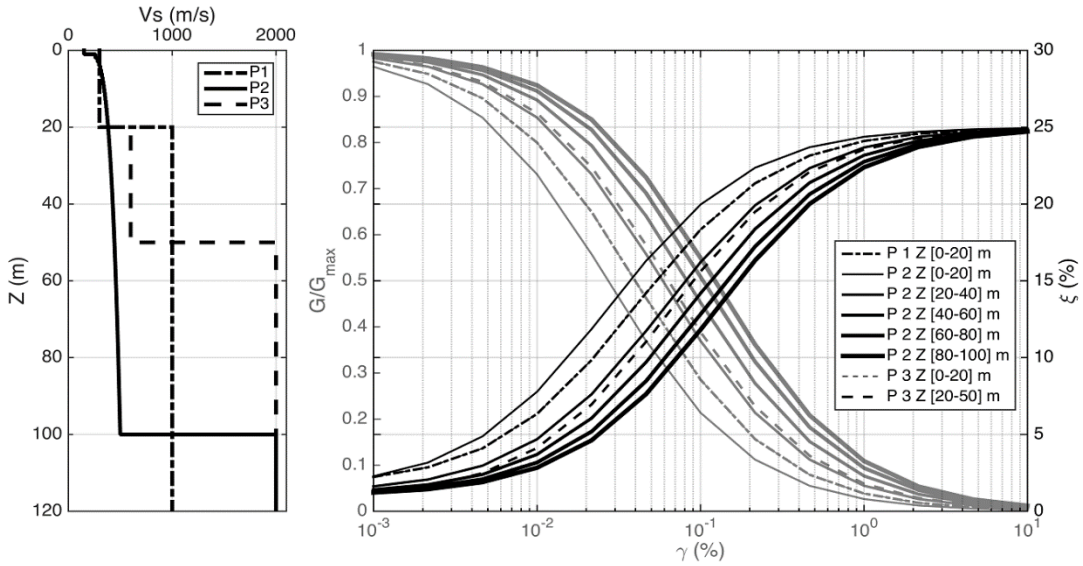

Figure IV.2.1 – V_S profiles, G/G_0 and damping curves for the three ideal profiles (Regnier et al., 2016)

The reference input motions used in the project are showed in Figure IV.2.2a, b and they consist of an analitycal pulse function (Ricker-beta wavelet with central frequency of 4 Hz – labelled as 'Pulse' in Fig. IV.2.2a) and two real recorded accelerograms characterised by high and low frequency contents (with central frequencies about of 11.4 – labelled as 'Real LF'- and 4.8 Hz – labelled as 'Real HF' - respectively), each scaled to three PGA levels (0.005, 0.01 and 0.05 g), in order to generate a wide range of shear strain levels in the soil column. They are used as input motion at the base of the soil column (at the sediment/bedrock interface) to assess the soil responses. Two boundary conditions at the sediment/bedrock interface were tested, elastic and rigid. The latter condition was considered because in the stage of validation down-hole recordings are used as reference motion (Stewart et al., 2008).

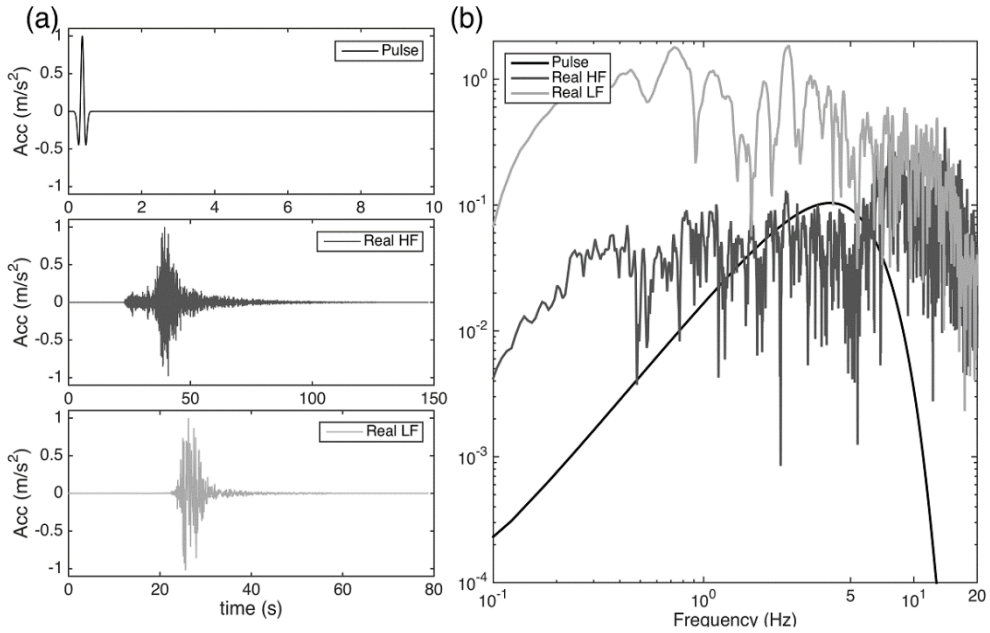

Figure IV.2.2 – Normalized input motions (a) and related Fourier response spectra (b)

A total of 72 computations were performed for each code during the verification phase. Figure IV.2.3 displays the comparison for the P1 profile of the surface acceleration time history for the pulse-like motion and elastic substratum condition, for the linear elastic computation for a short window (3 s) of signal. All results converged towards the analytical solution calculated with the Haskell-Thompson method (Haskell, 1953; Thomson, 1950) that was achieved among all the partecipant codes after the second iteration.

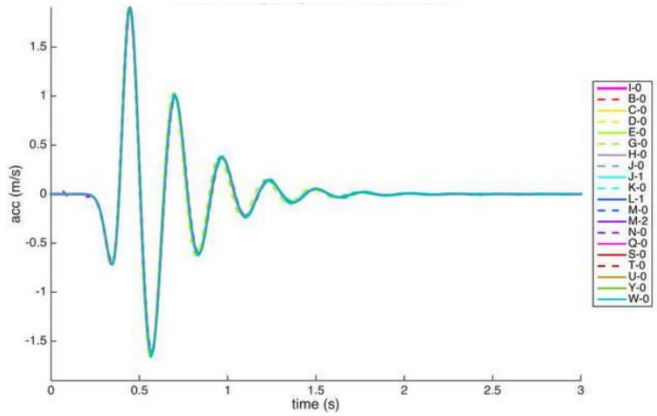

Figure IV.2.3 – Comparison of the acceleration time history at the surface of P1 profile for the pulse-like input motion for the linear elastic computation and elastic bedrock (Regnier et al., 2016)

The comparison of the results of SCOSSA code with that obtained by the other teams are reported in Figure IV.2.4 for the strongest input motion with PGA equals to 0.5 g. The comparison of the transfer fucntions shows that the SCOSSA results are always inclided in the shadow of the others codes for both the bedrock conditions and for the three different ideal soil profiles.

The comparison in terms of maximum shear strain profiles (labelled as ε_{max} in Figure IV.2.4b) and stress-strain curves shows that the maximum shear strains exceed slightly the range at the base of the homogeneus profile (P1 and P2) and at the interface between the layers in the P3 profile.

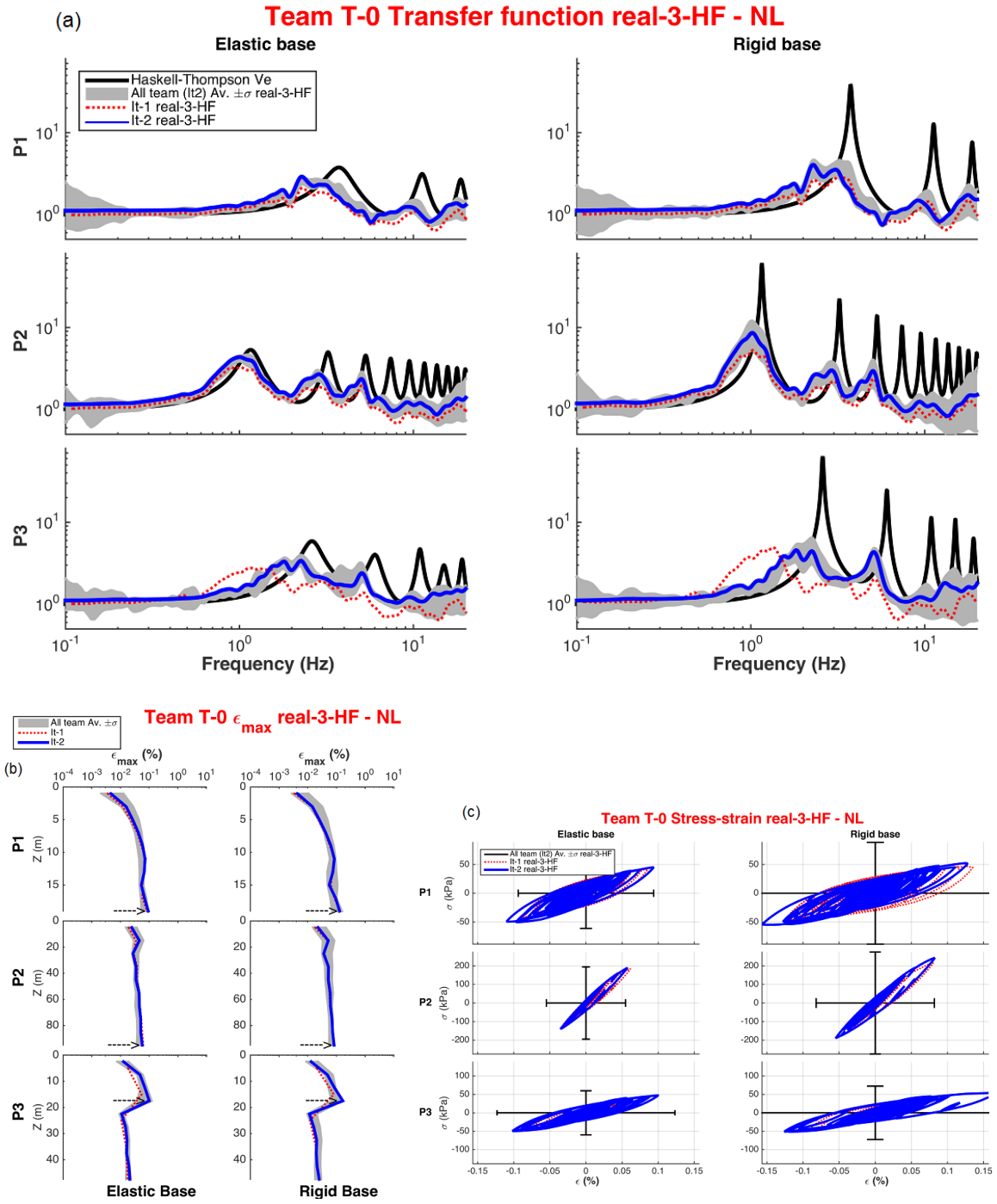

Figure IV.2.4 – Results of the non linear analyses performed by SCOSSA code on three ideal soil profiles for the input motion real-3-HF in case of elastic and rigid bedrock compared with the results of the other codes in terms of transfer function (a) maximum shear strain profiles (b) and stress-strain cycles (c)

IV.2.1.2. The validation phase

To validate the numerical code predictions, the results obtained from the models have been compared with actual observations for a selection of sites with direct measurement of the seismic response. The sites are as close as possible to a 1D soil geometry (horizontal stratification) and associated with available sets of downhole and surface recordings for weak and strong motions. Such informations were completed with careful in-situ and laboratory measurements sufficient to calibrate the parameters of constitutive models. The sites were selected within the Japanese KiK-net and PARI (Port and Airport Research Institute) networks.
The site selection was performed by the organization team on the following requirements: availability of both strong and weak events recordings, plausibility of a 1D geometrical soil configuration, i.e., satisfactory agreement between numerical and empirical site responses in the linear/weak motion range, and the downhole sensor must not be less than 250 m (Regnier, 2015b).
Finally, three sites were selected KSRH10 from KiK-net, Onahama and Sendai from PARI, to be fully characterized for the purpose of the validation phase. The KSRH10 site is mainly a clay soil and it not will be described in this study. The other two sites, Sendai and Onahama, are particularly interesting because they consist of sandy soil susceptible to liquefaction. So, they will be widely described and all the analyses results and comparisons will be shown in the chapter V.

IV.3. Compatibility of non-linear stiffness and strength

The MKZ model implemented in SCOSSA code belongs to the hyperbolic model family (Konder and Zalasko, 1963; Hardin and Drnevich, 1972; Darendeli, 2001; Menq, 2003). These shear modulus reduction curves fit their parameters directly to cyclic laboratory test results. However, cyclic laboratory tests often are not run to failure shear stress levels and, consequently, the model G/G_0 curves are well constrained by the data at small to moderate shear strains, but do not necessarily provide an accurate representation of soil strength at large shear strains. In some cases, the shear strength can be grossly inaccurate, which may result in significant errors for analyses involving shear stress levels at or near failure (Gingery and Elgamal, 2013).
This this inaccuracy is not acceptable when liquefaction phenomena are involved, or more generically, when non-linear effects induced by strong motions want to be simulated. Moreover, the proposed pwp pressure model works on cyclic resistance parameters, one of them, the threshold shear stress ratio, SR_t, can be determined directly on the backbone curve. So, it is very important that coherence between stiffness and strength will be garanteed.

Several researchers have proposed G/G_0 curve adjustment procedure. Stewart et al. (2008) propose to assume the constant value of shear strength when a certain shear strain level (tipically 0.1 -0.3 %) is reached. This procedure can produce a noticeable singularity in the modulus reduction curve, and additional smoothing is necessary to achieve a satisfactory result. Hashash et al. (2010) proposed manually strength corrections since the backbone curve could underestimated or overestimated shear strength depending on the case. Such corrections are often time-consuming and highly subjective, so that Groholski et al. (2015) proposed directly a new model defines the shear strength of soil at failure, still providing the ability to represent small-strain stiffness nonlinearity.

In this study, an interpolation scheme presented by Gingery and Elgamal (2013) is adopted, which provides a smooth, kinkless hyperbolic-like curve to transition between moderate and failure-level shear strains. G/G_0 vs γ curves simultaneously match the hyperbolic models at small to moderate strains and the shear strength at large strains.

The Gingery and Elgamal correction can be applied to any model belonging to the hyperbolic family curves; in particular, in this study it has been applied to the MKZ model (IV.1.4), where the normalized shear modulus reduction curve is defined as

$$\left(\frac{G}{G_0}\right)_{MKZ} = \frac{1}{1+\beta(\gamma/\gamma_r)^{s'}} \tag{IV.3.1}$$

The Gingery and Elgamal procedure (GH model) scales equation (IV.3.1) using a raised cosine function to force the backbone curve at the correct shear strength byintercepting a G/G_0 value at a defined shear strain value (i.e., the supposed failure strain) . Analytically, three different range of shear strain are identified by two limit values of shear strain, γ_1 and γ_2. The equation (IV.3.1) is multiplied by a raised cosine weighting function, *W*, as

$$\left(\frac{G}{G_0}\right)_{GH} = W \cdot \left(\frac{G}{G_0}\right)_{MKZ} \tag{IV.3.2}$$

where

$$W = \begin{cases} 1 & \text{for } \gamma \le \gamma_1 \\ 1+\left[\dfrac{(G/G_0)_{\tau_{ff},\gamma_2}}{(G/G_0)_{MKZ,\gamma_2}}-1\right]\cdot\left\{\dfrac{1}{2}-\dfrac{1}{2}\cos\left[\pi\dfrac{\ln(\gamma)-\ln(\gamma_1)}{\ln(\gamma_2)-\ln(\gamma_1)}\right]\right\}^n & \text{for } \gamma_1 < \gamma \le \gamma_2 \\ \dfrac{\tau_{ff}}{\gamma \cdot G_0 \cdot (G/G_0)_{MKZ,\gamma}} & \text{for } \gamma > \gamma_2 \end{cases} \tag{IV.3.3}$$

The GH model uses equation (IV.3.1) for $\gamma<\gamma_1$, between γ_1 and γ_2 the equation (IV.3.1) is multiplied by a raised cosine weighting function, *W*, and for $\gamma>\gamma_2$, G/G_0 is provided in order to have the shear stress equals to the strenght, τ_{ff}.

The G/G_0 value that provides the correct shear strenght at γ_2 is:

$$\left(\frac{G}{G_0}\right)_{\tau_{ff},\gamma_2} = \frac{\tau_{ff}}{G_0 \cdot \gamma_2} \qquad \text{(IV.3.4)}$$

$(G/G_0)_{MKZ,\gamma_2}$ in eq. IV.33 is the shear modulus reduction value predicted by the MKZ model at γ_2. The exponent *n* can be used to modify the shape of the raised cosine weighting function, but a value equal to unity is enough to have a good correction. The suggested value of 0.05% and 6% for γ_1 and γ_2 respectively, are generally adequate for a wide range of conditions (Gingery and Elgamal, 2013). An example of modified G/G_0 curve is shown in Figure IV.3.1.

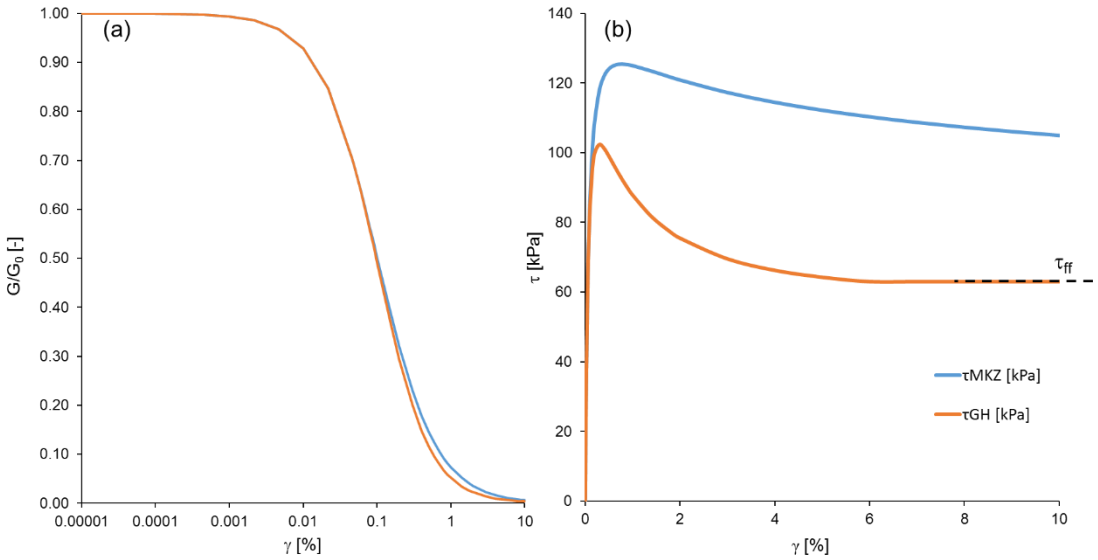

Figure IV.3.1 – Normalized shear modulus reduction (a) and shear stress vs shear strain (b) curves computed using the MKZ and the GH model

The value of shear strength, τ_{ff}, depends on the initial stress conditionin the soil and on how the shear stress is applied. For initial geostatic stress conditions and shear stress applied to horizontal and vertical planes, τ_{ff} can be calculates, as reported by Hardin and Drnevich (1972), as

$$\tau_{ff} = \left[\left(\frac{1+K_0}{2}\cdot\sigma'_v \cdot sen\varphi' + c'\cdot\cos\varphi'\right)^2 - \left(\frac{1-K_0}{2}\cdot\sigma'_v\right)^2\right]^{1/2}$$

(IV.3.5)

where K_0 is the coefficient of lateral stress at rest; σ_v is the vertical effective stress and c' and φ' are the static strength parameters in terms of effective stress. Hardin and Drnevich (1972) precised that effective stress conditions are used in equation (IV.3.5) even though undrained conditions occur for dynamic loading.

The modified G/G_0 curve, obtained from the application of the GH model, can be interpretated again with the MKZ model. In this way, the final parameters of the MKZ model not only are representative of the best fitting on the available laboratory data, but they are also respectful of the shear strength of the soil.

IV.4. Modelling the pore pressure buildup and dissipation and the induced stiffness changes

The excess pore pressure generation and dissipation model, described in chapther II, has been implemented in the SCOSA code. The pore pressure change induced a variation of the effective stress state, which has important consequences on the stiffness and strength of the soil. The effect of confining pressure on dynamic properties should taking into account so that the implementation could be really effective in the code.

The influence of effective confining stress state on the small - strain shear modulus and material damping is a well-established knowledge since 60's years and many relationships have been published (Hardin and Richart, 1963; Seed and Idriss, 1970; Hardin and Drnevich, 1972; Ishibashi and Zang, 1993; d'Onofrio et al., 1999).

Moreover, EPRI (1993) and Darendeli (2001) show that an increase of confining pressure results in a higher nomalized shear modulus and a smaller damping for a given strain value (Figure IV.4.1).

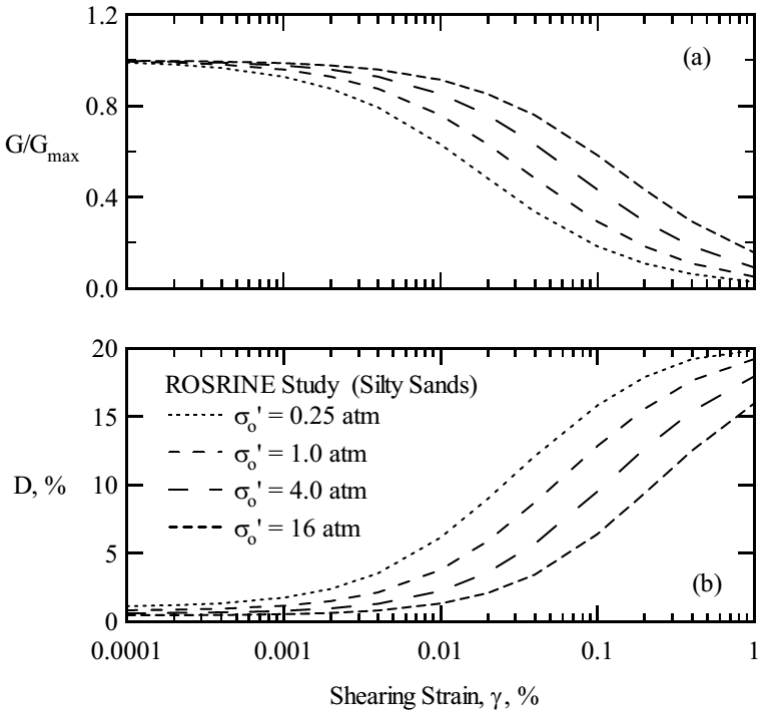

Figure IV.4.1 – The effect of confining pressure on normalized modulus reduction (a) and damping (b) curves of silty sand (Darendeli, 2001)

Hashash and Park (2001) included the effect of confining pressure on the shear modulus model (IV.1.4); the reference strain γ_r is no longer a constant for a soil type, but a variable that depends on the effective stress, as follows

$$\gamma_r = a\left(\frac{\sigma'_v}{\sigma_{ref}}\right)^b \qquad \text{(IV.4.1)}$$

Where σ'_v is the vertical effective stress at the midpoint of the soil layer, σ_{ref} is a reference confining pressure of 0.18 MPa and *a*, *b* are curve fitting parameters. In the same way, the small strain damping is related to the confinig pressure through other two curve fitting parameters. The calibration of these curve fitting required a great amount of experimental data which are rarely available in the engineering practice.

Matasovic and Vucetic (1993) propose a simpler degrading model, in which the shear modulus is directly linked to the excess pore water pressure. This cyclic degradayion model have been frequently used in effective stress analyses codes (e.g. DESRA-2, Lee and Finn, 1978; D-MOD2000, Matasovic and Ordónez, 2011), and it has been implemented also in SCOSSA code in conjuction with the pwp model.

According to this degradation model, the normalized shear modulus reduction curve (equation IV.3.1) is modified as

$$\left(\frac{G}{G_0}\right)=\frac{\sqrt{1-ru}}{1+\beta\left(\frac{\gamma}{\gamma_r}\cdot\frac{\sqrt{1-ru}}{1-ru^{v}}\right)^{s'}} \tag{IV.4.2}$$

where β, γ_r and s' are the parameters of the backbone curve as defined on the laboratory test data, *ru* is the excess pore pressure ratio and ν is exponential constant which expresses the sensitivity of the backbone curve to porewater pressure changes. Matasovic and Vucetic (1993) defined the costant ν on the cycles obtained from strain-controlled DSS tests on californian sandy soils and it assumes average values between 3.5 and 5.

Defining a stress degradation index function, δ_τ, as

$$\delta_\tau=1-ru^{v} \tag{IV.4.3}$$

And the corresponding modulus degradation index function, δ_G, as

$$\delta_G=\sqrt{1-ru} \tag{IV.4.4}$$

the stress-strain relationship (i.e. the backbone curve) for loading of equation (IV.1.6) can be generalized by

$$F_{bb}(\gamma)=\frac{\delta_G\cdot G_0\cdot\gamma}{1+\beta\left(\frac{\gamma}{\gamma_r}\cdot\frac{\delta_G}{\delta_\tau}\right)^{s'}} \tag{IV.4.5}$$

In the same way, also the stress-strain relationship for unloading-reloading formulation (IV.1.7) of Phillips and Hashash (2009) has been generalized by Moreno-Torres et al. (2010) including degradation model

$$F_{ur}(\gamma)=F^{*}(\gamma_m)\cdot\left[\frac{G_0\cdot\delta_G(\gamma-\gamma_c)}{1+\beta\left(\frac{\delta_G}{\delta_\tau}\right)^{s'}\cdot\left(\frac{\gamma-\gamma_c}{2\gamma_r}\right)^{s'}}-\frac{G_0\cdot\delta_G(\gamma-\gamma_c)}{1+\beta\left(\frac{\delta_G}{\delta_\tau}\right)^{s'}\cdot\left(\frac{\gamma_m}{\gamma_r}\right)^{s'}}\right]+\frac{G_0\cdot\delta_G(\gamma-\gamma_c)}{1+\beta\left(\frac{\delta_G}{\delta_\tau}\right)^{s'}\cdot\left(\frac{\gamma_m}{\gamma_r}\right)^{s'}}+\tau_c \tag{IV.4.6}$$

Figure IV.4.2 shows as the shear modulus reduction curve is updated every time an excess pore pressure change occurs.

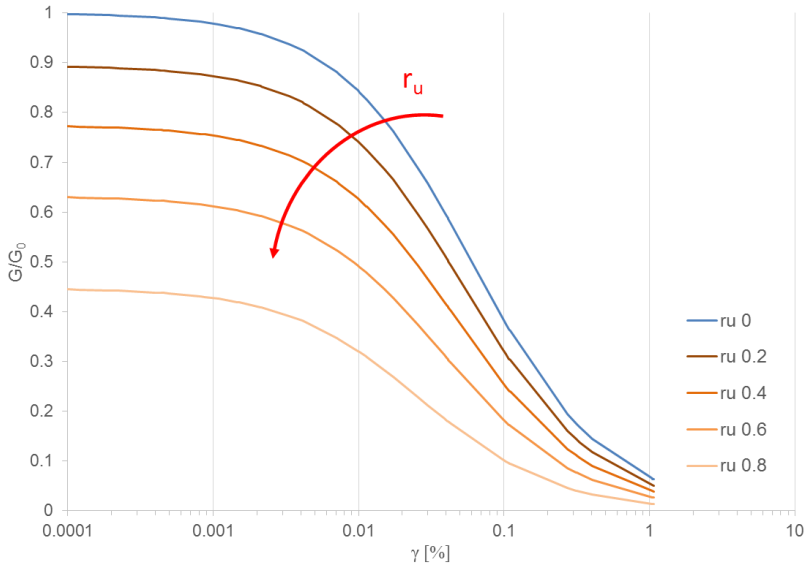

Figure IV.4.2 – Family of degraded normalized shear reduction curves corresponding to different pore pressure ratio values

IV.4.1. Numerical integration

The numerical integration of the updated version of SCOSSA code with pwp and degradation model implemented is described in this section.

SCOSSA uses the Newmark β method (Newmark, 1959) to numerically integrate at each time step the equations of motion

$$\begin{cases} \mathbf{M}\ddot{\mathbf{u}}_{t+1} + \mathbf{C}\dot{\mathbf{u}}_{t+1} + \mathbf{K}\mathbf{u}_{t+1} = \mathbf{f}_{t+1} \\ \dot{\mathbf{u}}_{t+1} = \dot{\mathbf{u}}_t + \Delta t \cdot (1-\gamma_N) \cdot \ddot{\mathbf{u}}_t + \Delta t \cdot \gamma_N \cdot \ddot{\mathbf{u}}_{t+1} \\ \mathbf{u}_{t+1} = \mathbf{u}_t + \Delta t \cdot \dot{\mathbf{u}}_t + \Delta t^2 (1/2 - \beta_N) \ddot{\mathbf{u}}_t + \Delta t^2 \beta_N \cdot \ddot{\mathbf{u}}_{t+1} \end{cases} \quad \text{(IV.4.7)}$$

The default coefficients are set equal to $\gamma_N = 0.5$ e $\beta_N = 0.25$, so that the method is unconditionally stable and no numerical damping is introduced.

For a model with *n* degrees of freedom, the system (IV.4.7) can be easily solved if expressed in the form

$$\mathbf{A} \cdot \mathbf{x}_{t+1} = \mathbf{B} \cdot \mathbf{x}_t + \mathbf{q}_{t+1} \quad \text{(IV.4.8)}$$

where **x** is the vector of the unknown variables

$$\mathbf{x} = \{\ddot{\mathbf{u}}^T \quad \dot{\mathbf{u}}^T \quad \mathbf{u}^T\}^T \quad \text{(IV.4.9)}$$

In equation (IV.4.8), **q** is the vector of the external forces, where the first *n* elements are equal to **f**, as defined in equation (IV.1.2), and the remaining 2*n* elements are null; **A** and **B** are the matrices of the integration method, defined as

$$\boldsymbol{A}=\begin{bmatrix} \boldsymbol{M} & \boldsymbol{C} & \boldsymbol{K} \\ -\Delta t\cdot\gamma_N\cdot\boldsymbol{I} & \boldsymbol{I} & \boldsymbol{0} \\ -\Delta t^2\beta_N\cdot\boldsymbol{I} & \boldsymbol{0} & \boldsymbol{I} \end{bmatrix} \qquad \mathbf{B}=\begin{bmatrix} \mathbf{0} & \mathbf{0} & \mathbf{0} \\ \Delta t\cdot(1-\gamma_N)\cdot\mathbf{I} & \mathbf{I} & \mathbf{0} \\ \Delta t\cdot(1/2-\beta_N)\cdot\mathbf{I} & \Delta t\cdot\mathbf{I} & \mathbf{I} \end{bmatrix} \tag{IV.4.10}$$

where **I** and **0** are the unit and null matrix , respectively, with $n\times n$ dimension.

The numerical solution of system (IV.4.8) is reduced to the inversion of the $3n\times 3n$ matrix **A** for each time step, which can be performed with exact or iterative methods. The code uses an exact inversion method based on the Crout-Doolittle factorization algorithm, modified for bounded matrices.

For non-linear analyses, the variability of the stiffness matrix, **K**, depending on the solution of the system, has to be considered. At each time step, the value of the stiffness for the j-th sub-layer, k_j, is computed by estimating the tangent shear modulus, G_j, as follows

$$k_j=\frac{G_j(\gamma_j)}{h_j}=\frac{1}{h_j}\cdot\frac{\Delta F_j}{\Delta\gamma_j} \tag{IV.4.11}$$

In equation (IV.4.11), ΔF_j is the increment of spring reaction force in the j-th sub-layer during the time interval Δt, to be evaluated from the current shear strain level through either equation (IV.4.5) or equation (IV.4.6) in function of the excess pore pressure ratio, ru, coming from the dissipation and generation pwp model.

The shear strain increment, $\Delta\gamma_j$, is computed through

$$\Delta\gamma_j=\frac{\Delta u_j-\Delta u_{j+1}}{h_j} \tag{IV.4.12}$$

where $\Delta u_j = u_j{}^{t+1} - u_j{}^{t}$ is the displacement variation in the time interval Δt and h_j is the sub-layer thickness.

Due to the mutual dependency between **K** and the system solution, **x**, an iterative computation needs to be done at each time step.

In detail, as a first attempt, the stiffness matrix is set equal to that calculated at the previous instant, i.e. $[\mathbf{K}^{t+1}]_{k=0}=\mathbf{K}^{t}$; The system is solved and the strain, $[\boldsymbol{\gamma}^{t+1}]_{k=0}$, and stress, $[\boldsymbol{\tau}^{t+1}]_{k=0}$, vectors are calculated, by which the stiffness matrix of the layering is again evaluated as $[\mathbf{K}^{t+1}]_{k=1}$. The procedure is iterated until the maximum value of the relative error, ε_{rel}, of two subsequent solutions, $[x^{t+1}]_{k-1}$ and $[x^{t+1}]_{k}$

$$\varepsilon_{rel}=\max\left\{\frac{\left|\left[x_j\right]_k^{t+1}-\left[x_j\right]_{k-1}^{t+1}\right|}{10^{-6}+\left|\left[x_j\right]_k^{t+1}\right|}\right\} \quad \text{with } j=1,\,2,\,\ldots,\,n \text{ (layer index)} \tag{IV.4.13}$$

is less than a fixed tolerance value, ε_{toll}. This iterative solution reduces the numerical instability occurring at the reversal points in the hysteresis loop modelled with the Masing criteria.

IV.5. References

Darendeli M.B. (2001). Development of a new family of normalized modulus reduction and material damping curves. PhD Dissertation, Univesity of Texas at Austin, USA.

d'Onofrio A., Silvestri F., Vinale F. (1999). Strain rate dependent behaviour of a natural stiff clay. Soils and Foundations, 39(2): 69-82.

EPRI (1993). Guidelines for determining design basis ground motions. EPRI Tr-102293, Electric Power Reserch Institute, Palo Alto, CA, USA.

Gingery J.R., Elgamal A. (2013). Shear stress-strain curves based on the G/Gmax logic: a procedure for strength compatibility. *The 2nd IACGE International conference on Geotechnical and earthquake engineering,* Chengdu, China.

Groholski D.R., Hashash Y.M.A., Musgrove M., Harmon J., Kim B. (2015). Evaluation of 1-D non-linear site response analysis using a general quadratic/hyperbolic strength-controlled constitutive model. Proceeding of the 6th International Conference on Earthquake Geotechnical Engineering, Christchurch, New Zealand.

Hardin B.O., Drnevich V.P. (1972). Shear modulus and damping in soils: design eqaution and curves. *Journal of Soil Mechanics and Foundations Division*, ASCE, 98(7): 667-691.

Hardin B.O., Richart F.E. (1963). Elastic wave velocities in granular soils. Journal of Soil Mechanics and Foundations Division, ASCE, 89 (SM1): 33–65.

Hashash Y.M.A., Park D. (2002). Viscous damping formulation and high frequency motion propagation in non-linear site response analysis. Soil Dynamics and Earthquake Engineering, 22(7): 611–624.

Hashash Y.M.A., Park D. (2001). Non-linear one-dimensional seismic ground motion propagation in the Mississippi embayment, Engineering Geology, 62: 185-206.

Hashash Y.M.A., Phillips C., Groholski D.R. (2010). Recent advances in non-linear site response analysis. The 5th International Conference in Recent Advances in Geotechnical Eartqhuake Engineering and Soil Dynamics, San Diego, CA. CD-Volume: OSP 4.

Haskell N.H. (1953). The dispersion of surface waves in multilayered media. Bull. Seismol. Soc. Am. 43: 17–34.

Ishibashi I., Zhang X. (1993). Unified dynamic shear moduli and damping ratios of sand and clay. Soils and Foundations, 33(1): 182-191.

Kondner R.L., Zelasko J.S. (1963). Hyperbolic stress-strain formulation of sands. In Proceedings of the 2nd Panamerican Conference on Soil Mechanics and Foundation Engineering, Sao Paulo, Brazil. Associação Brasileira de Mecânica dos Solos, 1: 289-324.

Lee K.W., Finn W.D.L. (1978). DESRA-2, dynamic effective stress response analysis of soil deposits with energy trasmitting boundary including assessment of liquefaction potential. University of British Columbia, faculty of Applied Science, Vancouver, Canada.

Lysmer J., Kuhlemeyer L. (1969). Finite dynamic model for infinite media. *Journal of the Engineering Mechanics Division* ASCE, 95(4): 859-877.

Matasovic N., Ordónez G.A. (2011). D-MOD2000. A computer program for seismic response analysis of horizontally layered soil deposit, earthfill dams and solid waste landfills. User manual. GeoMotions.

Matasovic N., Vucetic M. (1993). Cyclic characterization of liquefiable sands. Journal of Geotechnical Engineering, ASCE, 119(11): 1805-1822.

Menq F.Y. (2003). Dynamic properties of sandy and gravelly soil. PhD Dissertation, University of Texas at Austin, USA.

Moreno-Torres O., Hashash Y.M.A., Olson S.M. (2010). A simplified coupled soil-pore water pressure generation for use in site response analysis. GeoFlorida advances in analysis, modeling & design, West Palm Beach, Florida, USA.

Newmark N.M. (1959). A method of computation for structural dynamics. *Journal of the Engineering Mechanics Division* ASCE, 85(3): 67–94.

Phillips C., Hashash Y.M.A. (2009). Damping formulation for non linear 1D site response analyses. *Soil Dynamics and Earthquake Engineering*, 29(7): 1143–1158.

Regnier J., Bonilla L.F., Bard P.Y. at al. (2016). International benchmark on numerical simulations for 1D, non-linear site response (PRENOLIN): verification phase based on canonical cases. *Bulletin of the Seismological Society of America* (submission).

Regnier J., Bonilla L.F., Bard P.Y., Kawase H., Bertrand E., Hollender F., Marot M., Sicilia D., Nozu A. (2015b). PRENOLIN Project: A benchmark on numerical simulation of 1D non-linear site effect. 2 – Results of the Validation phase. Proceeding of the 6th International Conference on Earthquake Geotechnical Engineering, Christchurch, New Zealand.

Regnier J., Bonilla L.F., Bard P.Y., Kawase H., Bertrand E., Hollender F., Marot M., Sicilia D. (2015a). PRENOLIN Project: A benchmark on numerical simulation of 1D non-linear site effect. 1 – Verification phase based on canonical Cases. Proceeding of the 6th International Conference on Earthquake Geotechnical Engineering, Christchurch, New Zealand.

Seed H.B., Idriss I.M. (1970). Soil moduli and damping factors for dynamic response analysis. Report No EERC 70-10, University of California, Berkeley, California, USA.

Stewart J.P., Kowk A., Hashash Y.M.A., Matasovic N., Pyke R., Wang Z., Yang Z. (2008). Benchmarking of nonlinear geotechnical ground response analysis procedures. PEER report 2008/04.

Thomson W.T. (1950). Transmission of elastic waves through a stratified solid medium. *Journal of Applied Physics*, 21(2): 89–93.

Tropeano G., Chiaradonna A., d'Onofrio A., Silvestri F. (2016). An innovative computer code for 1D seismic response analysis including shear strength of soils. Géotechnique, 66(2): 95-105.

V. VALIDATION

In this chapter, the performances of SCOSSA code are assessed on well documented case histories in which vertical array records and, sometimes, pore pressure buildup measurements, are available. Both the accuracy and practical usefulness of the code are assessed by comparing calculated predictions and field records.

V.1. Sendai site

Sendai is an array site from the PARI network in the north-est of Japan (Figure V.1.1). The recorded station consists of a surface sensor and a downhole sensor at 10.4 m depth, located near the Sendai port. The array is founded on a Holocene sedimentary soil, called “beach ridge”, consisting of gravel and sand, formed through transportation and sedimentation by waves. This surface deposit is underlain by the Pliocene “Geba formation”, forming the northern and eastern hills and consisting of gravel stone, sandstone, tuff, tuffaceous siltstone and lignite (OYO Corporation, 2014).

As anticipating in chapter IV, the site was chosen in the Prenolin Project for the 1D geometrical soil configuration, also checked with MASW measurements (Regnier et al., 2015).

An extensive investigation campaign was carried out to obtain the in-situ shear wave profile, using downhole PS logging, and the non-linear soil parameters, using laboratory tests on samples obtained by the SPT, the undisturbed sampling and recovered boring cores.

Figure V.1.1 - Location of Sendai in Japan (a) and focus on Sendai with location of the vertical array (b)

These data and observed linear empirical site response were used by the organizing team to define a soil column on which all participants performed total stress simulations in the first iteration of the validation phase. In the second and third iterations a soil profile based on literature shear modulus and damping curves has been also adopted in the simulations (SC1 profile), which has given back a better result on the surface.

In the following sections, the experimental soil column using in the first iteration will be described and the total and effective stress analyses carried out on it by SCOSSA code will be shown. Finally, the results will be compared with the results obtained using the soil profile based on literature curves.

V.1.1. Recorded input motions

Nine recorded input motions were selected, representing 3 different PGA levels (≥ 0.06, 0.02-0.03 g and ≤ 0.01 g at the downhole sensor) and approximately 3 distinct frequency contents. The numbering of input motion corresponds to decreasing PGA level from #1 to #9 (Regnier et al., 2015).

For semplicity, only the EW components are considered and the characteristics of the dowhole and surface records are reported in Table V.1.1.

Table V.1.1 – EW components of the downhole and surface records

Record	Frequency content	downhole PHA [g]	surface PHA [g]
1	Low frequency	0.251	0.405
4		0.025	0.075
8		0.005	0.0085
2	Intermediate frequency	0.063	0.223
5		0.026	0.052
9		0.004	0.0097
3	High frequency	0.062	0.183
6		0.035	0.074
7		0.012	0.033

V.1.2. Description of the array site

The stratigraphic sequence revealed by the investigations is shown in Figure V.1.2, together with SPT and V_S profiles and the corrispondent values reported on the array station by the PARI website (PARI, 2015).

The upper part of the soil column is composed of loose gravel and gravelly sand with a thickness of 1.25 m, underlying fine sand moderately cmpacted. In this latter, a 5 cm thick sand with silt layer is revealed, which contains organic silt and shell fractions. From 7.15 m in depth there is a slate, generally hard, which can be considered the rigid bedrock. The ground water table is located at 1.45 m from the ground surface.

The results of the investigations performed by OYO Corporation show significant discrepancies from the data reported by PARI for both SPT blow count and shear wave velocity profiles, while density are quite similar. NSPT profiles show a reduction around 4.5 – 6 m, which is not present in the shear velocity profile.

Main differences in the velocity profile are related to the first four meters below the ground level, where OYO reported a velocity of 240 m/s, which is almost two times the value of 130 m/s reported by PARI.

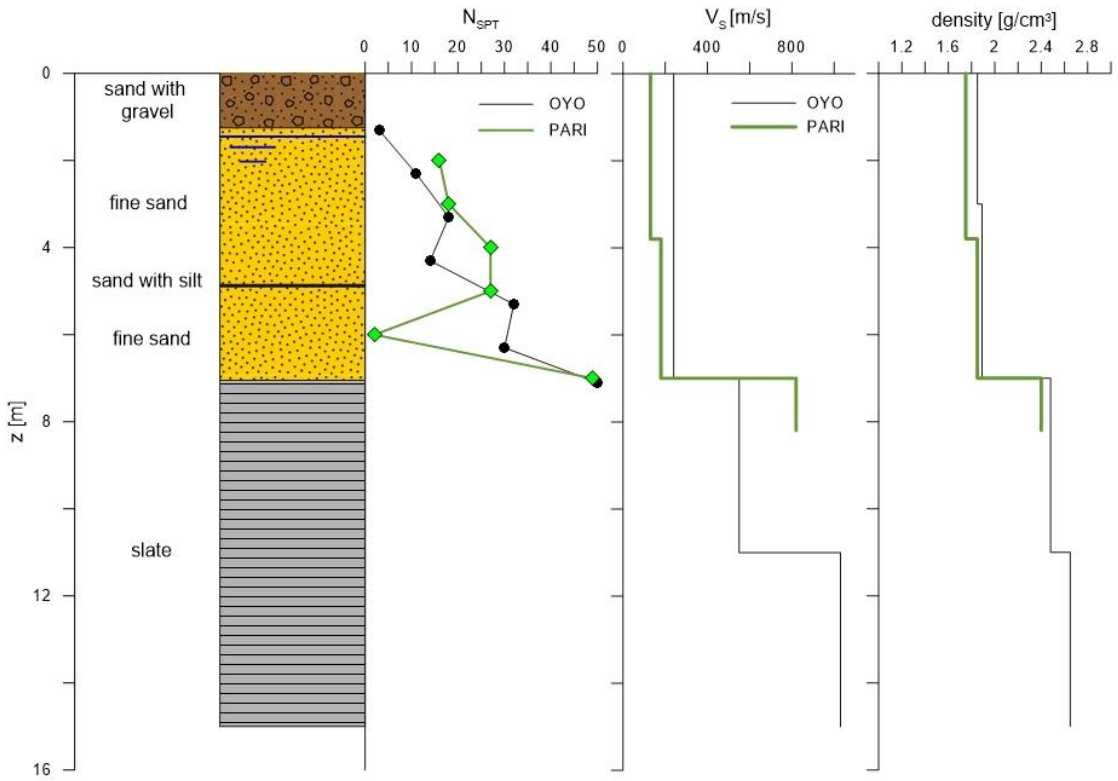

Figure V.1.2 – Soil profile, SPT, density and V_S measurement for Sendai site

Undisturbed samples were retrieved at the mean depth of 3.3 and 5.4 m to conduct laboratory tests. Both samples were subjected to cyclic triaxial test to determine deformation properties of soil, while on the shallower sample a stress-controlled cyclic undrained triaxial test (CTX) and a consolidated drained triaxial test (CID) were performed. Cohesion equals to 1.2 kN/m^2 and internal friction angle equals to 43.63 degree were computed from the CID test.

V.1.3. Simulations

In the onedimensional analyses carried out by SCOSSA code the rigid bedrock was assumed at the depth of 10.4 m, where the downhole sensor is located and downhole acceleration record is applied as input motion. The geotechnical model is reported in Figure V.1.3 and Table V.1.2. The assumed shear velocity profile has been proposed by Prenolin organization team; it is an adjustment of the OYO shear wave profile in order to match the empirical borehole Fourier transfer function (Regnier et al., 2015).

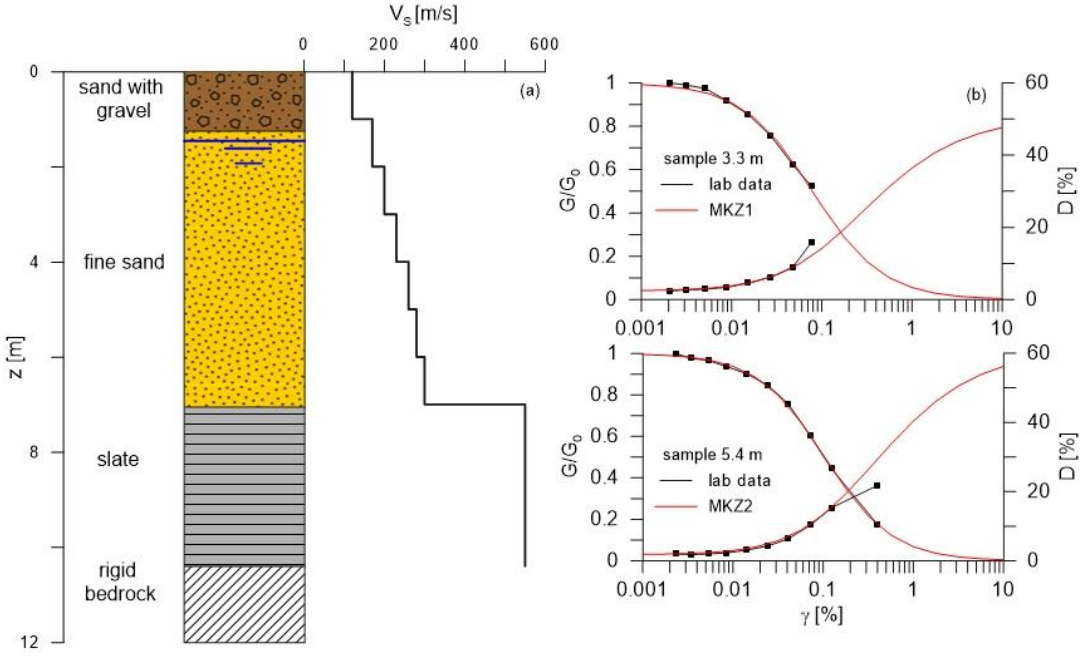

Figure V.1.2 – Soil model and V_S profile (a) and experimental and modelled normalized shear modulus and damping curves (b)

The experimental equivalent Young modulus vs axial strains, ε_a, curves related to the 5th cycle of cyclic triaxial tests have been used for the defining the normalized shear modulus curves. According to the criteria of equality of maximum values of shear stress and strain (Silvestri, 2001), the axial strains have been converted in shear strains, γ, as

$$\gamma = 1.5 \cdot \varepsilon_a \qquad \text{(V.1.1)}$$

while the ratio E/E_0 has been assumed equals to G/G_0. The experimental and modelled curves are reported in Figure V.1.4b.

Table V.1.2 – Subsoil model

Depth [m]	Soil type	Unit weight, γ [kN/m³]	S-wave, Vs [m/s]	G/G0 and D curves	PWP model (only in TE)
0 – 1.0	Sand with gravel	18.15	120	MKZ1	-
1.0 – 1.45	Fine sand	18.15	170	MKZ1	-
1.45 – 2.0		18.15	170	MKZ1	SR_t = 0 .15 α = 0.434 SR_r = 0.158 a = 0.95 b = 0.47 c = -0.05
2.0 – 3.0		18.15	200	MKZ1	
3.0 – 4.0		18.54	230	MKZ2	
4.0 – 5.0		18.54	260	MKZ2	
5.0 – 6.0		18.54	280	MKZ2	
6.0 – 7.0		18.54	300	MKZ2	
7.0 – 8.0	Slate (rock)	24.33	550	elastic	-
8.0 – 10.4		24.33	550	elastic	-

The rock layer above the downhole sensor has been modelled as an elastic material with constant damping equals to 1 %.

In effective stress analyses, cyclic resistance parameters have been assigned to the fine sand layer below the ground water table. Figure V.1.5 shows the cyclic resistance and pore pressure ratio curves and the result of the CTX test performed on undisturbed sample at 3.3 m depth.

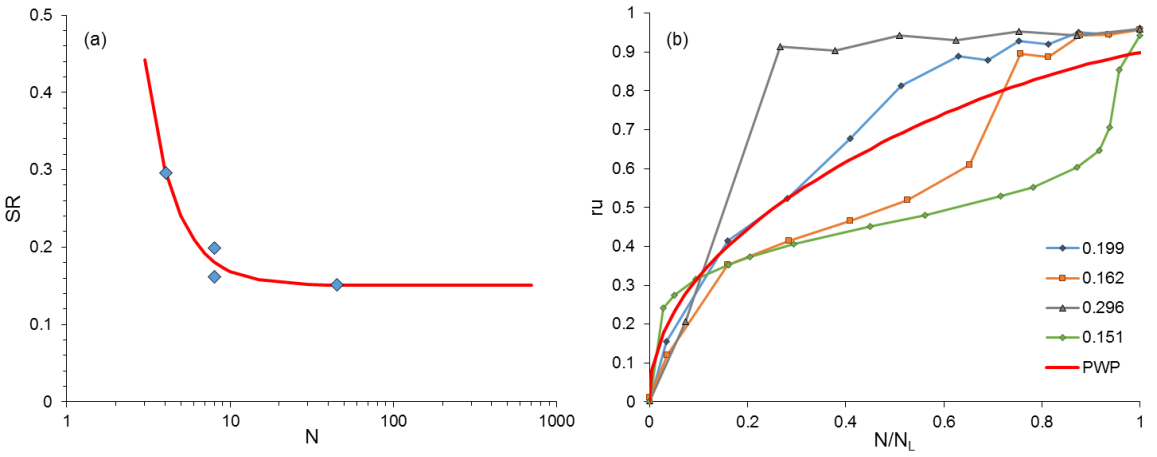

Figure V.1.3 – Experimental and simulated liquefaction strength of fine sand layer espressed as cyclic stress ratio vs number of cycles (a) and excess pore pressure ratio relationship (b)

An univocal *ru* relationship has not been highlighted in the experimental results, since the pore pressure ratio curves are strongly dependent from the cyclic stress ratio applied in the tests. Consequently, a pore pressure ratio curve has been defined on the whole set of data (in red, Figure V.1.3b).

V.1.3.1. Total stress analyses results

In the total stress analyses (TT) the pore pressure model is neglected and the non linear behaviour of the soil is modelled only through the shear modulus and damping curves reported in Figure V.1.2.

The results are expressed in terms of comparison between recorded and simulated acceleration time histories and response spectra at the surface. For uniforming the rapresentation scale, the spectral accelerations have been normalized respect to the PGA recorded at the surface for each input motion.

Figures V.1.4, V.1.5, V.1.6 show the results of the simulations in total stress conditions for the low, intermediate and high frequency content input motions, respectively.

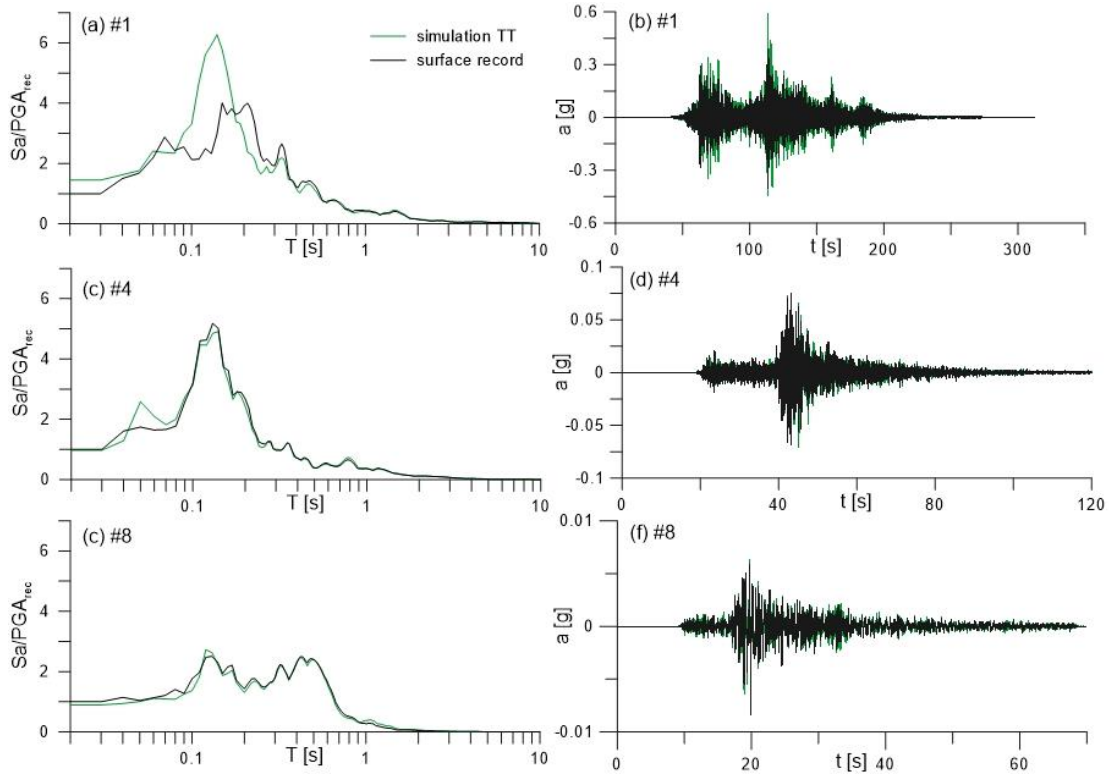

Figure V.1.4 – Comparison for the low frequency input motions between recorded and simulated acceleration response spectra and time histories at the surface in the total stress analysis

For the low frequency input motions, the computed numerical response spectra are in good agreement with the recorded one for input #8 and #4, which have low intensity. The same good match is highlighted by the comparison of the time histories at the surface.

Significant overestimation is related to the input motion #1, which strongly mobilizes the non-linear behavior of the soil. Both simulated PGA and maximum spectral acceleration are overstimeted of 1.5 times respect to the recorded values.

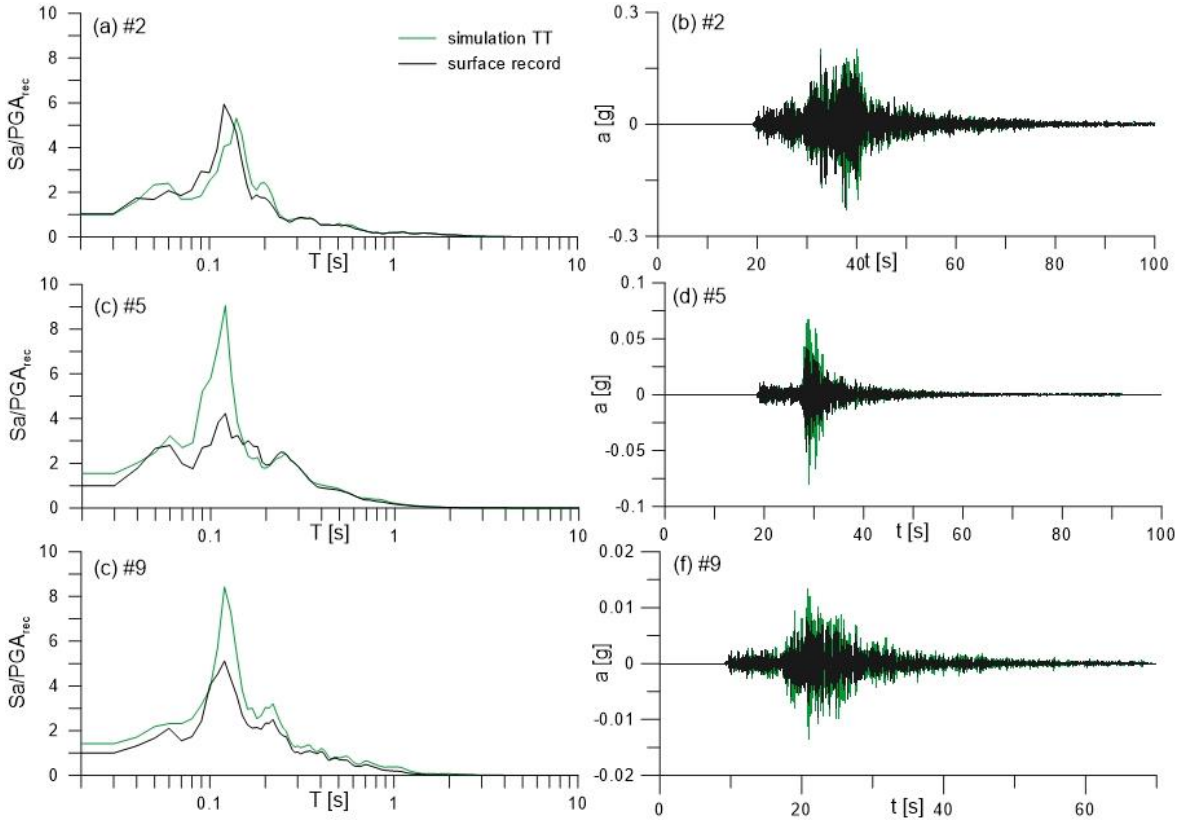

Figure V.1.5 - Comparison for the intermediate frequency input motions between recorded and simulated acceleration response spectra and time histories at the surface in the total stress analysis

For the low frequency input motions, Figure V.1.5 shows that the simulations in total stress conditions overstimate the response at the surface for low values of the applied actions. The maximum amplification in the response spectra of input #5 and #9 is around 0.12 s, which is also the natural period of the assumed soil column. Overstimation of the PGA can be noticed from both the acceleration time histories and response spectra for the input #5 and #9.

This result suggests that some uncertainties still remain on the definition of soil properties in linear elastic conditions.

As regard to the strongest input motion, a good prediction of the PGA of the record #2 has been returned by the simulation and the differences in the predicted and recorded time histories are limited respect to the others input.

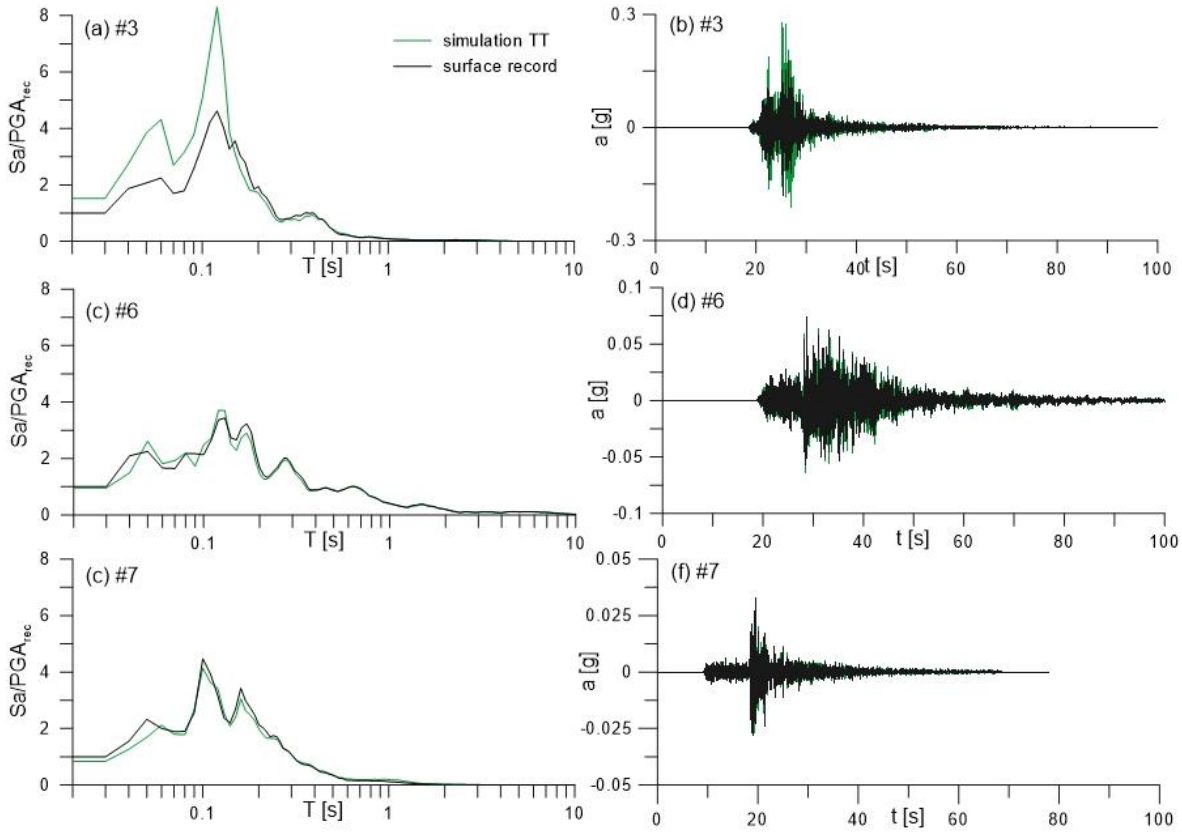

Figure V.1.6 - Comparison for the high frequency input motions between recorded and simulated acceleration response spectra and time histories at the surface in the total stress analysis

The results of analyses on the high frequency input motions show a good prediction of the response spectra and time histories of the input #6 and #7, while a great overestimation is related to the input #3 for periods minor than 0.15 s.

V.1.3.2. Effective stress analyses results

Effective stress analyses have been performed on the all set of input motions, but the PWP model was triggered only for the input #1, #2 and #3, which have recorded dowhole PGA more than 0.06 g. So, effective and total stress analyses results coincide for all the others input motions and they need further comment.

Results of effective stress analyses for the strongest input motions are reported in Figure V.1.7, together with the comparison with recorded and total stress simulations.

Spectra comparisons show that effective stress analyses induced a significant improvement in the surface response, maximum recorded spectral accelerations are well-reproduced and also the predominant period is matched.

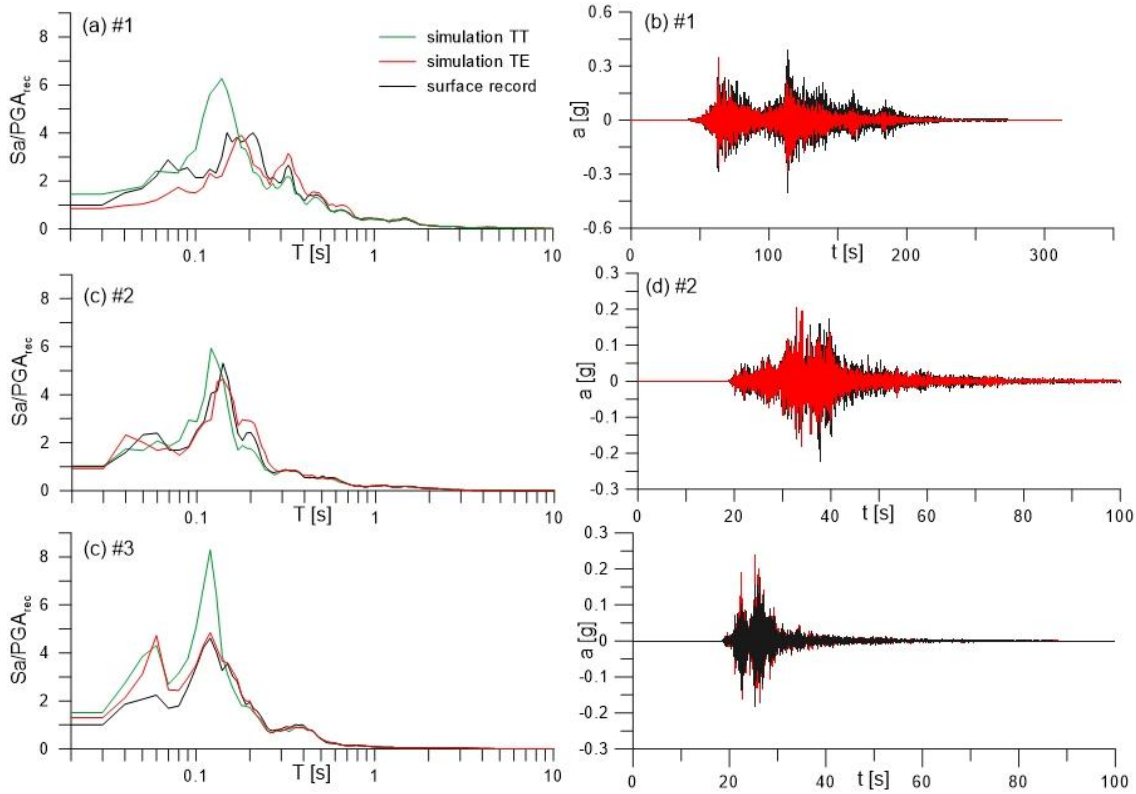

Figure V.1.7 – Comparison for the strongest input motions between recorded and simulated response spectra and time histories at the surface in the total and effective stress analyses

Analitycally, the analyses results are reported in Table V.1.3 in terms of variance of spectral acceleration in the range of 0.02 ÷ 10 s. The introduction of the PWP model reduced the variance more than three times respect to the total stress analyses for the input #1 and #3, and two times for the input #2. On average, the simulations have been improved of three times taking into account the pore water pressure effects.

Table V.1.3 – Variances between simulated and recorded acceleration response spectra for total and effective stress analyses

Analysis type	Input #1	Input #2	Input #3	mean
TT	9.49	0.64	1.45	3.86
TE	3.02	0.31	0.31	1.21

The maximum pore pressure profile induced by the strongest input motions is reported in Figure V.1.8a. The input motion #1 caused the full liquefaction of the saturated sand layer, because is characterized by the strongest intensity, while the input #2 caused the liquefaction only of the upper part of the deposit and the input #3 reached the maximum pore pressure ratio of 0.70. The pore pressure time histories at 2.5 m depth the ground level, where the highest pwp are generated, are also reported in Figure V.1.8 for the three input motions.

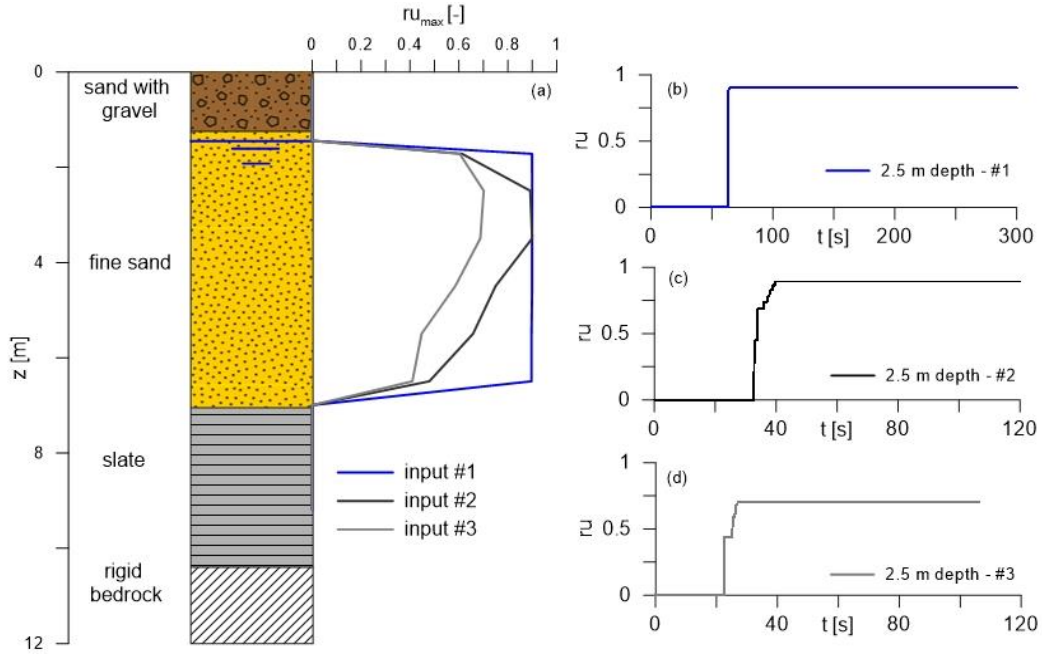

Figure V.1.8 – Excess pore pressure profile (a) and time history at 2.5 m depth in the effective stress analysis for the strong ground motion #1 (b), #2 (c) and #3 (d)

V.1.4. Comparison with other simulations

The effective stress analyses results have been compared with that obtained using the profile based on literature G/G_0 and damping curve. In details, during the second iteration of the Prenolin project, Darendeli (2001) curves were defined in function of the litostatic stress state along the soil column and adopted in the analyses instead of the laboratory curves. The computed normalized shear modulus curves are defintely more non linear compared to the laboratory ones, while the damping is lower at high values of shear strains (Figure V.1.9).

The results of the total stress analyses performed by SCOSSA code on this last profile, called SC1 profile, are reported in terms of response spectra in Figure V.1.10.

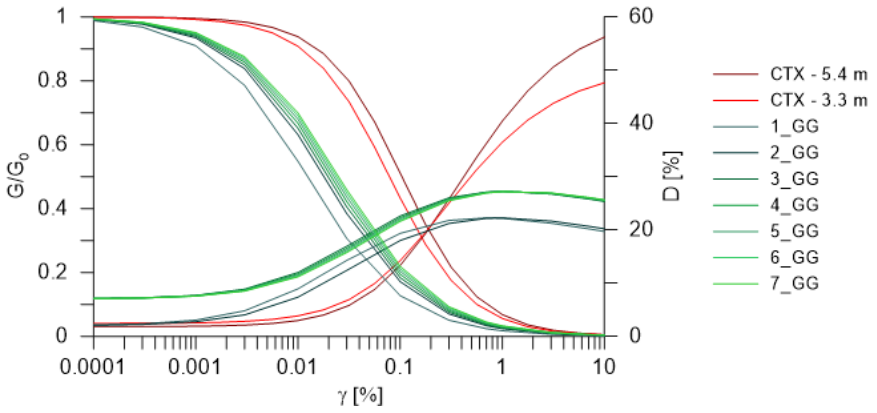

Figure V.1.9 – Comparison of the normalized shear modulus and damping curves from CTX tests (red lines) and the Darendeli curves (green lines) considered in the SC1 profile

Moreover, effective stress simulations were on Sendai site by a group of partecipants to the prenolin project, identified as W – team, who used an advanced constitutive model, called SANISAN, to model the behaviour of sand. In details, SANISAND is a simple anisotropic sand constitutive models developed within the framework of critical state soil mechanics and bounding surface plasticity (Taiebat and Dafalias, 2008).

Results of the W-team are also reported in terms of response spectra in Figure V.1.10 and compared with the results of SCOSSA analyses, both on SC1 profile in total stress conditions and on profile with laboratory curves in effective stress conditions, previous described.

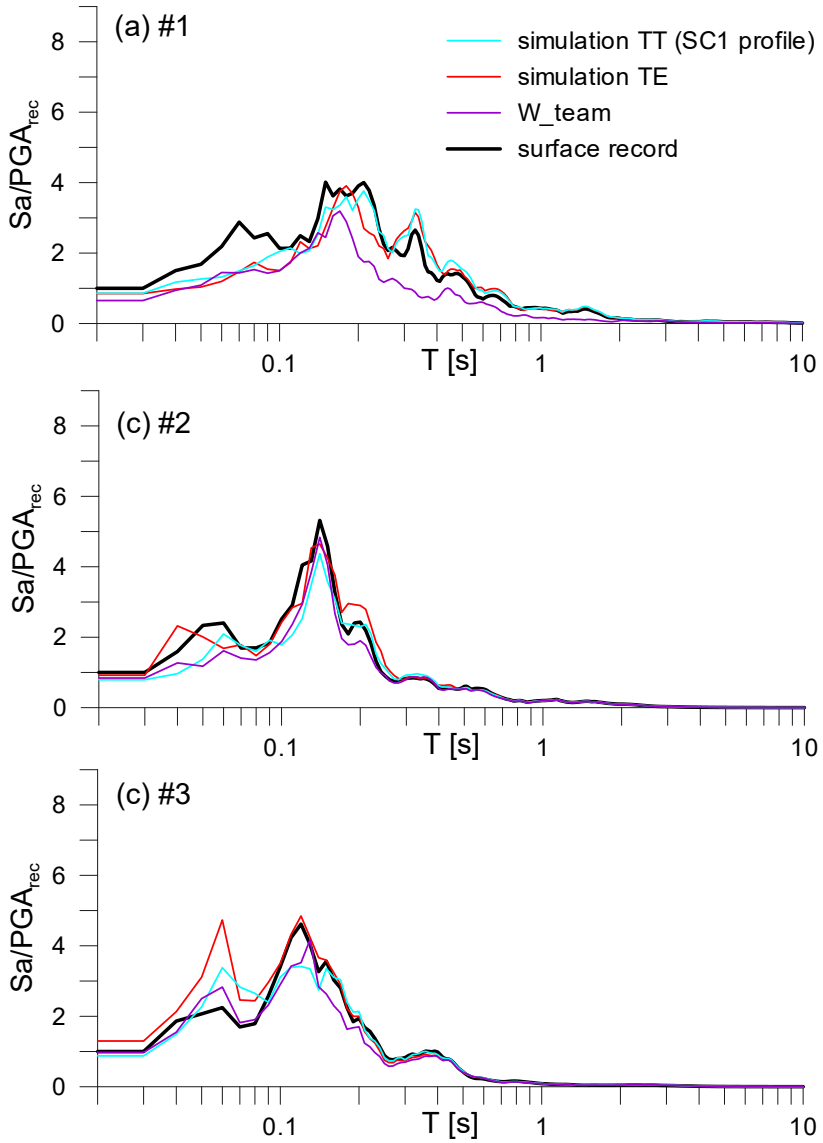

Figure V.1.10 - Comparison for the strongest input motions between recorded and simulated response spectra and time histories at the surface performed by W-team (violet lines) and by SCOSSA code on SC1 profile in the total conditions (orange lines) and on experimental profile in effective stress conditions (red lines)

The comparison in Figure V.1.10 shows that the SC1 profile returned the best prediction on the input motion #1, while the differences for the input #2 and #3 are limited in a narrow range. It can be noticed that the PWP model implemented on SCOSSA code is able to return predictions which are comparable with more sophisticated and advanced constitutive models.

V.2. Port Island site

Port Island is definitely the most famous case history about liquefaction. After the 1995 earthquake, widespread evidences of liquefaction induced effects on ground surface were massively observed at numerous sites on the man-made island.

Port Island is the first artificial island (the secondi s Rokko Island) constructed in the south of Kobe city, in the Osaka bay. This island was constructed in two phases. During the first phase, between 1966 and 1981, a 436 hectare area was reclaimed. In the second phase, the island was then extended southward by reclaiming 319 additional hectare (Figure V.2.1). A decomposite granite soil known as 'Masado' was used in the first reclamation phase, while sandstone, mudstone and tuff, were employed in the construction of the southern part of the reclaimed island. (Shibata et al., 1996).

A vertical array was installed in the northern area of Port Island by the Development Division, Kobe city, in October 1991 (Iwasaki and Tai, 1996). The vertical array includes triaxial accelerometers at the surface as well as at depths of 16 m, 32 m, 83 m from the ground surface. No piezometers were installed at the array site.

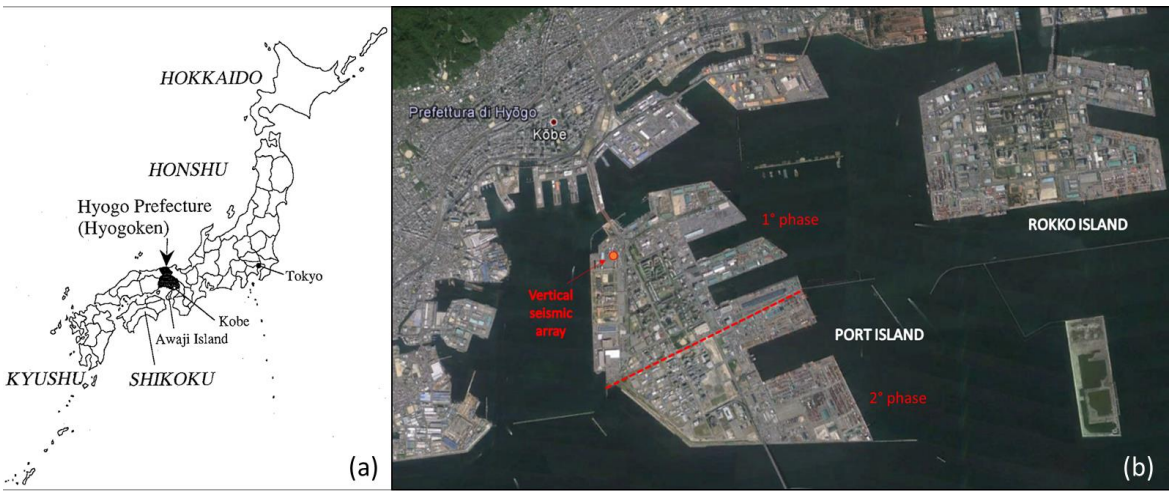

Figure V.2.1 - Location of Hyogoken and Kobe in Japan (Kimura, 1996) (a) and focus on Rokko Island and Port Island with location of the vertical array (b). The dashed line separates the part of the island constructed during the first and the second phase

V.2.1. The 1995 Hyogoken Nanbu earthquake

On January 17, 1995 at 5:46 AM, the 1995 Hyogoken-Nambu earthquake with a local magnitude of 7.2 stuck the southern part of Hyogo Prefecture. The epicenter was 15 km north of Awaji Island, and the hypocenter depth was located 14.3 km below the sea level (Shibata et al., 1996).

Liquefaction spreads throughout the whole island. As shown in Figure V.2.2, earthquake triggered extensive liquefaction induced effects especially in the first phase reclamation area: settlements of 20 cm were observed on average with peak values exceeding 50 cm in the most severely damaged locations. Witnesses reported that the ejection of liquefied materials continued on Port Island for nearly one hour after the earthquake (Shibata et al., 1996). Since liquefied Masado soil contains gravel, the ejection of coarse gravel was also observed around the foundation of a highway near Kobe bridge on Port Island.

Less significant liquefaction occurred in the second phase reclamation area, since during the construction sand or rod compaction pile an sand drains were adopted to accelerate consolidation of the layers underlying the reclaimed soil (Shibata et al., 1996).

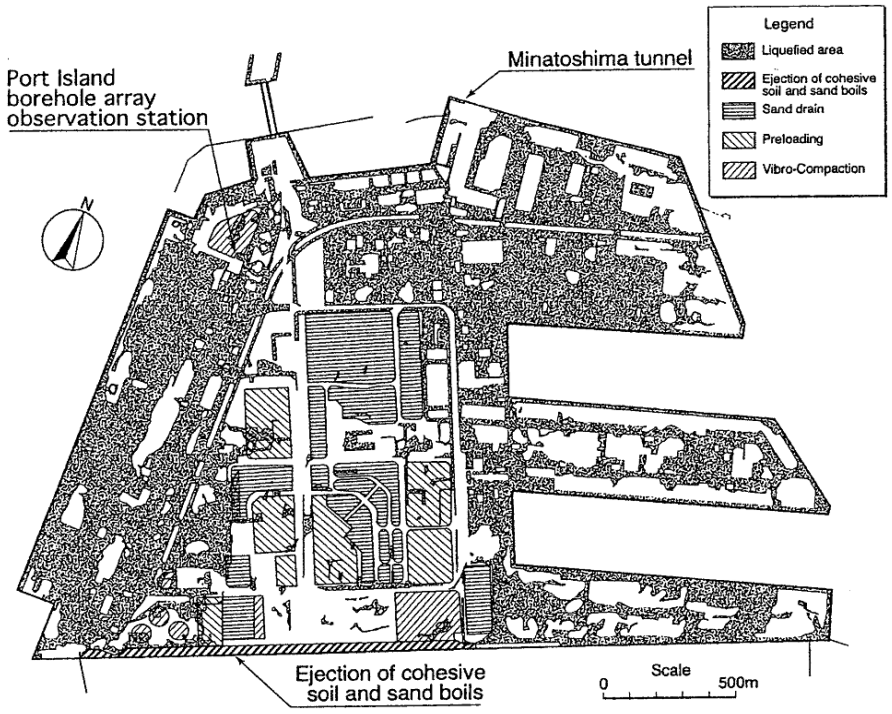

Figure V.2.2 – Distribution of liquefaction on Port Island (first phase) and areas were soil improvement were used (Shibata et al., 1996)

The vertical array recorded the main shock at different depth. The peak accelerations for each components at four depths are listed in Table V.2.1.

Table V.2.1 – Recorded peak ground acceleration (mod. from Iwasaki and Tai, 1996)

Depth [m]	N-S PHA [g]	E-W PHA [g]	U-D PVA [g]
GL 00	0.35	0.29	0.57
GL -16	0.58	0.55	0.80
GL -32	0.55	0.47	0.20
GL -83	0.69	0.31	0.19

The horizontal acceleration was not amplified at the ground surface, because the liquefaction of the reclaimed fill material shallower than 16 m caused de-amplification of the higher frequency components.

Pore water pressure was measured several kilometers south of the array site, in an alluvial sand layer with the same geological conditions as the vertical array site at 30 m depth. An increase of pore water pressure of more than 167 kPa was recorded 14 minutes after the earthquake, and it was also observed decrease with time (Iwasaki and Tai, 1996).

V.2.2. Description of the array site

The stratigraphic sequence at the array site is shown in Figure V.2.3. The top layer is sandy fill called 'masa' or 'masado' soil, a decomposed granite transported from the nearby Rokko Mountains, overlying a Holocene silty clay layer. These layers are followed by alternating layers of Pleistocene gravel and clay. The measured velocities for each soil layer are listed in Table V.2.2. The ground water table is located at 3 m below the surface (Ziotopoulou, 2010).

Table V.2.2 – Velocity of P and S waves of the soil layers (mod. from Iwasaki and Tai, 1996)

Depth [m]	Soil type	Soil origin	P-wave, V_P [m/s]	S-wave, V_S [m/s]
0 – 2.0	Gravel	Fill soil	260	170
2.0 – 5.0	Gravel		350	170
5.0 – 12.6	Gravel		780	210
12.6 – 19.0	Gravelly sand		1480	210
19.0 – 27.0	Alluvional silty clay	Holocene	1180	180
27.0 – 33.0	Gravelly sand and silt	Upper Pleistocene	1350	245
33.0 – 50.0	Gravelly sand and silt		1530	305
50.0 – 61.0	Gravelly sand and silt		1610	350
61.0 – 79.0	Stiff alluvial silty clay		1610	303
79.0 – (85.0)	Gravelly sand		2000	320

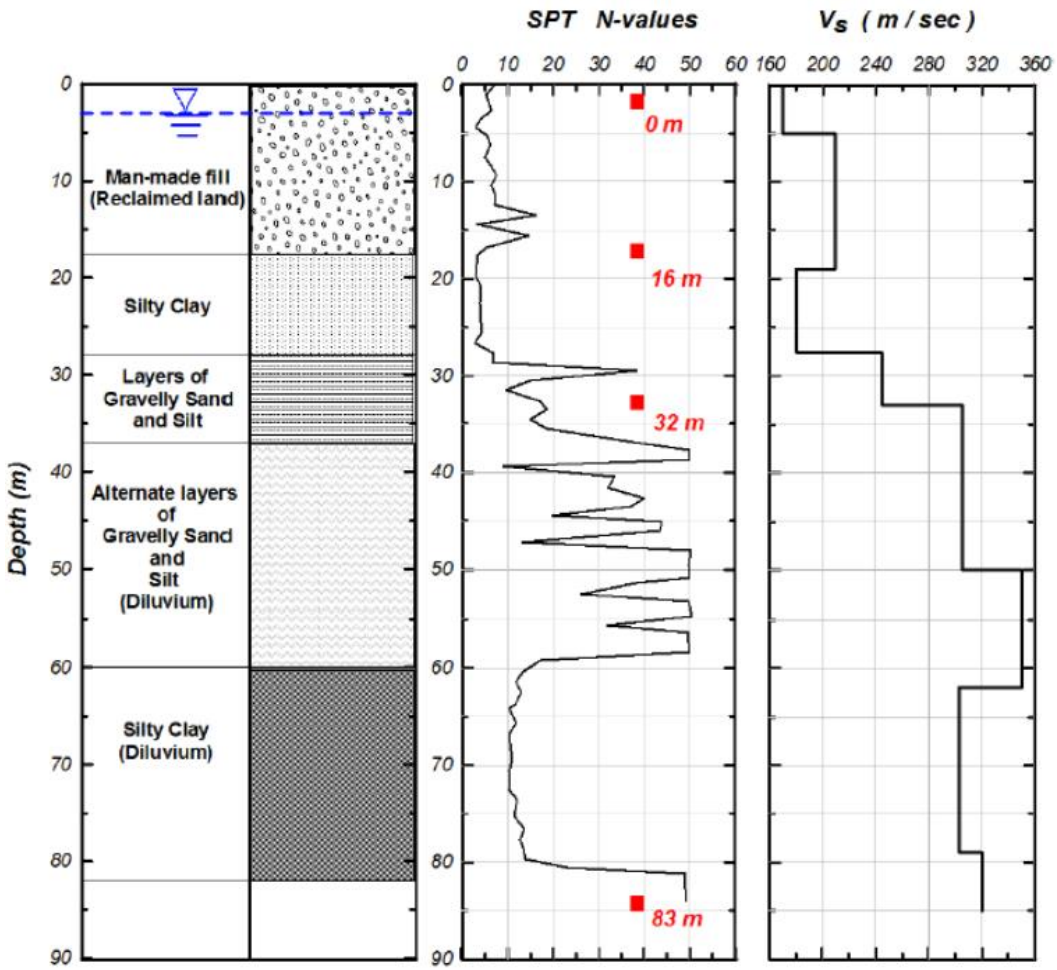

Figure V.2.3 – Soil profile; SPT and V_S measurements for Port Island array (Ziotopoulou, 2010)

V.2.3. Simulations

In the onedimensional analyses carried out by SCOSSA code the bedrock was assumed at the depth of the three available records (16 m, 32 m and 83m). The best prediction was obtained considering the bedrock at 16 m, since the uncertainties about the mechanical behaviour of the soil were limited to that of the the only liquefiable layer of Masado soil. In the following the results of the numerical analyses and the comparison with the records will be just referred to the profile shown in Figure V.2.4.

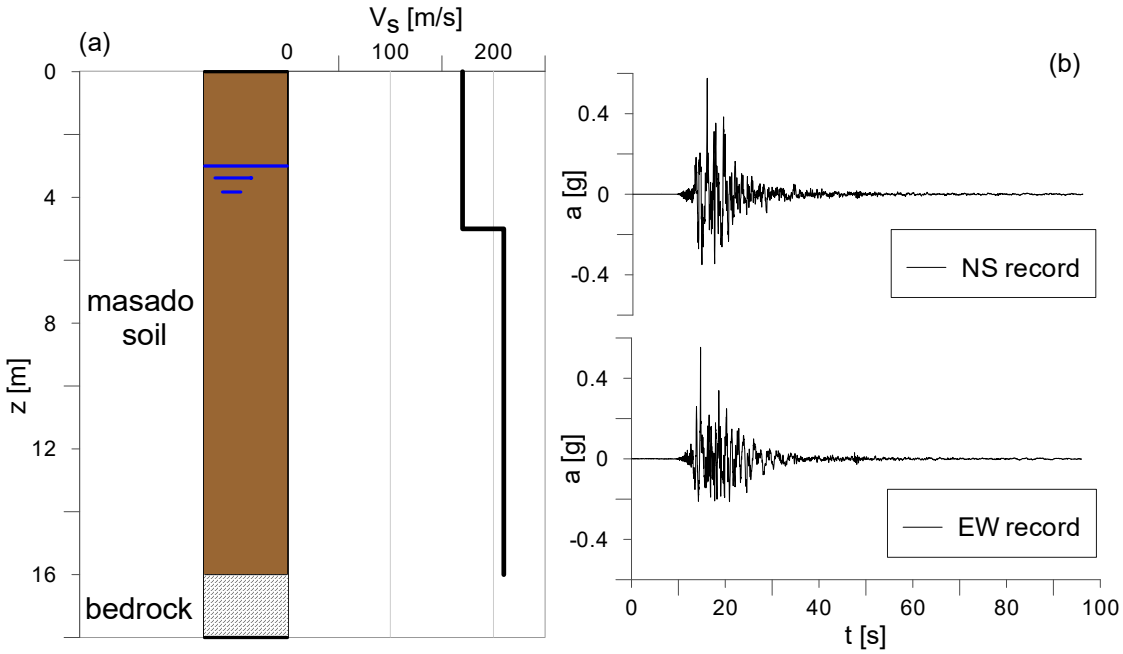

Figure V.2.4 – Soil model and V_S profile (a) and records at 16 m depth used as input motion (b)

The record at 16 m depth was used as input motion and applied to the rigid bedrock (Figure V.2.4b). The most demanding phase was the geotechnical model of the masado soil to be used in the numerical simulations.

V.2.4. Geotechnical model of Masado soil

The soil used for reclamation was transported by conveyer belt from montain areas far inland. While the soil was in transit, crushing and weathering altered the grain size distribution to one higher in fines content than the natural material (Shibata et al., 1996).

Figure V.2.5 shows the grain size distribution curve of the Masado, including coarse gravel smaller than 150 mm. It should be noted that the masado soil is well-graded, containing a fairly large portion of gravel, about 55%.

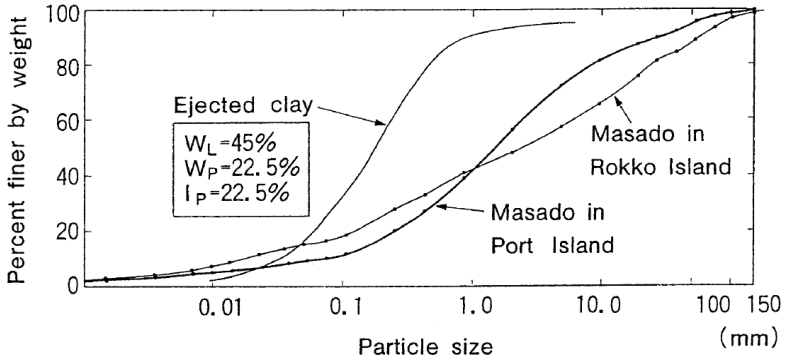

Figure V.2.5 – Particles size distribution curves of Masado including coarse gravel up to 150 mm and ejected cohesive soil (Shibata et al., 1996)

A relative density of 47% for the silty sand portion of undisturbed sample of masado was reported by Ishihara et al., 1996.

Prior to earthquake, a series of cyclic triaxial test was performed by Nagase on undisturbed samples recovered from the bottom of a cut (Ishihara et al., 1996).

After the event, cyclic undrained tests were performed by Hatanaka (1997) on undisturbed samples recovered using the in-situ freezing samples method, while other comprehensive laboratory studies on Masado soils are reported by Yoshida (2000) and Cubrinovski et al. (2000).

All these data are plotted in Figure V.2.6, together with the results of Suetomi and Yoshida (1998), that measured the liquefaction strength of undisturbed samples not far from the site of the earthquake observations. In the same Figure V.2.6, the cyclic resistance curve assumed in the analysis is also reported.

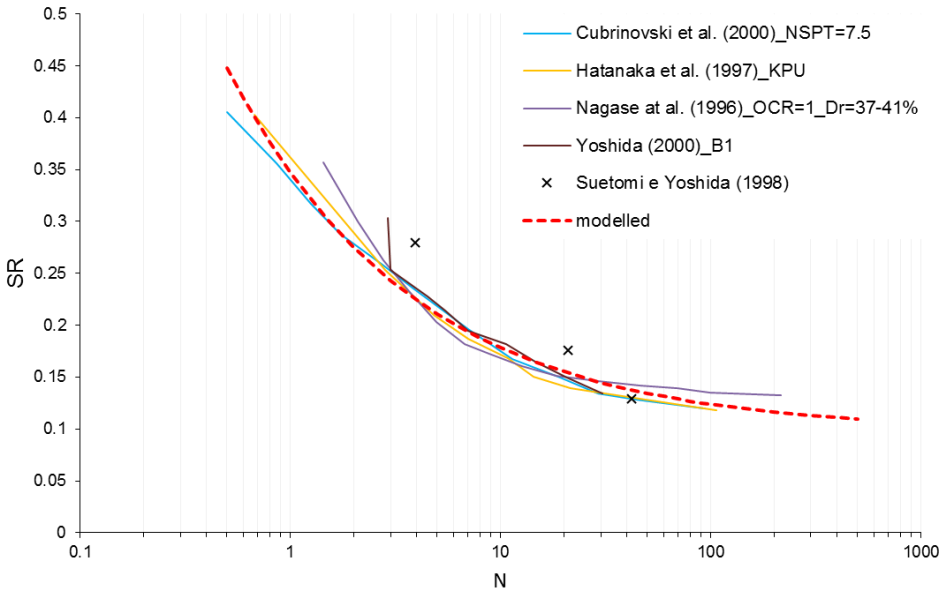

Figure V.2.6 – Cyclic resistance curves of Masado soil as proposed by different authors and curve assumed in the analysis

As regard to the excess pore pressure ratio curve, a relationship for gravelly soils of similar grain size distribution and relative density reported in Flora and Lirer (2013) has been considered in the analyses since no measurements were available from undisturbed samples of Masado soil (Figure V.2.7).

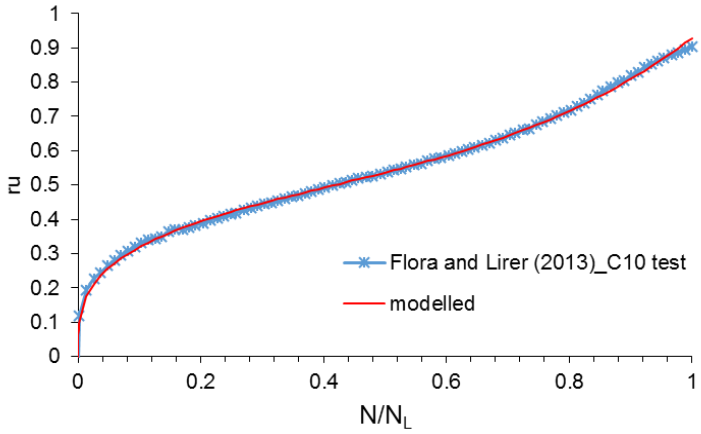

Figure V.2.7 – Excess pore pressure ratio relationship considered for masado soil

The non linear and dissipative behaviour of the soil was analysed by Suetomi and Yoshida (1998) that performed also cyclic torsional shear tests on disturbed and undisturbes samples of masado soil, deposited about 18 m depth from the ground surface (Figure V.2.8). In Figure V.2.8 the experimental results are compared with the literature curves proposed by Rollins et al. (1994) for gravelly soils: they seems to be well fitted by the mean curve proposed by Rollins that was than adopted to model the non linear and dissipative behaviour of the soil.

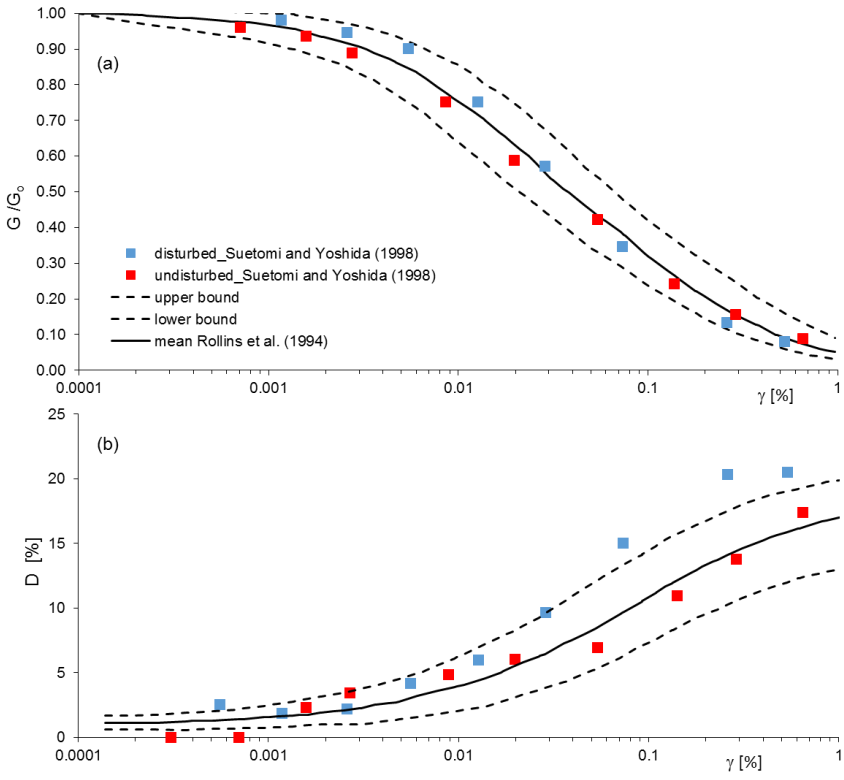

Figure V.2.8 – Non-linear characteristics of Masado soil: (a) normalized shear modulus and (b) damping ratio vs shear strain

V.2.5. Results of total stress and effective stress analyses

Since the liquefation phenomena lasted more than one hour, perfect undrained condition could be assumed during the earthquake and the dissipation has been neglected in all the analyses.

In the total stress analyses (TT) the pore pressure model is neglected and the non linear behaviour of the soil is modelled only through the shear modulus and damping curves reported in Figure V.2.8.

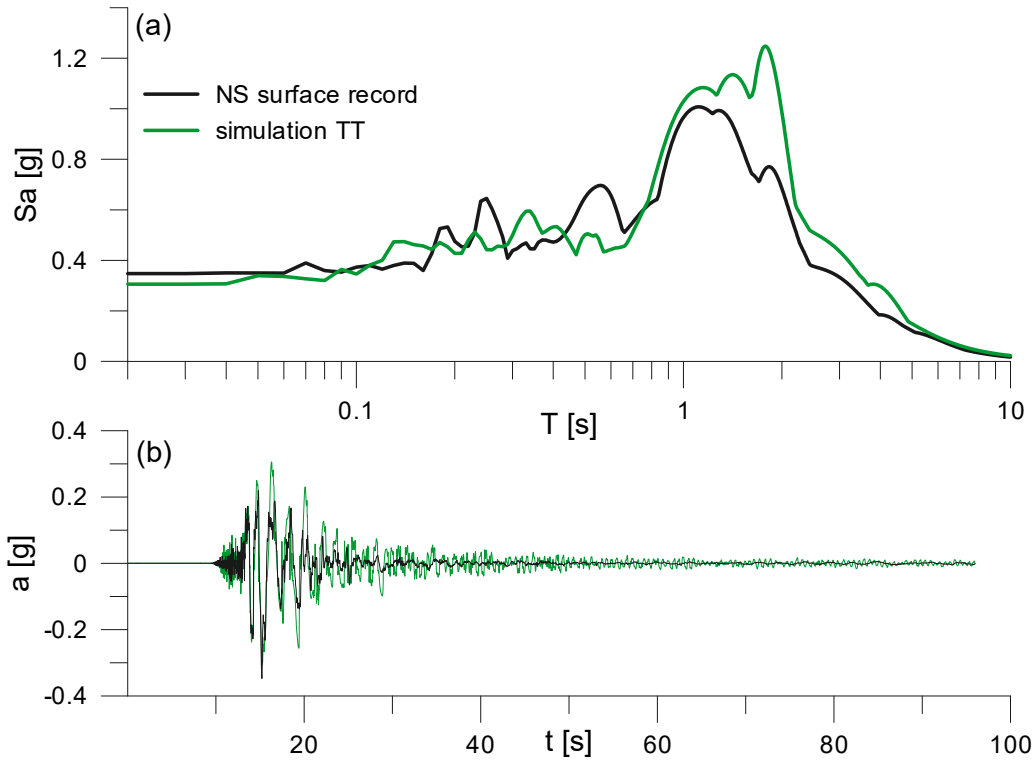

Figure V.2.9 – Comparison for the NS component between recorded and simulated (a) acceleration response spectra and (b) time histories at the surface in the total stress analysis

In Figure V.2.9 the numerical results are compared with the recorded ones in terms of acceleration response spectra and time histories. In details, the computed NS component of the numerical response spectra seems to be in a quite good agreement with the recorded one even if it shows higher spectral accelerations for periods higher than 0.8 s. The acceleration overestimation of the numerical analyses at low frequencies can be clearly detected also in the comparison between the recorded and computed acceleration time histories where a numerical noise at high frequencies is also evident.

The total stress analysis well reproduces the PGA of the EW component, as shown in Figure V.2.10 while significantly overestimates the spectral ordinates in the range berween 0.8 and 5 s. High frequencies are predominant in the simulated time history, visible discordance between record and simulation are observed after 17 s (Figure V.2.10).

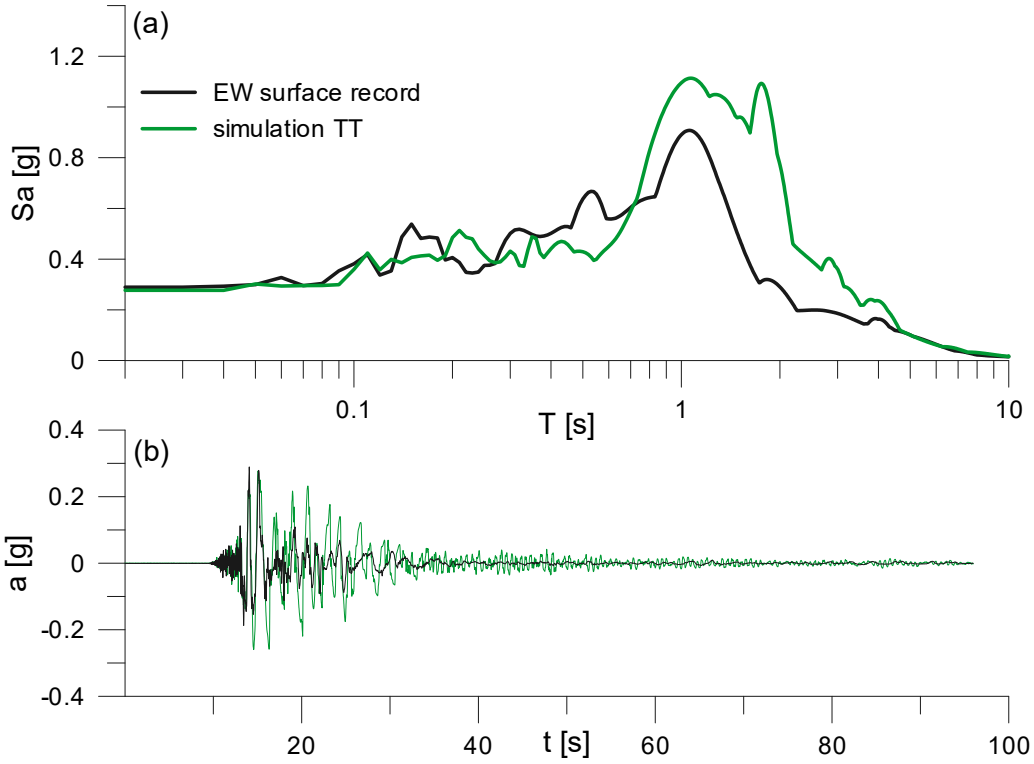

Figure V.2.10 – Comparison for the EW component between recorded and simulated (a) acceleration response spectra and (b) time histories at the surface in the total stress analysis

The results of the effective stress analysis are reported in terms of response spectrum and time history of the acceleration of the two horizontal components, in Figures V.2.11 and V.2.12 where they are again compared with the records.

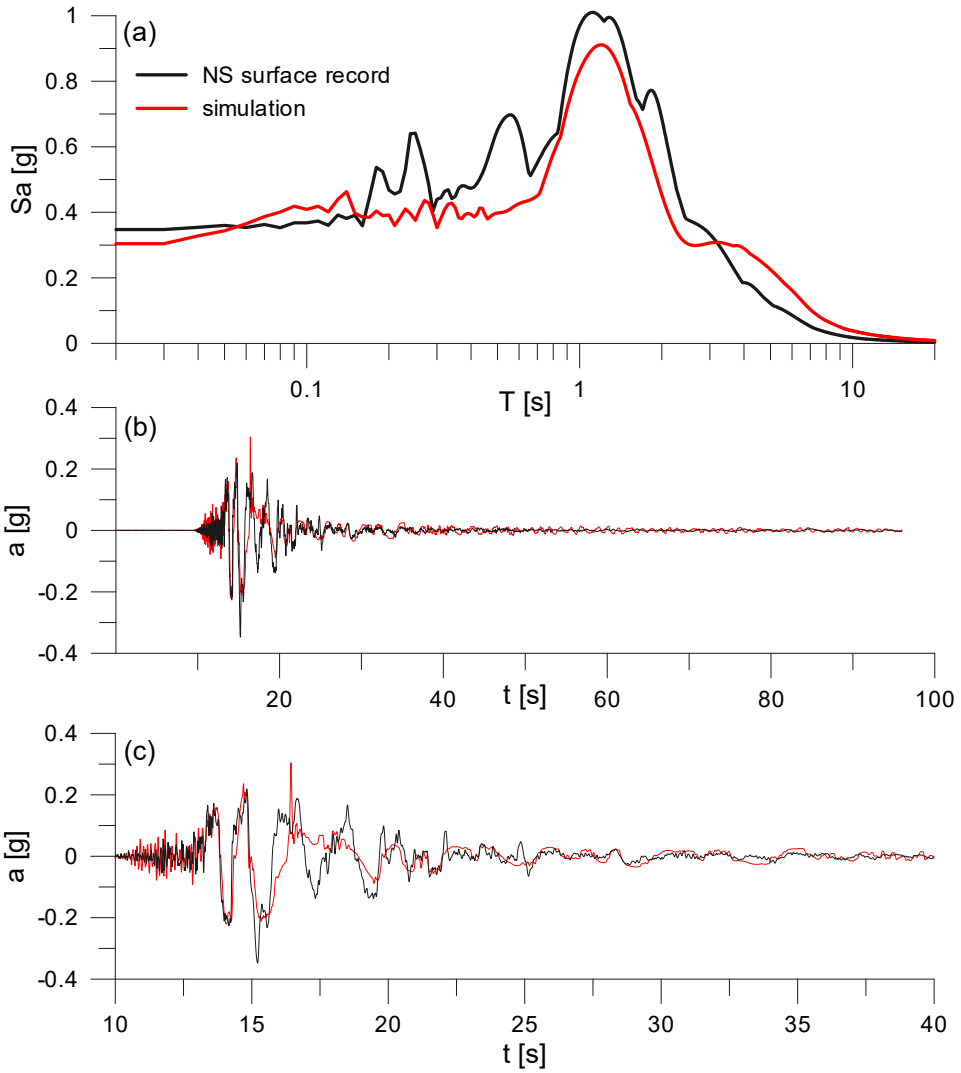

Figure V.2.11 – Comparison for the NS component between recorded and simulated (a) acceleration response spectra and (b) time histories at the surface with (c) detail between 10 and 40 s in the effective stress analysis

The computed spectral ordinates of the NS component are lower than the recorded in the range of 0.2 ÷ 3 s and the time history is characterized by smaller accelerations if compared to the observed values. The detail of the time histories in the range 10 ÷ 40 s shows that the simulated accelerations are in phase with the records (Figure V.2.11).

Effective stress analysis of the recorded EW component is able to predict the peak spectral acceleration and slightly overpredicts the spectral ordinates beyond 1 s. Excepting the overestimation under 0.08 s and the underestimation between 0.25 ÷ 0.8 s, the shape of the recorded spectrum is well reproduced as such as the surface acceleration time history (Figure V.2.12).

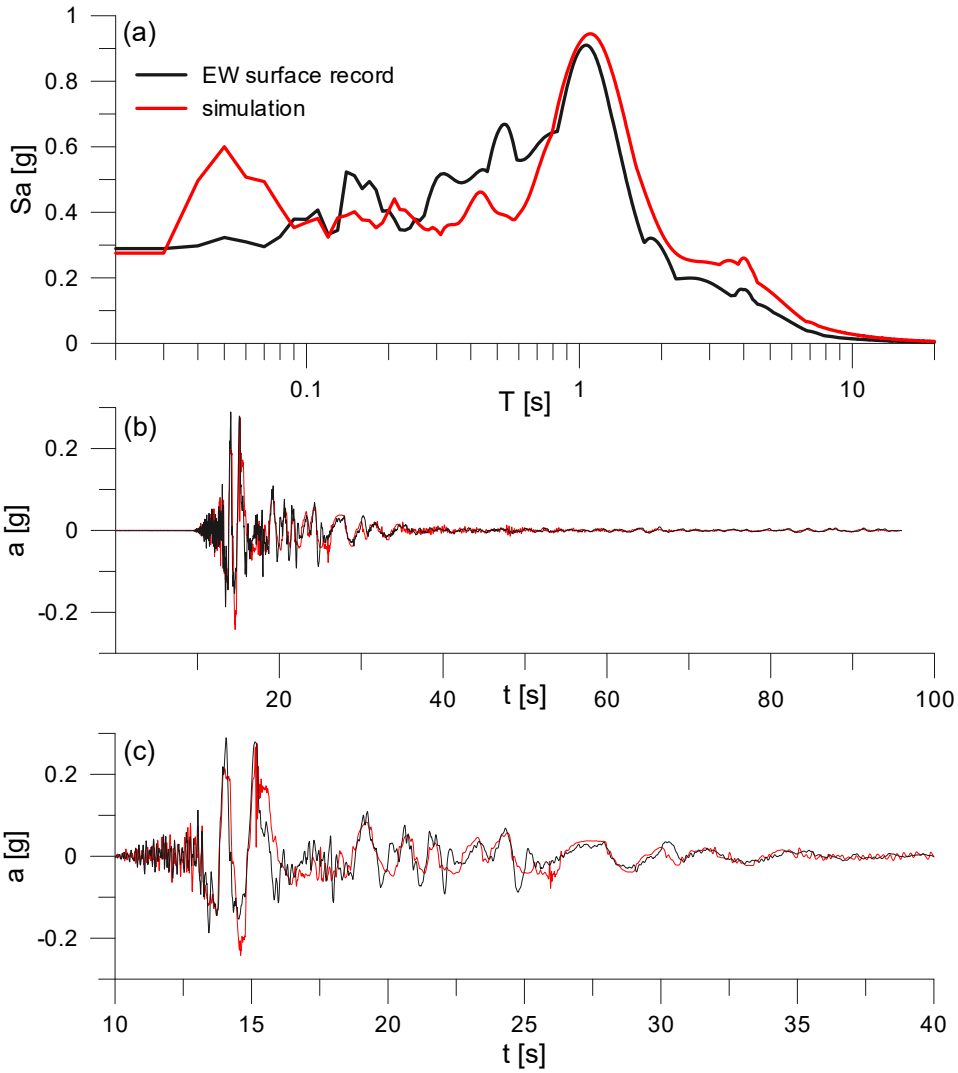

Figure V.2.12 – Comparison for the EW component between recorded and simulated (a) acceleration response spectra and (b) time histories at the surface with (c) detail between 10 and 40 s in the effective stress analysis

The liquefaction strength attributed to the masado soil caused the excess pore pressure accumulation in the saturated soil after about 13 s and the initial liquefaction condition is reached at around 17 s between 8 and 14 m under the ground level (Figure V.2.13).

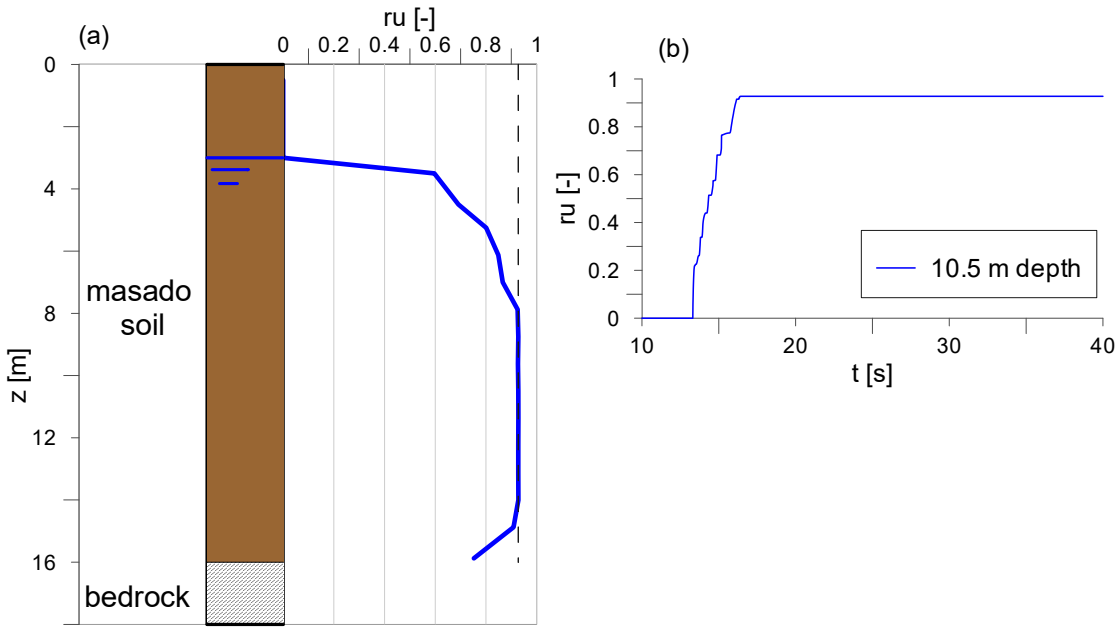

Figure V.2.13 – Excess pore pressure profile (a) and time history at 10.5 m depth in the effective stress analysis for the NS component

The analyses results, summarized in terms of variance of spectral acceleration in the range of 0.02 ÷ 20 s, are reported in Table V.2.3. The mean variance becomes more than 3 times smaller from a total to effective stress analysis, showing that, notwithstanding the simple model adopted to model the pore pressure buildup, the effective stress analysis provides a substantial improvement of the prediction respect to that given by the total stress simulation.

Table V.2.3 – Variances between simulated and recorded acceleration response spectra for total and effective stress analyses

Analysis type	N-S	E-W	mean
TT	13.20	34.58	23.89
TE	8.07	5.11	6.59

V.2.6. Comparison with literature simulations

Several authors perfomed simulation on Port Island site using both equivalent linear (Iwasaki and Tai, 1996) and effective stress analysis (Elgamal et al., 1996; Suetomi and Yoshida, 1998; Cubrinovski et al., 2000; Yoshida, 2000; Ziotopoulou, 2010).

An undrained effective-stress finite-element analysis of the site amplification was conducted by Elgamal et al. (1996), and the excess pore pressure ratio time history at 8 m depth was computed.

In order to compare the SCOSSA result with the prediction of Elgamal et al. (1996), the NS and EW recorded components at the surface and at 16 m depth have been proiected along the N44W direction. The computed N44W recorded component at the surface has been overlapped to the available figure reported in Elgamal et al. (1996) as to set the zero of the accelerogram as considered by Elgamal at al. (1996) (green line in Figure V.2.14a).

The N44W recorded accelerogram at 16 m depth has been used as input motion of the analysis.

Finally, the excess pore pressure time history generated at 8 m depth has been compared with the results of Elgamal et al. (1996) at the same depth. The ordinate scale of excess pore pressure ratio has been adjusted in consideration that the maximun excess pore pressure ratio attained in the SCOSSA computer code is less than the unity.

SCOSSA predicts excess pore pressure accumulation at the same time istant of Elgamal et al. (1996), while the liquefaction condition is reached slightly in advance (Figure V.2.14b).

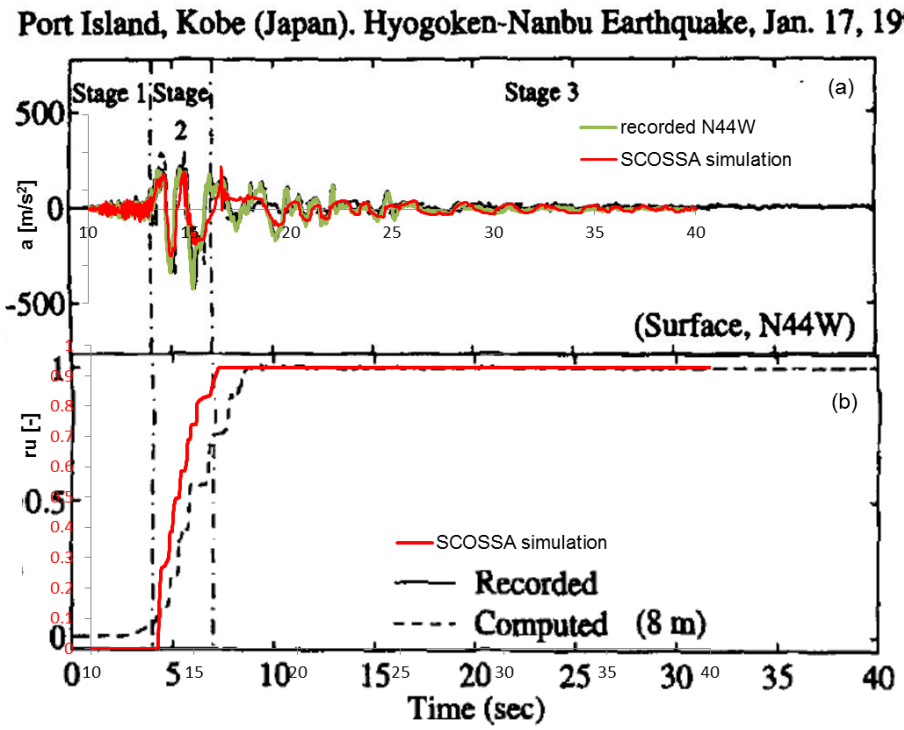

Figure V.2.14 – Comparison for the N44W component (a) between recorded and simulated acceleration time history at the surface and (b) excess pore pressure ratio time history computed by Elgamal et al. (1996) and by SCOSSA code (mod. after Elgamal et al., 1996)

Recently, Ziotopoulou (2010) performed simulations on Port Island site using three different advanced costituitive models implemented in a finite difference code. Figure V.2.15 shows the comparison between the surface acceleration response spectra reported by Ziotopoulou and

the SCOSSA results. The comparison shows that the predictions of SCOSSA code are quite reasonable even though the simple modelling of the pore pressure generation.

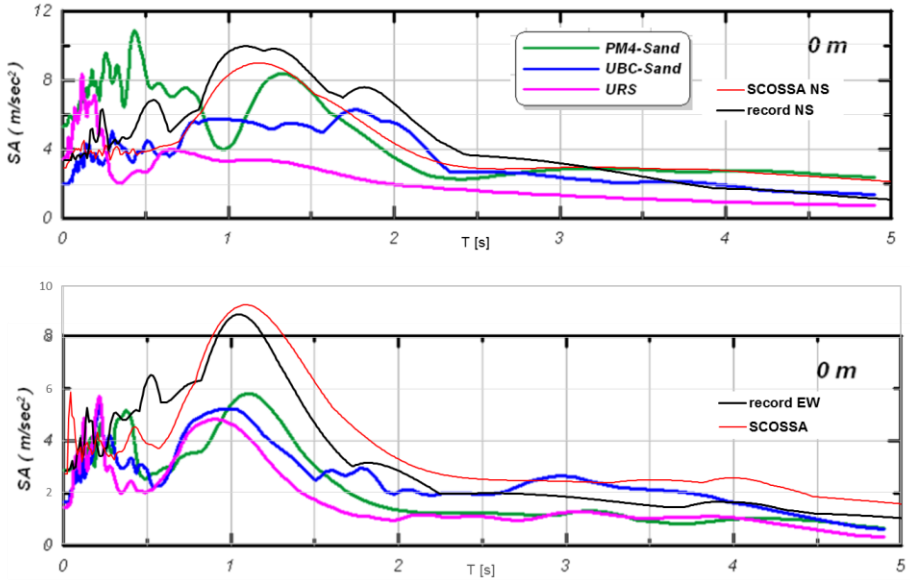

Figure V.2.15 – Comparison between the acceleration response spectra performed by SCOSSA code and the results of other constitutive models for the EW (a) and NS (b) component (mod. after Ziotopoulou, 2010)

V.3. Wildlife site

Wildlife site is located in one of the most seismic areas of North America, along the popular system of strike-slip faults which crosses the California region along the NW - SE direction (Figure V.3.1).

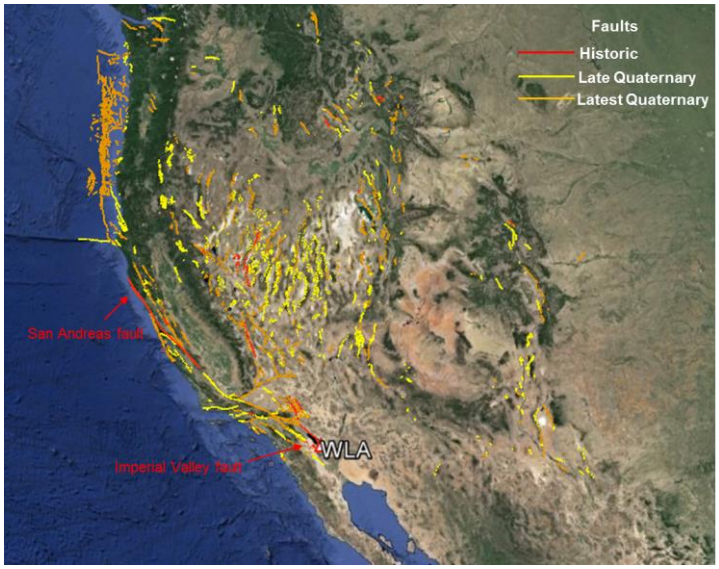

Figure V.3.1 – Map of the faults in the west side of North America, classified for geological age with highlighting the Wildlife site and, in red, the faults historically known (mod. after NEES website)

The Wildlife Liquefaction Array (WLA) is located in the foodplain of the Alamo River, in the Imperial Valley, 160 km east of San Diego, California (Figure V.3.2a). In this area, liquefaction manifestations were observed during the 1930, 1950, 1957, 1981 and 1987 earthquakes. Because of the high seismicity of this region, USGS (United States Geological Survey) decided to install accelerograms and piezometers in 1982.

Thanks to the plain topographyc condition and the sedimented horizontal deposits (Figure V.3.2b), Wildlife constitutes a natural laboratory for monitored earthquake responses and many researchers used the collected data for developing or verifying models for predicting ground response and ground deformation.

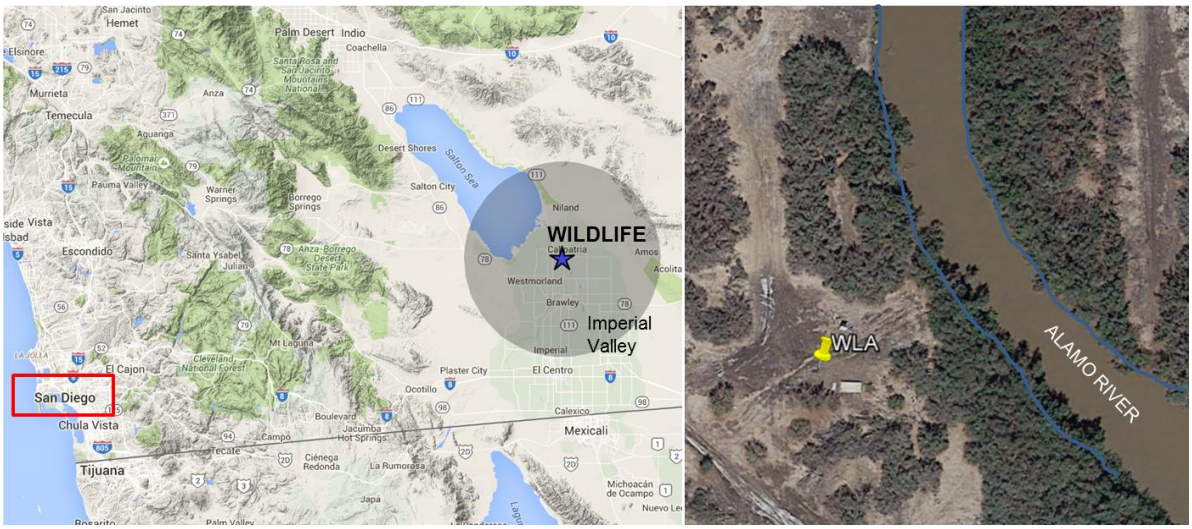

Figure V.3.2 - Location of Wildlife Liquefaction array in the Imperial Valley, California (a) and satellite image of the array site (b)

The site was equipped with surface and downhole accelerometers and six electrically transduced piezometers (Figure V.3.3). The downhole sensor was placed at a depth of 7.5 m, immediately below the liquefiable layer, and five of the six piezometers were placed within the liquefiable layer. Figure V.3.3a is a plan view of the instrumentation and Figure V.3.3b is a cross section showing the soil stratigraphy and the positions of the six piezometers and accelerometers (Bennett et al., 1984).

The soil profile can be broken into four general soil layers. The upper 2.5 m consists of sandy silt, silt and clayey silt, which is interpreted as a food-plain deposits. Cone penetration test data indicates that sediments are very loose and soft. Extending 4.3 m below, this is a silty sand layer, which is understood to be the liquefiable layer in the profile. This deposits contains two subunits identified as Wildlife sand *A* and *B* (WSA and WSB), respectively; the first 1 meter consists of very loose to loose sandy silt while the second subunit consists of loose to medium silty sand to very fine sand. The contact between the two subunits is gradational. This second

layer is interpreted to be a point-bar deposit, because located on the concave side of the river meander curve. A lacustrine silty clay deposit is extended from 6.8 to 12 m depth, underlain a cemented silt (Bennett et al., 1984).

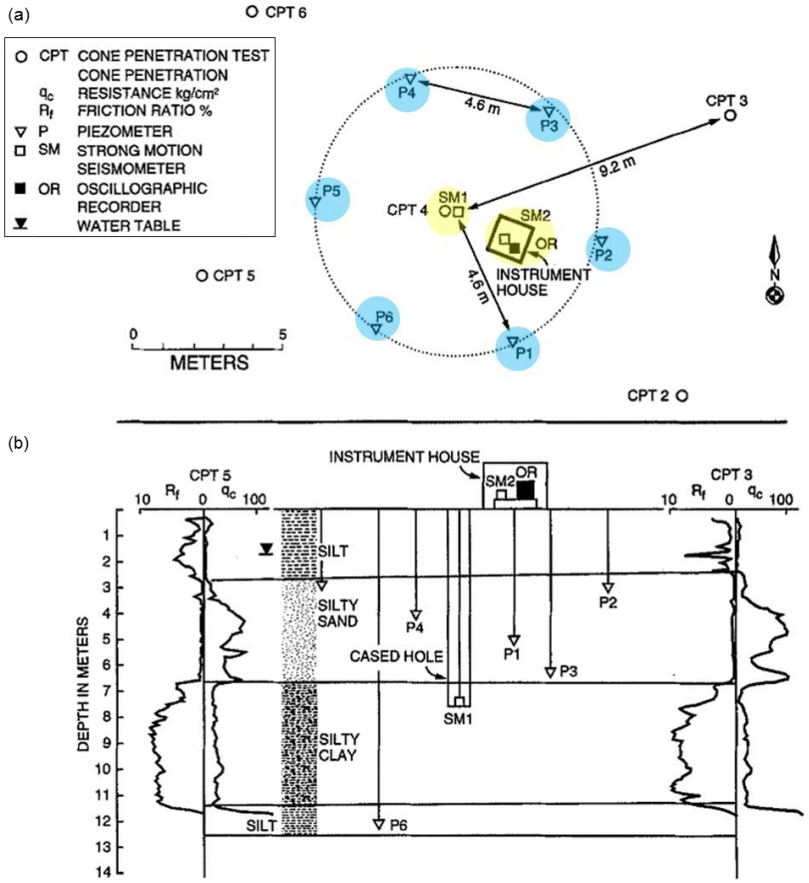

Figure V.3.3 – Plan (a) and cross section (b) of Wildlife Liquefaction Array (after Youd and Holzer, 1994)

Moreover, after the 1981 Westmoreland earthquake, a cooperative was undertaken by the University of Texas, Rensselaer Polytechnic Institute and Woodward-Clyde Consultans for making investigation of some of the sites at which prominent liquefaction occurred. An extensive cyclic strain-controlled laboratory testing program, including both triaxial and simple shear tests on intact and reconstituted sand specimens were performed by Vucetic and Dobry (1986), while resonant column tests were carried out by Haag (1985).

In details, in January 1983, subsurface investigations and field seismic tests were performed at Wildlife and others sites. At this time, approximately 27 tubes of undisturbed soil were recovered, eight of that were later transported to the Woodward-Clyde Laboratory in New Jersey and twelve were transported to the Rensslaer Polytechnic Institute in Troy, New York. The remaining seven tubes remained at Austin for laboratory testing.

Figure V.3.4 reportes the exact location of the investigation, with ubication of Cross-hole, MASW and other field tests.

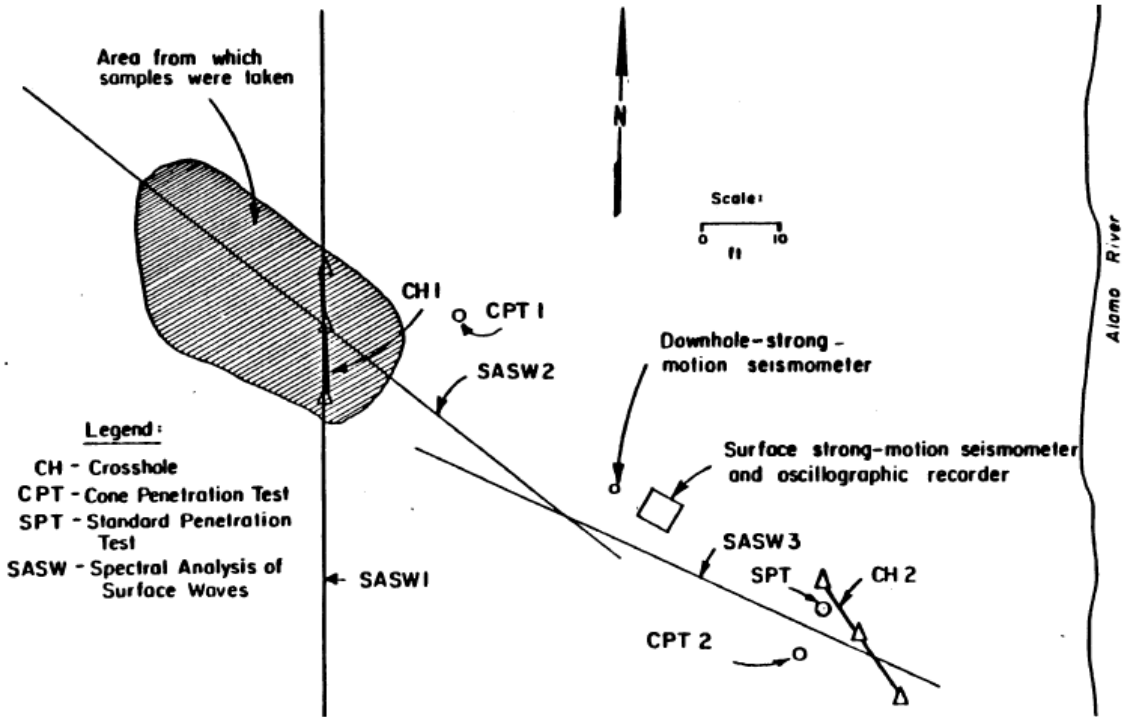

Figure V.3.4 - Location of the 1983 investigation (Haag, 1985)

V.3.1. The 1987 earthquakes

The Wildlife liquefaction array triggering four times during the Superstition Hills earthquake sequence of 23 and 24 November 1987 (Table V.3.1). The Elmore Ranch earthquake, a 6.2 magnitude event occurred on November 23rd, 1987, and the Superstition Hills earthquake, a magnitude 6.6 event that occurred the next day. The epicenters of the two main events respect to the array locetion are reported in Figure V.3.5.

Table V.3.1 – Seismic sequence of the 1987 earthquakes (Zeghal and Elgamal, 1994)

Event	Date (1987)	Time (PST)	Magnitude	Epicentral distance [km]	Peak horizontal surface accelaration [g]
Elmore Ranch	November 23	17:54	6.2 M_W	23	0.13
Aftershock	November 23	22:23	4.0 M_L	-	0.01
Superstition Hills	November 24	05:15	6.6 M_W	31	0.21
Aftershock	November 24	05:34	4.8 M_L	-	0.02

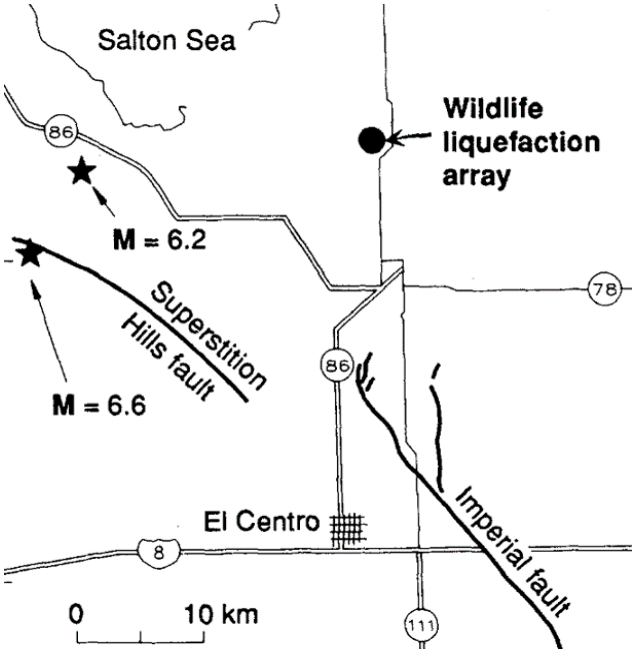

Figure V.3.5 – Epicenters of the 1987 earthquake (mod. after Youd and Holzer, 1994)

During Elmore Ranch earthquake, the level of the shaking was low, no seismic excess pore pressure were recorded, while Superstition Hills event caused full liquefaction (Thilakaratne and Vucetic, 1987). Sand boils erupted water and muddy sediment and turned the arid array site into a quagmire, affected an area in the foodplain of about 33 ha. Liquefaction interested the silty sand layer, especially in the upper part of the stratum (WSA) as reported by Vucetic and Dobry (1986). Extensive ground cracking indicative of lateral spreading accompanied liquefaction at the array and cumulative opening across ground cracks was 126 mm (Holzer et al., 1989).

The recorded acceleration time histories and acceleration spectra of the horizontal components of Elmore Ranch earthquake are reported in Figure V.3.6. The surface PGA recorded at the array station, was 0.127 g and 0.128 g for NS and EW component, respectively. At the downhole sensor depth, the recorded maximum acceleration was 0.078 g for the NS and 0.068 g for the EW component.

Both the components had the maximum spectral acceleration at 0.16 s while the maximum amplification between the downhole and surface records is at 0.26 s.

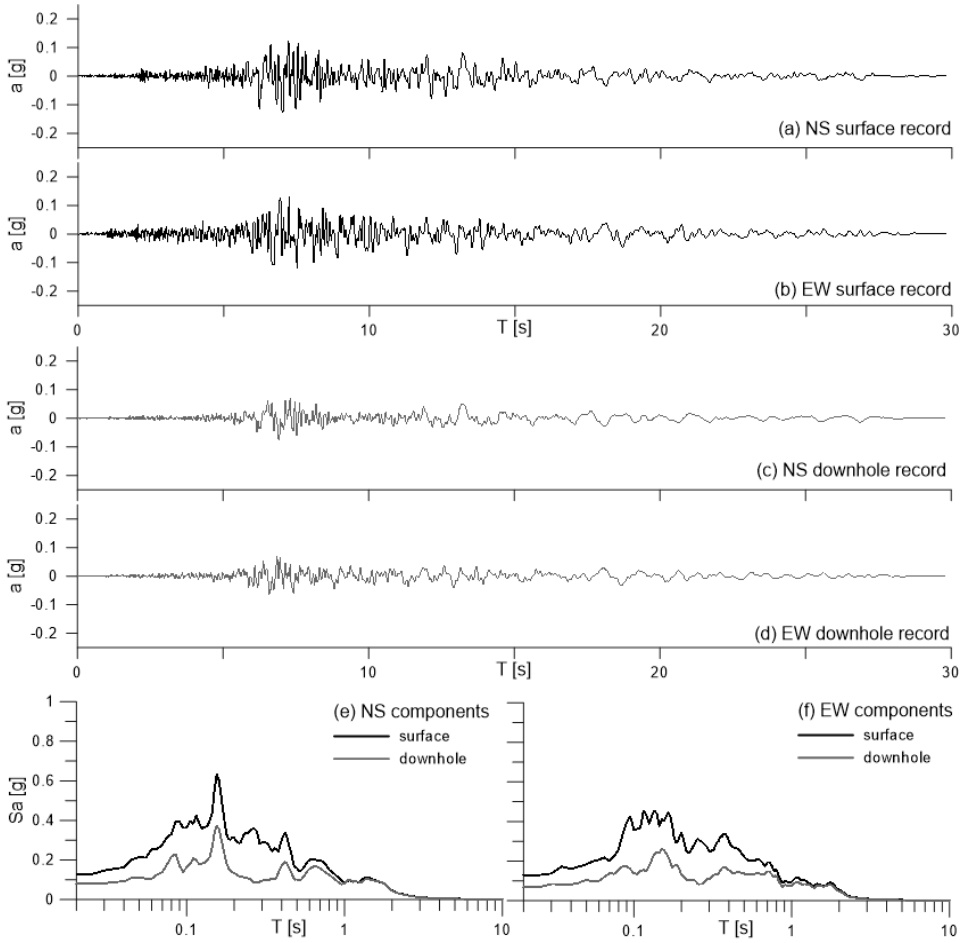

Figure V.3.6 - Recorded acceleration time histories of the Elmore Ranch earthquake at surface (a,b) and at the 7.5 m downhole sensor depth (c,d), and acceleration response spectra (e,f)

The acceleration time histories and spectra of the horizontal components of Superstition Hills earthquake are reported in Figure V.3.7. The surface PGA was 0.171 g for the NS and 0.105 g for the EW component. At the downhole sensor depth, the recorded maximum acceleration was 0.183 g for the NS and 0.205 g for the EW component.

For the EW components, the maximum spectral acceleration was reached at 0.13 s, which is the period that corresponds to the maximum amplification too (Figure V.3.7f). It can be observed that the EW components

For the NS components, the maximum spectral acceleration was reached at 0.34 s while the maximum spectral amplification was at 1.3 s (Figure V.3.7f). The mean period is 0.907 s for the downhole acceleration and 1.186 s at the surface.

The change in frequency content can directly be seen in ground surface accelerograms component, where a sudden change in frequency occurrs at approximately 15–18 s (Figure V.3.7a,b).

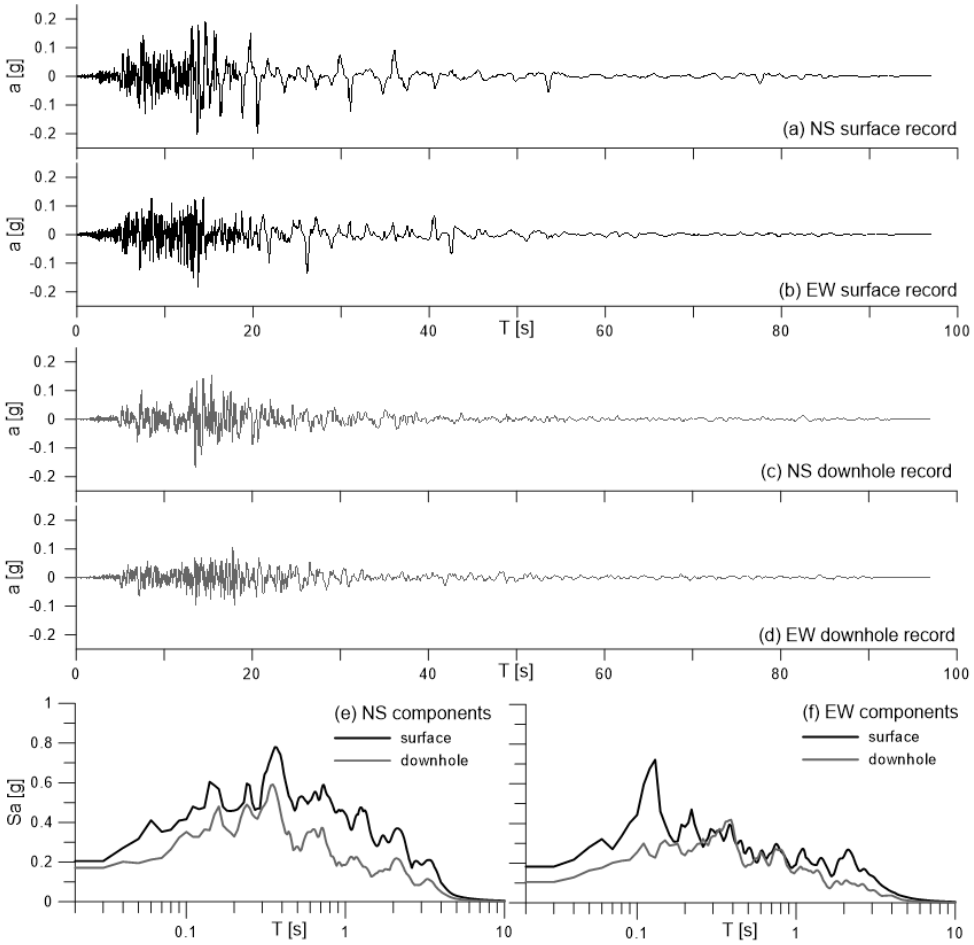

Figure V.3.7 - Recorded acceleration time histories of the Superstition Hills earthquake at surface (a,b) and at the 7.5 m downhole sensor depth (c,d), and acceleration response spectra (e,f)

The change in frequency content can directly be seen in ground surface accelerograms component, where a sudden change in frequency occurrs at approximately 15–18 s (Figure V.3.7a,b). Liquefaction triggering detection procedure can be performed using the Stockwell trasform (Stockwell et al., 1996), which combines elements of both short-time Fourier trasforms and wavelet trasforms for a balanced resoultion of both time and frequency (Kramer et al., 2015). Figure V.3.8 shows the normalized Stockwell spectrum for the NS component of the Superstition Hills record in the first 30 s. At time of 13 s, the normalized amplitudes of the high-frequency components quickly drop and the amplitudes of the very low-frequency components persist for the remainder of the motion. At around 20 and 27 s, strong high-frequency components can be observd, which are related to dilation pulses occurred after the initiation of liquefaction.

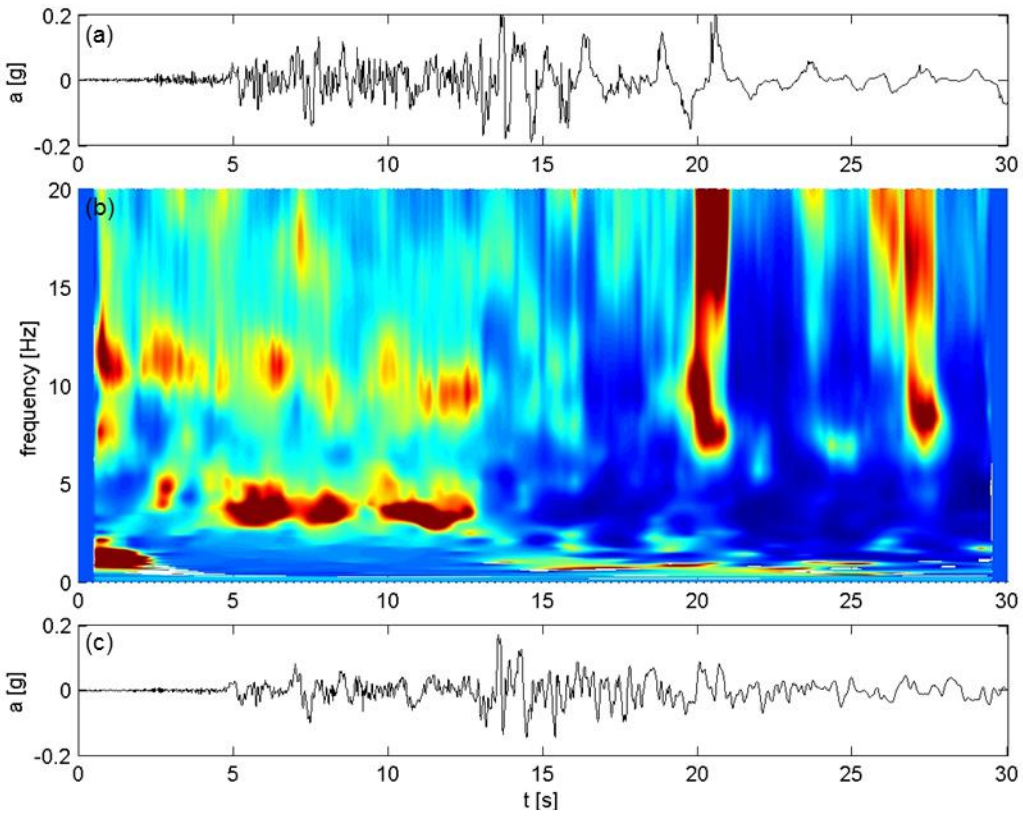

Figure V.3.8 – Acceleration record at surface (a); normalized Stockwell spectrogram (b) and recorded acceleration at the sensor depth (c) for NS component of Superstition Hills earthquake

Prevalence of low frequency motions in the latter part of the ground motion is the direct consequence of the pore water pressure increasing.

Except for the P4, all the piezometers worked during the event, but the accuracy of the recorded pore pressure signals has been the subject of some controversy over the years and only the piezometer P5 record at 2.9 m depth is considered actually reliable (Holzer and Youd, 2007). The P5 piezometer is very close to the surface and the drops in the record are in agreement with the mechanism of lateral spreading at the surface (Zorapapel and Vucetic, 1994). Similar but smaller pore water pressure drops can be also noticed on the record of the other shallow piezometer P2, while such distinctive drops cannot be seen on P1 and P3 records due to the larger depth (Figure V.3.9).

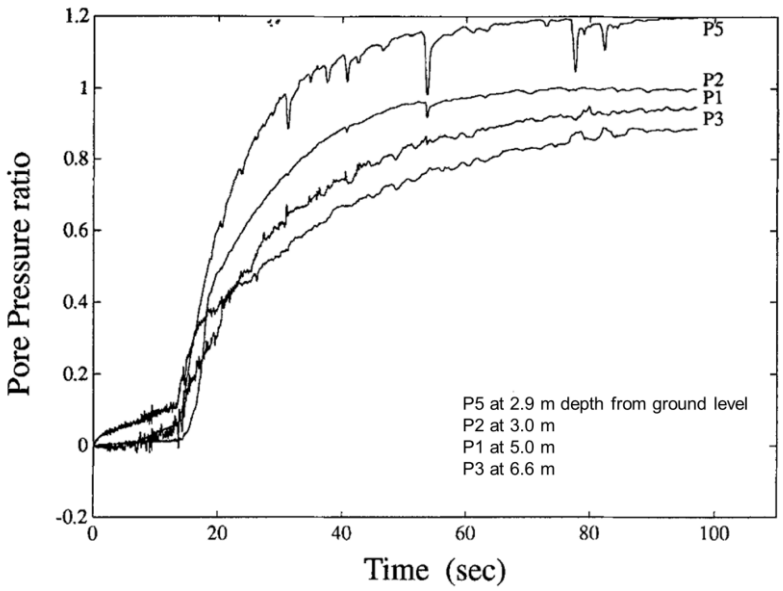

Figure V.3.9 – Pore pressure ratio time histories recorded during the Superstition Hills earthquake (mod. after Youd and Holzer, 1994)

V.3.2. Simulations

After that geotechnical model and the PWP model have been calibrated, effective stress analyses have been performed on Elmore Ranch and Superstition Hills earthquakes for checking the reliability of the simulations on events with different magnitude.

V.3.2.1. Geotechnical model

The modelled soil profile consists of a soil column, divided in three layers, with the rigid bedrock at 7.5 m depth, where the downhole sensor is located (Figure V.3.10). The ground water table has been assumed at 1.2 m depth as reported by Holzer and Youd (2007) and the physical properties of the soils are reported in Table V.3.2.

Table V.3.2 – Physical properties of the soils

Layer	Depth [m]	γ [kN/m^3]	D_{50} [mm]	Fines < 75 μm [%]	Clay < 5 μm [%]	w [%]	LL [%]	LP [%]	PI [%]
silt	0.0 ÷ 2.5	18.65	0.025	93	25	32	30	22	8
Silty sand (WSA)	2.5 ÷ 3.5	18.82	0.055	78	8	-	-	-	-
Silty sand (WSB)	3.5 ÷ 6.8	18.82	0.091	36	5	-	-	-	-
Silty clay	6.8 ÷ 7.5	19.18	0.005	98	60	28	59	30	29

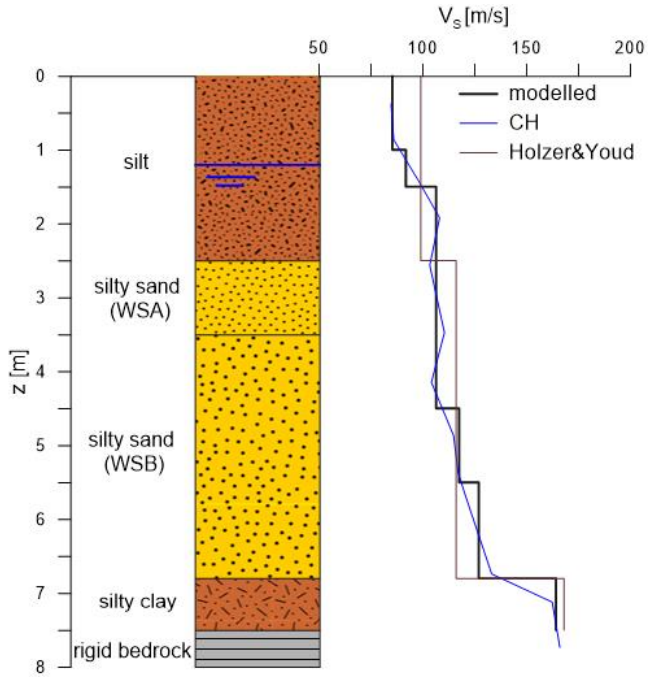

Figure V.3.10 – Soil column and comparison between different shear wave velocity profiles

The modelled V_S profile (in black) is based directly on the result of Cross-Hole test data (in blue) reported by Vucetic and Dobry (1986) and it is more detailed of the profile proposed by Holzer and Youd (2007).

V.3.2.2. Normalized shear moduli and damping curves

The mechanical properties of silty sand deposit has been built on the resonant column test data performed by Haag (1985) on specimens at a confining pressure of 55 kPa. Three specimens for each sublayer were analyzed by Haag (1985) and the corrispondent physical properties are reported in Table V.3.3. It was confirmed that the fine content significantly decreases in the sublayer WSB compared to WSA, where the the D_{50} is one order of magnitude smaller.

Table V.3.3 – Physical properties of the specimens subjected to resonant column tests (Haag, 1985)

Specimen	Depth [m]	LL [%]	D_{50} [mm]	Percent fines	D_{20} [mm]	Percent clay
W12A1	2.68	32.6	0.021	95	≤ 0.001	22
W11A1	2.68	23.3	0.072	50	0.022	11
W3A4	3.26	23.3	0.054	57	0.007	15
W3B1	4.45	21.5	0.140	12	0.100	2
W12B2	4.54	22.7	0.140	23	0.055	10
W3B3	4.82	24.7	0.097	38	0.004	11

These specimens were subjected to a detailed investigation program of the small-strains properties, summarized in terms of normalized shear modulus in Figure V.3.11. It is possible to individualize the mean behaviour of each sublayer with the highlithed curves in blue and red, respectively for WSA and WSB sublayers.

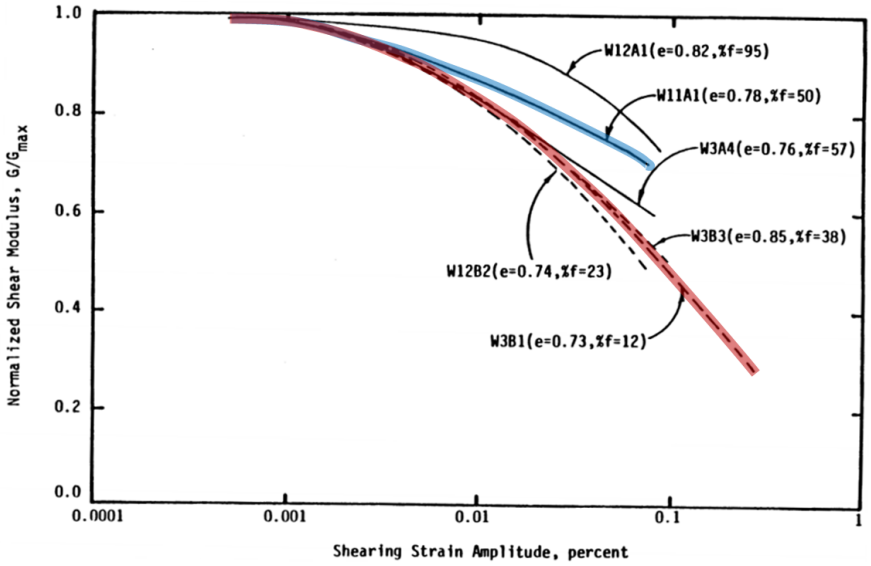

Figure V.3.11 – Variation of normalized shear modulus with shearing strain (mod. after Haag, 1985)

The parameters of the MKZ model for WSA and WSB sublayers have been calibrated on experimental data representative of the behaviour of each sublayer (Figure V.3.11). In the same way, the damping curves have been defined on the experimental data reported by Haag (1985).

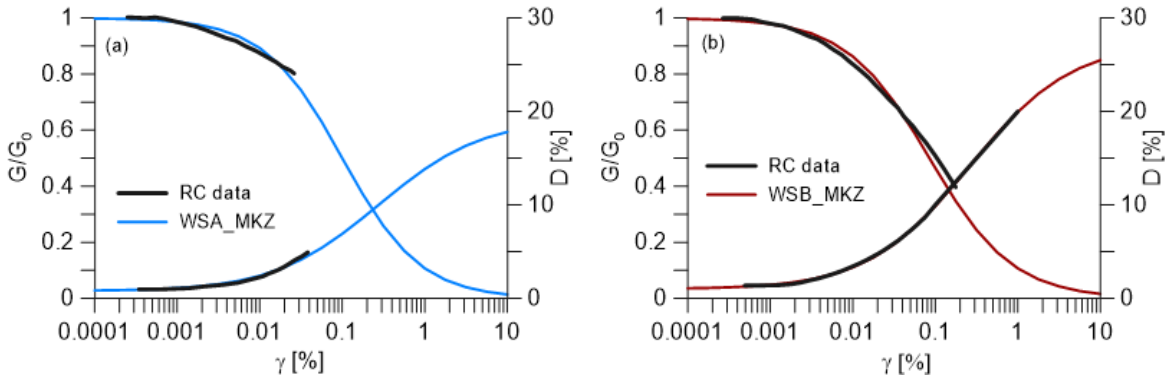

Figure V.3.12 – Normalized shear modulus and damping curves adopted in the model for WSA (a) and WSB (b) sublayers, based on RC test data reported by Haag (1985)

Since the experimental data are related to shear strains smaller than 0.1 %, an adjustment of the shear modulus reduction curves has been performed for obtaining compatibility between strength and stiffness, according to the procedure described in chapter IV.2.

Vucetic (1986) performed monotonic triaxial tests on samples of both WSA and WSB and the friction angle was found to be equal to 37°, practically the same for both sands. Using these resistance parameter in the Hardin and Drnevich (1972) relationship, a maximum shear stress of 23.4 kPa has been computed for the WSA layer at the mean depth of 3 m and a stress of 35.13 kPa has been determined for the WSB layer at the mean depth of 5 m. Finally, the shear modulus reduction curves of WSA and WSB have been modified in order to reach the previous computed strength.

The shear modulus reduction and damping curves adopted in the model for the WSA and WSB layers are compared with the results of cyclic triaxial and simple shear (DSS) tests data (Figure V.3.12). In the same figure are also reported upper and lower bound proposed by Seed and Idriss (1970) and the theoretical curves adopted by Vucetic (1986) for perfoming effective stress analyses. The shear moduli curve named $(K_2)_{max}$=30 is related to the application of the Seed and Idriss (1970) model to the experimental data.

As validation, it can be noticed that the curves adopted for modelling the WSA and WSB layers are very close to the experimental data at high shear strains. Further consideration that the curves have a more linear behaviour than the literature curves for sand proposed by Seed and Idriss (1970).

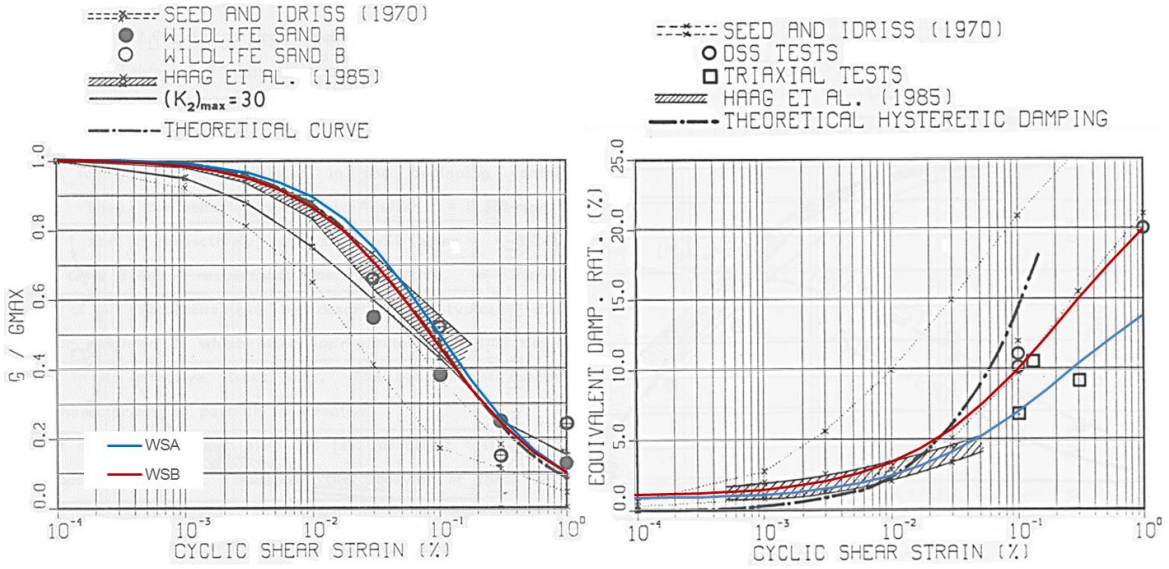

Figure V.3.13 - Shear moduli and damping curves for WSA and WSB layers compared with the cyclic triaxial test and simple shear test data reported by Vucetic (1986)

Since no laboratory tests were carried out on the silt and silty clay deposits, reduction curves could be defined on plasticity index of the soil as proposed by Vucetic and Dobry (1991). As reported in Table V.3.3 plasticity index is 8% for the silty layer and 29% for the silty clay

deposit. Vucetic and Dobry (1991) curves interpolated for PI between 0 and 15% and for PI equals to 30% are reported in Figure V.3.14. The comparison with the curves based on experimental data shows that the normalized shear modulus curve of Vucetic and Dobry (1991) for PI equals to 7.5% is definitely less linear than that for sand soils, which is physically unacceptable. Consequently, the WSA curves have been adopted to model the silty deposit in the upper part of the profile.

Finally, the normalized shear modulus and damping curves of Vucetic and Dobry (1991) for PI equals to 30% have been considered for represent the dynamic properties of silty clay deposit.

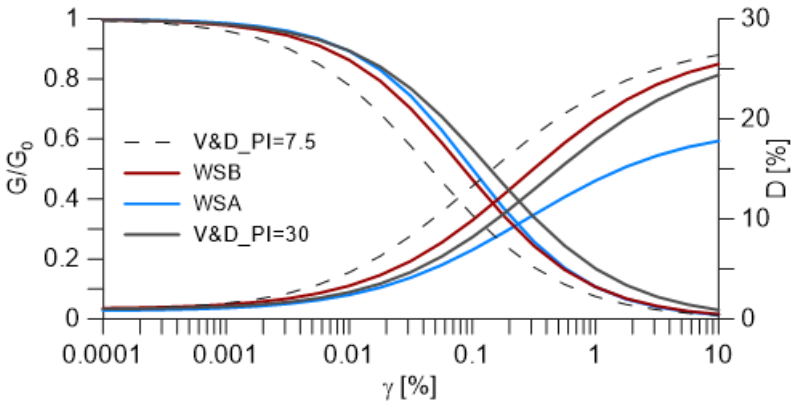

Figure V.3.14 – Shear moduli reduction and damping curves adopted in the analyses compared with literature curve for PI=7.5 (dotted lines)

V.3.2.3. Cyclic resistance curve and pore pressure relationship

A cyclic resistance curve has been computed from the available laboratory tests.

In the 1983 investigation, some stress-controlled cyclic triaxal tests were performed by Vucetic (1986) and Ladd (1984), but they are in number insufficient for defining a curve because related to different effective confining pressure. On the other hand, a great amount of strain-controlled cyclic triaxial tests was performed by Vucetic (1986) with the aim to apply his strain-based model for generation of excess pore pressure implemented in the computer code DESRA. All these tests were performed at the same effective confining pressure of about 96 kPa. Strain-controlled cyclic triaxial tests can be used for defining a cyclic resistance curve following the method proposed by Silver and Park (1976). This procedure consists in the representation of the the stress ratio measured during strain-controlled CTX tests in function of the deformation amplitude applied (Figure V.3.15a). In this plot is possible to identify curves with the same number of cycles. Finally, it is possible to define the maximum shear stress ratio of each iso-cycle curve and to assign it to the correspondent number of cycles.

Alternatively, the same curve can be obtained representing the data in function of the normalized pore water pressure, but this second procedure is less simple of the previous one (Figure V.3.15b).

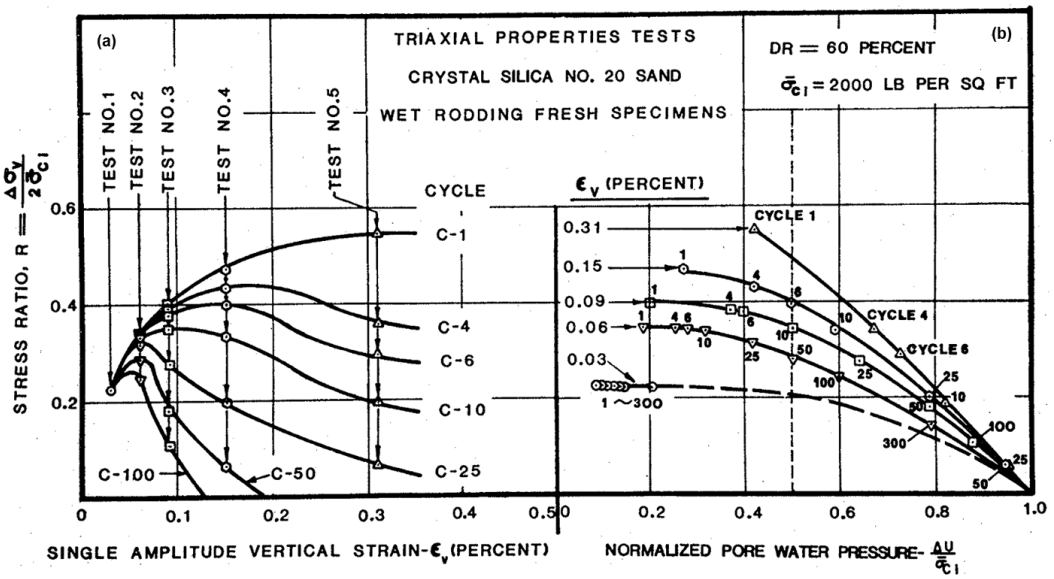

Figure V.3.15 - Method for defining CRC from strain-controlled cyclic triaxial tests (Silver e Park, 1976)

Figure V.3.16 shows the experimental data of six strain-controlled CTX tests performed on silty sand layer by Vucetic (1986) in the way prescribed by Silver and Park (1976). In red is highlighted the maximum of each iso-cycle curve.

Plotting the maximum points in the SR – N space has been obtained the cyclic resistance curve reported in Figure V.3.17. The experimental data of four stress-controlled cyclic tests carried out by Vucetic (1986) at a mean confining pressure of 24, 48 and 96 kPa are also reported for comparison. These latter are quite close to the cyclic resistance curve assumed in the simulations.

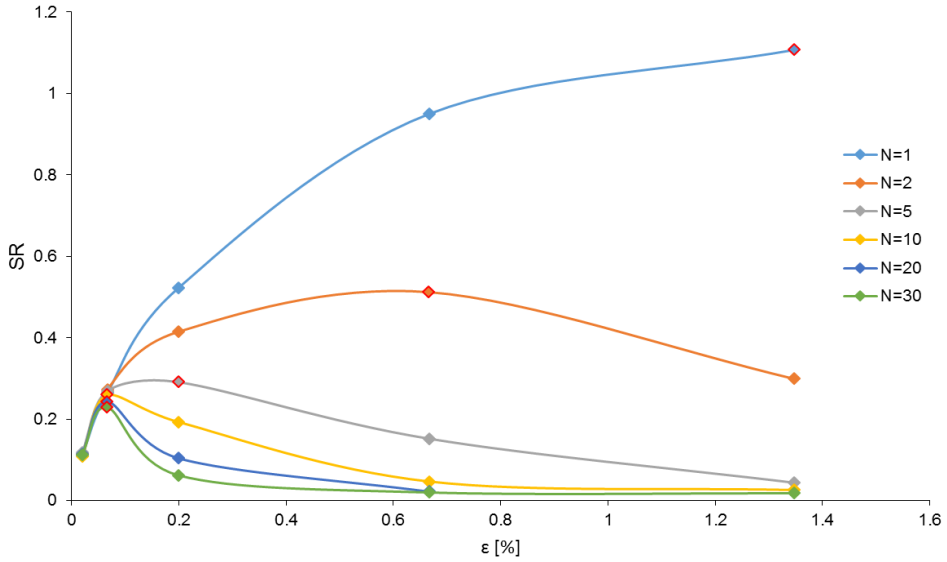

Figure V.3.16 - Representation of data of the CTX tests according to the Silver and Park (1976) method

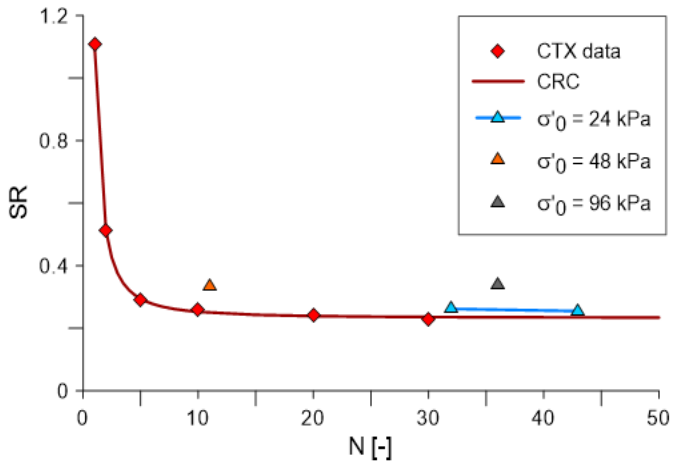

Figure V.3.17 – Cyclic resistance curve constructed according to the Silver and Park (1976) method and comparison with experimental data from stress-controlled CTX tests

The parameters of the normalized pore pressure relationship have been defined on the simple shear (DSS) tests data performed by Vucetic (1986) (Figure V.3.18). DSS data have been used to calibrate the pwp model since the quality of the data was better than that related to the cyclic triaxial tests.

The best fitting of the data gave a curve which is more rigid in the first part respect to the mean trend and an underestimation in the elbow. Moreover, the maximum value of the modelled curve has been set at 0.98, in order to leave a residual resistance to the liquefied soil.

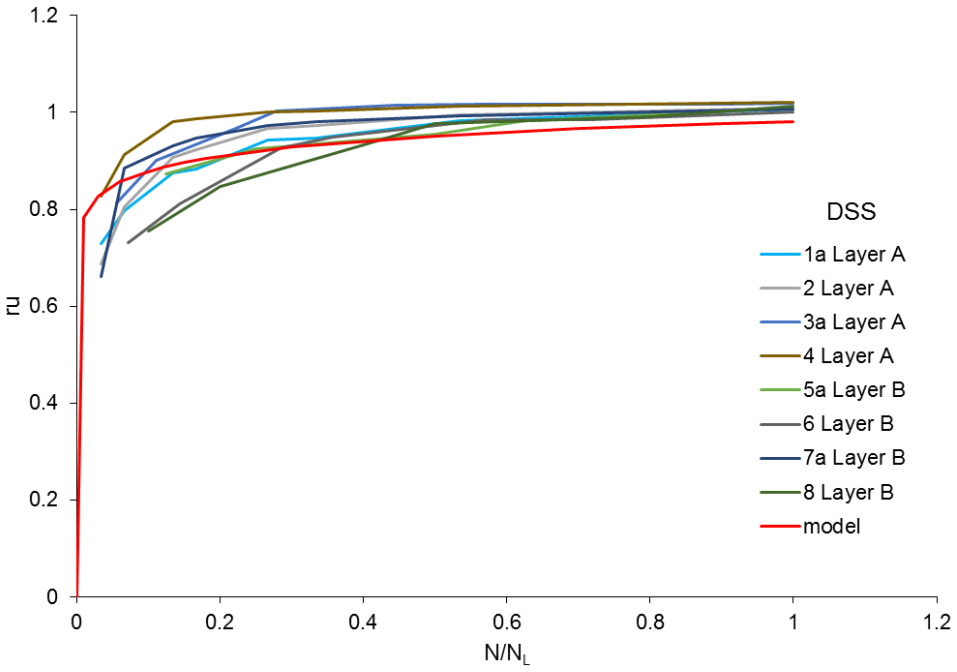

Figure V.3.18 - Experimental curves from DSS tests vs analytical curve (red line) used in the analyses

The numerical values of the pwp parameters are reported in Table V.3.4. The pwp parameters, calibrated on data related to the silty sand layer, have been adopted also for modelling the silty deposit under the ground water depth.

For the silty clay deposit at the bottom of the profile has been hypothesized that the volumetric threshold strain is greater enough to not induce significant excess pore water pressure during earthquake.

Table V.3.4 – Pwp parameters considered in the simulations

α	SR_t	SRr	a	b	c
0.6072	0.2328	0.243	0.9858	0.05	-0.00585

V.3.2.4. Simulations on Elmore Ranch earthquake

The results of the analyses in terms of acceleration time histories and acceleration response spectra at the surface are reported in Figure V.3.19 and V.3.20. As regards to the NS component, the predicted response spectrum is very close to the recorded one for low and high values of period while it underpredictes the record in the range of periods 0.07 ÷ 0.3 s. A good prediction is obtained also in terms of acceleration time history because the predicted accelerogram well reproduced the record, especially in the range of 15 – 20 s.

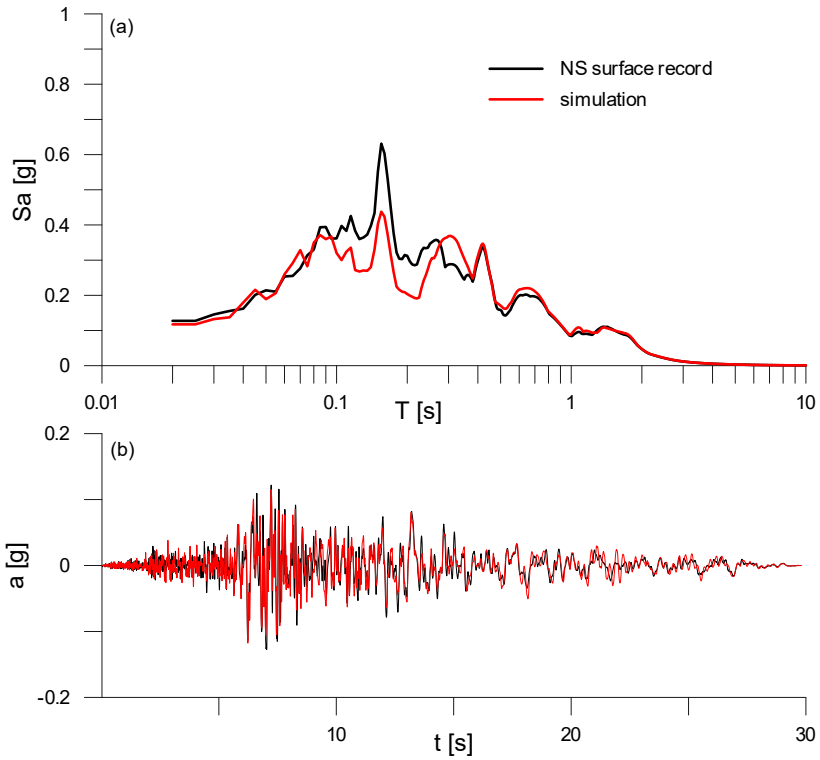

Figure V.3.19 - Comparison between recorded and simulated (a) acceleration response spectra and (b) time histories at the surface for the NS component of Elmore Ranch

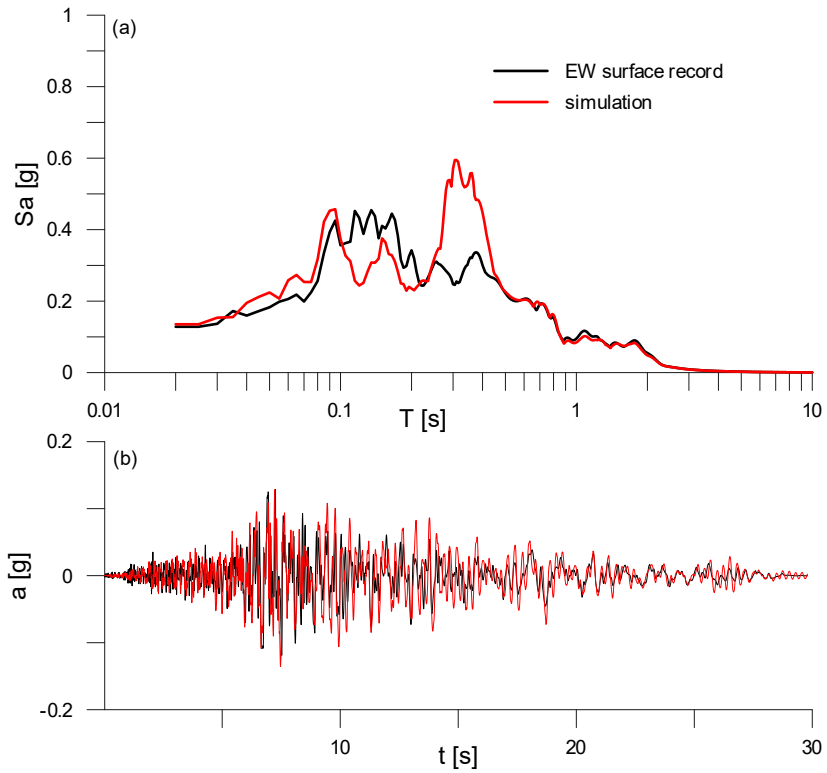

Figure V.3.20 - Comparison between recorded and simulated (a) acceleration response spectra and (b) time histories at the surface for the EW component of Elmore Ranch

As regard to the EW component at the surface, the response spectrum well simulates the recorded PGA, while underestimates the spectral ordinates in the range 0.1 ÷ 0.25 s and overestimates the spectral acceleration at around 3 s. In the simulated accelerogram can be observed amplitudes generally greater than the record (Figure V.3.20b).
In both simulations excess pore pressure are not generated, consequently total and effective stress analyses coincide for Elmore Ranch event.

V.3.2.5. Simulations on Superstition Hills earthquake

The results of the total and effective stress analyses in terms of acceleration time histories and acceleration response spectra at the surface are reported in Figure V.3.21 and V.3.22. For the NS component, the comparison of the response spectra at the surface shows that the total stress analysis induces significative overestimation of the spectral ordinates in the range 0.2 ÷ 0.8 s, while underpredictes the recorded ordinates for period greater than 0.8 s. The response spectrum of the effective stress analysis is more close to the recorded spectrum than the total stress analysis, even though a general underestimation of the spectral accelerations. In terms of time histories, it can be noticed a clear over-prediction of the recorded amplitude in the total stress analysis after 13 s, which is the istant when liquefaction triggered.

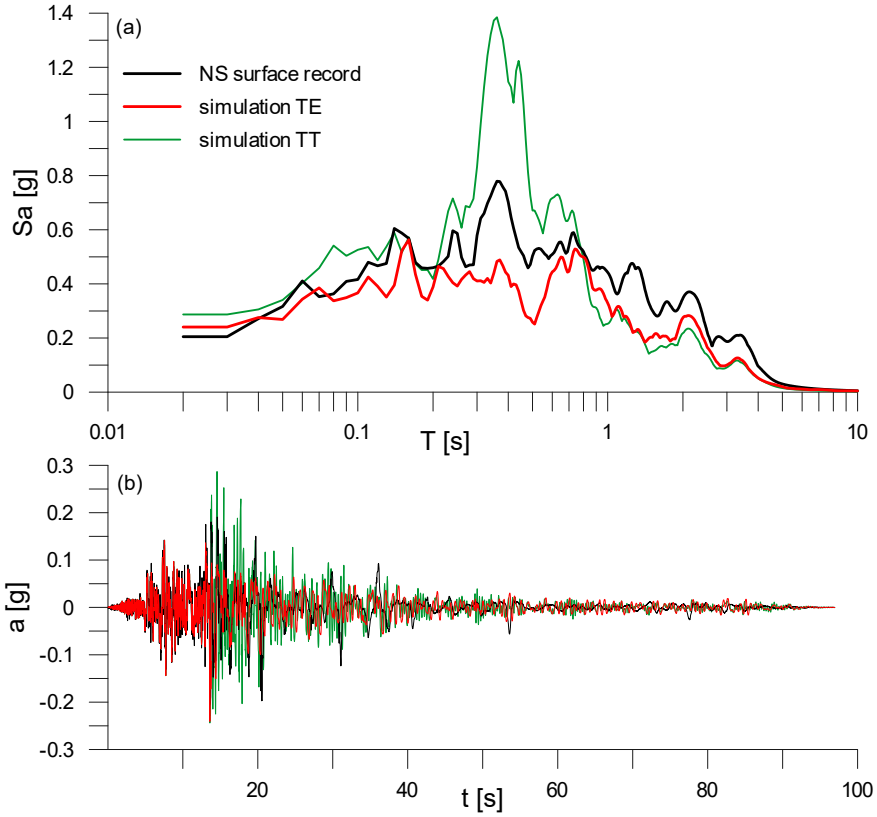

Figure V.3.21 - Comparison between recorded and simulated (a) acceleration response spectra and (b) time histories at the surface for the NS component of Superstition Hills

As regard to the EW component, the response spectrum of the effective stress analysis well-reproduces the recorded PGA and the peak of acceleration even though it is reached for a perdiod smaller than the recorded one. Both simulations show an irrealistic acceleration peak at around 0.4 s and underpredictes the spectral acceleration in the range 1 ÷ 4 s.

The comparison in terms of time histories clearly shows an overprediction of the recorded amplitude after 15 s in the total stress analysis, while the effective stress simulation is more close to the recorded trend.

Table V.3.5 reports the results of the analyses in terms of variance of spectral acceleration in the range of 0.02 ÷ 20 s. The introduction of the pwp model riduces the variance more than two times on average, and almost three times for the EW component.

Table V.3.5 – Variances between simulated and recorded acceleration response spectra for total and effective stress analyses

Earthquake	Analysis type	N-S	E-W	mean
Elmore Ranch	TE	0.481	1.878	1.180
Superstition Hills	TE	5.364	4.880	5.122
	TT	11.558	13.690	12.624

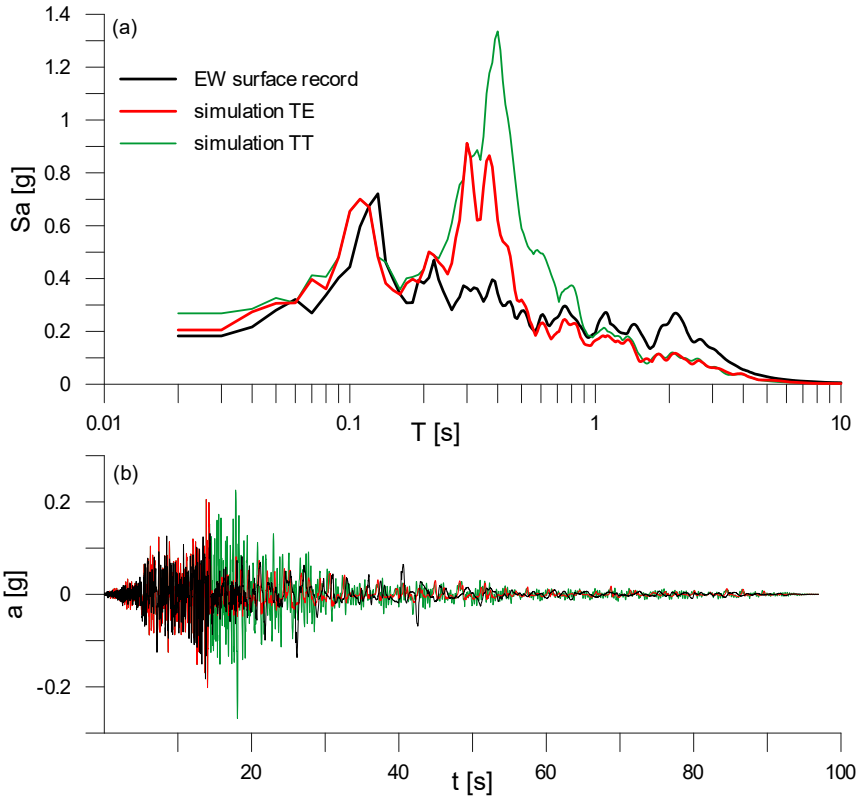

Figure V.3.22 - Comparison between recorded and simulated (a) acceleration response spectra and (b) time histories at the surface for the EW component of Superstition Hills

Both the recorded components show dilation pulses after the liquefaction triggers which are not reproduced in the SCOSSA simulations.

In the EW accelerogram of the effective stress analysis is clear the drop of amplitudes after 15 s as the recorded one (Figure V.3.22 b), while the same change is not clearly detected in the simulated NS component of effective stress analysis (Figure V.3.21b). The change in frequency occurred at initial liquefaction can be observed in the ratio between Stockwell spectrogram of simulated accelerogram at surface and recorded at the downhole sensor in the first 30 s (Figure V.3.23 d,e,f). The drop in frequency content happens at 13 s as in the normalized Stockwell spectrogram of the recorded accelerograms (Figure V.3.23 a,b,c). In the simulated spectrogram the high frequencies completely disappear after that liquefaction triggered and frequencies around 8 Hz appear after the twentieth second. In the recorded spectrogram the drop of frequency content is less drastic and high frequencies are correlated to the occurrence of dilation pulses.

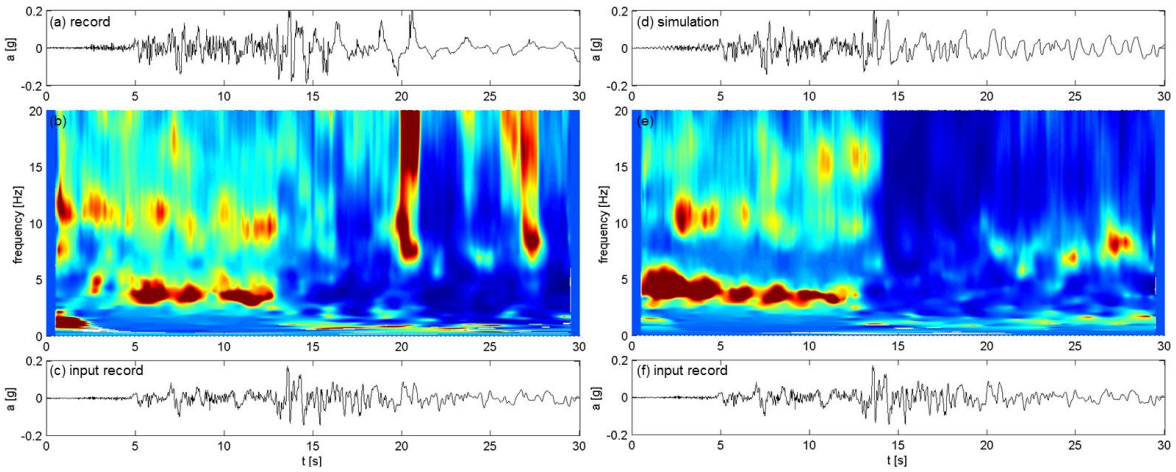

Figure V.3.23 – Comparison between normalized Stockwell spectrogram of recorded (a,b,c) and simulated (d,e,f) acceleration time histories of the NS component of Superstition Hills earthquake

At 13 s starts also the accumulation of excess pore pressure even if the trend of the simulated history is less gradual than the record of P5 piezometer (Figure V.3.24). Indeed, the generation of pwp is concentrated in few seconds between the istant times 13 and 22 s. It should be precised that the recorded time history is still object of discussion since the increase of excess pore pressure seems to continue at the end of the event.

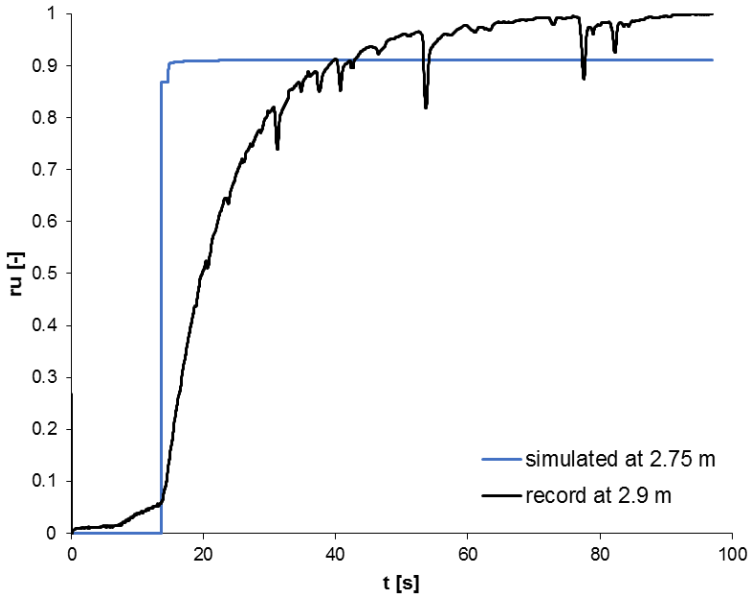

Figure V.3.24 - Comparison between the recorded and simulated time history of excess pore pressure time history at 2.9 m depth for NS component

V.3.3. Comparison with literature simulations

The prediction performed in this study has been compared with the simulation performed by other authors and computer codes. Figure V.3.25 shows the comparison between the surface acceleration response spectra at the surface performed with three different advanced constitutive models (Ziotopoulou, 2010) and the SCOSSA results. The comparison for the NS component shows that the predictions of SCOSSA code is comparable with the performance of more complex models and quite close to the best of the three predictions (Figure V.3.25a).

As regard to the EW component, all the simulations seem to return the same respone after 1 s, while they are very different for low periods. The SCOSSA response overestimates the accelerations around 0.3 s even if it catches the first peak of the recorded spectrum. The same peak is predicted in advance by the URS model, while it is completely absent in the simulation of the PM4-sand model, which is the best prediction in the range 0.25 ÷ 1 s (Figure V.3.25b).

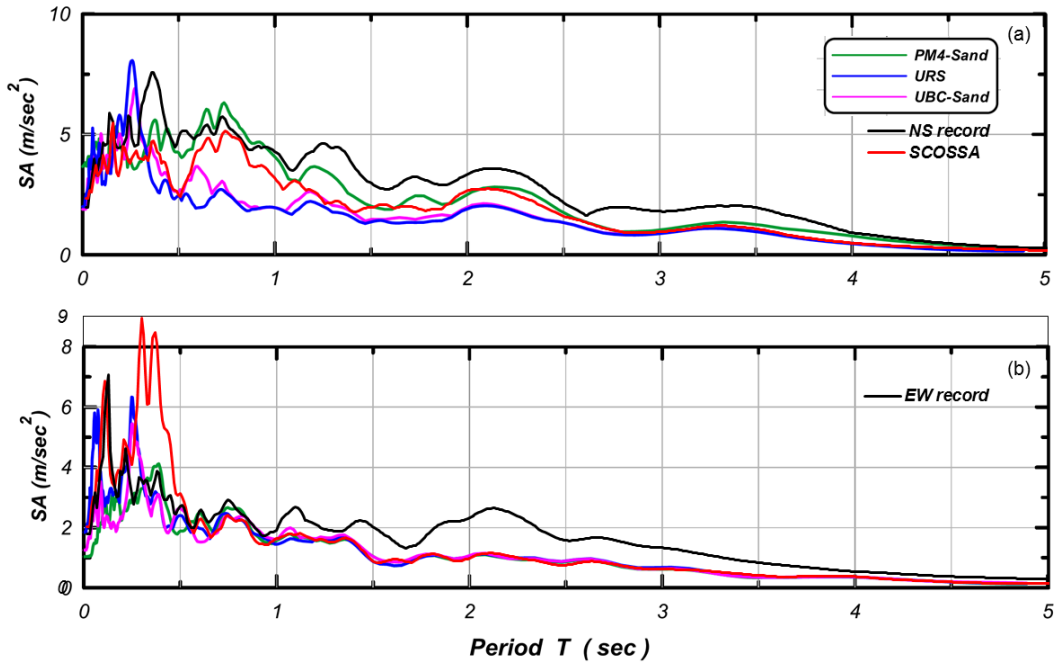

Figure V.3.25 - Comparison among acceleration response spectra performed by SCOSSA and results of other costitutive models for the NS (a) and EW (b) component of Superstition Hills event (mod. after Ziotopoulou, 2010)

Figure V.3.26 shows the comparison of SCOSSA results with the prediction of two codes: D-MOD2000 (Geomotions, 2007) and WAVE (Horne, 1996). The first code ignores phase transformation behavior as SCOSSA does, but the second is able to model it. It is possible to observe that SCOSSA returns the best prediction at low periods, until 0.5 s, while, for greater periods, WAVE code reproduces better the recorded spectra.

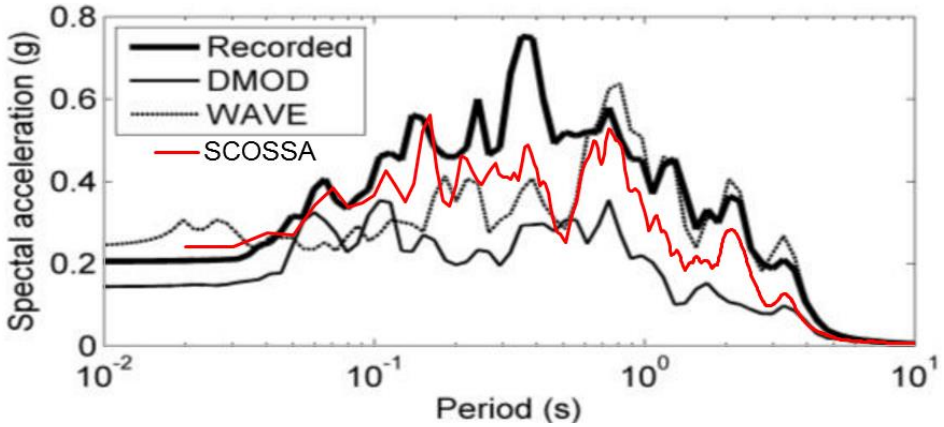

Figure V.3.26 – Comparison among acceleration response spectra performed by SCOSSA and results of other 1D codes for the NS component of Superstition Hills event (mod. after Kramer et al., 2011)

V.4. References

Bennett M.J., McLaughlin P.V., Sarmiento J.S., Youd T.L. (1984). Geotechnical investigation of liquefaction sites, Imperial Valley, California. US Geological survey, Menlo Park, California, USA.

Cubrinovski M., Ishihara K., Furukawazono K. (2000). Analysis of two case histories on liquefaction of reclaimed deposits. The 12th World Conference on Earthquake Engineering, Auckland, New Zealand.

Darendeli M.B. (2001). Development of a new family of normalized modulus reduction and material damping curves. Univesity of Texas at Austin.

Elgamal A., Zeghal M., Parra E. (1996). Liquefaction of reclaimed island in Kobe, Japan. Journal of Geotechnical Engineering, 122(1): 39-49.

Flora A., Lirer S. (2013). Small strain shear modulus of undisturbed gravelly soils during undrained cyclic triaxial tests. Geotechnical and Geological Engineering, 31(4): 1107-1122.

Geomotions (2007). MOD2000 - A computer program for seismic response analysis of horizontally layered soil deposits, earthfill dams and solid waste landfills. Geomotion, Lacey, Washington, USA.

Haag E.D. (1985). Laboratory investigation of static and dynamic properties of sandy soils subjected to the 1981 Westmoreland earthquake. Research report, University of Texas at Austin, USA.

Hardin B.O., Drnevich V.P. (1972). Shear modulus and damping in soils: design eqaution and curves. Journal of Soil Mechanics and Foundations Division, ASCE, 98(7): 667-691.

Hatanaka M., Uchida A., Ohara J. (1997). Liquefaction characteristics of a gravelly fill liquefied during the 1995 Yogoken-Nanbu earthquake. Soils and Foundations, 37(3): 107-115.

Holzer T.L., Youd T.L. (2007). Liquefaction, ground oscillation and soil deformation at the Wildlife array, California. Bulletin of the Seismological Society of America, 97(3): 961-976.

Holzer T.L., Youd T.L., Hanks T.C. (1989). Dynamics of liquefaction during the 1987 Superstition Hills, California, earthquake. Science, 244: 56-69.

Horne J.C. (1996). Effects of liquefaction- induced lateral spreading on pile foundations. PhD Disseratation, University of Washington, USA.

Ishihara K., Yasuda S., Nagase H. (1996). Soil characteristics and ground damage. Special issue of Soil and Foundations, 109-118.

Iwasaki Y., Tai M. (1996). Strong motion records at Kobe Port Island. Special issue of Soil and Foundations, 29-40.

Kimura M. (1996). Damage statistics. Special issue of Soil and Foundations, 1-5.

Kramer S.L., Asl B.A., Ozener P., Sideras S.S. (2015). Effects of liquefaction on ground surface motions. Perspective on earthquake geotechnical engineering, Ansal A., Sakr M. eds, Springer, 285- 309.

Kramer S.L., Hartvigsen A.J., Sideras S.S., Ozner P.T. (2011). Site response modelling in liquefiable soil deposits. 4th IASPEI/IAEE International Symposium: Effects of surface geology on seismic motion, University of California Santa Barbara, California, USA.

Ladd R.S. (1984). Laboratory investigation of sands from Wildlife site. (unpublished).

Nagase H., Yasuda S., Tsujino S., Shinji R., Yanagihata T. (1996). Liquefaction strength characteristics of overconsolidated sand samples. Proceedings of the Eleventh World Conference on Earthquake Engineering. Paper 1089, Elsevier Science Ltd.

NEES@UCBS (2015). http://nees.ucsb.edu/facilities/wla

OYO Corporation (2014). Report of soil investigation: Sendai District and Onahama District. Report from the PreNoLin Project, Nice, France.

PARI (2015). http://www.eq.pari.go.jp/kyosin/data/pnt/sendai-g.htm

Regnier J., Bonilla L.F., Bard P.Y., Kawase H., Bertrand E., Hollender F., Marot M., Sicilia D., Nozu A. (2015). PRENOLIN Project: A benchmark on numerical simulation of 1D non-linear site effect. 2 – Results of the Validation phase. Proceeding of the 6th International Conference on Earthquake Geotechnical Engineering, Christchurch, New Zealand.

Rollins K.M., Evans M.D., Diehl N.B., Daily IIII W.D. (1998). Shear modulus and damping relationships for gravels. Journal of Geotechnical and Geoenvironmental Engineering, ASCE, 124(5): 396-405.

Seed H.B., Idriss I.M. (1970). Soil moduli and damping factors for dynamic response analyses. Earthquake Engineering Research Center. Report No EERC 70-10.

Seed H.B., Idriss I.M. (1970). Soil moduli and damping factors for dynamic response analysis. Report No EERC 70-10, University of California, Berkeley, California, USA.

Shibata T., Oka F., Ozawa Y. (1996). Characteristics of ground deformation due to liquefaction. Special issue of Soil and Foundations, 65-79.

Silver M.L., Park T.K. (1976). Liquefaction potential evaluated from cyclic strain-controlled properties tests on sands. Soils and foundations, 16 (3): 51-65.

Silvestri F. (2001). Looking for objective criteria in the interpretation of laboratory stress-strain tests. Pre-failure deformation characteristics of geometerials. Jamiolkowski, Lancellotta e Lo Presti (eds). Swets and Zeitlinger, Lisse, ISBN 9058090752.

Suetomi I., Yoshida N. (1998). Non linear behavior of surface deposit during the 1995 Hyogoken-Nambu earthquake, Special issue of Soil and Foundations, 11-22.

Taiebat M., Dafalias Y.F. (2008). SANISAND: simple anisotropic sand plasticity model. International Journal for numerical and analytical methods in geomechanics, 32: 915 – 948.

Thilakaratne V., Vucetic M. (1990). Analysis of the seismic response at the Imperial Wildlife Liquefaction Array in 1987. Proceedings of Fourth US National Conference on Earthquake Engineering, May 1990, Palm Springs, California, vol. 3.

Vucetic M. (1986). Pore pressure buildup and liquefaction at level sandy sites during earthquakes. PhD Dissertation. Rensselaer Polytechnic Institute, Troy, NY, USA.

Vucetic M., Dobry R., (1991). Effect of soil plasticity on cyclic response. Journal of Geotechnical Engineering, ASCE. 117(1): 89-117.

Vucetic M., Dobry R., (1991). Effect of soil plasticity on cyclic response. Journal of Geotechnical Engineering, ASCE. 117(1): 89-117.

Yoshida N. (2000). Liquefaction of improved ground in Port Island and its effect on vertical array record. The 12th World Conference on Earthquake Engineering, Auckland, New Zealand.

Youd T.L., Holzer T.L. (1994). Piezometer performance at Wildlife liquefaction site, California. Journal of Geotechnical Engineering, 120: 975-995.

Zeghal M., Elgamal A.W. (1994). Analysis of site liquefaction using earthquake records. Journal of Geotechnical Engineering, 120: 996-1017.

Ziotopoulou K, (2010). Evaluating model uncertainty against strong motion records at liquefiable sites. Master of Science in Civil and Environmental Engineering, University of California, Davis, USA

Ziotopoulou K, (2010). Evaluating model uncertainty against strong motion records at liquefiable sites. Master of Science in Civil and Environmental Engineering, University of California, Davis, USA.

Zorapapel G.T., Vucetic M. (1994). The effects of seismic pore water pressure on ground surface motion. Earthquake spectra, 10(2): 403-438.

VI. INTERPRETING THE DEFORMATION PHENOMENA ON SCORTICHINO DYKE

In this chapter, the case history of a dyke damaged during the seismic sequence occurred in Emilia plain (Italy) in May, 2012 is presented. An extensive in-situ and laboratory investigation have been allowed the characterization of the subsoil model. Potential liquefaction phenomena of the shallow sandy soils were also taken into account in simplified analyses. Slope stability and liquefaction potential evaluations of the embankment have been highlighted some criticisms on the foundation soils of the dyke. Effective stress analyses have been adopted for studying deeply the source of damage induced by the Emilia 2012 earthquake, taking into account also the sequence of three seismic events occurred in less than ten minutes.

VI.1. The May 20, 2012 Emilia events and effects induced on Scortichino dyke

The seismic sequence that in May 2012 struck a large area of the river Po Valley (Emilia-Romagna region, Northern Italy) triggered significant fractures and deformations in a number of riverbanks located close to the earthquake epicenter. Among them, one of the most severely damaged structures turned out to be the banks of an irrigation canal known as Diversion channel of Burana, flowing through the small village of Scortichino (Municipality of Bondeno), near the historic town of Ferrara (Figure VI.1.1).

Figure VI.1.1 – Scortichino bank stretch and location of the investigated sections (Tonni et al., 2015)

The diversion channel of Burana was designed in 1884 with a dual aim. During the winter season, the channel collects rainwater from the countryside and several small villages through a dense network of secondary channels and then it delivers the rainwater in the Panaro river. On the contrary, the direction of the water flow is reverse during the summer season when the Burana channel works as an irrigation canal for the surrounding plain.

The channel becomes a hanging canal along the Scortichino village, where an embankment was built on the purpose. Over the centuries, houses and small productive activities settled on the crest of embankment, forming little settlements along the channel where the cross section of the enbankment is wider (Figure VI.1.1).

After the 2012 Emilia earthquake, large, longitudinally-oriented ground cracks where observed along a 3 km bank stretch, causing in turn severe structural damages to a large part of the approximately one hundred houses and productive activities built on the bank crown. Many of the buildings were affected by a series of failures, such as detachments and rotations of bordering buildings, cracks in walls of houses and structural damage (Figure VI.1.2).

This surface evidences did not occur with the same intensity along the bank, but they were particularly concentrated along four sections, named a-a', b-b', c-c' and d-d' (Figure VI.1.1).

Figure VI.1.2 – Seismic-induced damages to structures on the crest embankment (Tonni et al., 2015)

As described in chapter I, the Emilia earthquake was characterized by widespread ground effects, and in particular liquefaction occurrence. The observed cracks pattern seems compatible with liquefaction phenomena, but surface evidences were not observed along the crest embankment. Nevertheless the lack of liquefaction evidences on the surface do not exclude the possible liquefaction of deep sandy layers, as shown by Kramer et al. (2011). Indeed, if the liquefiable soil is overlain by a thick non-liquefiable crust, sand boils will not form even if liquefaction does occur.

Moreover, Sinatra and Foti (2015) recently performed studies on the role of aftershocks in the liquefaction phenomena. They found that the excess pore pressure caused by the mainshock was likely fully retained when two subsequent aftershocks occurred about two and three minutes after the mainshock. This situation was caused by typical stratigraphic conditions where liquefiable layers are confined on top and at the bottom by low permeability layers, such as revealed in San Carlo and Mirabello (see chapter I.1). Also in Scortichino, the saturated soil of the dyke could be suffered the effects of the increasing of excess pore water pressure.

Also according to Facciorusso et al. (2014) the sequence of seismic events may have determined an accumulation of excess pore water pressure corresponding to a single event with an "equivalent" magnitude M_{eq} = 6.68 greater than that of the only main event.

VI.2. Field and laboratory investigation

In order to interpret the response of such soil structure during the 2012 earthquake by identifying possible damage causes as well as to suggest relevant remedial measures and seismic risk mitigation actions towards possible future earthquakes, the Emilia-Romagna regional authority launched an in-depth study carried out by a number of research groups from various Italian universities in cooperation with technical experts of the Geological, Seismic and Soil Survey Regional Department.

To this purpose, a number of geotechnical investigations were performed, in situ and laboratory tests, for defining an accurate geotechnical model. The soil investigation was concentrated around the four aforementioned cross sections of the dyke (Figure VI.2.1). A greater number of investigations were carried out around the cross section c – c' respect to the others, since the most serious damage were observed there.

The field investigation consists of 5 boreholes, during with were retrieved 29 undisturbed samples, 12 static penetration tests with piezocone (CPTU) and 4 seismic dilatometer tests (SDMT). As shown in Figure VI.2.2, penetration tests were performed both at the crest of the riverbank and at the toe, until a depth variable between 25 – 35 m. Three of the four SDMTs

were performed from the crest of the embankment, while a SDMT was perfomed at the base of the slope in the area of study D, where cracks was observed after the earthquake.

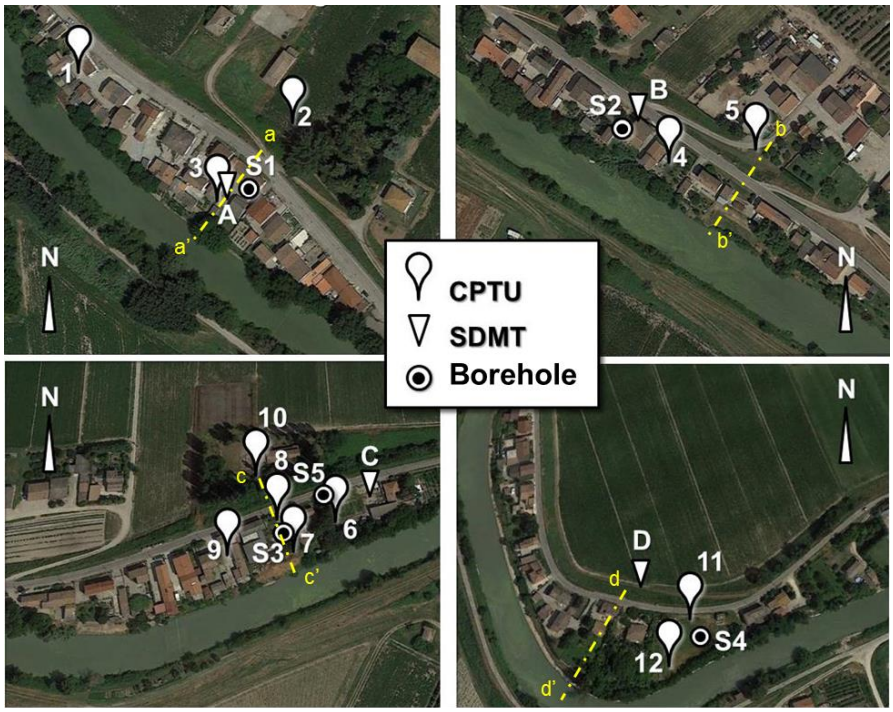

Figure VI.2.1 – Location of investigations for the four areas of study (mod. after Tonni et al., 2015)

The boreholes reached 20 – 30 m under the ground level except for the borehole S3 that was performed until to 50 m depth.

The boreholes S1 and S3 were equipped with two inclinometers until 20 m depth, while the S2, S4 and S5 with Norton piezometers in order to measure the water pressure between 12 and 20 m, 16 and 20 m and 12 and 20 m under the ground level, respectively.

Finally, in-situ permeability tests were performed using the Lefranc method in the borehole S3 at the depth of 8 and 15 m.

The undisturbed samples were subjected to several laboratory tests at University of Florence, Naples Federico II, Rome La Sapienza and Reggio Calabria. The program of laboratory investigation consisted of 12 triaxial isotropic undrained tests (TX-CIU), 4 direct shear tests (ST), 4 cyclic torsional tests (CTS) and 4 resonant column tests (RC), 5 double specimen direct simple shear tests (DSDSS) and 4 cyclic simple shear tests (CSS).

Finally, Figure VI.2.2 reports the topographic profiles of the four sections detected after the seismic events (Figure VI.2.2). The height of the dyke is variable from a minimum of 5 m in the section b-b', to a maximum of 8 m in the section d-d', where is also the widest crest of the dyke (about 55 m). Moreover, Figure VI.2.2 highlighted that the slope is more steeper along the countryside respect to the riverside.

A detailed description and interpretation of both field and laboratory tests is reported in Tonni et al., (2015).

In the following sections, the c – c' cross section will be described in detail and considered in the analysis, since it has been subjected to the most severe damage. Also the widest section d –d', will be considered for some final consideration.

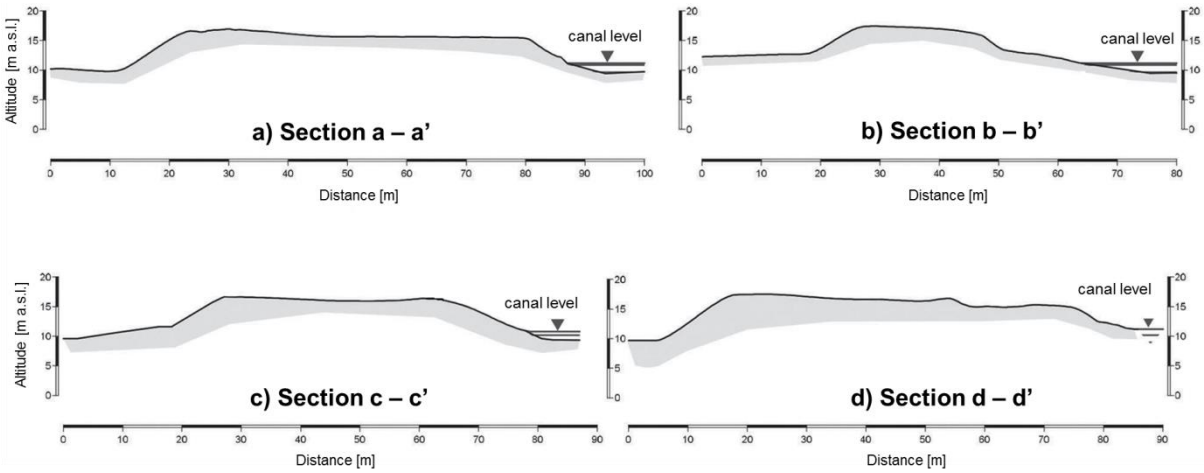

Figure VI.2.2 – Topographic profiles of the investigated cross sections (mod. after Tonni et al., 2015)

VI.3. Characterization of subsoil model

The geotechnical model of the dyke has been based on the soil investigations. The stratigraphic model is composed by four deposits, indicated for simplicity as AR, B, C, A units in the selected cross sections of the dyke (Figure VI.3.1). In the same figures are also reported the profiles of the penetrometric resistance, q_t and pore water pressure, u, from the CPTU tests and the V_S profiles resulted from the SDMT tests.

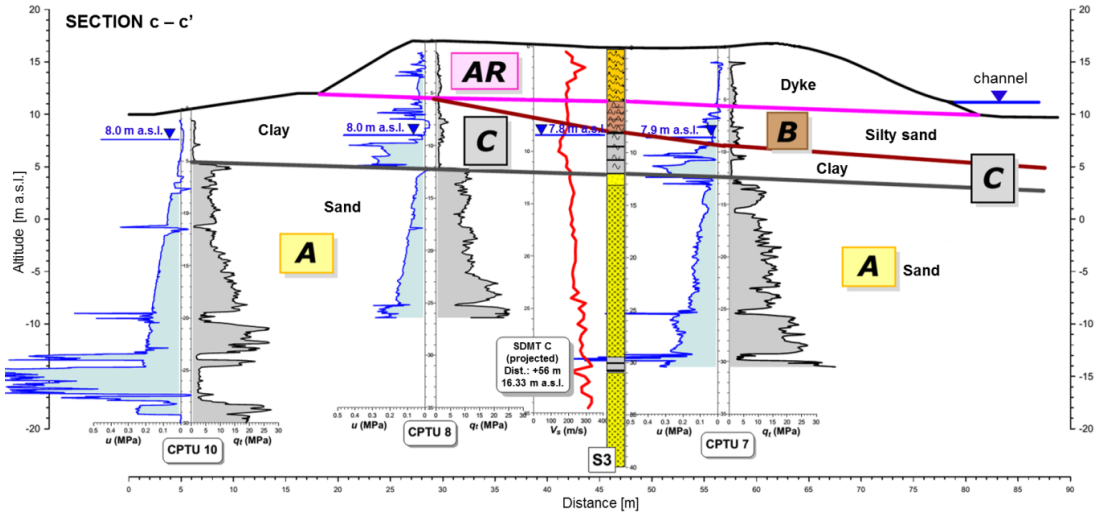

Figure VI.3.1 – Stratigraphic model of the cross section c – c' (mod. after Tonni et al., 2015)

In the stratigraphic model, the embankment is composed by subsequent layers of sand, sandy silt and silty sand, generally 10 cm thick, identified as AR unit (Figure VI.3.2a). Unit B consists of a silty sand deposit that is attributable to natural levee or river deposit from a geological point of view. Since the dyke was built with material coming from the surrounding areas, the units AR and B are basically the same material, as revealed by the grain size curves (Figure VI.3.3).

A clay or silty clay deposit is denominated unit C and, sometimes, it contains thin peat layers. This clayey soil is characterized by a plasticity index equals to 40%. As shown in Figure VI.3.1, unit C is not constantly present along the cross section of the dyke and it has a variable thick along the longitudinal axis of the dyke. Moreover, the investigation detected that the clay deposit is present only on the landside of the d – d' section (Figure VI.3.2).

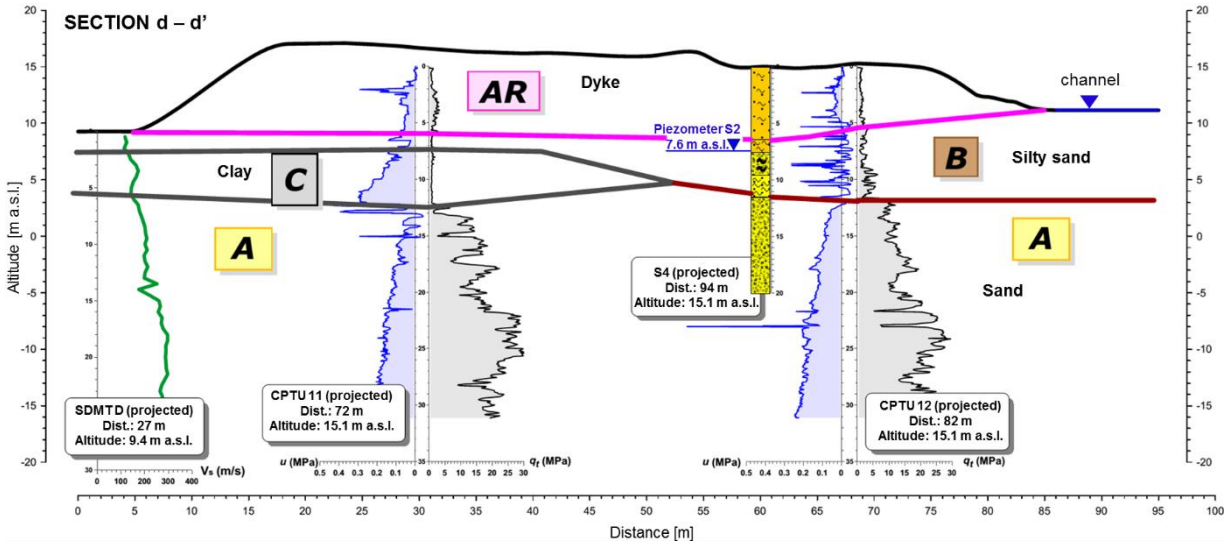

Figure VI.3.2 - Stratigraphic model of the cross section d – d' (mod. after Tonni et al., 2015)

Finally, the sand layer, unit A, is a deposit of the Po River which is typical in the whole Po plain, about 40 m thick, and it consists of coarse sand with a high degree of uniformity (Figure VI.3.4). Moreover, the deepest borehole has showed that there are thin layers of clay inside the sand deposit between 30 and 34 m from the crest of the dyke.

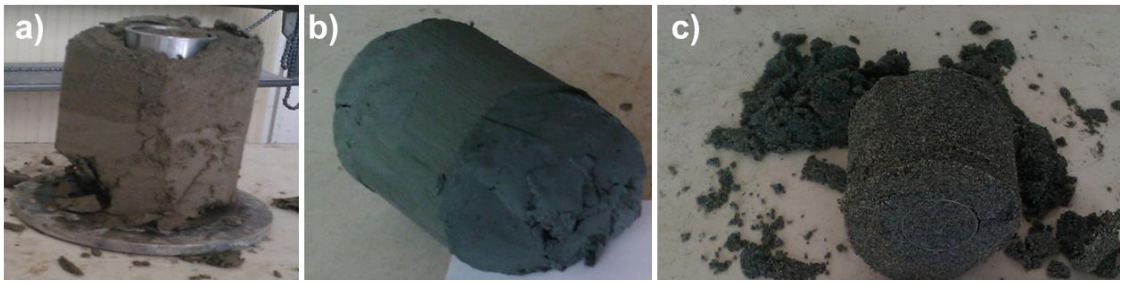

Figure VI.3.3 – Samples of silty sand - AR and B units (a), clay - unit B (b) and sand – unit A (c)

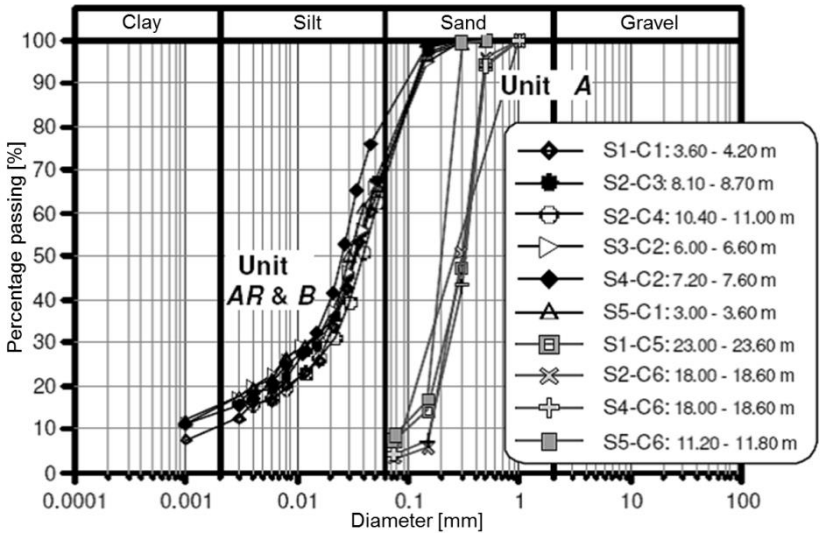

Figure VI.3.4 – Size distribution of samples from soil units AR, B and A (Tonni et al., 2015)

The resistance parameters are mainly defined on the estimates obtained from the tests piezocone, in order to have a continuous description with depth of the shear strength of the sediment. The resulting estimates were subsequently validated on the basis of the comparison with the results of the triaxial tests. From TX-CIU tests, a peak friction angle of about 34° has been computed for the AR and B units and 37° for unit A (Figure VI.3.5). The clayey unit C exhibited a lower resistance of about 22°, resulted from a direct shear test (Tonni et al., 2015).

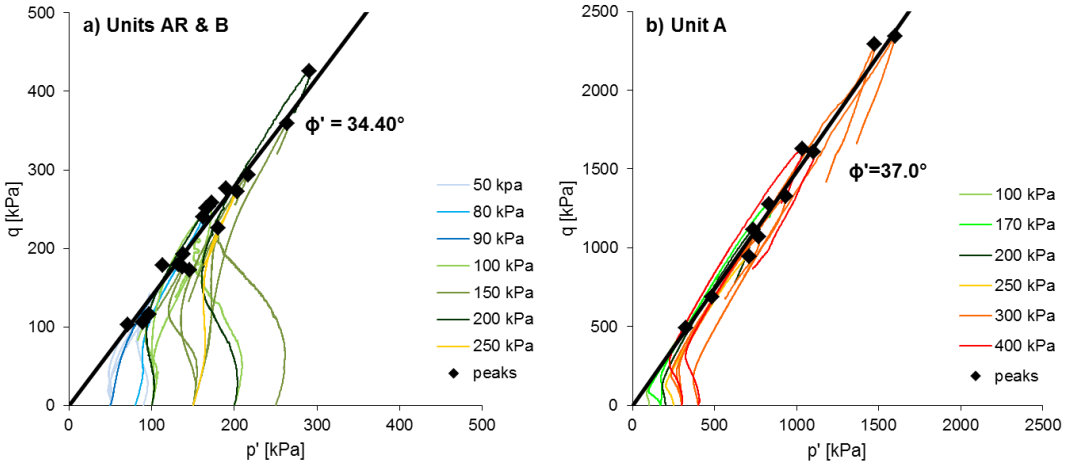

Figure VI.3.5 – Stress paths and failure envelopes from TX-CIU tests on units AR and B (a) and A (b)

To perform dynamic analyses, it was necessary to identify the depth of the seismic bedrock and the shear wave velocity profile, V_S, up to that depth. Geological studies show that the area of the Po plain is characterized by a thick layer of deformable soil, with a depth of the rigid bedrock greater than 100 m (Tonni et al., 2015). The shear wave velocity profile has been

defined by integrating the results of the SDMTs with measurements of two Cross-Hole tests carried out in the towns of Mirandola and Medolla (about 20 km distant from the area of study) which reach 130 m depth (Laurenzano and Priolo, 2013). The borehole related to the Cross-Hole tests made possible to reconstruct the stratigraphic sequence at Scortichino over 50 m deep. The deep stratigraphy essentially consists of a powerful sand layer (Unit A) resting on an alternation of centimetric layers of sands and silts (AL unit).

Figure VI.3.6 shows the shear wave velocity profiles for the two vertical related to the *d – d'* and *c – c'* sections. The adopted model provides the bedrock at 120 m depth from the crest of the embankment. This model was validated by comparing amplification functions calculated by linear analysis and the spectral ratio H/V from seismic noise recorded at Scortichino. The experimental ratio H/V shows a peak at 0.9 Hz, while the subsequent peaks are located at frequencies of 1.8 and 2.5 Hz (Figure VI.3.7). For the validation of the model have been carried out various analyzes where the position of the bedrock was varied between 90, 120 and 150 m depth below the surface level. Figure VI.3.7 shows the sensitivity of the numerical amplification function to the bedrock depth. The best agreement between the experimental and numerical amplification is found for the bedrock depth at 120 m from ground level.

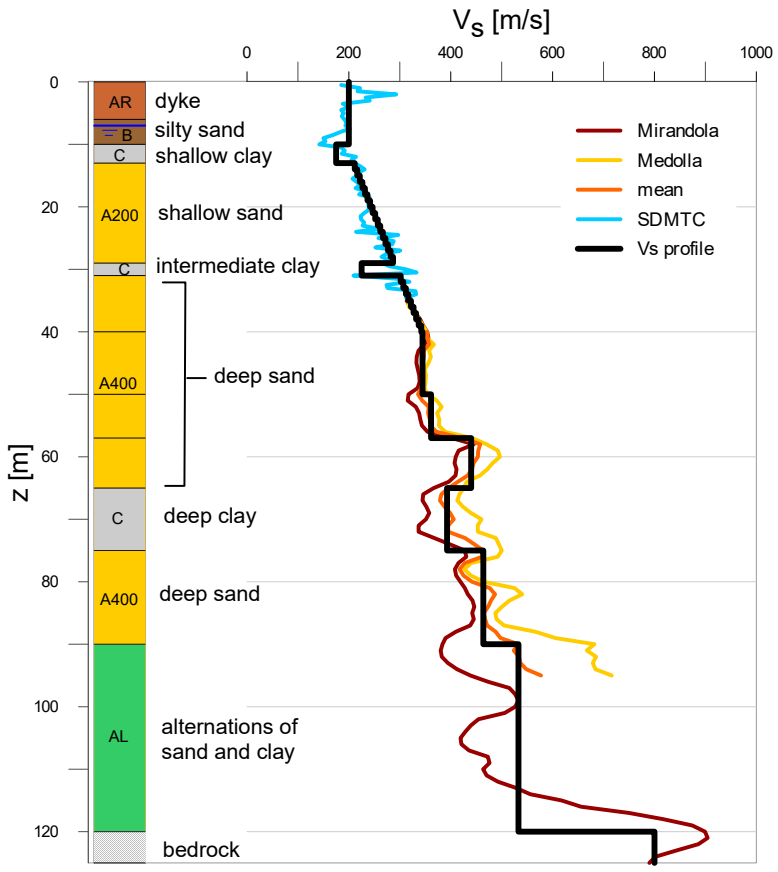

Figure VI.3.6 - Soil and shear wave velocity profile for section c-c'

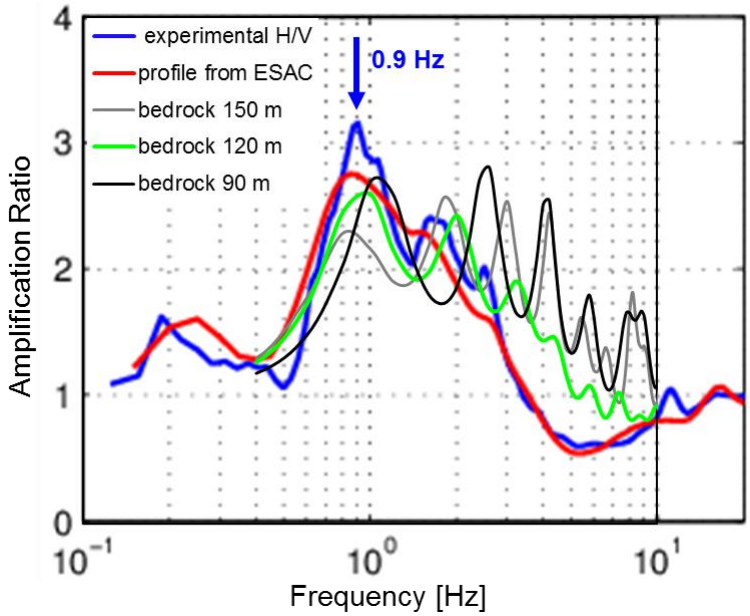

Figure VI.3.7 - Comparison of the experimental spectral ratio H/V and the amplification functions provided by the model varying the bedrock depth

The nonlinear behaviour of the soils has been defined on the results of RC and DSDSS tests (Figure VI.3.8). It can be observed that the DSDSS tests are able to reach shear strains until 10%, showing a decay of the damping ratio over that value.

The characterization of the first 30 m of sand layer has been referred to tests performed at confining pressure between 180 and 200 kPa, while the tests related to a confining pressure of 400 kPa has been used to characterize the deepest sands. The respective curve have been named A200 and A400, and this nomenclature will be adopted also in the following.

For the alternation (AL) unit, average curves between those of clay and deepest sands have been adopted. The normalized shear modulus curves have been interpreted with the Ramberg-Osgood model (1943), while the damping ratio curves have been modelled with the modified Masing criteria, as suggested by Santucci de Magistris et al. (2004).

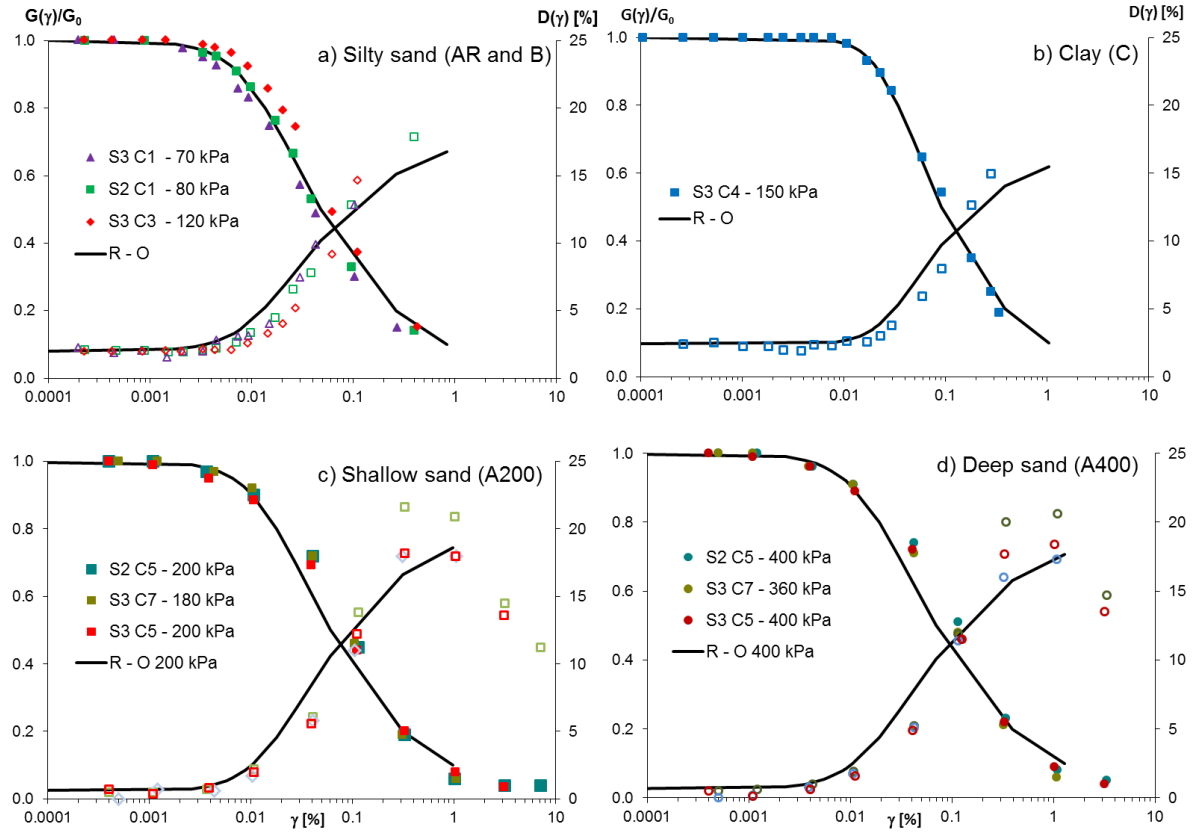

Figure VI.3.8 – G(γ)/G0 and D(γ) curves from RC and DSDSS tests for unit AR and B (a), clay (b), shallow sand (c), deep sand (d)

VI.4. Summary of simplified analyses

Analyses on slope stability and susceptibility to liquefaction of the embankment soils were performed using the results of seismic response analyses. In the next session, it will be described the input motion adopted for the seismic response analyses and the related results. Then, it will be described the seismic slope stability analyses of the embankment and the susceptibility analyses to liquefaction.

VI.4.1. Input motion

Since no acceleration records were available at the site of Scortichino, a selection of recorded accelerograms was adopted in the simplified analyses in order to simulate the 20th May event. The input motion was defined through a selection of records within the Italian database ITACA (Pacor et al., 2011), based on the magnitude (5.5 – 6.5) and distance (5 – 10 km) bins approach.

Table VI.4.1 reports the characteristics of temporal traces resulting from the research. To them was added the component parallel to the fault (FP) of the L'Aquila earthquake of April 6, 2009, recorded at the AQG station and deconvoluted at the bedrock (Landolfi, 2013), in order to consider also a near-fault event in the set of accelerograms. The selected time histories were then scaled to the PGA estimated at the site through the attenuation law proposed by Bindi et al. (2011). Figure VI.4.1 reportes the average spectrum (black line) of the selected accelerograms, showing a good agreement with that provided by the law of attenuation (grey line) over the whole range of periods.

Table VI.4.1 – Input motions

Event	date	M_w	station	Soil class	R_{epi} [km]	Component	PGA [g]
Friuli 4° after	15/09/1976	6.0	Tarcento (TRC)	A	8.5	NS	0.129
Val Nerina	19/09/1979	5.8	Cascia (CSC)	A*	9.3	EW	0.202
Val Comino	05/11/1984	5.5	Villetta Barrea (VLB)	A*	8.6	E-W	0.201
Appennino Lucano	09/09/1998	5.6	Lauria (LRS)	A*	9.8	N-S	0.165
L'Aquila	06/04/2009	6.3	Colle Grilli (AQG)	A	5.3	FP	0.308

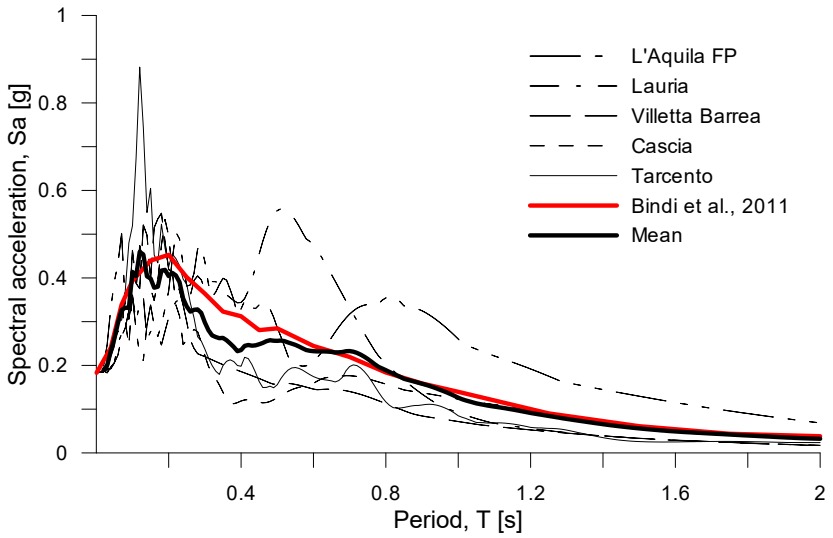

Figure VI.4.1 – Acceleration spectra of the selected input motions

VI.4.2. Seismic response analyses

Seismic response analysis were conducted assuming one-dimensional propagation of shear waves through a horizontal stratigraphy. EERA (Bardet et al., 2000) code was adopted to perform equivalent linear analysis in the frequency domain.

The bedrock was modeled as a linear visco-elastic material, characterized by V_S = 800 m/s, and damping of 0.5%. The unit weights employed for the various layers came from laboratory determinations on undisturbed samples and SDMT tests.

The results of the analyses are shown in Figure VI.4.2 in terms of profiles of the maximum values of acceleration, a_{max}, shear stress, τ_{max}, and shear strain, γ_{max}, reached during the shaking. Each diagram shows the results for the different inputs and the average profile.

All the acceleration profiles show a more or less accentuated amplification on the surface, with a_{max} ranging from 0.20 to 0.35 g. The trends of the profiles in the embankment shows some irregularities, reflecting the asynchronous motion of the silt-clay formations, B and C. Moreover, in the same layers are attained maximum values of shear strains greater than the corresponding volumetric thresholds strain, γ_v, measured in the resonant column tests, variable in the range 0.025 and 0.030%.

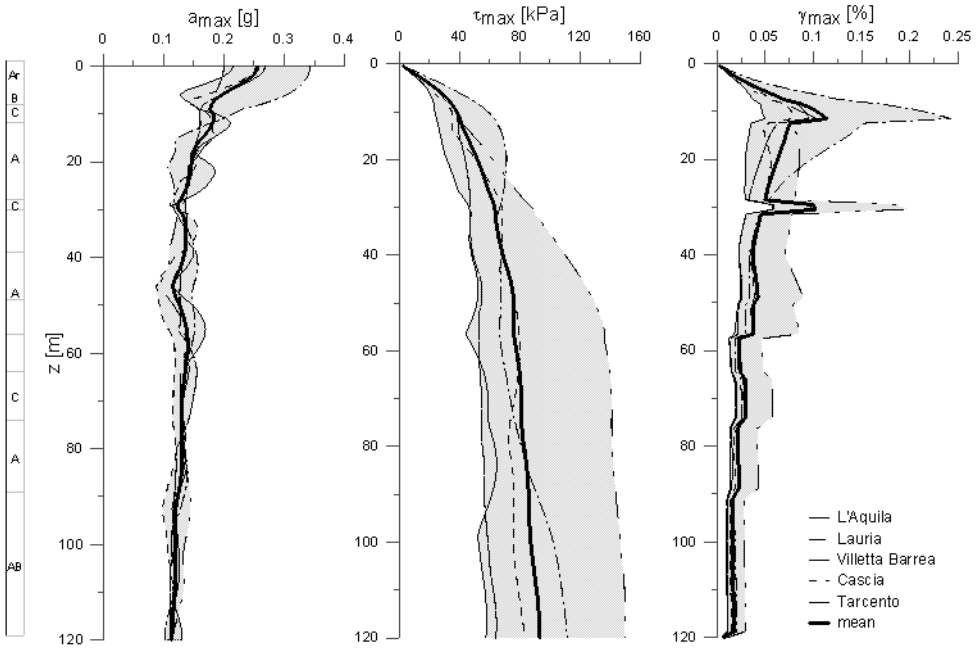

Figure VI.4.2 – Profile of maximum acceleration, shear stress and shear strain (section c – c')

VI.4.3. Susceptibility analyses to liquefaction

Tonni et al. (2015) evaluated the susceptibility to liquefaction using a simplified approach in terms of total stresses (AGI, 2005). Essentially, this approach is based on a comparison between the stress induced by seismic event at generic depth, described by the cyclic stress ratio (CSR), and the ability of soil to resist to liquefaction, represented by the cyclic resistance ratio (CRR).

CSR values with depth were obtained by the maximum shear stress profile of the seismic response analysis. As described in chapter II, conventionally, the irregular shear stress history is converted in a cyclic uniform load of amplitude equals to 65% of the maximum stress.

With reference to the CRR values, they were carried out with parallel independent estimates based on the profiles of the shear waves velocity, Vs, horizontal coefficient, K_D, both obtained from SDMT tests, and on the penetrometric measures. A further calculation of CRR was based on the results of the CSS tests. In this case, the CRR is computed on the experimental cyclic resistance curve for a number of equivalent cycles correspondent to the earthquake magnitude of 6.1 which is characteristic of the 20th May mainshock.

The results of the analyses are reported in terms of safety factor, FS_{liq}, defined as ratio between cyclic resistance ratio and stress ratio. Figure VI.4.3a reportes the results of the analyses carried out with the Andrus and Stokoe (2000) method, related to the shear wave velocity profile of the SDMT C test. Figure VI.4.3b shows the results of the analyses on four CPTU tests located around the section c – c'. Results of the analyses on CPTU show the presence of several FS_{liq} <1 along the vertical profile, especially in the silty sand layer of the unit B. Conversely, contradictory results come from the laboratory CSS test and the V_S profile regarding to the sand layer of the unit A.

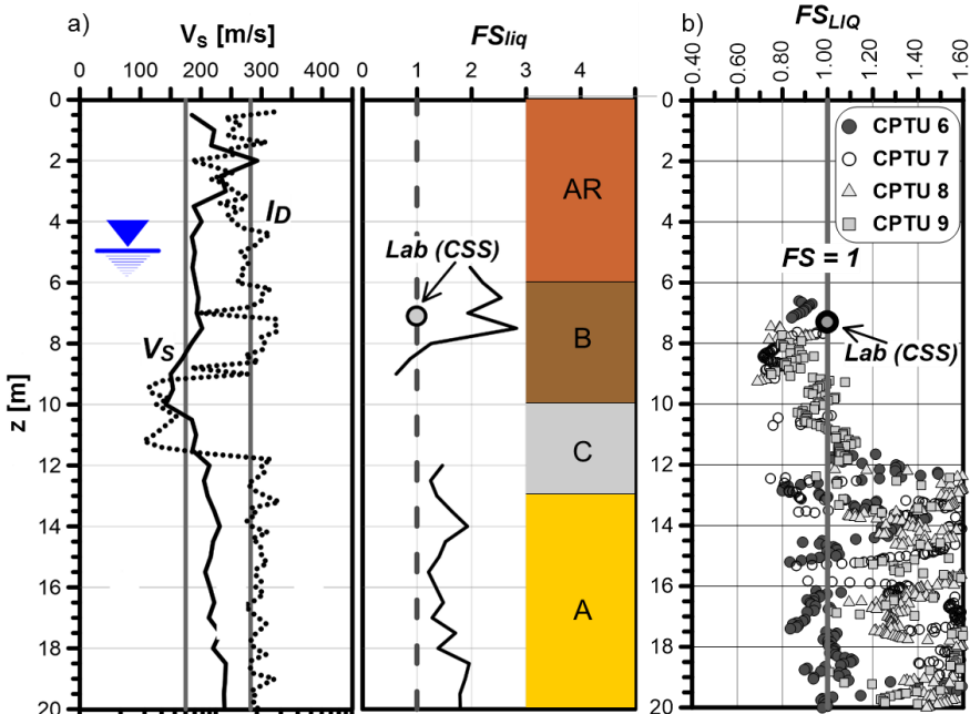

Figure VI.4.3 – Liquefaction analyses based on Vs profile from SDMT (a) and CPTU test (b) (mod. after Tonni et al., 2015)

VI.4.4. Seismic slope stability analyses

The seismic stability analyses were performed with both pseudo-static approach, using the SLOPE/W software (GEOSLOPE International Ltd, 2007), and displacement method (Newmark, 1965). In both cases, the seismic actions were determined from the local seismic response analyses already described.

For such of simplicity, the water table was assumed coincided with the water level in the channel, equals to 11.2 meters above sea level, for the analysis of riverside slope, while it was assumed equals to 8 m for that of landside slope as indicated by piezometer measures. A uniformly distributed load was placed on the crest of the embankment for taking into account the buildings founded there, but the overload road was neglected due to the low service level of the local road (Figure VI.4.4).

Static analyses confirmed the stability of the structure before the earthquake, with a factor of safety greater than unity.

In the pseudo-static analyses, the equivalent seismic coefficient, $k_{h,eq}$ was determined with reference to the average profile of the maximum acceleration obtained from the seismic response analyses. In details, the equivalent seismic coefficient, $k_{h,eq}$, was computed as

$$k_{h,eq} = \beta \frac{a_{\max,eq}}{g} \qquad \text{(VI.4.1)}$$

where $a_{max,eq}$ was the average value along the height of the landslide mass and β is a coefficient linked to torelable displacements. Since the high degree of urbanization of the embankment, β was assumed equals to 0.5 corresponded to displacements of 2 – 3 cm. Morgenstern and Price (1965) method provides a factor of safety of 1.003 and 1.159 for the land and riverside slope analysis, respectively (Figure VI.4.4). Due to the greater steepness, the landside slope is characterized by a safety factor lower than that on the riverside.

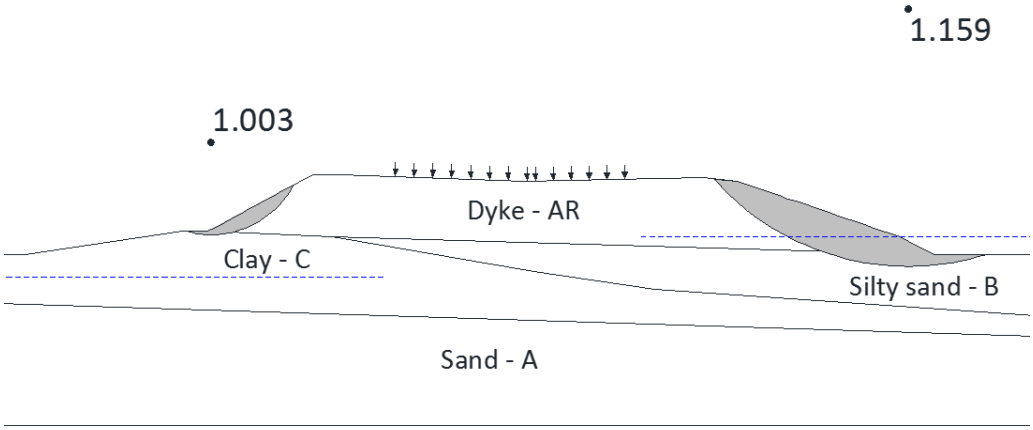

Figure VI.4.4 – Pseudo-static analyses of both slopes of the dyke

Moreover, displacement analyses were performed using the Newmark method. According to a pseudo-static approach, the critical acceleration, a_c, and the associated critical failure surface were preliminarily determined. Assimilating the slope at an overposition of horizontal layers subject to vertical propagation of S - waves, an equivalent accelerogram, $a_{eq}(t)$, was obtained as the ratio of the time history of shear stress, coming from seismic response analysis, and the total vertical stress at the base of the landslide mass.

Figure VI.4.5 shows the values of accumulated displacements along the riverside and landside of the dyke, calculated for the five selected seismic signals. The calculated displacements are compared with the estimates obtained by the application of some empirical correlations (Rampello et al., 2010, for deformable soil; Ausilio et al., 2007, and Madiai, 2009, for rock and soil) for predicting the displacements induced by the earthquake. As expected, the displacements of the landside slope are systematically higher than those calculated on the opposite side.

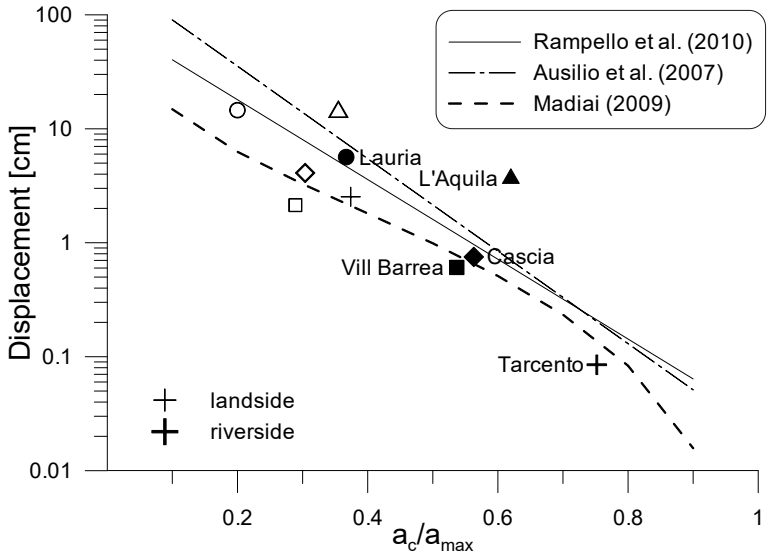

Figure VI.4.5 – Displacement computed on both riverside and landside of the dyke and relative prediction by different empirical correlations

VI.5. Advanced analyses

Simplified analyses have excluded severe damage due to the stability of the slopes of the dyke, while local liquefaction phenomena are not excluded. Consequently, a deep study is necessary to reconstruct the condition of the dyke at the time of the earthquake. First of all, it is necessary to define the effective stress state inside the embankment in order to define clearly the saturated soil which are susceptible of liquefaction.

VI.5.1. Effective stress state inside the embankment

Filtration analysis with the code SEEP/W (GEOSLOPE International Ltd, 2007) has been possible to reconstruct the system of pore pressure within the embankment section (Figure VI.5.1), consistent with the piezometric measurements performed within the sands deep. The high degree of saturation of the undisturbed samples (> 95%), taken at small depth from the ground level, allowed to develop the analysis only with reference to the saturated permeability of soils. Hydraulic conductivity of the soils has been deducted from field investigations, both directly from Lefranc tests and indirectly using empirical correlations with CPT tests.

The boundary conditions are constituted by the free surface in the channel and the no-flow condition along the perimeter of the section, while the piezometer level equals to 8 m above sea level has been applied along the opposite side of the cross section, as indicated by the piezometric measures (Figure VI.3.1).

The presence of the channel triggers a steady-state filtration inside the embankment, but the thick layer of clay (unit C) above the sands of the Po (unit A) determines a storage basin of water in the sand layer silty (unit B).

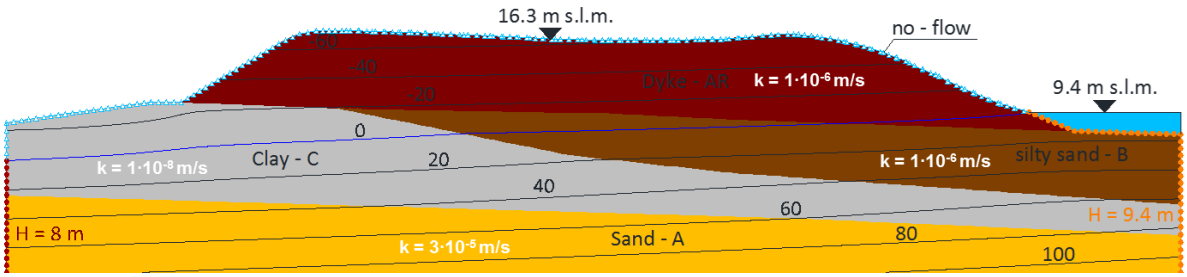

Figure VI.5.1 - Simulation of the pore pressure inside the embankment section (isobars in kPa)

This configuration allows to identified the soil potentially liquefiable and make some first consideration about the observed damage. Indeed, the saturated soils are overlain by a non-liquefiable crust of significant thickness, at least 7 m thick in correspondence of the crest.

According to the existing relationship between the thickness of the liquefiable soils and the crust and the liquefaction manifestations at the surface, it appears that the non-liquefiable crust is too thick, thus sand boils could not be occurred, even if liquefaction happened in the depth layers (Figure VI.5.2).

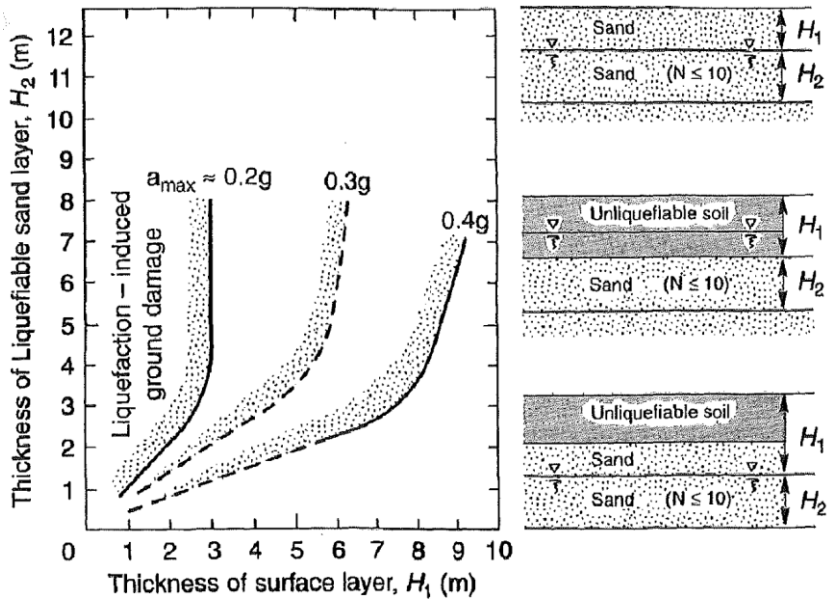

Figure VI.5.2 – Relationship between thickness of liquefiable layer and thickness of overlying layer at sites for which surface manifestation of liquefaction were observed (Kramer et al., 2015)

VI.5.2. Preliminary one-dimensional effective stress analysis

Dynamic analyses have been carried out by total and effective stress analyses through the non-linear code SCOSSA. The stratigrafic profile is the same adopted in the analyses of the previuos sections, only the thick of the first deposits has been adapted to the vertical section at the edge of the riverside (Figure VI.5.3 a).

With reference to the input motion, the five selected accelerograms have been further processed following the criteria suggested by Athanasopoulos-Zekkos and Saadi (2012) for selecting reference ground motions for liquefaction analysis of earth levees. The NS component of the mainshock of Irpinia earthquake (11/23/1980), recorded at the Lauria station was finally selected and adopted as input motion in the analyses (Figure VI.5.3).

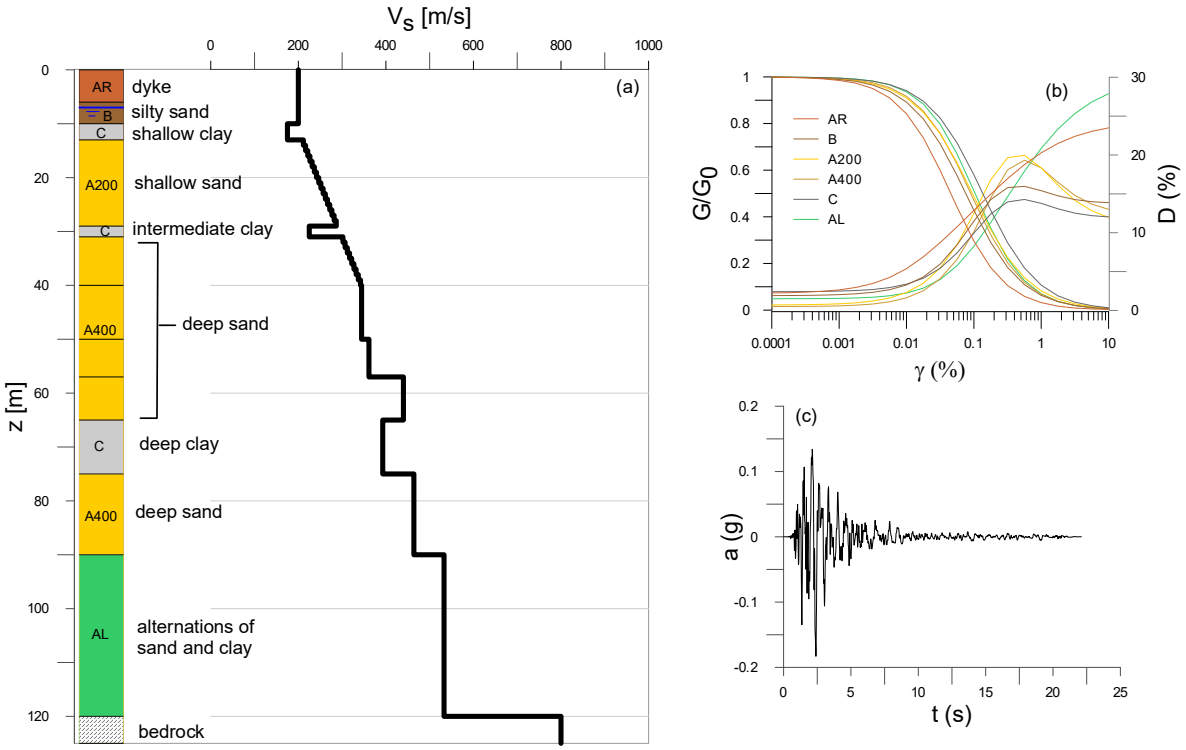

Figure VI.5.3 - Soil profile (a), stiffness and damping vs strain (b), and reference input motion (c)

Figure VI.5.3b shows the normalized shear modulus and damping ratio curves, obtained from resonant column and double specimen direct simple shear tests and adopted to simulate the non-linear soil behaviour. The shear modulus reduction curves were analytically fitted by the MKZ model, modified according to the procedure for strength compatibility proposed by Gingery and Elgamal (2013), widely described in chapter IV. As an example, Figure VI.5.4 reports the analytical curves obtained for the silty sand deposit (B).

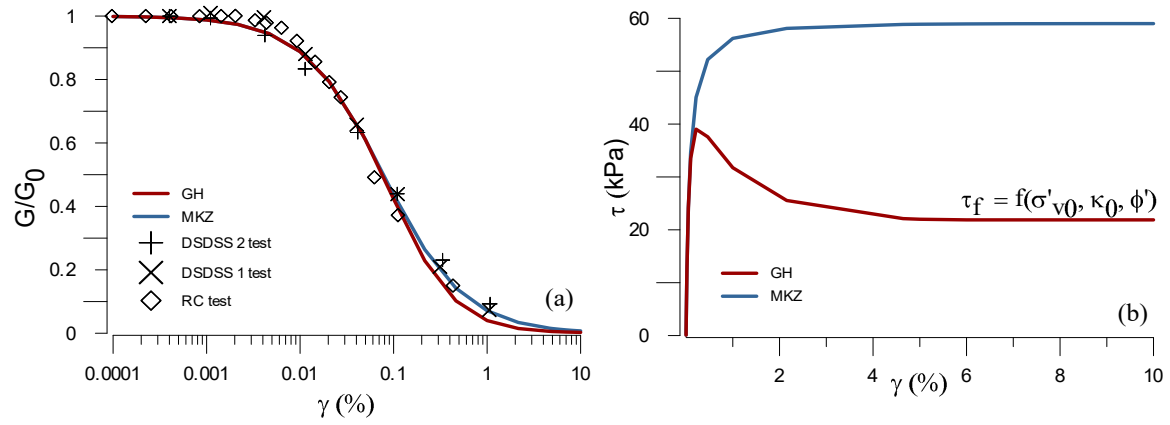

Figure VI.5.4 - Shear modulus reduction curve (a) and backbone curve (b) reproduced by MKZ and Gingery and Elgamal (2013) models in the silty sand deposit B

Data from cyclic simple shear tests (CSS) were used to calibrate the parameters of the PWP model for silty sand (B) and sand (A) deposits. Figure VI.5.5 reportes the experimental results and the modelled curves used in the analyses. The relationship between the pore pressure ratio and the damage parameter was defined as the best fitting function through the available laboratory results. The number of cycles at liquefaction, N_L, was established assuming that liquefaction occurs at a pore pressure ratio ru=0.90. Since the threshold shear stress ratio was not clearly defined by the experimental data, SR_t was estimated from the backbone curve as that corresponding to the volumetric threshold strain measured in RC tests (Figure VI.5.6). The parameter α was finally determined from the slope of the cyclic resistance curve in the logarithmic plot (Figure VI.5.5a).

For the clay unit (C), the cyclic resistance curve was not measured in the laboratory, so it has been estimated by averaging from literature data on clays (Boulanger and Idriss, 2006). The threshold value, SR_t, was defined from the volumetric threshold strain measured by resonant column tests, as described for unit A and B. The pore pressure ratio relationship has been defined on the result of simple cyclic shear test carried out on the sample of the unit B with maximum clay fraction. It can be observed that the accumulation of excess pore pressure is characterized by a different shape respect to that typical of the sandy materials (Figure VI.5.5b). The calibrated parameters for the three soil deposits are reported in Table VI.6.1.

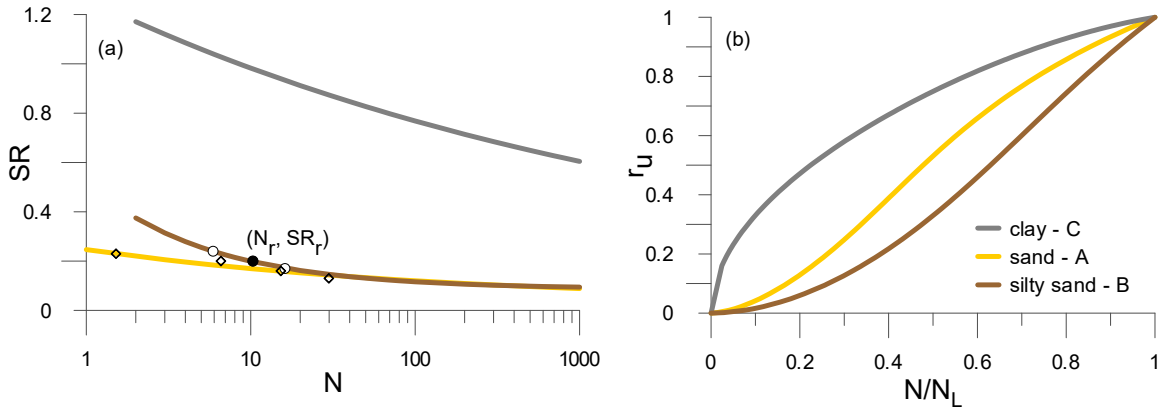

Figure VI.5.5 - Cyclic resistance curves (a) related pore water pressure relationship (b)

Table VI.5.1 – Parameters of the pore water pressure model

Soil deposit	α	SR_t	SR_r	a	b	c
Silty sand - B	1.71	0.087	0.176	0.902	0.534	0.098
Clay - C	8.548	0.075	0.940	1.076	0.513	-0.076
Sand - A	5.20	0.032	0.159	0.702	0.613	0.298

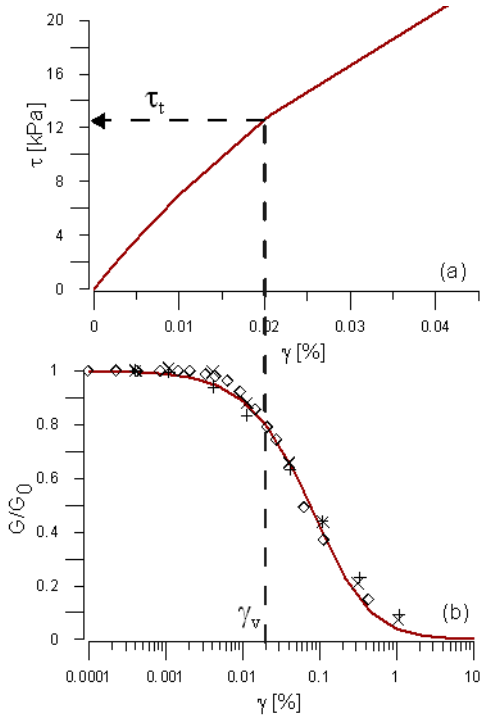

Figure VI.5.6 - backbone curve τ - γ (a) and shear modulus reduction curve (b) for defining SR_t

The results of the coupled analysis are plotted in Figure VI.5.7 in terms of maximum acceleration, shear strain and shear stress profiles (green lines). The distribution of the maximum strain shows the highest value at a depth of 15.5 m, which corresponds also to a peak acceleration. In the coupled analysis the profiles of a_{max} and γ_{max} show two singular spikes at 13.5 m and 25 m in the sand (A) layers, which are not observed in the decoupled analysis. Excess pore water pressure is significant between 7 and 30 m depth, but liquefaction condition is reached only in the sand layer (A). According to the PWP model, liquefaction triggers in sand deposit (A) after 3.2 s from the beginning of the seismic event, while in the silty sand deposit (B) a maximum pore pressure ratio of 0.47 is reached (Figure VI.5.8). The excess pore pressure ratio in Figure VI.5.7 show that only the first seconds of the input motion are meaningful to the accumulation of excess pore water pressure.

Similarly, an effective stress analyses have been performed also for the d – d' section, considering a vertical soil column in correspondence of the borehole S4 (Figure VI.3.2).

The results are shown in Figure VI.5.9. Excess pore water pressure is significant between 7 and 30 m depth, but no liquefaction conditions are reached conversely from the c – c' section. Compared to total stress analysis, also in this case, the profiles of a_{max} and γ_{max} show two singular spikes at 10.9 m and 15.1 m, respectively in the silty sand (B) and sand (A) layers.

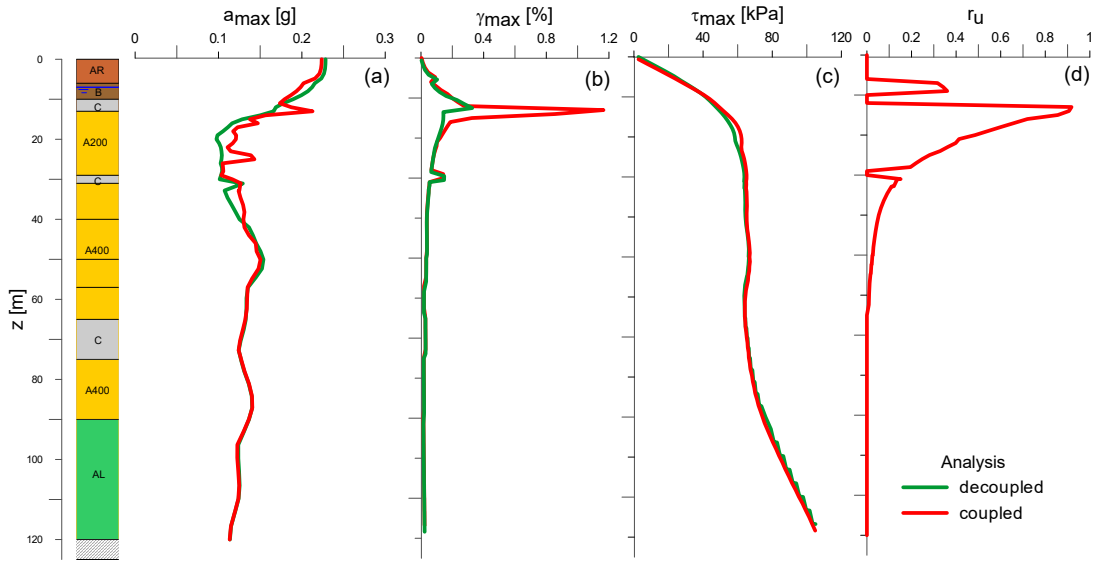

Figure VI.5.7 - Vertical profiles resulting from coupled and decoupled dynamic analyses on c – c' section

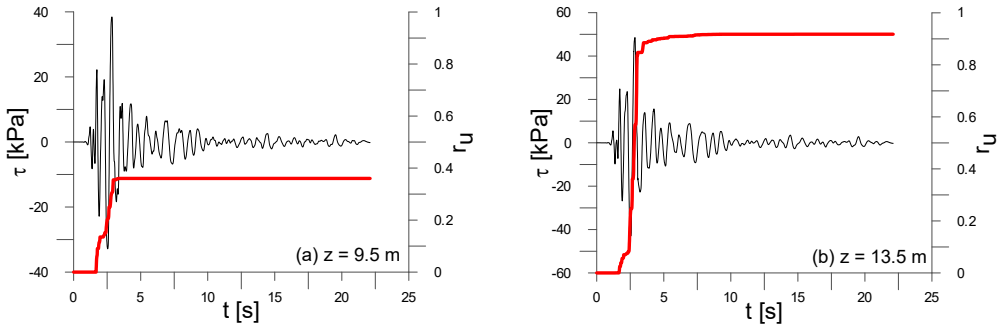

Figure VI.5.8 - Shear stress and excess pore pressure ratio histories at 10.9 m (a) and at 15.1 m (b) from effective stress analysis

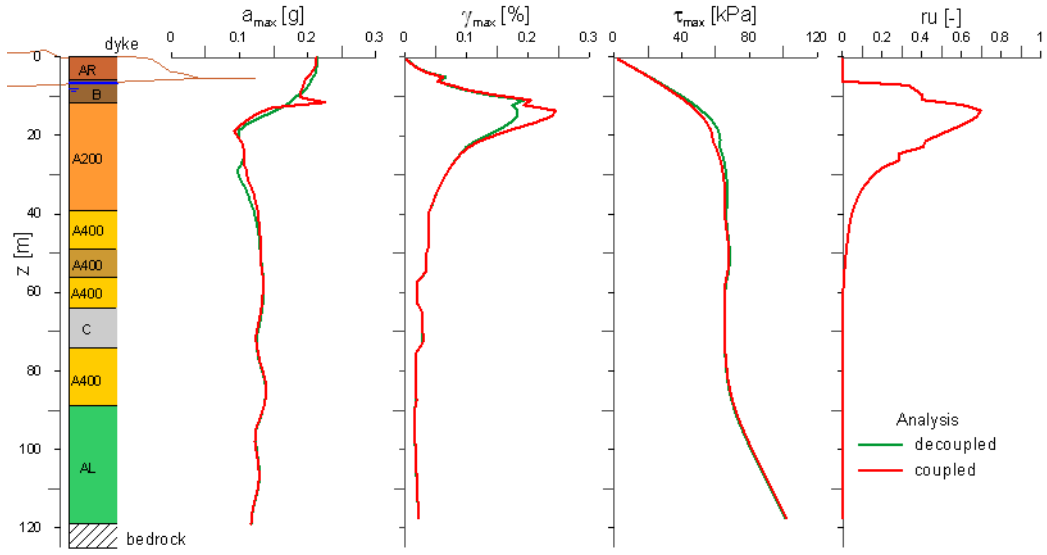

Figure VI.5.9 - Vertical profiles resulting from coupled and decoupled analyses on d – d' section

To sum up, preliminary effective stress analysis seems to indicate a significant increase of the pore water pressure inside the sand deposit (A). Such hypothesis about the damage source can be verified only through a reconstruction of the actual earthquake that struck the dyke. To this purpose, a definition of the most notable shocks of the 20th May 2012 is performed in the next paragraph. In detail, an input motion comprehensive of the three main shocks of the May, 20 will be considered in order to assess also the role of aftershocks in the observed damage.

VI.5.3. Ground motions of May 20th, 2012

The mainshock of the Emilia 2012 seismic events occurred on May 20th, 2012 at 02:03:53 UTC time (04:03:53 local time). The mainshock was followed by two strong aftershocks of local magnitude, M_L, 4.8 and 5.0, respectively (Table VI.5.2). The first aftershock occurred two minutes and half after the main event, while the second aftershock occurred one minute after the first.

Table VI.5.2 – Main seismic events of May 20th, 2012

Event	Time (UTC)	M_L	Epicenter coordinates		Depth [km]
			Lat [°]	Long [°]	
Mainshock	02:03:53	5.9	44.90	11.26	9.5
I aftershock	02:06:26	4.8	44.91	11.16	4.3
II aftershock	02:06:28	5.0	44.81	11.27	6.1

The station of the Italian Strong Motion Network (DPC) located in Mirandola recorded the strong motion and the subsequent aftershocks. This station is named MIRANDOLA (NAPOLI) in the Italian accelerometric archive (ITACA, 2016), because it is located in Napoli Street of the Mirandola Municipality, and it is identified by the station code MRN. Such station recorded the highest PGA during the mainshock of May 20th, 2012 as shown in Figure VI.5.10, since it is very close to the epicenter (Lat = 44.8782°, Long = 11.0617°). The same station recorded also the subsequent shocks which can be downloaded from the ITACA website. Unfortunately, the aftershocks recorded at the MRN station are still unprocessed on the ITACA website. Moreover, Figure VI.5.11 shows that the same data are provided for the first and the second aftershock. This acceleration time history lasts more than four minutes and this indicates that it is comprehensive of both the aftershocks and, probably, of other smaller events.
Remembering that the aim of the study is to define an input motion that includes the main three shocks of May, 20th, it has been necessary to work on the unprocessed data for uniformity, even if only the processed data of the mainshock are available on the ITACA

website. Thus, the unprocessed accelerograms of the two horizontal components of the mainshock and of the aftershocks have been downloaded from the ITACA website.

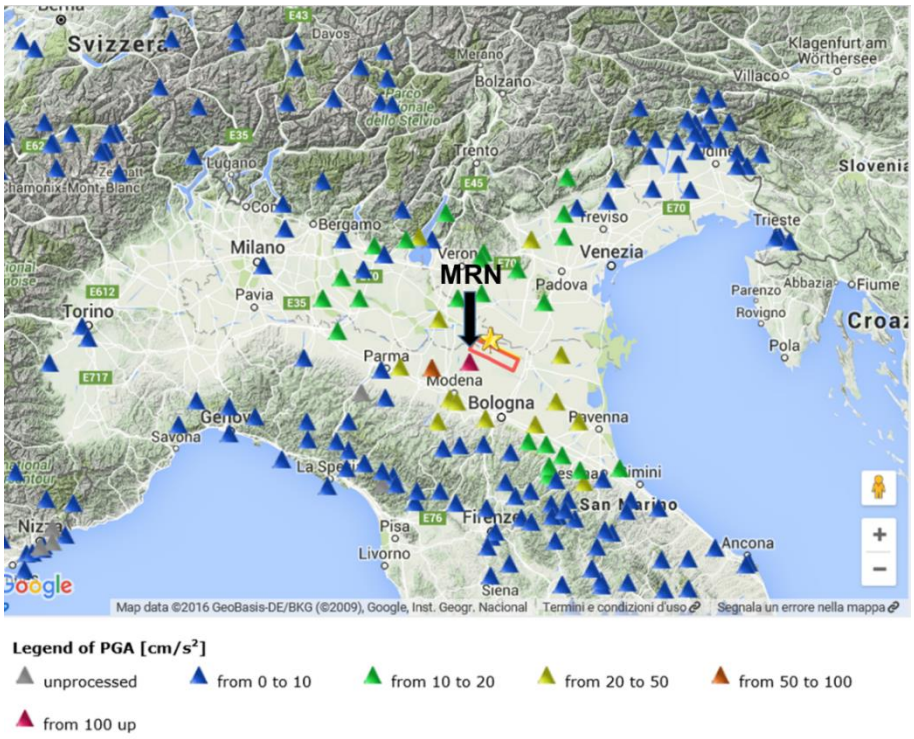

Figure VI.5.10 – Distribution of the PGA recorded by the accelerometric stations after the mainshock of May, 20th in Northern Italy

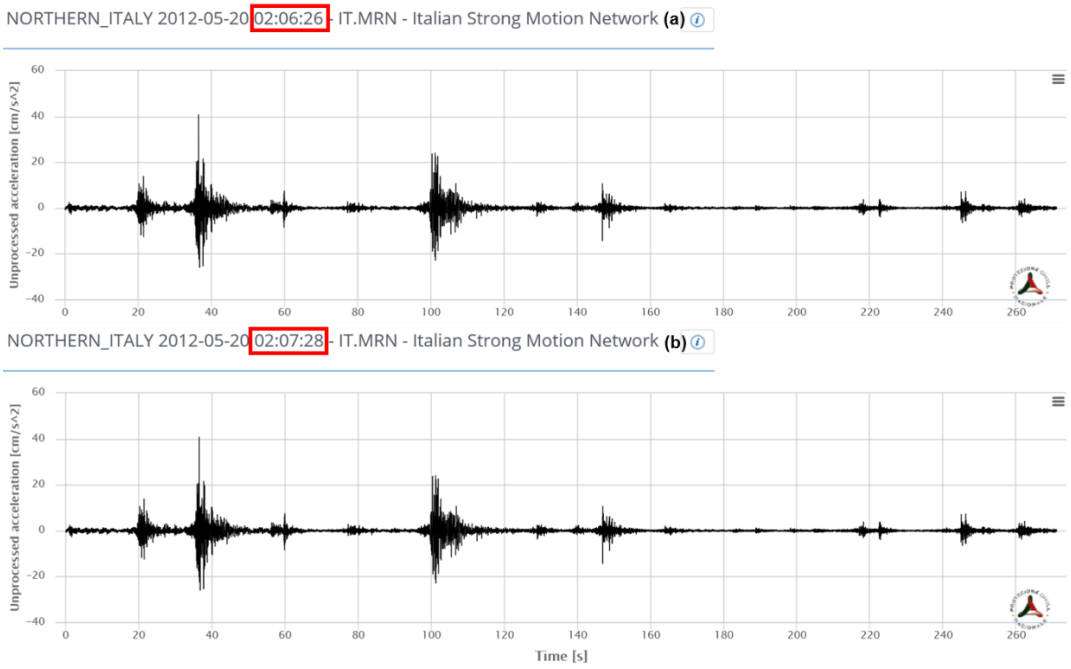

Figure VI.5.11 – EW acceleration time histories provided for the first (a) and the second (b) aftershock by the ITACA website (ITACA, 2016)

The original records of the station have been reconstructed by plotting one after one the unprocessed records of the mainshock and the aftershocks. This procedure has been possible since station was continuously recording, and the initial time of each shock is known (Table VI.5.2). From this elaboration it emerged that the time histories of the mainshock and the aftershock have an overlapping time interval (Figure VI.5.12). In fact, a perfect overlap of the time histories between 150 and 175 s was observed by reversing the sign of the aftershock record for both components.

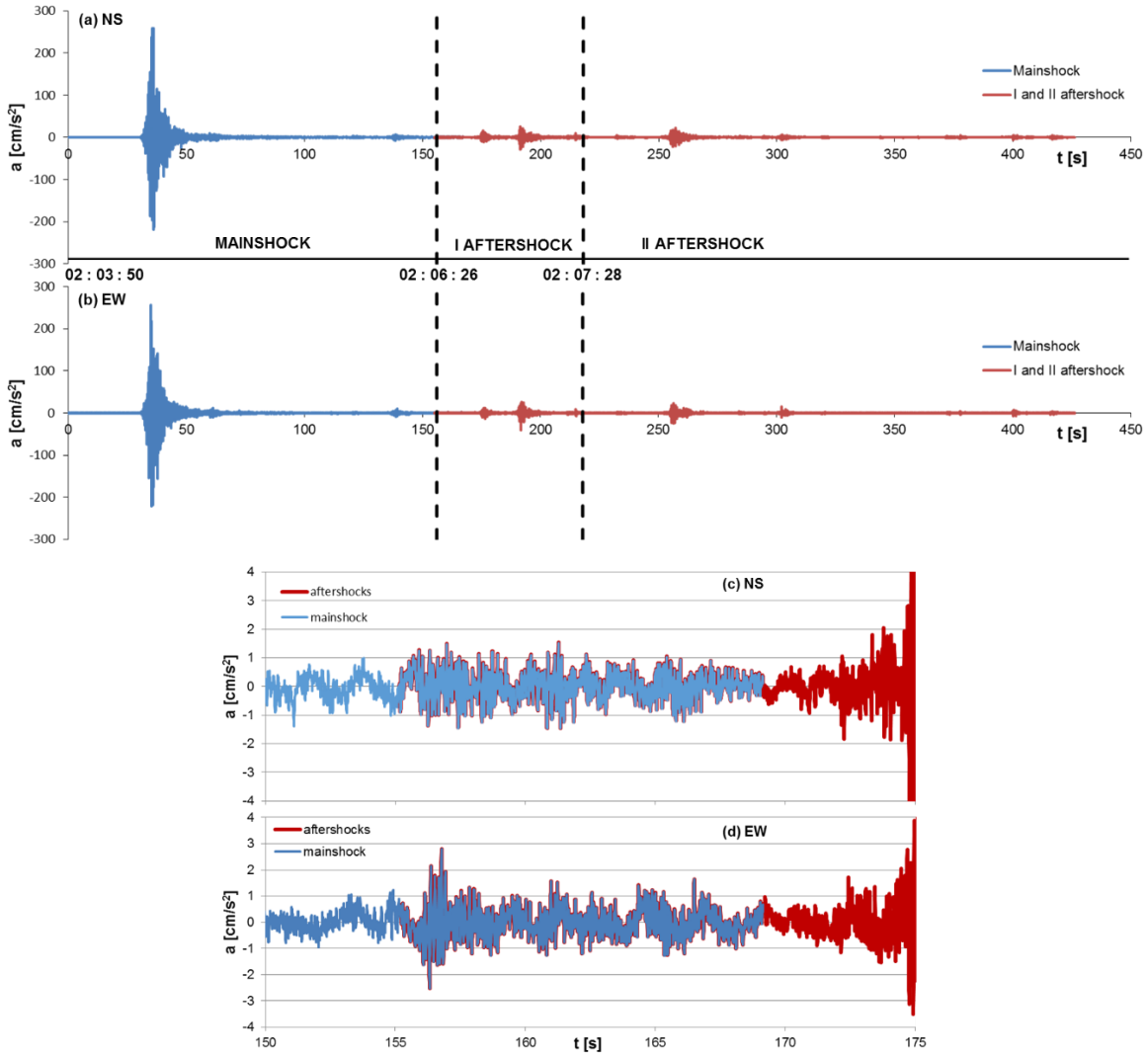

Figure VI.5.12 – Unprocessed NS (a) and EW (b) components of the main shocks of May, 20th and focus on the overlapping time intervals (c-d)

These records cannot be used as input motions in the analyses, because the station is located on a class C site, with a $V_{S,30}$ = 208 m/s according to the EC 8 code. Indeed, as widely described in sec. II.1, the 2012 seismic sequence interested an alluvial plain with a significant

depth of the seismic bedrock, so that the closest class A stations are located too far from the epicenter to provide useful input motions for the analyses.

To overcome this problem, the record in Figure VI.2.12 has been split into three events; each one of that has been de-convoluted to the bedrock and, finally, the de-convoluted outcrop motion has been scaled to account for the epicentral distance of each shock.

The original record has been split giving the three records separately. Each of them has been corrected with the same procedure applied to the processed records of the mainshock, i.e. each record has been baseline-corrected with a linear function and corrected with a 2th order Butterworth bandpass filter between 0.04 and 40 Hz.

The EW and NS components are considered in the following, since the plot of the acceleration motion in the NS –EW plane does not highlight the same preferential direction for the three seismic events (Figure VI.5.13).

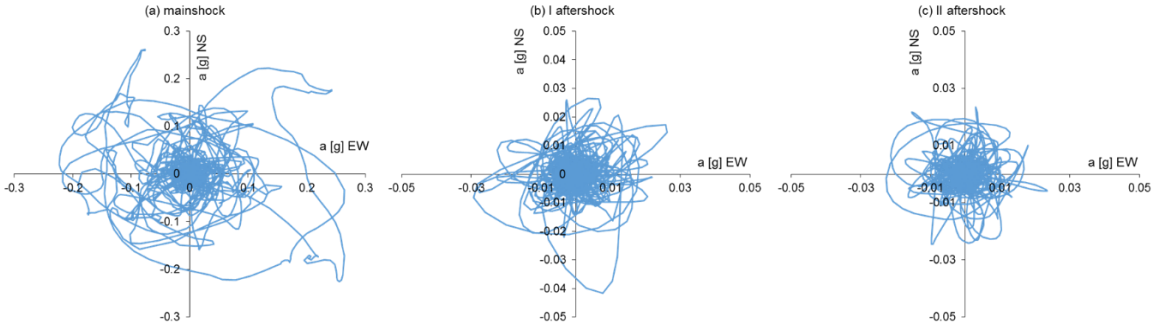

Figure VI.5.13 – Acceleration paths for the (a) mainshock, (b) first aftershock and (c) second aftershock

VI.1.1.1. *De-convolution of surface motion*

A de-convolution procedure requires the definition of the subsoil model under the recording station. The MRN station is located along Napoli street in Mirandola municipality, very close (≈100 m) to the site where a downhole seismic array has been deployed after the earthquakes (Figure VI.5.14). During the deployment of the array, a cross-hole test was carried out until 125 m depth. Figure VI.5.15 reports the stratigraphic sequence and the shear wave velocity profile obtained from the cross-hole test. This configuration has been adopted for defining the subsoil model under the recording station. Since no site-specific laboratory data are available, the shear modulus reduction and damping curves were assumed to be the same of the soil deposit at Scortichino.

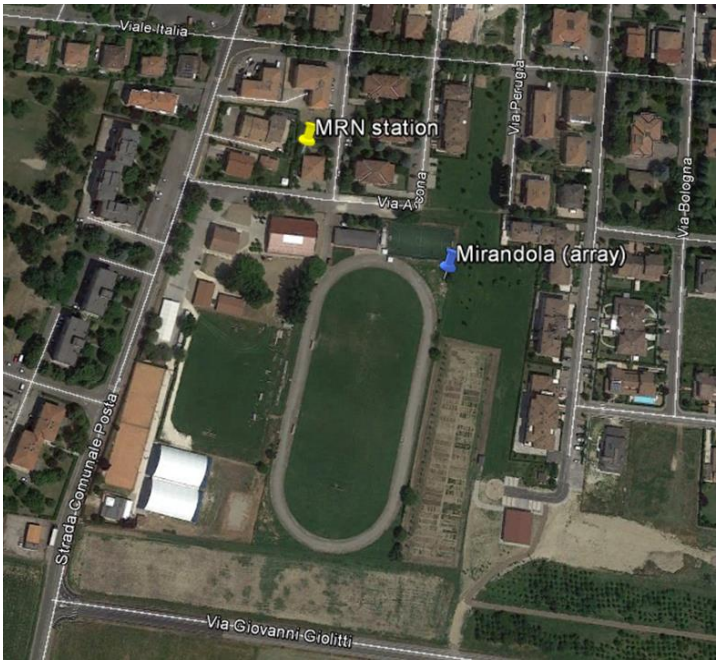

Figure VI.5.14 – Location of the MRN station and array site in Mirandola

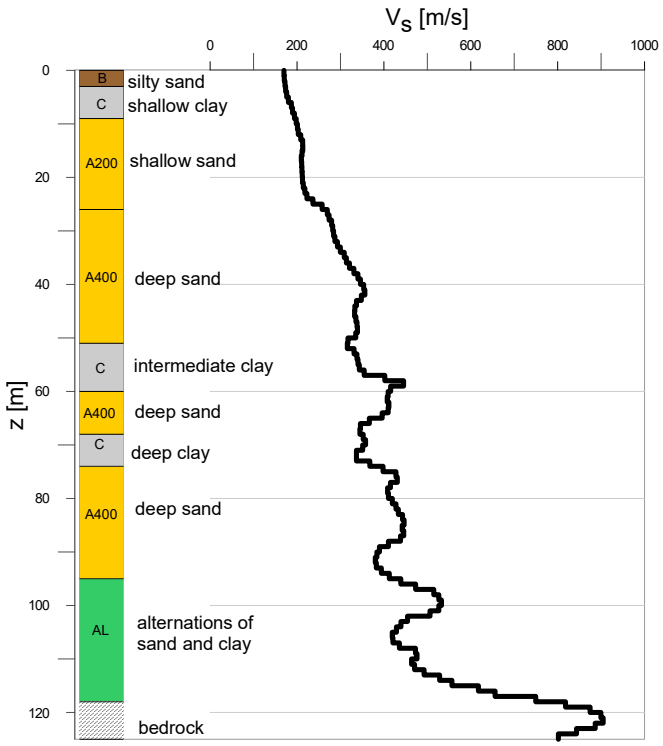

Figure VI.5.15 – Subsoil model for de-convolution analyses

De-convolution consists of assigning a recorded ground motion at the surface of a 1D soil column and using a linear equivalent analysis to calculate the acceleration time history at a point beneath the ground surface.

For soft sites, Silva (1988) measured the coherence in order to provide an estimate of goodness between the simulated propagated motion and that recorded at surface. The results of Silva (1988) research shows that frequency content beyond 15 Hz should be filtered out prior to de-convolution, since the coherence falls off at 15 Hz between the recorded surface motion and that analytically propagated to surface. For this reason, a low pass (LP) filter at 15 Hz has been applied to the recorded surface motion to be used for the de-convolution analysis. Moreover, from the coherence analysis it appears that the maximum power that is propagated as normally incident shear waves is about 75%. The remaining energy may be due to scattered waves and perhaps to P-waves. This has significant implications on the non-linear behavior of the soils. In particular, attempting to de-convolute the total surface motion as vertically propagating shear waves may result in too much energy predicted at depth, leading to excessive estimates of modulus-reduction and mobilized damping. The overall effect is to overestimate the motion at depth that is required to produce the total observed surface motion (Silva, 1988).

The guidelines for equivalent-linear de-convolution proposed by Silva (1988) were summarized by Markham et al. (2015) in the following steps:

(1) a low pass (LP) filter was applied to the recorded surface motion to be used for the de-convolution analysis at 15 Hz and scaled by 0.87; SeismoSignal was used to perform a 4th order, LP Butterworth filter;
(2) the filtered and scaled motion from step 1 was assigned as input motion at the surface of a 1D soil column;
(3) the motion from a layer of interest at some depth below the surface is obtained via an equivalent linear solution;
(4) the final iteration values of shear modulus reduction and material damping for each layer during the de-convolution process is obtained;
(5) the de-convolution process was performed again by using a linear analysis with the final values of G/G_0 and D from step 4 for each layer of the 1D soil column and introducing the LP filtered (15 Hz) full surface motion (i.e., not scaled by 0.87) at the top of the column to obtain the “final”, outcropping, de-convoluted motion.

In this study, the EERA code was utilized to perform all de-convolution analyses. The de-convoluted outcrop input motions are reported in Figure VI.5.16. The time histories of the II aftershock has been cut at 125 s, since the Arias intensity reaches the 95% around the 90th second.

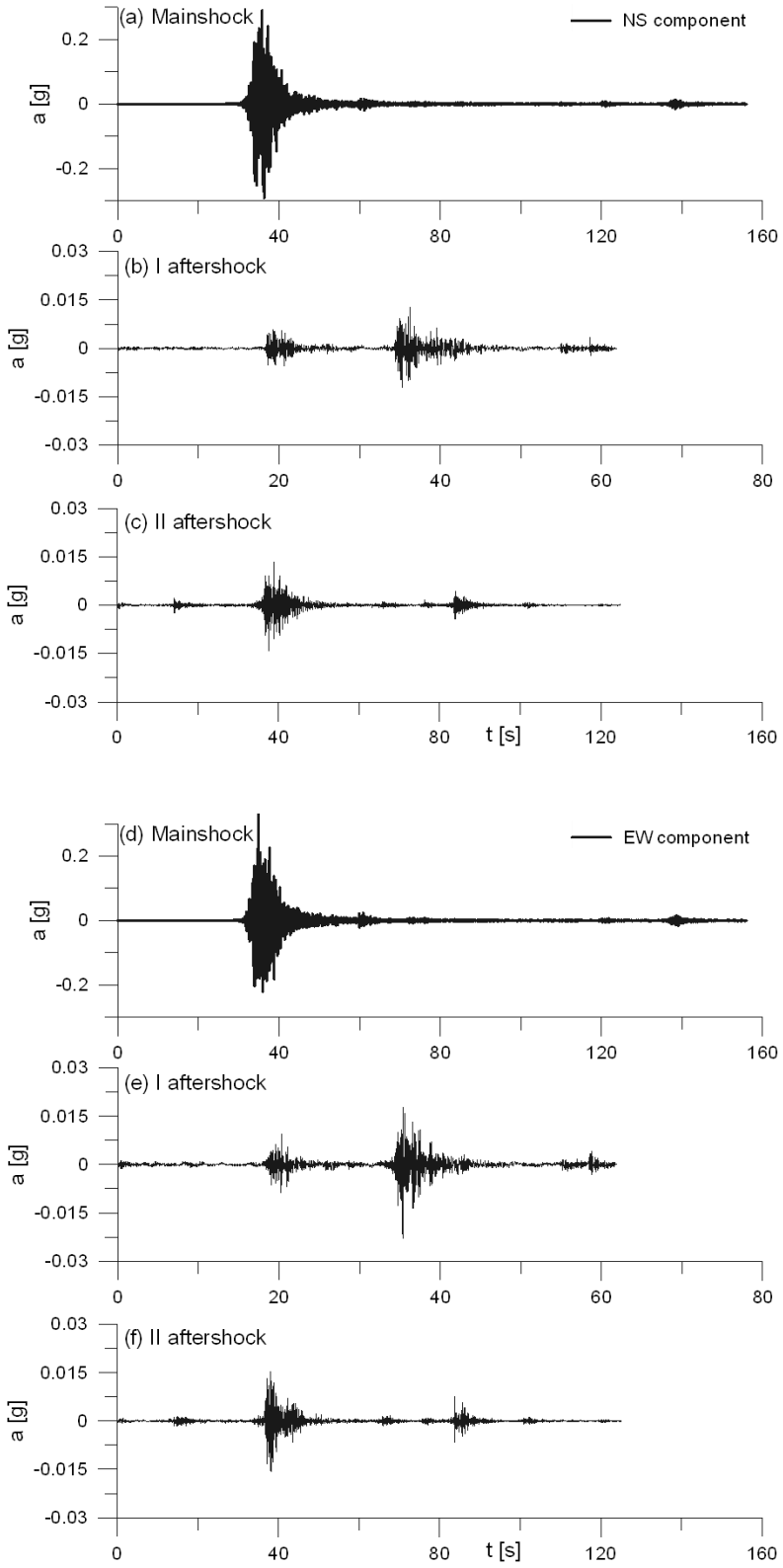

Figure VI.5.16 – De-convoluted outcrop motions of the NS (a-c) and EW (d-f) components of the three shocks

VI.5.3.1. Attenuation law

As shown in Figure VI.5.17, two of three seismic events occurred much closer to Scortichino dyke than Mirandola station. Due to the great difference in distance from the epicenter of the MRN station and of the dyke site, a study of ground motion attenuation is necessary. This consists essentially of predicting ground motion at a particular site by means of attenuation laws, formulated on the basis of large strong motion databases and depending on soil type and faulting mechanism.

Similarly to Sinatra and Foti (2015), a ground motion prediction equation (GMPE) based on the Italian strong motion database has been adopted (Bindi et al., 2011). For peak ground acceleration (PGA, cm/s^2), GMPE is characterized by the following functional form

$$\log(PGA) = e_1 + F_D(R,M) + F_M(M) + F_S + F_{sof} \quad \text{(VI.5.1)}$$

where e_1 is a constant term equals to 3.672, F_D (R, M), F_M (M), F_S and F_{sof} represent the distance function, the magnitude scaling, the site amplification and the style of faulting correction, respectively. M is the moment magnitude, M_w, and R is the Joyner-Boore distance, R_{jb}, or the epicentral distance, R_{epi}, when the fault geometry is unknown (generally when M<5.5).

Figure VI.5.17 – Location of the epicenters of the three main shocks

The proposed equation for the distance function is

$$F_D(R,M) = \left[c_1 + c_2\left(M - M_{ref}\right)\right]\log\left(\frac{\sqrt{R^2+h^2}}{R_{ref}}\right) - c_3\left(\sqrt{R^2+h^2} - R_{ref}\right) \quad \text{(VI.5.2)}$$

while the proposed magnitude function is:

$$F_M(M) = \begin{cases} b_1 (M - M_h) + b_2 (M - M_h)^2 & \text{for } M \le M_h \\ b_3 (M - M_h) & \text{otherwise} \end{cases} \quad \text{(VI.5.3)}$$

The numerical values of the constants for peak ground acceleration are reported in Table VI.5.3.

Table VI.5.3 – Constants and Coefficients for PGA considering the geometrical mean of the horizontal components (Bindi et al., 2011)

c_1	c_2	h	c_3	b_1	b_2	M_{ref}	M_h	R_{ref} [km]
-1.940	0.413	10.322	$1.34 \cdot 10^{-4}$	-0.262	-0.0707	5	6.75	1

The functional form F_S in Equation VI.5.1 represents the site amplification and it is given by

$$F_S = s_j \cdot C_j \quad \text{for } j=1,...,5 \quad \text{(VI.5.4)}$$

where C_j are dummy variables used to denote the five different EC8 site classes from A to E.
The functional form F_{sof} in Equation VI.5.1 represents the type of faulting correction and it is given by

$$F_{Sof} = f_j \cdot E_j \quad \text{for } j=1,...,4 \quad \text{(VI.5.5)}$$

where E_j are dummy variables used to denote fault classes. Bindi et al. (2011) considered four types of style faulting: normal (N), reverse (R), strike-slip (SS) and unknown (U).
Table VI.5.4 shows the numerical values of the s_j and f_j coefficients. The columns s_A through s_E show the site coefficients for the EC8 classes. The columns f_1 through f_4 show the style of faulting coefficients for normal (f_1), reverse (f_2), strike slip (f_3) and unknown (f_4) mechanisms. The total (σ), the between-event (σ_B) and within-event (σ_W) standard deviations are shown as well.

Table VI.5.4 – Site and style of faulting coefficients for horizontal PGA (Bindi et al., 2011)

s_A	s_B	s_C	s_D	s_E	f_1	f_2	f_3	f_4	σ_B	σ_W	σ
0	0.162	0.240	0.105	0.570	$-5.03 \cdot 10^{-2}$	$1.05 \cdot 10^{-1}$	$-5.44 \cdot 10^{-2}$	0	0.172	0.290	0.337

For the mainshock (Mw = 6.1), the fault mechanism is thrust (reverse) type (ITACA, 2016). The fault projection on the ground surface allows for computing the Joyner-Boore distance of the MRN station, R_{jb}= 4.34 km (Figure VI.5.18). It can be observed that Scortichino dyke is located inside the surface projection of the fault (R_{jb} = 0 km), and an amplification of the recorded motion at MRN station is expected.

Figure VI.5.18 – Fault projection of the mainshock

Table VI.5.5 – Input coefficients for defining the GMPE of the three mainshocks and R distances for MRN station and Scortichino dyke.

Event	Time (UTC)	M	Site class A (F_S)	Style of faulting	F_{sof}	R [km] MRN station	R [km] Scortichino c-c' section
Mainshock	02:03:53	6.1	0	R	$1.05 \cdot 10^{-1}$	4.34	0.00
I aftershock	02:06:26	4.8	0	U	0	8.53	15.20
II aftershock	02:06:28	5.0	0	U	0	16.50	5.96

Figure VI.5.19 reports with black lines the GMPEs of the three mainshocks, defined using the input parameters of Table VI.5.4. The same plots report also PGAs of the de-convoluted outcrop motions of the three shocks (red points).

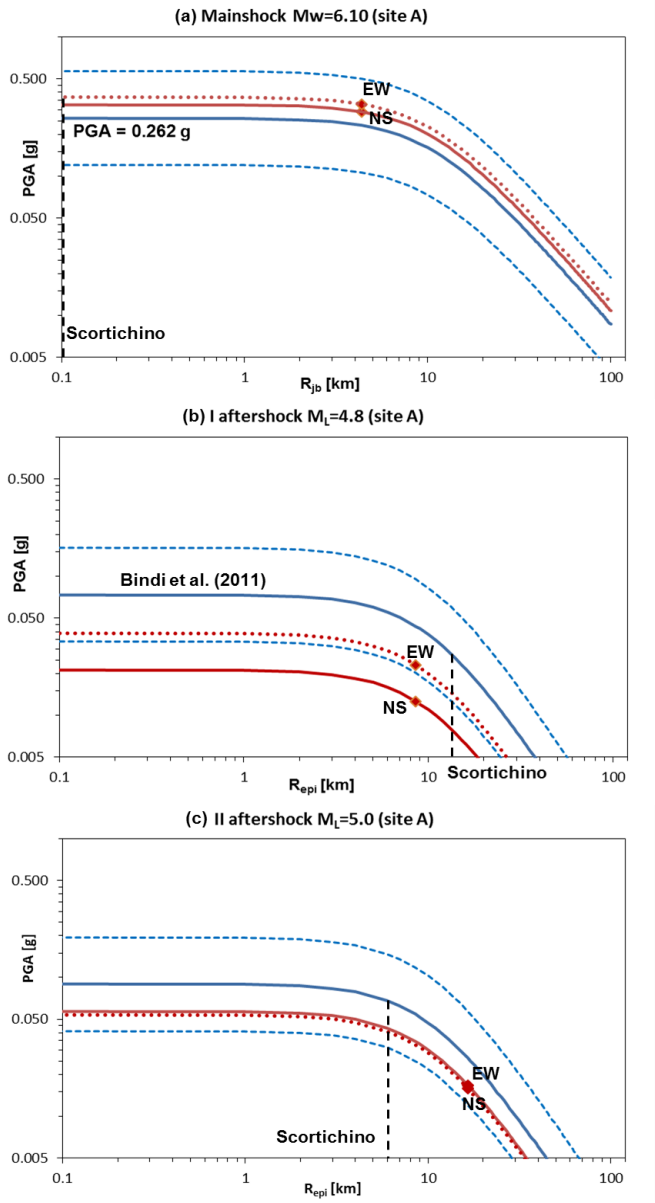

Figure VI.5.19 - Ground motion attenuation for mainshock (a), first aftershock (b) and second aftershock (c)

The GMPEs have been scaled to the PGAs of the de-convoluted components. This latter have been used to define the values of PGA expected at the site of Scortichino.

Every de-convoluted motion (mainshock and aftershock separately) has been scaled to so-computed peak acceleration value; then, the three motions have been re-assembled in an unique record. In order to avoid aliasing during these merging operation, the complete time history has been once again baseline-corrected (Figure VI.5.20).

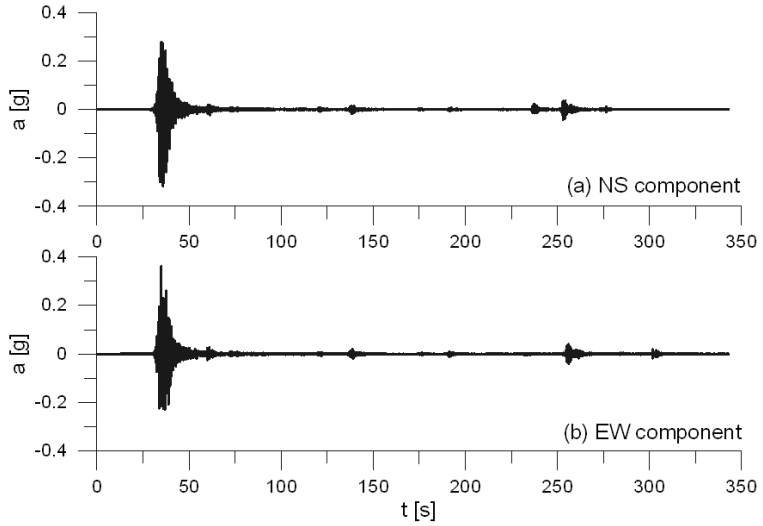

Figure VI.5.20 - Input motion time history at Scortichino, May 20, 2012 mainshock and aftershocks

VI.5.4. Simulation of the 20th May events

Effective stress analyses have been performed using the geotechnical model of the c-c' section of Scortichino dyke, already described in the previous sec. VI.5.3.

The results of the analyses are plotted in Figure VI.5.21 in terms of maximum acceleration, shear strain and shear stress profiles. The acceleration profile is characterized by a significant reduction of acceleration between the surface and the water table depth.

According to the time histories at 14.5 m depth, the mainshock triggers liquefaction, while the aftershocks are ineffective to generate excess pore water pressure, since the shear stress ratio is always under the threshold values (Figure VI.5.22).

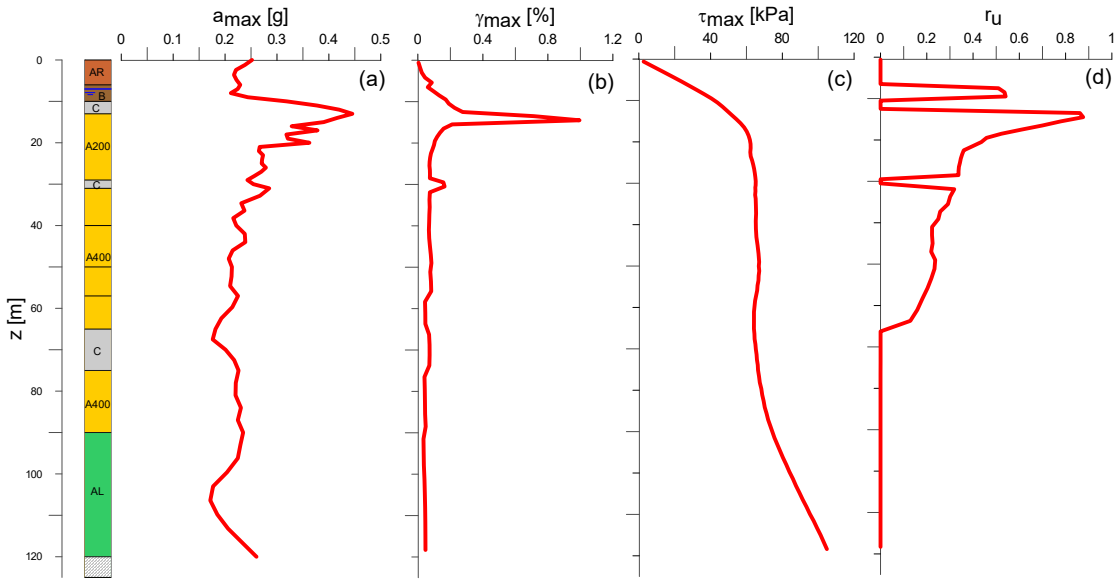

Figure VI.5.21 - Coupled analysis on c – c' section for the recorded EW seismic sequence

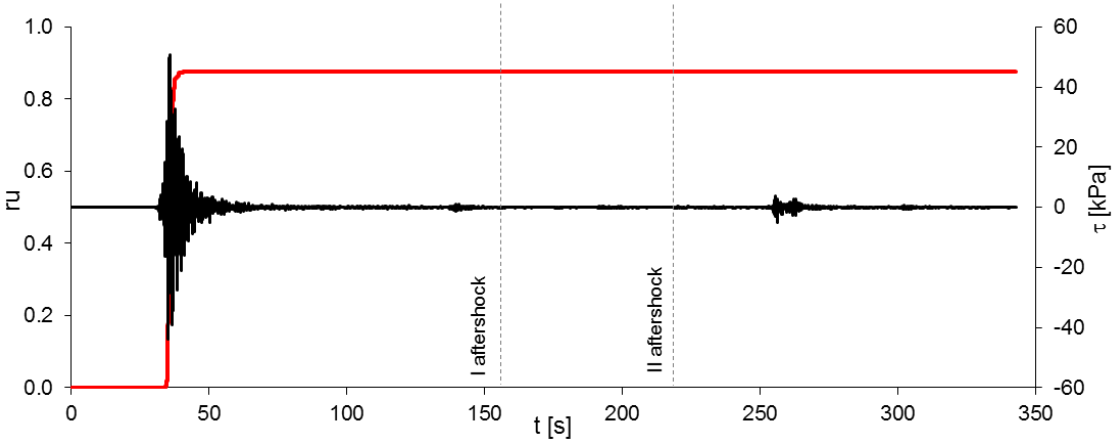

Figure VI.5.22 - Histories of excess pore pressure ratio from coupled analysis on c – c' section

Effective stress analyses have also been performed along the d – d' section of the dyke. Due to the lack of the shallow clay layer in the soil column (Figure VI.5.9), the consolidation properties of the soils are taken into account in the analysis. Permeability coefficients are the same already adopted for the different units (Figure VI.5.1) and a Poisson coefficient equals to 0.3 for all soil layers has been considered.

Figure VI.5.23 reports the results of the analyses in terms of maximum profiles of acceleration, shear strain and shear stress. In this case, liquefaction conditions are not reached and the maximum values of r_u is equal to 0.68 at 19.7 m in the shallow sandy layer (A).

The acceleration profile is characterized by a significant reduction of acceleration between the surface and the base of the dyke, as observed also in the previous case. In both cases, this effect can be attributed to the liquefiable/degraded soils A200 and B, which work as dampers against the motion on the surface.

Figure VI.5.23 shows the time history of excess pore pressure at 15 m depth. It can be noted that the consolidation process starts at 42 s and continues for the rest of the time. Even though the dissipation process induces an increase of the soil stiffness, the shear stress due to the aftershock does not overcome the shear threshold value (dotted line in Figure VI.5.24) and, consequently, additional excess pore pressure is no longer generated.

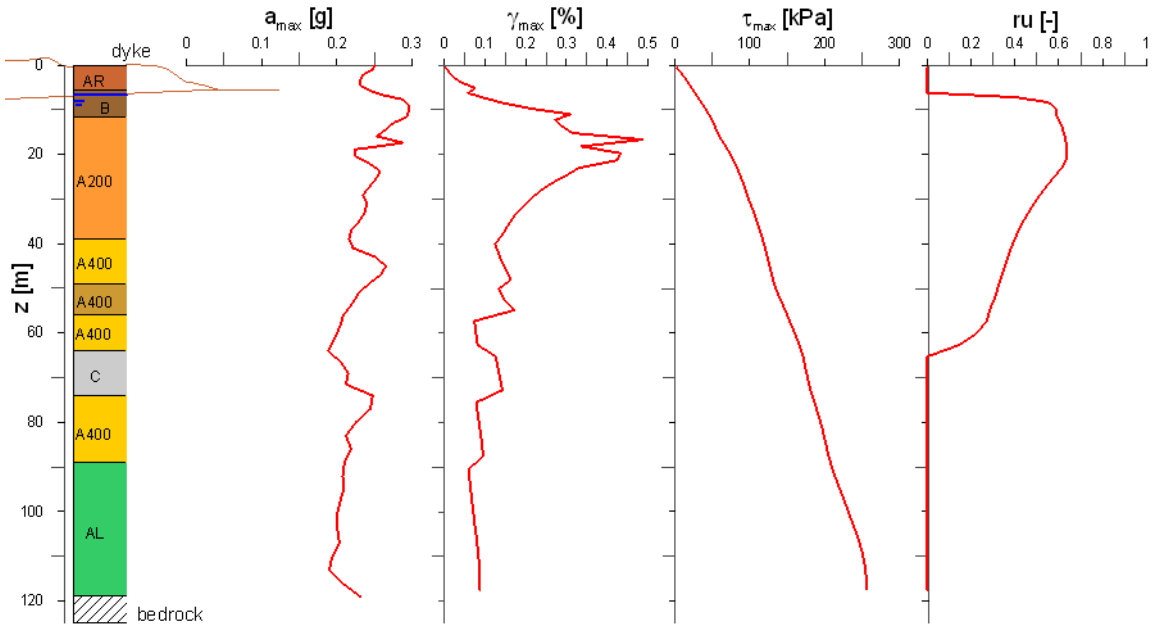

Figure VI.5.23 - Coupled analysis on d – d' section for the recorded NS seismic sequence

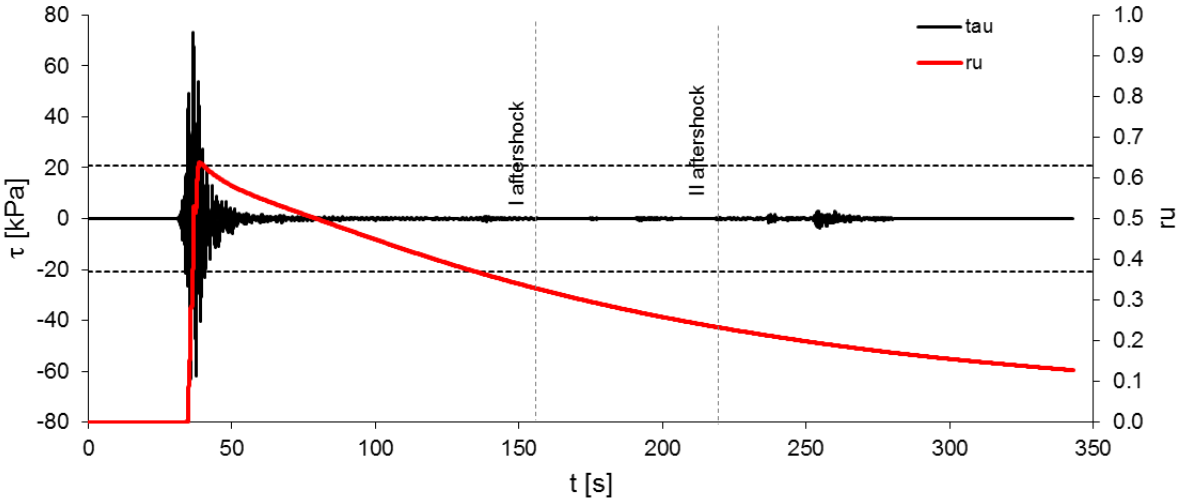

Figure VI.5.24 – Shear stress and excess pore pressure ratio histories at 19.7 m depth from coupled analysis on d – d' section

Finally, a Newmark displacement analysis has been performed considering the simulated accelerogram at the depth of the critic surface failure, detected similarly to as described the previous paragraph VI.4.4. The critic acceleration has been computed equals to 0.175 g, adopting the Morgenstern – Price (1965) method.

Figure VI.5.25 shows the result of the displacements analysis. As expected, accumulation of displacements occurs during the main seismic event, while the acceleration values are always lower than the critic acceleration in the aftershock.

The final accumulated displacement results slightly greater to 1.5 cm, which is compatible with the amplitude of the cracks observed along the crest of the dyke.

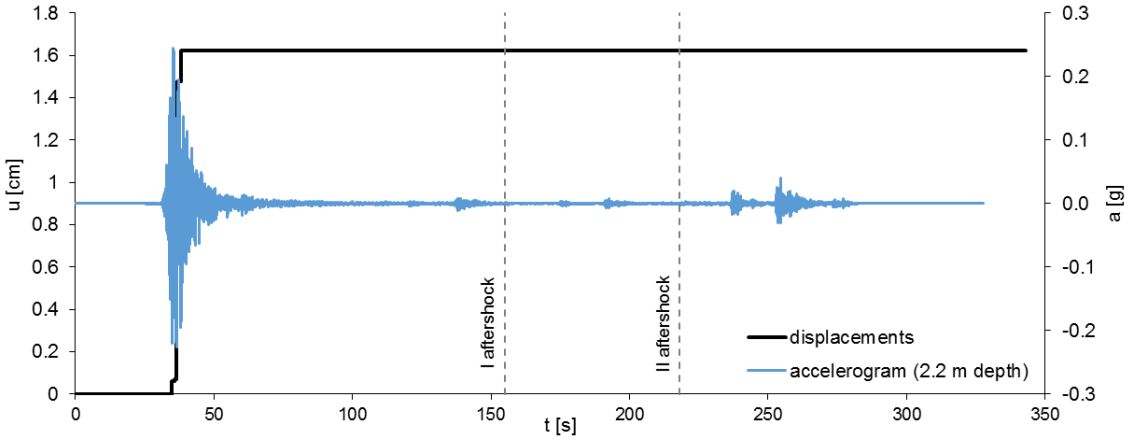

Figure VI.5.25 - Acceleration and displacement time histories from coupled analysis on d – d' section

VI.6. References

AGI (2005). Aspetti geotecnici della progettazione in zone sismiche. Guidelines of the Italian Geotechnical Society. Pàtron Editore, Bologna (in Italian).

Andrus R.D., Stokoe K.H. II (2000). Liquefaction resistance of soils from shear-wave velocity. Journal of Geotechnical and Geoenvironmental Engineering, 126 (11): 1015 - 1025.

Athanasopoulos-Zekkos A., Saadi M. (2012). Ground motion selection for liquefaction evaluation analysis of earthen levees. Earthquake Spectra, 28 (4): 1331-1351.

Ausilio E., Silvestri F., Tropeano G. (2007). Simplified relationships for estimating seismic slope stability. ISSMGE – ETC12 Workshop: Geotechnical aspects of EC8. September 24 - 27, Madrid, Spain.

Bardet J. P., Ichii K., Lin C.H. (2000). EERA – A computer program for equivalent-linear earthquake site response analyses of layered soil deposits. University of Southern California.

Bindi D., Pacor F., Luzi L., Puglia R., Massa M., Ameri G. and Paolucci R. (2011). Ground motion prediction equations derived from the Italian strong motion database. Bulletin of earthquake engineering, 9 (6): 1899–1920.

Boulanger R.W., Idriss I.M. (2006). Liquefaction susceptibility criteria for silts and clay. Journal of Geotechnical and Environmental Engineering, ASCE, 132 (11): 1413 - 1426.

Facciorusso J., Madiai C., Vannucchi G. (2014). Effetti di liquefazione osservati a San Carlo (FE) durante il terremoto del 20 Maggio e stima del rischi di liquefazione. Proceedings of the XXV Convegno Nazionale di Geotecnica, Baveno, Italy, 2: 157-164 (in Italian).

GEOSLOPE International Ltd (2007). SLOPE/W User's manual. Calgary, Alberta, Canada.

Gingery J.R., Elgamal A. (2013) Shear stress-strain curves based on the G/Gmax logic: A procedure for strength compatibility. The 2nd International Conference on Geotechnical and Earthquake Engineering, Chengdu, China.

Kramer S.L., Asl B. A., Ozener P., Sideras S.S. (2015). Effects of liquefaction on ground surface motions. Perspectives on Earthquake Geotechnical Engineering. Ansal A. and Sakr (eds), Springer.

ITACA (2016). ITalian ACcelerometric Archive (1972-20) version 2.1, http://itaca.mi.ingv.it/ItacaNet/

Laurenzano G., Priolo E. (2013). Studio sismologico per la caratterizzazione della risposta sismica di sito ai fini della microzonazione sismica di alcuni comuni della Regione Emilia-Romagna, Relazione sull'attività svolta. Istituto Nazionale di Oceanografia e di Geofisica Sperimentale (in Italian).

Madiai C. (2009). Correlazioni tra parametri del moto sismico e spostamenti attesi del blocco di Newmark. Italian Geotechnical Journal, 1: 23-43 (in Italian).

Marcaccio M., Martinelli G. (2012). Effects on the groundwater levels of the May-June 2012 Emilia seismic sequence. Annals of geophysics, 55 (4): 811 – 814.

Morgenstern N.R., Price V.E. (1965). The Analysis of the Stability of General Slip Surfaces. Geotechnique, 15: 79-93.

Markham C.S., Bray J.D., Macedo J. (2015). Deconvolution of surface motions from the Canterbury earthquake sequence for use in nonlinear effective stress site response analyses. Proceedings of the 6th International Conference on Earthquake Geotechnical Engineering, paper 176.

Newmark N.W. (1965). Effects of earthquakes on dams and embankments. Géotechnique, 15 (2), 139-160.

Pacor, F., Paolucci R., Luzi L., Sabetta F., Spinelli A., Gorini A., Nicoletti M., Marcucci S., Filippi L., Dolce M. (2011). Overview of the Italian strong motion database ITACA 1.0, Bulletin of Earthquake Engineering, 9(6), 1723–1739.

Ramberg W., Osgood W.R. (1943). Description of stress strain curves by three parameters. Technical Note 902, National Advisory Committee for Aeronautics, Washington, D.C.

Rampello S., Callisto L., Fargnoli P. (2010). Evaluation of slope performance under earthquake loading conditions. Italian Geotechnical Journal (RIG), 4: 29-41.

Santucci De Magistris F., d'Onofrio A., Sica S. (2004). A step into the definition of the seismic risk for the city of Benevento (Italy). Proceeding of the 5th International Conference on Case Histories in Geotechnical Engineering: 3041-3048, University of Missouri, Rolla, MO, US.

Sinatra L., Foti S. (2015). The role of aftershocks in the liquefaction phenomena caused by the Emilia 2012 seismic sequence. Soil dynamics and earthquake engineering, 75: 234 – 245.

Tonni L., Gottardi G., Amoroso S., Bardotti R., Bonzi L., Chiaradonna A., d'Onofrio A., Fioravante V., Ghinelli A., Giretti D., Lanzo G., Madiai C., Marchi M., Martelli L., Monaco P., Porcino D., Razzano R., Rosselli S., Severi P., Silvestri F., Simeoni L., Vannucchi G., Aversa S. (2015). Interpreting the deformation phenomena triggered by the 2012 Emilia seismic sequence on the Canale Diversivo di Burana banks. Italian Geotechnical Journal, 2: 28 - 58 (in Italian).

Working Group AGI – RER (2013). Amoroso S., d'Onofrio A., Fioravante V., Ghinelli A., Giretti D., Gottardi G., Lanzo G., Madiai C., Marchi M., Martelli L., Monaco P., Porcino D., Rosselli S., Silvestri F., Simeoni L., Tonni L., Vannucchi G. Analisi di stabilità in condizioni sismiche dell'argine diversivo in località Scortichino, Comune di Bondeno (FE). Final report (in Italian).

VII. CONCLUSIONS AND PERSPECTIVES

VII.1. Conclusions

The main objective of this work was to develop and verify a simplified model for a reliable prediction of pore pressure build-up and dissipation induced by seismic loading in granular soils. This new model was developed and validated in several steps.

First, it was searched for a simplified model easy to be applied in the engineering practice, yet able to catch the most significant aspects of the cyclic stress-strain behaviour and strength of potentially liquefiable soils. The model proposed by Park and Ahn (2013) was selected, since based on experimental data from cyclic laboratory tests and suitable to be implemented in a time domain seismic response analysis, avoiding the need to convert the irregular load history in an equivalent uniform cyclic loading. The original formulation was further developed, proposing updated functions for the cyclic resistance curve and the excess pore pressure relationship, as well as a straightforward procedure for the calibration of the model parameters.

Thereafter, the model so developed was implemented into an innovative computer code for the one-dimensional analysis of seismic soil response, originally written by Tropeano (2015). The code uses a nonlinear lumped mass approach, capable of simulating the seismic response of a horizontally layered soil profile, including stiffness degradation, shear strength, pore pressure build-up and dissipation.

The capabilities and limitations of the code were tested by applying it to several well-documented case histories. The study of the case histories provided considerable insight into the mechanics of the seismic response and associated pore pressure build-up in full-scale problems where liquefiable potentially soils are present, and/or there is the need of analysing post-seismic deformations and/or safety. The application of the code to four case histories suggests that the upgraded code encompasses the main aspects of the complex phenomenon of liquefaction. In particular, the code was verified to be capable to well-predict the initial triggering and occurrence of liquefaction, as well as the surface ground motion in terms of accelerograms and response spectra. Conversely, the inability of the constitutive model to simulate the phase transformation behaviour can be viewed as a limitation for reproducing the post-liquefaction soil response.

Finally, the developed method was applied to a very complex case history of a dyke damaged by the recent 2012 Emilia earthquake. The proposed approach allowed for deeply investigating on the nature of damage, disproving the contradictory results obtained by the traditional simplified approaches.

Once again, the present study confirms that the seismic response of potentially liquefiable soils is a complex task; it cannot realistically be approached from a single perspective, e.g. focusing only on peak ground acceleration or earthquake magnitude like in semi-empirical methods, but considering the soil deposit as a system. Since thirty years to date, the problem is that semi-empirical approaches cannot be supplanted, until a feasible alternative is adequately supported by field observations. In this context, the constitutive model and the computer code developed may be viewed as a good-working integrated balance between the limitations of semi-empirical methods and the challenges, sometimes prohibitive for the practicing engineer, implied by the use of advanced constitutive models.

Future perspectives of the research are primarily related to further refinements of the pore water pressure model, such as introducing a dependency of the pore water pressure parameters on the stress ratio.

Moreover, further validations on better instrumented full or model scale case studies could be useful to deeply investigate on the role of dissipation and redistribution of excess pore pressure in the surface and in-depth ground motion, as well as on the post-liquefaction deformation.

Finally, the implementation of the phase transformation behaviour is envisaged.

A. APPENDIX

A.1. Cyclic resistance curves based on field test data

It is reported the script file for generation of cyclic resistance curves from field data.

```
clear all

SPT=[6 8 10 12 14 15 16 18 20 22 24 25]; %corrected SPT N-value
% we suppose clean sand, so (N1)60cs=(N1)60
N=[3 4 5 10 15 20 40 60 100 200 300]; %number of cycles
sig=[50 100 150 200 400 800]; %effective confining stress (in kPa)

A(3:length(N)+2,1)=N'; %set the first column of the matrix results equal
to the number of cycles

for m=1:length(sig)
A(1,(m-1)*length(SPT)+2:m*length(SPT)+1)=sig(m); %set the first row of
the matrix results equal to the effective confining pressure
sig(m) = sig(m)/101.3; %Convert from kPa to atm

    for p=1:length(SPT)
    A(2,(p+1)+(m-1)*length(SPT))=SPT(p); %set the second row of the
matrix results equal to the number of corrected blow count
    CRR(p)=                          exp((SPT(p)/14.1)+((SPT(p)/126)^2)-
((SPT(p)/23.6)^3)+((SPT(p)/25.4)^4)- 2.8) % equ. (2.25) by I&B 2014 with
PL=0.5

    %effect of initial effective confining pressure through overburden
correction factor
    Csig(p)=  min(0.3,1/(18.9-2.55*sqrt(SPT(p)))) %equ. (2.16c) by I&B
2014
    %for (N1)60<=37!!!
```

```
    Ksig(p)= min(1.1,1-Csig(p)*log(sig(m))) %equ. (2.16a) by I&B 2014

    %Magnitude scaling factor
    MSFmax(p)= min(1.09 + (SPT(p)/31.5)^2,2.2) %equ. (2.21) by I&B 2014

       for i=1:length(N)
       Nmin =((1/0.65)^(1/0.337))*(3/4); %equ. (3-12) by I&B 2004
       b(i)=log(MSFmax(p))/log(15/Nmin) %N(Mw=7.5)=15 from I&B 2004
       MSF(i)= (15/N(i))^b(i);
       MSF(i) = min(MSF(i), MSFmax(p))
       M = -4*log(((MSF(i) - 1)/(MSFmax(p) - 1) + 1.325)/8.64);

       CSR(i) = CRR(p)*MSF(i)*Ksig(p) %eq. (2.7) by I&B 2014

       %tau_sig(i) = CSR(i)/0.65 %eq.(2.1) by I&B 2014
       tau_sig(i) = CSR(i)
       end

    tau_sig=tau_sig';
    A(3:length(N)+2,(p+1)+(m-1)*length(SPT))=tau_sig; %put the result in
the column of the matrix results
    end
end

A
xlswrite('CRC', A)
```

B. APPENDIX

B.1. Database of experimental excess pore pressure ratio curves

All the experimental data have been collected in the following database, together with the results of the regression analysis. Each record is defined by an identification number (ID), grain size distribution, i.e. precentage of gravel (G), sand (S), silt (L), clay (A), plasticity index (PI), relative density (Dr), effective confing pressure applied (σ'_0), cyclic resistance ratio (CSR), type of test, i.e. cyclic triaxial test (CTX) or cyclic shear test (DSS), type of specimen, i.e. reconstituted (Rec) or undisturbed (Und) material. Reference of the data is also reported. Experimental curve that reach ru= 0.95 have been considered for the regression analysis (Liq= Y), otherwise the curva have been neglected (Liq = N). Finally, the pore pressure coefficients, a, b, c, are reported together with the related value of corrected determination coefficient.

ID	Name	%G	%S	%L	%A	PI	Dr (%)	σ'_0 [kPa]	CSR	Test type	Spec	Reference	Liq	a	b	c	R^2_{adj}
1	Adapazaru Silt_00	0	0	0	0	9	-	-	-	CTX	Rec	Pekcan et al. (2004)	Y	0.6784	0.1944	0.3259	0.9557
2	Adapazaru Silt_01	0	0	0	0	0	-	-	-	CTX	Rec	Pekcan et al. (2004)	Y	-	-	-	-
3	Adapazaru Silt_02	0	0	0	0	6	-	-	-	CTX	Rec	Pekcan et al. (2004)	Y	0.9254	0.2402	0.001274	0.9951
4	Adapazaru Silt_03	0	0	0	0	0	-	-	-	CTX	Rec	Pekcan et al. (2004)	Y	0.8382	0.521	0.1234	0.9986
5	Adapazaru Silt_04	0	0	0	0	8	-	-	-	CTX	Rec	Pekcan et al. (2004)	Y	-	-	-	-
6	Adapazaru Silt_05	0	0	0	0	32	-	-	-	CTX	Rec	Pekcan et al. (2004)	Y	0.8856	0.2028	0.0781	0.9968
7	Adapazaru Silt_06	0	0	0	0	8	-	-	-	CTX	Rec	Pekcan et al. (2004)	Y	-	-	-	-
8	Adapazaru Silt_07	0	0	0	0	9	-	-	-	CTX	Rec	Pekcan et al. (2004)	Y	-	-	-	-
9	Bangladesh Sand	0	95	5	0	0	-	166.7	0.3	CTX	Rec	Momimul et al. (2013)	Y	0.8114	0.2383	0.1188	0.9975
10	Bonnie Silt_00	0	8	85	7	0		80	0.48	CIU DSS	Rec	Arulmoli et al. (1992)	Y	0.5612	0.1998	0.4962	0.7054
11	Bonnie Silt_01	0	8	85	7	0		80	0.195	CIU DSS	Rec	Arulmoli et al. (1992)	Y	0.87	0.3741	0.0275	0.9922
12	Bonnie Silt_02	0	8	85	7	0		80	0.2	CIU DSS	Rec	Arulmoli et al. (1992)	Y	0.8853	0.5777	0.05598	0.9929
13	Bonnie Silt_03	0	8	85	7	0		80	0.21	CIU DSS	Rec	Arulmoli et al. (1992)	Y	0.9366	0.3711	-0.001936	0.9923

ID	Name	% G	%S	%L	%A	PI	Dr (%)	σ'_0 [kPa]	CSR	Test type	Spec	Reference	Liq	a	b	c	R^2_{adj}
14	Bonnie Silt_04	0	8	85	7	0		160	0.36	CIU DSS	Rec	Arulmoli et al. (1992)	Y	0.5573	0.2628	0.3782	0.982
15	Cristal Silica Sand_00	0	0	0	0	0	60	95.76		CTX	Rec	Silver and Park (1976)	Y	0.2347	0.1883	0.6976	0.9873
16	Cristal Silica Sand_01	0	0	0	0	0	60	95.76		CTX	Rec	Silver and Park (1976)	Y	0.4743	0.2986	0.4768	0.9955
17	Cristal Silica Sand_02	0	0	0	0	0	60	95.76		CTX	Rec	Silver and Park (1976)	Y	0.5004	0.2454	0.4396	0.993
18	Cristal Silica Sand_03	0	0	0	0	0	60	95.76		CTX	Rec	Silver and Park (1976)	Y	0.813	0.4191	0.1368	0.99987
19	S1_C2_proviN1	0	60	33	7	0	0	130	0.2	CIU DSS	Und	Porcino (2013)	Y	1.013	0.5254	-0.0611	0.9983
20	S1_C2_proviN2	0	60	33	7	0	0	130	0.2	CIU DSS	Und	Porcino (2013)	Y	0.9821	0.6244	-0.02286	0.9932
21	S1_C2_proviN4	0	60	33	7	0	0	130	0.17	CIU DSS	Und	Porcino (2013)	Y	0.9653	0.4755	-0.01065	0.9982
22	S1_C2_proviN5	0	60	33	7	0	0	130	0.25	CIU DSS	Und	Porcino (2013)	N		-	-	-
23	S1_C2_proviN6	0	60	33	7	0	0	130	0.26	CIU DSS	Und	Porcino (2013)	N	-	-	-	-
24	S1_C4_proviN3	0	95	5	0	0	86	100	0.2	CIU DSS	Rec	Porcino (2013)	N	-	-	-	-
25	S1_C4_proviN4	0	95	5	0	0	86	100	0.16	CIU DSS	Rec	Porcino (2013)	Y	0.4922	0.442	0.429	0.9945
26	S1_C4_proviN5	0	95	5	0	0	86	100	0.13	CIU DSS	Rec	Porcino (2013)	Y	0.5467	0.3772	0.3431	0.9861

ID	Name	% G	%S	%L	%A	PI	Dr (%)	σ'_0 [kPa]	CSR	Test type	Spec	Reference	Liq	a	b	c	R^2_{adj}
27	S1_C4_proviN6	0	95	5	0	0	86	100	0.23	CIU DSS	Rec	Porcino (2013)	Y	1.769	1.653	-0.8182	0.9903
28	S4_C3_proviN1	0	77	18	5	0	0	150	0.17	CIU DSS	Und	Porcino (2013)	Y	0.7193	0.4516	0.2669	0.9947
29	S4_C3_proviN2	0	77	18	5	0	0	150	0.2	CIU DSS	Und	Porcino (2013)	Y	0.9285	0.5572	0.04326	0.9934
30	S4_C3_proviN3	0	77	18	5	0	0	150	0.13	CIU DSS	Und	Porcino (2013)	N	-	-	-	-
31	S4_C3_proviN5	0	77	18	5	0	0	150	0.24	CIU DSS	Und	Porcino (2013)	N	-	-	-	-
32	S5_C2_proviN3	0	28	62	10	0	0	100	0.25	CIU DSS	Und	Porcino (2013)	Y	1.18	0.6599	-0.2487	0.9851
33	S5_C2_proviN4	0	28	62	10	0	0	100	0.21	CIU DSS	Und	Porcino (2013)	N	-	-	-	-
34	S5_C2_proviN5	0	28	62	10	0	0	100	0.17	CIU DSS	Und	Porcino (2013)	Y	0.8522	0.3975	0.09101	0.9975
35	S5_C2_proviN6	0	28	62	10	0	0	100	0.23	CIU DSS	Und	Porcino (2013)	N	-	-	-	-
36	RiverSand	0	0	0	0	0	40	100	0.1	CIU DSS	Rec	Karbasi and Byrne (2010)	Y	0.4928	0.4968	0.3674	0.9789
37	EgyptSand	8	92	0	0	0	40	100	0.225	CTX	Rec	Elmamlouk et al. (2013)	Y	-	-	-	-
38	MonteraySand_00	0	0	0	0	0	54	55	-	CIU DSS	Rec	De Alba et al. (1976)	Y	0.5169	0.7195	0.3525	0.9884
39	MonteraySand_01	0	0	0	0	0	68	55	-	CIU DSS	Rec	De Alba et al. (1976)	Y	0.6396	0.6626	0.3116	0.999

ID	Name	%G	%S	%L	%A	PI	Dr (%)	σ'_0 [kPa]	CSR	Test type	Spec	Reference	Liq	a	b	c	R^2_{adj}
40	MonteraySand_02	0	0	0	0	0	82	55	-	CIU DSS	Rec	De Alba et al. (1976)	Y	0.7593	0.706	0.2086	0.9979
41	MonteraySand_03	0	0	0	0	0	90	55	-	CIU DSS	Rec	De Alba et al. (1976)	Y	0.8605	0.7356	0.1068	0.9981
42	Fuso_SiltyClay_sup	0	0	0	0	0	0	-	-	CTX	Rec	El Hosri et al. (1984)	Y	1.226	0.5266	-0.3298	0.9784
43	Fuso_SiltyClay_inf	0	0	0	0	0	0	-	-	CTX	Rec	El Hosri et al. (1984)	Y	1.084	0.5827	-0.1511	0.9918
44	Fuso_Monteray_00 sup	0	0	0	0	0	0	-	-	CTX	Rec	Lee et Albasia (1974)	Y	0.781	0.5386	0.1308	0.9962
45	Fuso_Monteray_00 inf	0	0	0	0	0	0	-	-	CTX	Rec	Lee et Albasia (1974)	Y	0.365	0.5149	0.4941	0.9897
46	Fuso_Monteray_01 sup	0	0	0	0	0	0	-	-	CTX	-	Seed et al. (1976)	-	-	-	-	-
47	Fuso_Monteray_01 inf	0	0	0	0	0	0	-	-	CTX	-	Seed et al. (1976)	-	-	-	-	-
48	Fuso_Monteray_02 sup	0	0	0	0	0	0	-	-	DSS	-	Seed et al. (1976)	-	-	-	-	-
49	Fuso_Monteray_02 inf	0	0	0	0	0	0	-	-	DSS	-	Seed et al. (1976)	-	-	-	-	-
50	Ghiaie_00	0	0	0	0	0	0	200	0.22	CIU CTX	Und	Flora and Lirer (2013)	Y	0.8227	0.3458	0.1335	0.9929
51	Ghiaie_01	0	0	0	0	0	0	200	0.58	CKoU CTX	Und	Flora and Lirer (2013)	N	-	-	-	-
52	Ghiaie_02	0	0	0	0	0	0	200	0.33	CKoU CTX	Und	Flora and Lirer (2013)	N	-	-	-	-

ID	Name	% G	%S	%L	%A	PI	Dr (%)	σ'_0 [kPa]	CSR	Test type	Spec	Reference	Liq	a	b	c	R^2_{adj}
53	Ghiaie_03	0	0	0	0	0	0	200	0.24	CIU CTX	Und	Flora and Lirer (2013)	Y	0.6954	0.3222	0.3159	0.9925
54	Ghiaie_04	0	0	0	0	0	0	200	0.43	CKoU CTX	Und	Flora and Lirer (2013)	N	-	-	-	-
55	Ghiaie_05	75	25	0	0	0	0	400	0.35	CIU CTX	Und	Flora and Lirer (2013)	Y	0.9792	0.6023	-0.1389	0.9102
56	Ghiaie_06	75	25	0	0	0	0	200	0.5	CKoU CTX	Und	Flora and Lirer (2013)	Y	1.158	0.3623	-0.2542	0.9765
57	Ghiaie_07	75	25	0	0	0	0	200	0.32	CIU CTX	Und	Flora and Lirer (2013)	Y	1.077	0.4873	-0.1326	0.9899
58	LeightonBuzzard_00	0	0	0	0	0	68.8	294	0.175	CTX	-	Buckanm (1980)	Y	0.4364	0.3104	0.1681	0.9986
59	LeightonBuzzard_01	0	0	0	0	0	69.6	294	0.2	CTX	-	Buckanm (1980)	Y	0.356	0.223	0.5055	0.9593
60	LeightonBuzzard_02	0	0	0	0	0	72.5	294	0.2	CTX	-	Buckanm (1980)	N	-	-	-	-
61	LeightonBuzzard_03	0	0	0	0	0	69.9	294	0.175	CTX	-	Buckanm (1980)	Y	0.3827	0.2128	0.4432	0.9419
62	MonteraySand_04	0	95	5	0	0	-	-	-	CIU CTX	-	Polito (1999)	Y	0.7054	0.465	0.2144	0.9944
63	MonteraySand_05	0	90	10	0	0	-	-	-	CIU CTX	-	Polito (1999)	Y	0.7091	0.624	0.2278	0.9962
64	MonteraySand_06	0	85	15	0	0	-	-	-	CIU CTX	-	Polito (1999)	Y	0.8665	0.9228	0.1035	0.9972
65	MonteraySand_07	0	75	25	0	0	-	-	-	CIU CTX	-	Polito (1999)	Y	0.6415	0.5944	0.3131	0.9978

ID	Name	% G	%S	%L	%A	PI	Dr (%)	σ'_0 [kPa]	CSR	Test type	Spec	Reference	Liq	a	b	c	R^2_{adj}
66	MonteraySand_08	0	65	35	0	0	-	-	-	CIU CTX	-	Polito (1999)	Y	0.6268	0.6957	0.3236	0.999
67	MonteraySand_09	0	50	50	0	0	-	-	-	CIU CTX	-	Polito (1999)	Y	1.077	1.045	-0.111	0.9973
68	MonteraySand_10	0	25	75	0	0	-	-	-	CIU CTX	-	Polito (1999)	Y	0.8278	0.6381	0.1496	0.9912
69	Canada_Silt00	0	5	85	10	8	-	100	0.143	DSS	-	Verma and Wijewickreme (2015)	N	-	-	-	-
70	Canada_Silt01	0	5	85	10	8	-	100	0.148	DSS	-	Verma and Wijewickreme (2015)	N	-	-	-	-
71	Canada_Silt02	0	5	85	10	8	-	102	0.146	DSS	-	Verma and Wijewickreme (2015)	N	-	-	-	-
72	Canada_Silt03	0	5	85	10	8	-	104	0.145	DSS	-	Verma and Wijewickreme (2015)	N	-	-	-	-
73	NevadaSand_00	0	100	0	0	0	40	40	0.46	CIU DSS	Rec	Arulmoli et al. (1992)	Y	1.031	1.224	-0.0919	0.9799
74	NevadaSand_01	0	100	0	0	0	40	40	0.46	CIU DSS	Rec	Arulmoli et al. (1992)	Y	0.5727	0.4083	0.4439	0.9526
75	NevadaSand_02	0	100	0	0	0	40	40	0.6725	CIU DSS	Rec	Arulmoli et al. (1992)	Y	0.5273	0.3897	0.4266	0.9969
76	NevadaSand_03	0	100	0	0	0	40	80	0.3675	CIU DSS	Rec	Arulmoli et al. (1992)	Y	0.4978	0.3024	0.3429	0.986
77	NevedaSand_04	0	100	0	0	0	40	80	0.538	CIU DSS	Rec	Arulmoli et al. (1992)	Y	0.6686	0.4071	0.3375	0.9561
78	NevadaSand_05	0	100	0	0	0	40	160	0.2987	CIU DSS	Rec	Arulmoli et al. (1992)	Y	1.117	0.4326	-0.2286	0.8897

ID	Name	% G	%S	%L	%A	PI	Dr (%)	σ'_0 [kPa]	CSR	Test type	Spec	Reference	Liq	a	b	c	R^2_{adj}
79	NevadaSand_06	0	100	0	0	0	60	40	0.4475	CIU DSS	Rec	Arulmoli et al. (1992)	Y	0.5674	0.2838	0.3472	0.9923
80	NevadaSand_07	0	100	0	0	0	60	40	0.45	CIU DSS	Rec	Arulmoli et al. (1992)	Y	0.5599	0.3036	0.3642	0.9935
81	NevadaSand_08	0	100	0	0	0	60	40	0.65	CIU DSS	Rec	Arulmoli et al. (1992)	Y	0.5437	0.3099	0.3939	0.967
82	NevadaSand_09	0	100	0	0	0	60	80	0.37	CIU DSS	Rec	Arulmoli et al. (1992)	Y	0.4806	0.3877	0.4333	0.9888
83	NevadaSand_10	0	100	0	0	0	60	160	0.08	CIU DDS	Rec	Arulmoli et al. (1992)	Y	0.6114	0.438	0.391	0.9974
84	NumeRecalModel_00	0	0	0	0	0	30	100	0.081	DSS	Rec	Gingery et al. (2015)	Y	0.4304	0.8145	0.5316	0.9975
85	NumeRecalModel_01	0	0	0	0	0	70	100	0.241	DSS	Rec	Gingery et al. (2015)	Y	1.674	1.449	-0.7387	0.9925
86	OttawaSand_00	0	100	0	0	0	45	200	0.104	DSS	Rec	Bathia (1982)	Y	0.4849	0.4191	0.449	0.995
87	OttawaSand_01	0	100	0	0	0	45	200	0.089	DSS	Rec	Bathia (1982)	Y	0.4699	0.4067	0.444	0.9798
88	OttawaSand_02	0	100	0	0	0	45	200	0.076	DSS	Rec	Bathia (1982)	Y	0.5529	0.3998	0.3362	0.9761
89	OttawaSand_03	0	100	0	0	0	45	200	0.074	DSS	Rec	Bathia (1982)	Y	0.5811	0.4386	0.3385	0.9873
90	OttawaSand_04	0	100	0	0	0	45	200	0.064	DSS	Rec	Bathia (1982)	Y	0.6772	0.4336	0.2416	0.9894
91	OttawaSand_05	0	100	0	0	0	45	200	0.98	DSS	Rec	Bathia (1982)	Y	0.4498	0.4005	0.434	0.949

ID	Name	% G	%S	%L	%A	PI	Dr (%)	σ'_0 [kPa]	CSR	Test type	Spec	Reference	Liq	a	b	c	R^2_{adj}
92	OttawaSand_06	0	100	0	0	0	45	200	0.834	DSS	Rec	Bathia (1982)	Y	0.5041	0.4215	0.3583	0.9626
93	OttawaSand_07	0	100	0	0	0	45	200	0.79	DSS	Rec	Bathia (1982)	Y	0.5713	0.4321	0.3466	0.9884
94	OttawaSand_08	0	100	0	0	0	45	200	0.635	DSS	Rec	Bathia (1982)	Y	0.6291	0.3831	0.279	0.9946
95	OttawaSand_09	0	100	0	0	0	45	200	0.578	DSS	Rec	Bathia (1982)	Y	0.5569	0.4008	0.2924	0.9795
96	OttawaSand_10	0	100	0	0	0	60	200	0.126	DSS	Rec	Bathia (1982)	Y	0.523	0.3253	0.3754	0.9871
97	OttawaSand_11	0	100	0	0	0	60	200	0.112	DSS	Rec	Bathia (1982)	Y	0.6489	0.3736	0.2312	0.9749
98	OttawaSand_12	0	100	0	0	0	60	200	0.097	DSS	Rec	Bathia (1982)	Y	0.5158	0.3045	0.352	0.9466
99	OttawaSand_13	0	100	0	0	0	40	-	0.08	DSS	-	Park et al. (2014)	Y	0.7381	0.4503	0.1913	0.9917
100	OttawaSand_14	0	100	0	0	0	40	-	0.1	DSS	-	Park et al. (2014)	Y	0.7362	0.5334	0.179	0.9838
101	OttawaSand_15	0	100	0	0	0	40	-	0.13	DSS	-	Park et al. (2014)	Y	0.9481	0.9361	0.05835	0.9999
102	OttawaSand_16	0	100	0	0	0	60	-	0.15	DSS	-	Park et al. (2014)	Y	0.7514	0.3711	0.1615	0.9863
103	OttawaSand_17	0	100	0	0	0	60	-	0.18	DSS	-	Park et al. (2014)	Y	0.9493	0.4762	-0.0452	0.9802
104	OttawaSand_18	0	100	0	0	0	60	-	0.2	DSS	-	Park et al. (2014)	N	-	-	-	-

ID	Name	% G	%S	%L	%A	PI	Dr (%)	σ'_0 [kPa]	CSR	Test type	Spec	Reference	Liq	a	b	c	R^2_{adj}
105	OwiSand	0	73	27	0	0	-	100	0.334	CTX	Rec	Ishihara et al. (1981)	Y	1.188	0.6549	-0.2528	0.9637
106	PomiceSand_00	10	90	0	0	0	67.7	100	0.28	CTX	Rec	Orense and Pender (2012)	Y	1.063	0.6844	-0.1103	0.9986
107	PomiceSand_01	10	90	0	0	0	25	100	0.18	CTX	Rec	Orense and Pender (2012)	Y	0.6127	0.3008	0.3105	0.9881
108	PomiceSand_02	10	90	0	0	0	25	100	0.2	CTX	Rec	Orense and Pender (2012)	Y	0.7512	0.441	0.2094	0.9962
109	PomiceSand_03	10	90	0	0	0	25	100	0.22	CTX	Rec	Orense and Pender (2012)	Y	0.739	0.5661	0.1804	0.991
110	PomiceSand_04	10	90	0	0	0	25	100	0.25	CTX	Rec	Orense and Pender (2012)	Y	0.8367	0.6831	0.1028	0.9968
111	PomiceSand_05	10	90	0	0	0	25	100	0.25	CTX	Rec	Orense and Pender (2012)	Y	0.8421	0.6886	0.09701	0.9963
112	PomiceSand_06	10	90	0	0	0	70	100	0.25	CTX	Rec	Orense and Pender (2012)	Y	0.8283	0.4685	0.1321	0.9968
113	PomiceSand_07	0	100	0	0	0	-	75	0.25	CTX	Und	Orense and Pender (2012)	Y	0.6763	0.3593	0.2468	0.9959
114	QuioSand	0	100	0	0	0	43	100	0.1	DSS	Rec	PorciN and MarciaN (2010)	Y	0.8456	0.459	0.1167	0.9973
115	India_00	0	100	0	0	0	70	100	0.2	CTX	Rec	Wamy et al. (2010)	Y	0.617	0.1986	0.2468	0.9697
116	India_01	0	70	30	0	0	70	100	0.2	CTX	Rec	Wamy et al. (2010)	Y	0.7562	0.4598	0.1575	0.97

ID	Name	% G	%S	%L	%A	PI	Dr (%)	σ'_0 [kPa]	CSR	Test type	Spec	Reference	Liq	a	b	c	R^2_{adj}
117	India_02	0	50	40	10	0	70	100	0.2	CTX	Rec	Wamy et al. (2010)	Y	0.8388	0.5553	0.07682	0.9876
118	India_03	0	100	0	0	0	40	100	0.125	CTX	Rec	Wamy et al. (2010)	Y	0.5774	0.325	0.3039	0.9919
119	India_04	0	70	30	0	0	40	100	0.125	CTX	Rec	Wamy et al. (2010)	Y	0.7398	0.4238	0.1898	0.9945
120	India_05	0	50	40	10	0	40	100	0.125	CTX	Rec	Wamy et al. (2010)	Y	0.747	0.4744	0.1753	0.9928
121	India_06	0	100	0	0	0	20	100	0.1	CTX	Rec	Wamy et al. (2010)	Y	0.578	0.3614	0.3252	0.9914
122	India_07	0	70	30	0	0	20	100	0.1	CTX	Rec	Wamy et al. (2010)	Y	0.7132	0.4263	0.2257	0.9972
123	India_08	0	50	40	10	0	20	100	0.1	CTX	Rec	Wamy et al. (2010)	Y	0.7388	0.4796	0.2074	0.9984
124	India_09	0	50	40	10	0	40	50	0.1	CTX	Rec	Wamy et al. (2010)	Y	0.7704	0.3842	0.2029	0.9963
125	India_10	0	50	40	10	0	40	100	0.1	CTX	Rec	Wamy et al. (2010)	Y	0.7487	0.3959	0.1815	0.996
126	India_11	0	50	40	10	0	40	200	0.1	CTX	Rec	Wamy et al. (2010)	Y	0.6629	0.3926	0.225	0.9899
127	India_12	0	70	30	0	0	40	50	0.1	CTX	Rec	Wamy et al. (2010)	Y	0.6383	0.3646	0.303	0.9962
128	India_13	0	70	30	0	0	40	100	0.1	CTX	Rec	Wamy et al. (2010)	Y	0.6663	0.3878	0.2537	0.9944
129	India_14	0	70	30	0	0	40	200	0.1	CTX	Rec	Wamy et al. (2010)	Y	0.2837	0.3733	0.6219	0.9876

ID	Name	% G	%S	%L	%A	PI	Dr (%)	σ'_0 [kPa]	CSR	Test type	Spec	Reference	Liq	a	b	c	R^2_{adj}
130	India_15	0	100	0	0	0	40	100	0.125	CTX	Rec	Wamy et al. (2010)	Y	0.5695	0.3201	0.3153	0.9883
131	India_16	0	100	0	0	0	40	100	0.15	CTX	Rec	Wamy et al. (2010)	Y	0.6301	0.349	0.2654	0.9883
132	India_17	0	100	0	0	0	40	100	0.175	CTX	Rec	Wamy et al. (2010)	Y	0.6195	0.3308	0.2992	0.9904
133	India_18	0	100	0	0	0	40	100	0.2	CTX	Rec	Wamy et al. (2010)	Y	0.6744	0.3446	0.2566	0.9938
134	India_19	0	0	0	0	0	40	50	0.15	CTX	Rec	Wamy et al. (2010)	Y	0.6211	0.3244	0.2745	0.9911
135	India_20	0	0	0	0	0	40	100	0.15	CTX	Rec	Wamy et al. (2010)	Y	0.6483	0.3045	0.2823	0.9957
136	India_21	0	0	0	0	0	40	200	0.15	CTX	Rec	Wamy et al. (2010)	Y	0.5672	0.2368	0.3482	0.9874
137	India_22	0	100	0	0	0	40	100	0.2	CTX	Rec	Wamy et al. (2010)	Y	0.668	0.3175	0.2478	0.9951
138	SabbiaTedesca_00	0	100	0	0	0	60	50	0.8	CTX	Rec	Witchmann et al. (2010)	Y	0.4955	0.3887	0.4375	0.9938
139	SabbiaTedesca_01	0	100	0	0	0	60	100	0.4	CTX	Rec	Witchmann et al. (2010)	Y	0.5264	0.5113	0.4151	0.9997
140	SabbiaTedesca_02	0	100	0	0	0	60	200	0.2	CTX	Rec	Witchmann et al. (2010)	Y	0.4884	0.4472	0.4375	0.998
141	SabbiaTedesca_03	0	100	0	0	0	60	300	0.12	CTX	Rec	Witchmann et al. (2010)	Y	0.5402	0.523	0.4209	0.9997
142	SabbiaTedesca_04	0	100	0	0	0	63	300	0.12	CTX	Rec	Witchmann et al. (2010)	Y	0.9075	0.0874	0.0412	0.997

ID	Name	%G	%S	%L	%A	PI	Dr (%)	σ'_0 [kPa]	CSR	Test type	Spec	Reference	Liq	a	b	c	R^2_{adj}
143	SabbiaTedesca_05	0	100	0	0	0	63	300	0.12	CTX	Rec	Witchmann et al. (2010)	Y	0.9343	0.07962	0.02446	0.9931
144	SabbiaTedesca_06	0	100	0	0	0	63	300	0.12	CTX	Rec	Witchmann et al. (2010)	Y	0.9104	0.04858	0.04135	0.9955
145	NewZealand	0	80	20	0	0	-	51	0.365	CTX	Und	Bray et al. (2015)	Y	1.211	0.4233	-0.2895	0.9017
146	SilicaSand_00	0	100	0	0	0	38.3	40	0.35	CTX	Rec	Du and Chian (2015)	N	-	-	-	-
147	SilicaSand_01	0	100	0	0	0	38.6	40	0.43	CTX	Rec	Du and Chian (2015)	Y	1.149	0.4939	-0.2625	0.9455
148	SilicaSand_02	0	100	0	0	0	38.3	40	0.52	CTX	Rec	Du and Chian (2015)	Y	1.219	0.4961	-0.3389	0.9303
149	TiciNSand_00	0	100	0	0	0	-	100	0.14	CTX	N-Tr	PorciN et al. (2011)	Y	-	-	-	-
150	TiciNSand_01	0	100	0	0	0	-	100	0.15	CTX	Tr	PorciN et al. (2011)	Y	1.265	0.321	-0.4295	0.8442
151	TiciNSand_02	0	100	0	0	0	-	100	0.14	CTX	N- Tr	PorciN et al. (2011)	N	-	-	-	-
152	TiciNSand_03	0	100	0	0	0	-	100	0.15	CTX	Tr	PorciN et al. (2011)	N	-	-	-	-
153	TiciNSand_04	0	100	0	0	0	-	100	0.14	DSS	N-Tr	PorciN et al. (2011)	N	-	-	-	-
154	TiciNSand_05	0	100	0	0	0	-	100	0.15	DSS	Tr	PorciN et al. (2011)	Y	0.8494	0.4442	0.1279	0.9663
155	TiciNSand_06	0	100	0	0	0	-	100	0.33	DSS	N-Tr	PorciN et al. (2011)	N	-	-	-	-

ID	Name	% G	%S	%L	%A	PI	Dr (%)	σ'_0 [kPa]	CSR	Test type	Spec	Reference	Liq	a	b	c	R^2_{adj}
156	TiciNSand_07	0	100	0	0	0	-	100	0.33	DSS	Tr	PorciN et al. (2011)	N	-	-	-	-
157	TiciNSand_08	0	100	0	0	0	81.5	100	0.31	CTX	N-Tr	Fioravante and Giretti (2015)	Y	1.079	0.3063	-0.1761	0.9449
158	TiciNSand_09	0	100	0	0	0	-	100	0.28	CTX	Tr	PorciN et al. (2011)	N	-	-	-	-
159	TiciNSand_10	0	100	0	0	0	-	100	0.28	CTX	Tr	PorciN et al. (2011)	N	-	-	-	-
160	TiciNSand_11	0	100	0	0	0	-	100	0.28	CTX	Tr	PorciN et al. (2011)	N	-	-	-	-
161	TiciNSand_12	0	100	0	0	0	-	100	0.28	CTX	Tr	PorciN et al. (2011)	Y	1.094	0.2887	-0.162	0.9368
162	TiciNSand_13	0	100	0	0	0	-	100	0.15	DSS	Tr	PorciN et al. (2011)	Y	1.224	0.6579	-0.2919	0.9799
163	TiciNSand_14	0	100	0	0	0	-	100	0.14	DSS	N-Tr	PorciN et al. (2011)	Y	0.4415	0.376	0.5144	0.9764
164	TiciNSand_15	0	100	0	0	0	-	100	-	DSS	N-Tr	PorciN et al. (2011)	Y	0.6312	0.6724	0.261	0.9902
165	TiciNSand_16	0	100	0	0	0	-	100	-	DSS	N-Tr	PorciN et al. (2011)	Y	0.5733	0.6142	0.3482	0.9958
166	ToyouraSand_00	0	100	0	0	0	20	500	0.11	CTX	Rec	Sze and Yang (2013)	N	-	-	-	-
167	ToyouraSand_01	0	100	0	0	0	20	500	0.11	CTX	Rec	Sze and Yang (2013)	N	-	-	-	-
168	ToyouraSand_02	0	100	0	0	0	50	100	0.25	CTX	Rec	Sze and Yang (2013)	Y	0.7022	0.3735	0.2541	0.9806

ID	Name	% G	%S	%L	%A	PI	Dr (%)	σ'_0 [kPa]	CSR	Test type	Spec	Reference	Liq	a	b	c	R^2_{adj}
169	ToyouraSand_03	0	100	0	0	0	50	100	0.175	CTX	Rec	Sze and Yang (2013)	Y	0.5158	0.2486	0.3037	0.8881
170	ToyouraSand_04	0	100	0	0	0	35	100	0.4	CTX	Rec	Sze and Yang (2013)	N	-	-	-	-
171	ToyouraSand_05	0	100	0	0	0	35	100	0.4	CTX	Rec	Sze and Yang (2013)	N	-	-	-	-
172	ToyouraSand_06	0	100	0	0	0	35	100	0.225	CTX	Rec	Sze and Yang (2013)	Y	0.5681	0.2704	0.3193	0.9651
173	ToyouraSand_07	0	100	0	0	0	35	100	0.125	CTX	Rec	Sze and Yang (2013)	Y	0.5416	0.3052	0.2791	0.9311
174	ToyouraSand_08	0	100	0	0	0	45	150	0.2	CTX	Rec	Ishihara (1996)	Y	0.6902	0.4534	0.2944	0.9868
175	ToyouraSand_09	0	100	0	0	0	71.7	98	0.295	CTS	Rec	Tatsuoka et al. (1986)	N	-	-	-	-
176	ToyouraSand_10	0	100	0	0	0	78.5	98	0.3	CTX	Rec	Toki et al. (1986)	Y	0.4496	0.2204	0.4335	0.9616
177	Yatesville_00	0	83	17	0	0	-	-	-	CTX	Rec	Polito (1999)	Y	0.7972	0.6409	0.1423	0.9753
178	Yatesville_01	0	83	8	0	0	-	-	-	CTX	Rec	Polito (1999)	Y	0.7065	0.481	0.2606	0.999
179	Yatesville_02	0	83	0	0	0	-	-	-	CTX	Rec	Polito (1999)	Y	0.8125	0.5369	0.1547	0.9977
180	Yatesville_03	0	83	5	0	7	-	-	-	CTX	Rec	Polito (1999)	Y	0.9208	0.5631	0.03918	0.9968
181	Yatesville_04	0	83	0	0	19	-	-	-	CTX	Rec	Polito (1999)	Y	0.9319	0.503	0.01775	0.9987

ID	Name	% G	%S	%L	%A	PI	Dr (%)	σ'_0 [kPa]	CSR	Test type	Spec	Reference	Liq	a	b	c	R^2_{adj}
182	Yatesville_05	0	88	12	0	0	-	-	-	CTX	Rec	Polito (1999)	Y	0.6707	0.6013	0.2429	0.9975
183	Yatesville_06	0	88	12	0	0	-	-	-	CTX	Rec	Polito (1999)	Y	-	-	-	-
184	Yatesville_07	0	0	0	0	0	-	-	-	CTX	Rec	Polito (1999)	Y	-	-	-	-
185	Yatesville_08	0	0	0	0	0	-	-	-	CTX	Rec	Polito (1999)	Y	0.5681	0.5331	0.3705	0.9912
186	Yatesville_09	0	0	0	0	0	-	-	-	CTX	Rec	Polito (1999)	Y	0.6357	0.5537	0.2531	0.9933
187	Yatesville_10	0	0	0	0	0	-	-	-	CTX	Rec	Polito (1999)	Y	0.7664	0.5176	0.168	0.9984
188	Yatesville_11	0	0	0	0	7	-	-	-	CTX	Rec	Polito (1999)	Y	0.8689	0.5121	0.05907	0.9972
189	Yatesville_12	0	0	0	0	8	-	-	-	CTX	Rec	Polito (1999)	Y	0.9288	0.4162	-0.0009503	0.9964
190	Yatesville_13	0	96	4	0	0	-	-	-	CTX	Rec	Polito (1999)	Y	0.7528	0.3938	0.2049	0.997
191	Yatesville_14	0	93	7	0	0	-	-	-	CTX	Rec	Polito (1999)	Y	0.7794	0.6336	0.1624	0.9993
192	Yatesville_15	0	88	12	0	0	-	-	-	CTX	Rec	Polito (1999)	Y	0.8317	0.4545	0.1121	0.9987
193	Yatesville_16	0	74	26	0	0	-	-	-	CTX	Rec	Polito (1999)	Y	0.8605	0.5098	0.09325	0.998
194	Yatesville_17	0	100	0	0	0	-	-	-	CTX	Rec	Polito (1999)	Y	0.7928	0.6136	0.1847	0.9926

ID	Name	% G	%S	%L	%A	PI	Dr (%)	σ'_0 [kPa]	CSR	Test type	Spec	Reference	Liq	a	b	c	R^2_{adj}
195	Yatesville_18	0	50	50	0	0	-	-	-	CTX	Rec	Polito (1999)	Y	0.8342	0.2811	0.1047	0.9963
196	Yatesville_19	0	83	17	0	0	-	-	-	CTX	Rec	Polito (1999)	Y	1.008	0.4835	-0.05602	0.9899
197	Yatesville_20	0	96	4	0	0	-	-	-	CTX	Rec	Polito (1999)	Y	0.6135	0.596	0.2615	0.9869
198	Yatesville_21	0	93	7	0	0	-	-	-	CTX	Rec	Polito (1999)	Y	0.6339	0.6229	0.3138	0.9961
199	Yatesville_22	0	83	17	0	0	-	-	-	CTX	Rec	Polito (1999)	Y	0.6112	0.4413	0.3162	0.9965
200	Yatesville_23	0	74	26	0	0	-	-	-	CTX	Rec	Polito (1999)	Y	0.9504	0.9964	-0.0007288	0.9999
201	Yatesville_24	0	50	50	0	0	-	-	-	CTX	Rec	Polito (1999)	Y	0.7394	0.7172	0.1843	0.998
202	Yatesville_25	0	25	75	0	0	-	-	-	CTX	Rec	Polito (1999)	Y	0.731	0.6045	0.2195	0.999
203	Yatesville_26	0	100	0	0	0	22.5	-	-	CTX	Rec	Polito (1999)	Y	0.6737	0.4751	0.2415	0.9974
204	Yatesville_27	0	100	0	0	0	-24.45	-	-	CTX	Rec	Polito (1999)	N	-	-	-	-
205	Yatesville_28	0	100	0	0	0	-55.8	-	-	CTX	Rec	Polito (1999)	N	-	-	-	-
206	Yatesville_29	0	100	0	0	0	-	-	-	CTX	Rec	Polito (1999)	Y	0.7209	0.3722	0.2366	0.9966
207	MonteraySand_11	0	100	0	0	0	47.9	-	-	CTX	Rec	Polito (1999)	N	-	-	-	-

ID	Name	% G	%S	%L	%A	PI	Dr (%)	σ'_0 [kPa]	CSR	Test type	Spec	Reference	Liq	a	b	c	R^2_{adj}
208	MonteraySand_12	0	100	0	0	0	42.6	-	-	CTX	Rec	Polito (1999)	Y	0.3554	0.2685	0.4221	0.946
209	MonteraySand_13	0	100	0	0	0	37.4	-	-	CTX	Rec	Polito (1999)	Y	0.4382	0.2981	0.4634	0.9906
210	MonteraySand_14	0	100	0	0	0	-0.35	-	-	CTX	Rec	Polito (1999)	N	-	-	-	-
211	Pomice_00	0	75	15	10	0	-	400	0.1	CTX	Rec	Licata (2015)	Y	0.8878	0.3103	0.03056	0.999
212	Pomice_01	0	75	15	10	0	-	400	0.15	CTX	Rec	Licata (2015)	Y	0.6796	0.2246	0.2502	0.9968
213	Pomice_02	0	75	15	10	0	-	400	0.2	CTX	Rec	Licata (2015)	Y	0.8901	0.3724	0.09136	0.9988